Vincent Hahn

On 3D Laser Micro- and Nanoprinting:
Faster,
Finer, and
More Affordable

On 3D Laser Micro- and Nanoprinting: Faster, Finer, and More Affordable

Zur Erlangung des akademischen Grades eines
DOKTORS DER NATURWISSENSCHAFTEN (Dr. rer. nat.)
von der KIT-Fakultät für Physik des
Karlsruher Instituts für Technologie (KIT)

genehmigte

DISSERTATION

von

MSc. Vincent Manuel Hahn
geboren in Heidenheim an der Brenz

Tag der mündlichen Prüfung: 10.06.2022
Referent: Prof. Dr. Martin Wegener
Korreferentin: Jun.-Prof. Dr. Eva Blasco

CONTENTS

Publications

Parts of this thesis have already been published . . .

. . . in scientific journals:

- V. Hahn, F. Mayer, M. Thiel, and M. Wegener, "3-D Laser Nanoprinting", Optics and Photonics News **30**, 28–35 (2019)

- V. Hahn, P. Kiefer, T. Frenzel, J. Qu, E. Blasco, C. Barner-Kowollik, and M. Wegener, "Rapid Assembly of Small Materials Building Blocks (Voxels) into Large Functional 3D Metamaterials", Advanced Functional Materials **30**, 1907795 (2020)

- V. Hahn and M. Wegener, "Response to 'Comment on Rapid Assembly of Small Materials Building Blocks (Voxels) into Large Functional 3D Metamaterials'", Advanced Functional Materials **30**, 2003402 (2020)

- P. Kiefer, V. Hahn, M. Nardi, L. Yang, E. Blasco, C. Barner-Kowollik, and M. Wegener, "Sensitive Photoresists for Rapid Multiphoton 3D Laser Micro- and Nanoprinting", Advanced Optical Materials **8**, 2000895 (2020)

- T. Frenzel, V. Hahn, P. Ziemke, J. L. G. Schneider, Y. Chen, P. Kiefer, P. Gumbsch, and M. Wegener, "Large characteristic lengths in 3D chiral elastic metamaterials", Communications Materials **2**, 1–9 (2021)

- V. Hahn, T. Messer, N. M. Bojanowski, E. R. Curticean, I. Wacker, R. R. Schröder, E. Blasco, and M. Wegener, "Two-step absorption instead of two-photon absorption in 3D nanoprinting", Nature Photonics **15**, 932–938 (2021)

- V. Hahn, P. Rietz, F. Hermann, P. Müller, C. Barner-Kowollik, T. Schlöder, W. Wenzel, E. Blasco, and M. Wegener, "Light-sheet 3D microprinting via two-colour two-step absorption", Nature Photonics, accepted for publication (2022)

... in patent applications:

- V. Hahn, P. Müller, E. Blasco, and M. Wegener, "Parallelisierte 3D-Lithographie mittels mehrstrahliger, mehrfarbiger lichtinduzierter Polymerisation", European pat. 2019078557W (Karlsruher Institut für Technologie, June 25, 2020)

- V. Hahn, T. Messer, and M. Wegener, "Photoresist Composition, System Comprising a Photoresist Composition, Method for Producing a Three-Dimensional Structure and Use of a Photoresist Composition in 3D-Printing", pat. 21 205 242.7 (Karlsruhe Institute of Technology)

... at scientific conferences (only own presentations):

- V. Hahn, J. Qu, T. Frenzel, P. Kiefer, P. Ziemke, P. Gumbsch, E. Blasco, C. Barner-Kowollik, and M. Wegener, "Rapid Multi-Focus Multi-Photon Three-Dimensional Laser Micro-Printing", invited talk, SPIE Photonics West (San Francisco, California, USA), Feb. 4, 2020

Additional related work has already been published . . .

. . . in scientific journals:

- T. K. Claus, B. Richter, V. Hahn, A. Welle, S. Kayser, M. Wegener, M. Bastmeyer, G. Delaittre, and C. Barner-Kowollik, "Simultaneous Dual Encoding of Three-Dimensional Structures by Light-Induced Modular Ligation", Angewandte Chemie International Edition 55, 3817–3822 (2016)

- B. Richter, V. Hahn, S. Bertels, T. K. Claus, M. Wegener, G. Delaittre, C. Barner-Kowollik, and M. Bastmeyer, "Guiding Cell Attachment in 3D Microscaffolds Selectively Functionalized with Two Distinct Adhesion Proteins", Advanced Materials 29, 1604342 (2016)

- V. Hahn, S. Kalt, G. M. Sridharan, M. Wegener, and S. Bhattacharya, "Polarizing beam splitter integrated onto an optical fiber facet", Optics Express 26, 33148–33157 (2018)

- M. M. Zieger, P. Müller, E. Blasco, C. Petit, V. Hahn, L. Michalek, H. Mutlu, M. Wegener, and C. Barner-Kowollik, "A Subtractive Photoresist Platform for Micro- and Macroscopic 3D Printed Structures", Advanced Functional Materials 28, 1801405 (2018)

- L. Yang, A. Münchinger, M. Kadic, V. Hahn, F. Mayer, E. Blasco, C. Barner-Kowollik, and M. Wegener, "On the Schwarzschild Effect in 3D Two-Photon Laser Lithography", Advanced Optical Materials 7, 1901040 (2019)

- A. Münchinger, V. Hahn, D. Beutel, S. Woska, J. Monti, C. Rockstuhl, E. Blasco, and M. Wegener, "Multi-Photon 4D Printing of Complex Liquid Crystalline Microstructures by In Situ Alignment Using Electric Fields", Advanced Materials Technologies 7, 2100944 (2022)

- L. Yang, A. Rahimzadegan, V. Hahn, E. Blasco, C. Rockstuhl, and M. Wegener, "In Situ Diagnostics and Role of Light-Induced Forces in Metal Laser Nanoprinting", Laser & Photonics Reviews 16, 2100411 (2022)

. . . at scientific conferences (only own presentations):

- V. Hahn, B. Richter, T. Claus, G. Delaittre, C. Barner-Kowollik, M. Wegener, and M. Bastmeyer, "Multiple Bio-functionalization in 3D-Scaffolds Realized by Orthogonal (Photo-)Chemistry", contributed talk, DPG-Frühjahrstagung (Regensburg, Germany), Mar. 10, 2016

1

Introduction

Humans have been using subtractive and formative manufacturing methods for thousands of years to shape materials such as metal, wood, ceramic, and, more recently, plastic. Conversely, additive manufacturing is a relatively young technology that offers new possibilities. The genesis of additive manufacturing, or 3D printing, is intimately related to the emergence of the personal computer, enabling the design of 3D objects and the control of 3D printers [1]. In particular, Chuck Hull's patent application for an "apparatus for production of three-dimensional objects by stereolithography" in the year 1986 [2] and the subsequent commercialization of 3D printers mark a milestone in additive manufacturing. However, the idea of 3D printing dates further back [3].

In 1864, François Willème had already conceived a method to fabricate wooden "photosculptures" from a series of angularly spaced photographs of an object [4]. Concepts thereof are reminiscent of "computed axial tomography", a recent development in 3D printing [5, 6]. About a hundred years later, with the invention of the laser, the idea of 3D photopolymerization became popular, as evidenced by a patent from the Battelle Memorial Institute [7], describing a process for holographic recording in a photosensitive material using two intersecting beams. Around the same time, the literature student Wyn Kelly Swainson filed a series of patents for a method, materials, and an apparatus for 3D printing using two intersecting light-beams of different wavelength [8] – a concept nowadays used in light-sheet 3D printing [9–12].

Despite its short history, 3D additive manufacturing is part of a new industrial revolution as it provides several advantages over traditional manufacturing processes [1, 13]. Parts can be easily customized in additive manufacturing, which is why it is referred to as "mass-customization technology" [1]. Even complex geometries may be manufactured using 3D printing while still being more resource efficient than subtractive manufacturing. Parts do not need to be carved out of larger blocks of material, and excess printing material can often be reused [13]. Additionally, 3D printing can happen on-demand and thereby reduce the inventory

risk. Furthermore, since users may transfer 3D model data stored on a computer directly to a 3D printer, 3D printing is commonly referred to as "rapid prototyping" technology [1]. Unlike formative manufacturing, no molds are required. As a result, product development timelines can be shortened. Finally, laser-based 3D printing has enabled the fabrication of 3D micro- and nanostructures [14]. While small parts like 100 μm large gears can still be manufactured by injection molding, smaller parts remain difficult to produce through formative manufacturing. Contrarily, using 3D laser micro- or nanoprinting, complex geometries with sub-micrometer resolution can be fabricated, enabling new applications such as 3D bioprinting and micro- and nanooptics.

Despite all these advantages, 3D printing has not replaced subtractive and formative manufacturing. For some applications, this may be due to the yet limited choice of materials that can be 3D printed [1]. In general, the reluctance to adopt 3D printing in mass production is due to the lack of economies of scale. Whereas the cost per unit reduces dramatically for high-volume production in formative processes like injection molding, the cost per unit is independent of the number of fabricated parts in 3D printing [3, 13]. For a 3D printed part, the total cost comprises material, energy, and device (depreciation) cost. Obviously, the device cost can be reduced by making 3D printers more affordable. Alternatively, the device cost could be amortized by increasing the printing throughput. In the past, these two goals were mutually exclusive.

This thesis aims to provide concepts for faster and more affordable 3D printing of high-resolution polymer parts. Two approaches have emerged to achieve high printing rates in laser-based 3D printing. Either one decreases the necessary exposure time per voxel, the building block of a 3D printed part, or multiple voxels are exposed in parallel. In the first part of the thesis, both concepts are applied in multi-photon 3D laser microprinting, i.e., rapid scanning of multiple focused laser beams to achieve printing rates beyond 10^6 voxels s^{-1}. Industrial inkjet 3D printers achieve a comparable printing rate – albeit at a lower resolution. I will show that scaling up this approach even further is costly due to the used expensive ultrafast lasers. In the second part of this thesis, the requirement for ultrafast lasers and their inherent limitations is bypassed by employing a novel technique called two-step-absorption 3D printing. Using one-color two-step absorption, 3D printing with 206 nm large voxels using an inexpensive laser diode becomes possible. Finally, I will demonstrate that two-color two-step absorption enables projection-based 3D printing of microstructures with thousands of focused laser beams in parallel. Thereby, typical 3D printing jobs take less than a second.

Outline of this thesis

In chapter 2, I summarize current techniques in 3D additive manufacturing by comparing the voxel size and printing rate of 13 different 3D printing approaches. Thereafter, I focus on photopolymerization 3D printing and explain the fundamental concepts of photoresin chemistry. Thereby, I provide a definition for the term "voxel size" and discuss the importance of nonlinearities.

The remainder of the thesis is split into two parts. Part I covers the results on rapid multi-focus multi-photon 3D printing.
In chapter 3, I discuss strategies to achieve high voxel printing rates in multi-photon 3D printing. Aiming at parallelized multi-photon 3D printing, I briefly review beam splitting techniques. I then describe the design, fabrication and characterization of a diffractive beam splitter, which is used in a dedicated custom-built multi-photon 3D printing setup. This setup is employed to print functional, large-scale metamaterial crystals, the results of which are shown in chapter 4. Following the discussion of the 3D printing results, I introduce the concept of a next-generation multi-focus 3D printer.

Part II covers two-step-absorption 3D printing as a more affordable alternative to multi-photon 3D printing.
First, I present the idea of one-color two-step absorption in chapter 5. With the help of rate-model calculations, I establish the criteria for viable two-step-absorption photoinitiators which need to assert the crucial nonlinear response of the photoresin. Based on these criteria, two photoinitiator candidates for two-step absorption are selected for subsequent experiments.

One of the two photoinitiator candidates, benzil, is introduced in chapter 6. First, I discuss benzil's intermediate-state properties. Then, benzil-containing photoresins are characterized and used to fabricate 3D structures, including demanding 3D resolution benchmarks, using a compact low-power laser diode. After comparing these results with previous works, perspectives for the broad applicability of two-step-absorption 3D printing are presented.

At the beginning of chapter 7, I introduce light-sheet 3D printing, which relies on a *two-color* two-step-absorption photoinitiator. Biacetyl, the second two-step-absorption initiator molecule selected, fulfills the criteria for a good two-color two-step-absorption photoinitiator and is characterized in detail. In chapter 8, a light-sheet 3D printer tailored for the biacetyl-containing photoresins is designed from scratch. Finally, using this printer, complex 3D microstructures are fabricated in a few hundred milliseconds – as fast as the blink of an eye.

In chapter 9, I summarize this thesis and provide an outlook on future developments.

2 | Chapter 2
FUNDAMENTALS

In this chapter, I will explain the basic terminology and concepts encountered in additive manufacturing. The first section will provide a broad overview of various three-dimensional (3D) printing methods. I will then focus on photopolymerization 3D printing, for which I explain the basic 3D printing workflow and introduce the photoresin threshold and accumulation model. Finally, we will look at the photochemical processes during the radical polymerization of photoresins.

2.1 3D ADDITIVE MANUFACTURING

According to the ISO/ASTM norm 52900, 3D additive manufacturing, more commonly known as "3D printing", is defined as the "process of joining materials to make parts from 3D model data..." [15]. The elementary volume building blocks in 3D additive manufacturing from which parts are assembled are called "voxels", named in analogy to its 2D equivalent, the pixel. Voxels play a central role in 3D printing. First, because the fabrication time of a 3D part scales with the number of voxels needed to assemble the part, making high voxel printing rates desirable Second, because the "smallest part feature that can controllably be built" [15] is governed by the voxel size (see section 2.5), making small voxel sizes worthwhile to achieve a high printing resolution. However, for a constant voxel printing rate, a smaller voxel size directly entails a lower volume printing rate. Therefore, the ideal voxel size is a trade-off between adequate part resolution and a tolerable printing time. In the following, these two figures of merit, the voxel size and the voxel printing rate, are gathered and surveyed for results of thirteen different 3D printing methods. The two figures of merit, the voxel size (in units of mm) and the voxel printing rate (in units of voxels s^{-1}), are summarized for various 3D printing methods in the double-logarithmic diagram in Figure 2.1. The figure shows the voxel size on the horizontal axis, covering voxel sizes from the millimeter to the sub-micrometer range. On the vertical
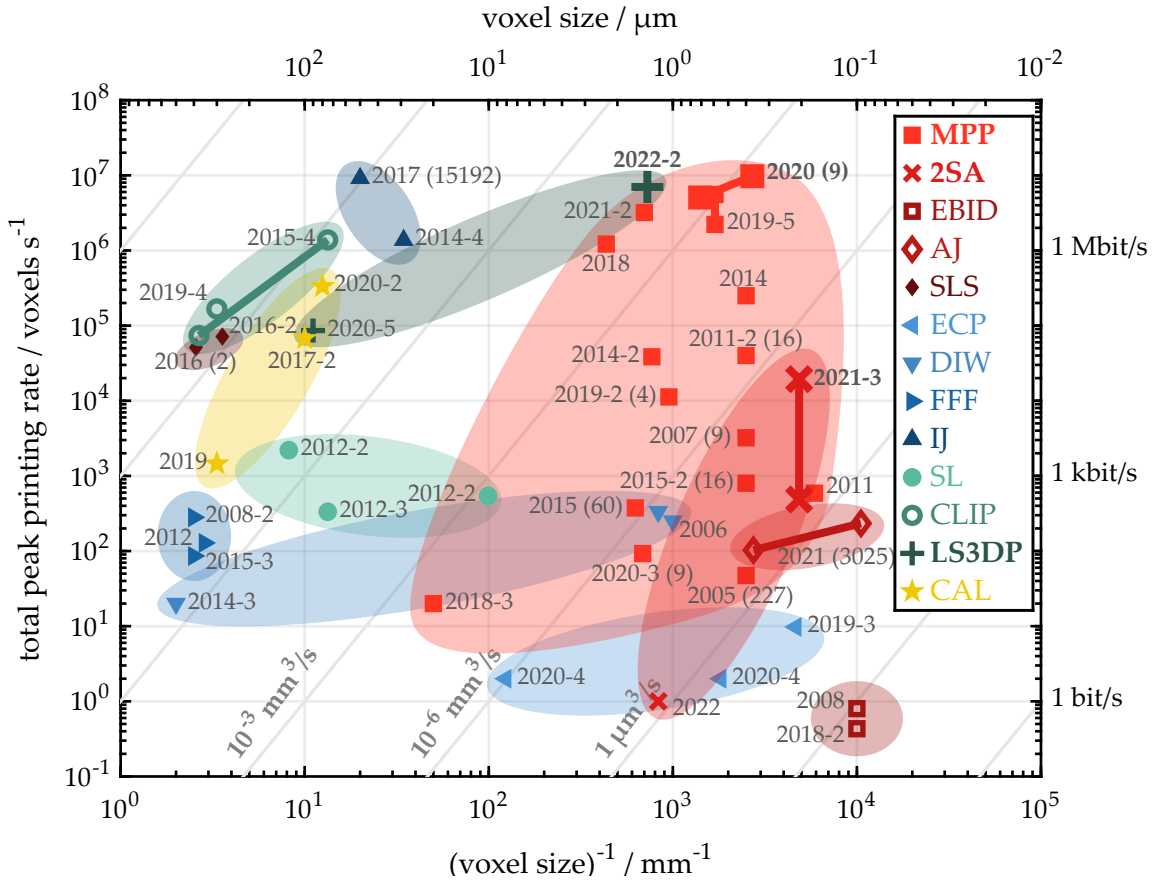
Figure 2.1: Comparison of the printing rate and the voxel size of different 3D printing methods. If multiple results are taken from a single reference, the symbols are connected by straight lines. Legend items, references, and symbols printed in bold highlight the methods and the results presented in detail in this work. Where available, the numbers in parentheses denote the number of voxels printed in parallel. Each gray diagonal line with a slope of three indicates points of constant volume 3D printing rate. The legend abbreviations are: multi-photon printing (MPP), two-step-absorption 3D printing (2SA), electron beam induced deposition (EBID), aerosol-jet 3D nanoprinting (AJ), selective laser sintering (SLS), electrochemical printing (ECP), direct ink writing (DIW), fused filament fabrication (FFF), inkjet printing (IJ), stereolithography (SL), continuous liquid interface printing (CLIP), light-sheet 3D printing (LS3DP), computed axial lithography (CAL).
The references are: 2005 [16], 2006 [17], 2007 [18], 2008 [19], 2008-2 [20] (data taken from [21]), 2011 [22], 2011-2 [23], 2012 [24] (data taken from Ref. [21]), 2012-2 [25–27] (data taken from Ref. [28]), 2012-3 [29], 2014 [30], 2014-2 [31], 2014-3 [32], 2014-4 [33], 2015 [34], 2015-2 [35], 2015-3 [36] (data taken from [21]), 2015-4 [37], 2016 [38], 2016-2 [39], 2017 [40], 2017-2 [28], 2018 [41] (preprint published in 2018), 2018-2 [42], 2018-3 [43], 2019 [5], 2019-2 [44], 2019-3 [45], 2019-4 [46], 2019-5 [47], 2020 [48], 2020-2 [6], 2020-3 [49], 2020-4 [50], 2020-5 [11], 2021 [51], 2021-2 [52], 2021-3 [53], 2022 [54], and 2022-2 [12]. This Figure is adapted from Refs. [12, 48] (CC BY 4.0).

axis, the total peak printing rate is shown, spanning the range of $0.1\,\text{voxels}\,\text{s}^{-1}$ to $10^8\,\text{voxels}\,\text{s}^{-1}$. Some of the printing methods are massively parallelized, e.g., multi-focus, multi-nozzle, and projection-based 3D printing methods. This is taken into account by plotting the *total* peak printing rate. Unfortunately, there is no established universal 3D printing benchmark structure for which the voxel size and printing rate of different 3D printing methods can be directly compared. Such a benchmark structure would include any overhead time, e.g., mechanical settling times or post-processing times. Since this data is not available for all 3D printing methods, the *peak* printing rate is summarized in Figure 2.1. The denoted voxel size is the average of the longest and shortest voxel dimension for anisotropic voxels. The labeled gray diagonals indicate a constant volume print rate. The data points are labeled with the publication year as reference code, which is linked to literature references in the Figure caption. Numbers in parentheses indicate the number of laser foci or dispenser nozzles used if this information is disclosed. An ideal 3D printer, that is a 3D printer with a small voxel size and a high printing rate, is located towards the top right in the diagram. In the following, the different print methods are briefly presented and discussed in the sequence of the legend entries.

Multi-Photon 3D Printing

In multi-photon 3D printing (MPP), also referred to as two-photon printing (2PP) or direct laser writing (DLW) [55], a focused femtosecond-pulsed laser beam is scanned through a liquid photoresin. At the laser focus position, high peak intensities electronically excite photoinitiator molecules by two-photon absorption (or, in general, multi-photon absorption). The excited photoinitiator molecules trigger a chemical reaction that solidifies the liquid photoresin. In the development step, The remaining liquid photoresin is removed in a solvent bath. Early implementations of multi-photon 3D printing were demonstrated in 1991 by Strickler et al. [56] and Maruo et al. [14]. In these works, primarily acrylic photoresin mixtures were used. In the meantime, the palette of printable materials also encompasses hydrogels [57], metals [58], and even fused silica [59]. Remarkably, already in the early publications, a lateral voxel size smaller than $1\,\mu\text{m}$ was achieved. Sub-micrometer axial and lateral voxel sizes are routinely reported for a high numerical aperture (NA) of the focusing lens. However, the voxel size also depends on the photoresin properties, e.g., the viscosity and quencher concentration [60, 61]. For single-focus 3D printing, maximum printing rates of $10^6\,\text{voxels}\,\text{s}^{-1}$ are achieved [62]. The printing rate is governed by the scanning mechanism, which is discussed in detail in section 3.2.

Multi-focus multi-photon 3D printing is a variant in which several laser foci are scanned simultaneously. Since the foci are not scanned independently, this method is suitable for 3D structures containing repetitive 2D patterns. Complete flexibility

is retained in the axial direction and outside the focus array. The first demonstrations of this technique go back to 2005, with as many as 227 foci scanned in parallel [16]. The data point labeled "2020" corresponds to the results obtained with the multi-focus 3D printing setup that is presented in chapter 3 and chapter 4. Multi-focus multi-photon with densely packed foci is problematic, since the interference of the coherent foci along the optical axis lead to Talbot planes [63, 64]. In the extreme case of projecting entire planes, the intensity decays only slowly along the optical axis. Instead of a plane, a block would be printed.

To mitigate this problem, temporal focusing has been introduced. In temporal focusing, the spectral components of the laser beam are displaced and coincide only in the focal plane. Thereby, short pulses and hence high peak intensities are only obtained in the focal plane. This technique is exploited in projection-based temporal-focusing multi-photon [47, 52]. There, amplified ultrafast pulsed lasers are used to project an entire display into the liquid photoresin, and thereby, as many as 1000 voxels are exposed by a single laser pulse [52]. Temporal-focusing multi-photon 3D printing profits further from the pulse-front tilt of the spectrally dispersed laser beam [65], leading to a line-scan effect of the focal plane [66].

Two-Step-Absorption 3D Printing

In two-step-absorption 3D printing, similar to multi-photon 3D printing (see above), a focused laser is scanned through a liquid photoresin, which comprises a two-step-absorption photoinitiator. Importantly, the photoinitiator only triggers a polymerization reaction when two photons are absorbed stepwise in rapid succession, which is more likely at high intensities, i.e., in the vicinity of the laser focus. The two-step absorption process can happen within one molecule [53] or in two molecules that transfer energy, e.g., in a triplet-triplet annihilation process [54]. In contrast to multi-photon 3D printing, continuous-wave (cw) laser diodes can be used at low laser powers, enabling compact and low-cost 3D printing setups. In chapter 6, results of two-step-absorption 3D printing are presented, for which voxel sizes of 200 nm and printing rates up to $2 \cdot 10^4$ voxels s^{-1} are achieved [53].

Electron Beam Induced Deposition

In (focused) electron-beam induced deposition (EBID), which is similar to focused ion-beam induced deposition, an electron beam is scanned through a low-pressure gas, depositing molecules from the vapor phase on a solid substrate [67]. A variety of dissimilar materials can be printed [67], however, at comparatively low voxel printing rates, which are on the order of 1 voxel s^{-1}. Furthermore, some geometries, e.g., lines perpendicular to the electron-beam, cannot easily be printed [42, 68]. Where EBID excels is in the achieved voxel size, which is only about 100 nm in size.

Aerosol-Jet 3D Printing

Aerosol-jet 3D printing (AJ) is a relatively young 3D printing technique in which a jet of charged ions and charged aerosols are deposited by electrostatic lenses on an electrically biased substrate [51]. While the maximum demonstrated printing rate of 233 voxels s^{-1} is still comparatively slow, the voxel size of 100 nm is on par with the small voxels achieved in EBID. Furthermore, the process happens in a dry atmosphere, i.e., without a photoresin or an ink. So far, the printing of several metals has been demonstrated.

Selective Laser Sintering

In selective laser sintering (SLS) and the related selective laser melting, a laser beam is focused on a flat bed of powdered material, which is thereby fused [69]. After one layer is fully exposed, a fresh layer of powder is dispensed, which is again scanned by the laser. Thereby, no support material is required. The voxel size is influenced by the powder grain size, which is on the order of 250 μm. For commercially readily available devices, peak printing rates of about 10^5 voxels s^{-1} are specified [38, 39].

Electrochemical Printing

In electrochemical printing (ECP) and the related electrohydrodynamic redox printing, metallic 3D structures are printed by locally reducing solvated metal ions in an electrochemical reaction on a conductive substrate [45, 50]. So far, printing rates up to 10 voxels s^{-1} and minimum voxel sizes of almost 200 nm are reported [45, 50].

Direct Ink Writing

In direct ink-writing (DIW), a nozzle deposits liquid ink while scanning over a substrate. On the substrate, the ink solidifies, for example, by coagulation or thermal curing [17, 32, 70, 71]. Since either the sample or the nozzle is mechanically actuated, the printing rates are comparatively low, with peak printing rates of less than 10^3 voxels s^{-1}. On the other hand, the achieved voxel size spans several orders of magnitude from 0.5 mm to 1 μm.

Fused Filament Fabrication

The probably most popular 3D printing method is fused filament fabrication (FFF), in which solid thermoplastic filament is heated and molten in an extrusion nozzle before it is deposited on a substrate. Similar to DIW, the sample or the extrusion head are mechanically scanned, leading to printing rates of below 1000 voxels s^{-1}.

The voxel size depends on the nozzle diameter and is typically on the order of $500\,\mu m$.

Inkjet Printing

Here, inkjet printing (IJ) summarizes two methods. The first method is binder jet 3D printing, which is similar to SLS in that powdered material is fused layer by layer. In contrast to SLS, the powder is not fused optically but by a liquid binding material deposited by an array of inkjet print nozzles. After printing, the hot powder bed is cooled, and unused powder is vacuumed off the 3D object. The voxel size of these methods is limited by the typically $50\,\mu m$ large powder grains, which is comparable to the inverse of the resolution at which the print head dispenses binder material. A voxel printing rate close to $10^7\,\text{voxels}\,\text{s}^{-1}$ is deduced from the volume printing rate. However, it must be emphasized that the printing rate value is an estimate and directly depends on the voxel size, which was not characterized in detail yet.

Polyjet 3D printing is the second method summarized in the IJ category. In polyjet 3D printing, droplets of photosensitive resin are deposited by an inkjet print head and subsequently cured by a UV lamp. In contrast to binder jet 3D printing, support material for overhanging features is necessary, requiring manual post-processing of 3D printed parts. For commercially available devices, a voxel size of $30\,\mu m$ and a printing rate of $10^6\,\text{voxels}\,\text{s}^{-1}$ are specified. Again, detailed resolution benchmark structures are yet missing. Noteworthy, in both methods, binder jet and polyjet 3D printing, multiple materials can be included easily in one 3D printed part.

Stereolithography

The term stereolithography (SL), which is derived from the Greek words στερεός ("solid"), λίθος ("stone"), and γράφειν ("to write"), is directly associated with Chuck Hull's infamous patent application from the year 1984 [2]. In SL, a photocurable liquid resin is photochemically cured layer-by-layer by scanned or projected ultraviolet (UV)-light. Two approaches exist. In the original top-down approach, the uppermost layer of the liquid photoresin is optically exposed, after which the solidified object is lowered into the photoresin vat. In the bottom-up approach, the light exposes the photoresin through a transparent window at the bottom of the photoresin container, and the exposed object is lifted out of the photoresin vat. A waiting time is necessary between subsequent layer exposures in both approaches, a. In the bottom-up approach, the liquid resin needs to level due to the sample's drag [25]. In the top-down approach, the printed layer must be slowly delaminated off the vat's bottom window. Thus, typical printing rates are on the order of $10^3\,\text{voxels}\,\text{s}^{-1}$[25, 27, 33] (some data points are extracted from

Fig. 4 in Ref. [28]). The photoresin's extinction, which is typically enhanced by nonreactive UV-absorbers [25], limits the penetration depth of the UV light and thereby constraints the layer height. So far, voxel sizes down to 10 µm were achieved.

Continuous Liquid Interface Production

Continuous liquid interface production (CLIP) is similar to projection-based bottom-up SL, with the difference that the window at the bottom of the photoresin vat is oxygen permeable [37]. Thereby, right above the window, the oxygen concentration in the photoresin is increased. The solvated oxygen locally suppresses the polymerization reaction of the liquid photoresin, leading to a "liquid interface" between the window and the first printed layer. Thereby, the delamination waiting time is rendered unnecessary, and the printing rate is increased, with reported printing rates exceeding 10^6 voxels s^{-1} and voxel sizes of approximately 100 µm [37]. In a further advancement of CLIP, the considerable heat generated in the photochemical processes is removed by placing the photoresin atop of an inert immiscible liquid stream, which continuously cools the photoresin [46].

Light-Sheet 3D Printing

Light-sheet 3D printing (LS3DP) is a projection-based 3D printing method in which slices of the printed object are projected into a liquid photoresin by light of a first wavelength. In contrast to CLIP or SL, the projected image is superposed with a flat light-sheet beam of a second, different wavelength. The photoresin is designed to polymerize only in locations irradiated by both wavelengths simultaneously, which can be thought of a logical AND-gate for light. Although the idea of light-sheet 3D printing was only recently published [9–11], the idea of two intersecting light beams triggering polymerization dates back to the earliest patents on 3D printing in general [3, 8]. In chapter 8 of this thesis, light-sheet 3D printing results with a voxel printing rate of $7 \cdot 10^6$ voxels s^{-1} and a voxel size of less than 2 µm are presented [12].

Computed Axial Lithography

In computed axial lithography (CAL), a liquid photoresin is exposed to projections of the printed object from multiple angles. Therefore, 2D images are projected into a rotating photoresin-filled vial. While implementations of such volumetric 3D printers are recent, the idea of reconstructing 3D objects from a sequence of angularly spaced projections dates at least back to a patent from 1864 by François Willème [3]. So far, printing rates of up to $3 \cdot 10^3$ voxels s^{-1} and voxel sizes of 80 µm have been published [5, 6, 28].
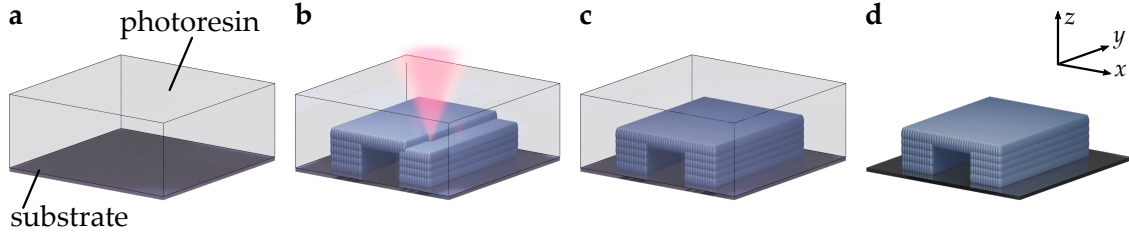
Figure 2.2: Photopolymerization 3D printing workflow. a, The substrate is coated with a photoresin. **b,** The bridge-like structure is 3D printed by scanning a focused laser beam in a line-by-line and layer-by-layer fashion. **c,** After 3D printing, the object is immersed in a developer solution (not depicted). **d,** The final 3D printed object. This Figure is based on Fig. 1a from Ref. [75].

2.2 PHOTOPOLYMERIZATION 3D PRINTING WORKFLOW

In this thesis, three different photopolymerization methods are employed, multi-photon 3D printing, two-step-absorption 3D printing, and light-sheet 3D printing. For multi-photon 3D printing and two-step-absorption 3D printing, the process workflow is shown in Figure 2.2. First, a negative-tone liquid photoresin is dispensed on a flat, transparent glass substrate, e.g., a microscope coverslip. The substrate is then mounted close to the focal plane of the objective lens in the 3D printing setup. Originally, multi-photon printing was done exclusively in the "immersion" configuration, in which the laser beam is focused through some immersion medium and the transparent substrate into the photoresin. Thereby, the maximum build height is limited due to optical aberrations and, ultimately, the free working distance of the objective lens. In the alternative "dip-in" configuration, the microscope objective lens is directly immersed in the photoresin [72]. Thereby, larger build heights are possible, and thick or opaque substrates can be used, e.g., optical fibers [73] or camera sensors [74]. Then, layer-by-layer, the photoresin is exposed and solidified by scanning the laser focus along a predefined trajectory through the photoresin.

Conceptually, the light-sheet 3D printing process shares similarities with the dip-in laser-scanning 3D printing process. However, in light-sheet 3D printing, the substrate is immersed in a vat of liquid photoresin. Further details are discussed in chapter 8.

After printing, the residual photoresin is washed-off in a solvent bath, e.g., in acetone, which only takes a few minutes. Optionally, to preserve delicate features in samples, the sample can be supercritically dried in CO_2. Therefore, the acetone-immersed sample is placed in a pressure-resistant chamber and cooled to $14\,°C$. Next, the acetone is exchanged by high-pressure liquid CO_2, after which the sample is heated above the critical point of CO_2, and the sample chamber is
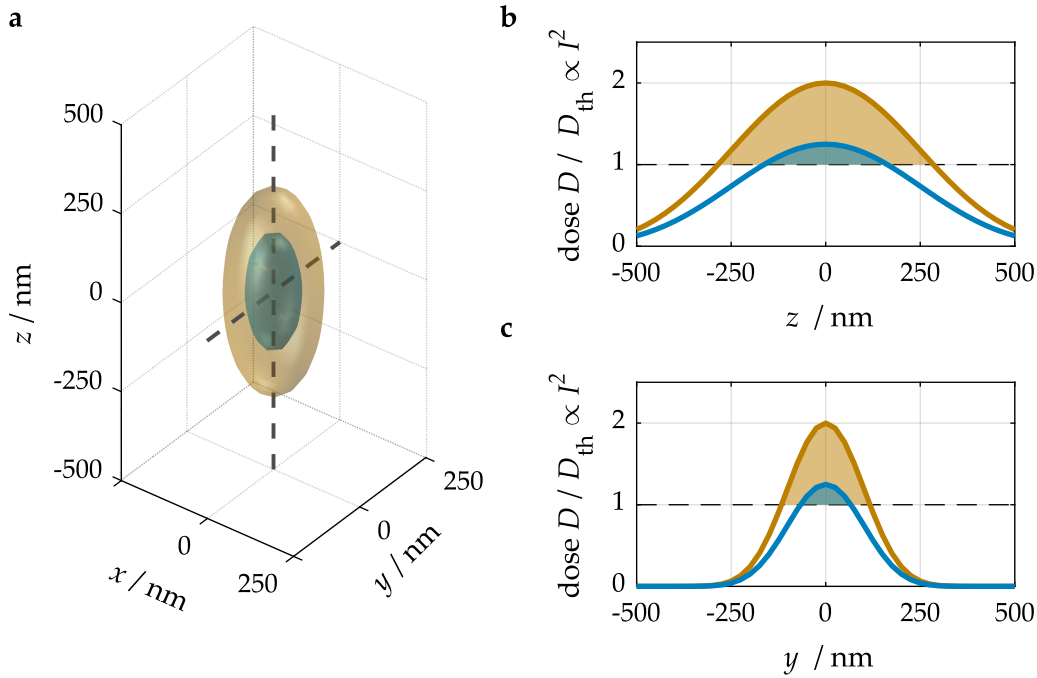
Figure 2.3: The threshold model illustrated. a, 3D isosurfaces of the squared intensity of an 800 nm wavelength laser beam, focused with an NA of 1.4. **b**, Dose profiles along the z-direction, as indicated by the black dashed line in **a**. **c**, Dose profile along the y-direction. The intensities I are calculated via the squared absolute value of the electric field. This Figure is based on Fig. 2.8 in Ref. [76].

gradually depressurized. This automated process takes about 60 min and is performed in the EM CPD300 Auto (Leica Microsystems GmbH). In contrast to other 3D printing methods [5, 11, 52], no other post-processing step, like baking or UV-curing, is necessary for the structures presented in this thesis.

2.3 THE THRESHOLD MODEL

The photochemical processes involved when exposing a photoresin are an interplay of radical generation, chain propagation, chain termination, and molecular diffusion. Solving the corresponding differential equations is a nontrivial task [60, 77]. In practice, a good approximation is given by the photoresin "threshold model", in which the complex photochemical processes are simplified by assuming that the photoresin solidifies only in locations where the exposure dose D exceeds the threshold dose D_{th}. For a single point exposure, the locally deposited dose D is given by

$$D \propto I^N \cdot t_{\text{exp}},\tag{2.1}$$

Figure 2.4: The accumulation model illustrated. In the accumulation model, the doses from three sequential, laterally displaced exposures (blue curves) add up (red curve). Hence, individual sub-threshold exposures can also lead to an accumulated dose above the threshold (red shaded area) and thereby to a solid voxel. This Figure is based on Figures in Refs. [80, 81].
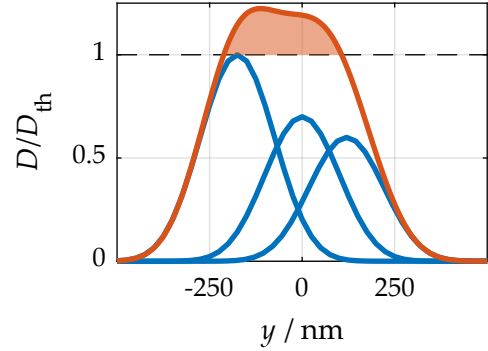
where I is the intensity, i.e., the optical power per unit area[1], t_{exp} the exposure time, and N the nonlinearity exponent, sometimes also referred to as "effective order of absorption" [78], which is $N = 2$ for canonical two-photon absorption. In polymer chemistry, the threshold, or more precisely the "gelation threshold", is formally defined via the resulting material's bulk and loss modulus [79]. For the 3D microprinting results presented herein, the threshold dose is reached when an exposed volume withstands the development procedure and can be observed, for example, with a microscope.

Figure 2.3 illustrates the thresholding process for $N = 2$ and a single voxel exposed by two differently intense laser beams. Note that the colors in the Figure do not encode a laser wavelength. The more intense laser beam results in the red voxel, with a lateral voxel diameter equal to the 220 nm squared intensity full-width half-maximum (FWHM) diameter. The less intense blue-colored beam, on the other hand, results in a voxel with a 130 nm lateral diameter. By decreasing the laser power even further, the voxel size can be made arbitrary small – at least in the context of the threshold model. This aspect will be addressed again below in section 2.5.

2.4 THE ACCUMULATION MODEL

At this point, we have not answered the question of how the resist behaves with respect to multiple temporally or spatially displaced exposures. This question is answered by the "accumulation model", which states that the photoresin locally adds up the doses of all exposures. In other words, the photoresin has an infinite memory of previous exposures. In fact, this assumption was tacitly made by the linear product with the exposure time t_{exp} in Equation 2.1. More formally, the

---

[1] The correct radiometric name for I is "irradiance". Following the convention in the field of 3D printing, it is referred to as "intensity" in this work.
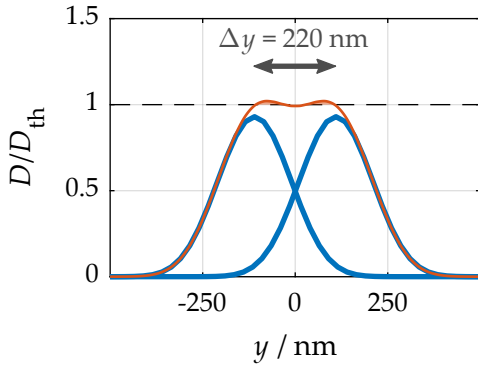
Figure 2.5: The Sparrow criterion in two-photon 3D printing. The accumulated dose profile (red curve) of two point exposures (blue curves), laterally separated by $\Delta y = 220\,\text{nm}$, has only a very shallow local minimum. This minimum vanishes for a slightly smaller spacing, $\Delta y = 200\,\text{nm}$, marking the two-photon Sparrow resolution criterion. The curves are calculated for 800 nm wavelength, nonlinearity exponent $N = 2$, and a numerical aperture of $\text{NA} = 1.4$.

total local dose obtained by multiple exposures is given by the integral

$$D\left(x,y,z\right) \propto \int I^{N}\left(x,y,z,t\right) \mathrm{d}t, \tag{2.2}$$

where $I\left(x,y,z,t\right)$ is the local intensity. The consequences of the accumulation model are illustrated in Figure 2.4, where three sub-threshold exposures (blue curves) add up to yield a total dose above the threshold (red curve) and thereby a solid voxel. The validity of the accumulation model is limited. For instance, photoresin diffusion processes, which may impact 3D printing results [60, 77], are neglected.

2.5 ON THE VOXEL SIZE AND THE RESOLUTION

Within the threshold model, the diameter of an individual voxel or the width of an isolated line does not have a lower limit and can be made arbitrarily small by a sufficiently low exposure intensity. Naively, one could also assume that gratings with an arbitrarily small pitch can be printed. However, as a consequence of the accumulation model, this is not the case.

Figure 2.5 illustrates the accumulated dose profile for two point exposures, spatially separated by $\Delta y = 220\,\text{nm}$. At $y = 0$, the accumulated dose has a shallow minimum. This minimum can be lowered underneath the threshold dose by carefully decreasing the exposure intensity, resulting in two separated voxels. However, for a slightly narrower spacing of $\Delta y = 200\,\text{nm}$, the local minimum vanishes, and the two exposures cannot be separated anymore, i.e., they are not resolved. According to the Sparrow criterion, the resolution is defined as the minimal distances Δy for which the total accumulated dose still exhibits a (local) maxima. In photopolymerization 3D printing, Sparrow's criterion limits the achievable resolution. Note that for the hypothetical case of a forgetful photoresin, i.e., a photoresin that does not obey the accumulation model, also the resolution is fundamentally unlimited. However, so far, no practical viable forgetting

photoresin has been demonstrated.

According to Sparrow's criterion, the resolution depends on the laser focus point spread function (PSF). The PSF in turn depends on the free-space wavelength λ and the numerical aperture

$$\mathrm{NA} = n\sin\left(\theta\right), \tag{2.3}$$

where n is the refractive index of the focused beam's immersion medium and θ is the maximal half-angle of the focus cone. Furthermore, since the deposited dose is proportional to I^N, the resolution also depends on the nonlinearity N of the photoresin. An approximation for the lateral resolution is given by [82]

$$\Delta y = \frac{1}{\sqrt{N}}\frac{\lambda}{2\,\mathrm{NA}}, \tag{2.4}$$

and likewise for the axial resolution

$$\Delta z = \frac{\mathrm{AR}}{\sqrt{N}}\frac{\lambda}{2\,\mathrm{NA}}. \tag{2.5}$$

In the latter formula, AR is the aspect ratio of the exposure volume, which depends on the numerical aperture NA and the refractive index n. For the parameters used in the calculation shown in Figure 2.5, the Equations 2.4 and 2.5 yield $\Delta y = 203\,\mathrm{nm}$ and $\Delta z = 508\,\mathrm{nm}$.

In summary, the diameter of an isolated voxel or the width of an isolated line is not fundamentally limited in photopolymerization 3D printing, whereas the resolution has a lower limit. Therefore, when referring to the "voxel size" in this thesis, the minimum feature size that can be achieved "in a general complex 3D architecture" [66] is meant. Within some margin, this definition of the voxel size agrees with the definition of "resolution" in the corresponding ISO/ASTM 52900 norm [15], stating that the resolution is given by the "dimensions of the smallest part feature that can controllably be built".

2.6 WHY NONLINEARITIES MATTER

When looking carefully at the photopolymerization 3D printing methods presented in section 2.1, besides CAL, all of them rely on some form of nonlinearity, e.g., multi-photon absorption or an exponential intensity decay in the photoresin. These nonlinearities are necessary to confine the optical excitation spatially. To understand this requirement, consider the case of 3D printing without nonlinearities, i.e., by (linear) one-photon absorption in a sufficiently transparent photoresin, such that the intensity decays slowly along the optical path. Upon exposure,
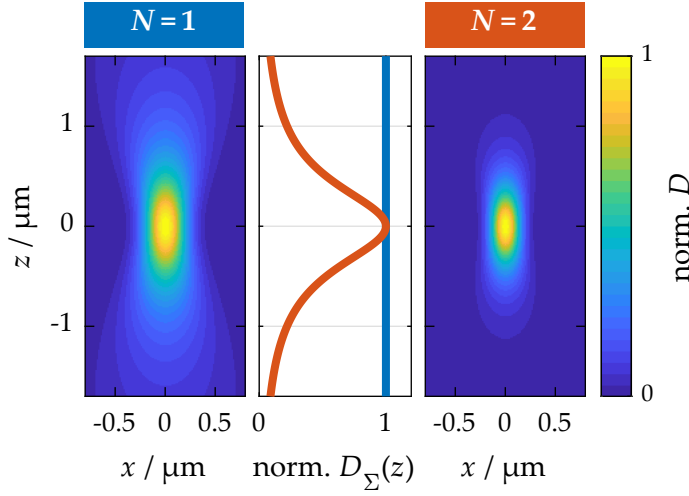
Figure 2.6: Total dose per layer for a single-voxel exposure using one-photon and two-photon absorption. For $N = 1$ (left panel, blue line), the total dose D_Σ is constant over z, whereas for $N = 2$ (right panel, red line), D_Σ rapidly decays for locations away from the focal plane. Calculations are for a Gaussian beam with 800 nm wavelength, 300 nm waist, and a refractive index of 1.5. Based on Fig. 2.3 of Ref. [76].

light is absorbed along the entire optical axis, i.e., the z-axis. For a single-voxel exposure with a focused beam, the intensity I is highest in the focus and decays quadratically in the cones of the focused beam, sufficiently far from the focal plane. Thus, the deposited dose D is maximal in the focus, allowing the printing of single voxels. Note, however, that the number of photons absorbed within each z-layer and hence the total dose per z-layer is constant[2], i.e.,

$$
D_\Sigma\left(z\right) = \iint\limits_{-\infty}^{+\infty} D\left(x, y, z\right) \, \mathrm{d}x \, \mathrm{d}y \approx \text{const.} \tag{2.6}
$$

This constant deposited dose is illustrated in the middle plot of Figure 2.6. The constant total dose becomes problematic when exposing an infinitely extended plane perpendicularly to the beam propagation axis. Then, by symmetry, the total dose deposited in the photoresin is constant everywhere, and one does not obtain the desired plane but an entire block. Hence, an exponent of $N = 1$ cannot be used to 3D print arbitrary geometries.

For larger exponents, i.e., $N > 1$, $D_\Sigma\left(z\right)$ is not constant anymore (see Figure 2.6) but is maximal in the focal plane. In this case, extended planes and other complex geometries can be printed.

The different 3D printing results for excitation with $N = 1$ or $N = 2$ are exemplified by printing a small table in Figure 2.7. There, the two different free-space wavelengths, 400 nm and 800 nm, are used to mimic a real-world example, where larger photon energies are necessary for exciting the same photoresin by one-photon absorption instead of two-photon absorption. Since the dose is proportional to the squared intensity for two-photon absorption ($N = 2$), the voxel size is

---

[2] This is only true when neglecting the weak intensity decay due to the photoresin's extinction.
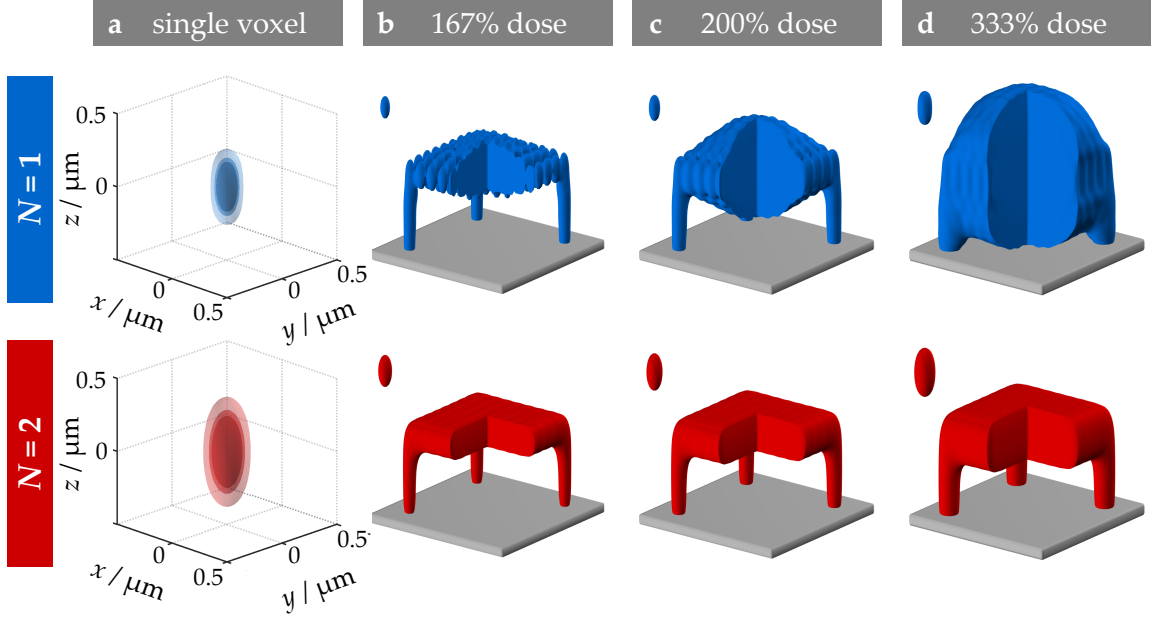
Figure 2.7: Comparison of 3D nanoprinting with one-photon absorption and two-photon absorption. **a**, Dose isosurfaces of a tightly focused beam (NA = 1.4) exposing a single voxel via one-photon absorption ($N = 1$, blue, 400 nm) or via two-photon absorption ($N = 2$, red, wavelength 800 nm) for $D = I^N = 167\% \cdot D_{th}$, $D = 200\% \cdot D_{th}$, and $D = 333\% \cdot D_{th}$ of the threshold dose D_{th}. **b–d**, Calculated dose isosurfaces when printing a 3D table with the voxels shown in panel a. The voxels are spaced by 200 nm. Despite the smaller voxels, large proximity effects can be observed for the one-photon 3D print attempt. This Figure is adapted from Ref. [83] (CC BY 4.0).

only larger by a factor of $\sqrt{2}$ than for one-photon absorption ($N = 1$). Three different exposures are considered, with single-voxel exposure doses of $D = 167\%D_{th}$, $D = 200\%D_{th}$, and $D = 333\%D_{th}$. While a single voxel is well resolved in both cases, one-photon absorption and two-photon absorption, the table is only adequately reproduced for two-photon absorption, and no processing window is available for one-photon absorption 3D printing. For low one-photon absorption doses, the center of the table is overexposed, whereas the periphery is corrugated by the voxel shape. For higher doses, the entire structure is overexposed.

It must be emphasized again that both, the threshold model and the accumulation model, describe the behavior of an idealized photoresin and do not account for nonlinear chemical processes or diffusion processes. Under extreme conditions, e.g., for long voxel exposure times or slow scan speeds, such processes potentially allow 3D printing using one-photon absorption. Examples thereof are again addressed in section 6.4.

2.7 PHOTOINITIATION

On a more fundamental level, the photochemistry in the photoresin is described by a set of chemical reactions. The initial step of the chemical crosslinking reaction in photopolymerization 3D printing is triggered by the absorption of light in a photoinitiator molecule. In the widely used free radical polymerization (see section 2.8), the photoinitiator then decays into polymerization initiating radicals $I^\bullet$. In more detail, the photoinitiator molecules are optically excited from the singlet ground state S_0 to a higher singlet state S_n. From this excited state, the molecule decays either directly to radicals or after intersystem crossing to the triplet manifold [84],

$$I \xrightarrow{h\nu} I^\bullet. \tag{2.7}$$

The optically excitable chromophore in many photoinitiators is a ketone [84]

$$\underset{R \qquad R'}{\overset{\displaystyle O}{\underset{\displaystyle \|}{}}},$$
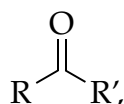
which has two typical radical decay reactions: the Norrish Type I and the Norrish Type II reaction. It should be emphasized that other photoinitiating mechanisms exist [84].

Norrish Type I reaction

The majority of commercially available photoinitiators, like Irgacure 369 or Irgacure 819, are so-called Norrish type I initiators [84], which fragment into two radicals from the excited state [84]. This fragmentation happens by a homolytic α-cleavage, i.e., the carbon-bond next to the keto-group is cleaved. For an efficient bond scission reaction, sufficient energy must be provided [84]. Typical bond scission energies are approximately 3 eV.

Norrish Type II reaction

If the bond-scission energy exceeds the provided photon energy, the Norrish type I reaction becomes improbable. In this case, an excited photoinitiator molecule may still abstract a hydrogen atom from a nearby hydrogen-donating group [84]. These Norrish type II photoinitiators are most efficient in the presence of a hydrogen-donating coinitiator like tertiary amines or an abstractable hydrogen in the gamma-position of the ketone.

2.8 FREE RADICAL POLYMERIZATION

After photoinitiation, a liquid (negative-tone) photoresin is solidified in a polymerization reaction, in which short-chain monomer units grow to large-molecular-weight polymers. Of the many established polymerization reactions in photopolymerization 3D printing, free radical polymerization is used herein. This reaction can be divided into four steps: radical generation (see section 2.7), chain initiation, chain propagation, and chain termination. The latter three steps are discussed in the nomenclature of Ref. [85].

Chain Initiation

In the second step of the free radical polymerization, generated radicals attack and attach to monomer groups, which then become a radical themselves. In this step, a polymer chain is initiated.

$$I^\bullet + M \longrightarrow I{-}M_1{}^\bullet. \tag{2.8}$$

For an acrylic monomer, this reaction proceeds as follows:
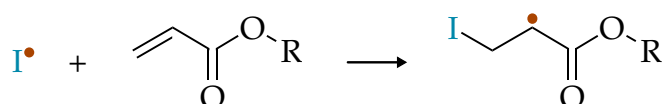
Here, R is a rest group. Other polymerizable groups used in free radical polymerization include methacrylates or styrenes, which are, however, less reactive [86].

Chain Propagation

During the chain propagation, monomer radicals continue to attack other monomer groups in a chain reaction, increasing their molecular weight. Consequently, the photoresin's viscosity increases, which gradually slows down the diffusion-driven polymerization process [87].

$$R{-}M_i{}^\bullet + M \longrightarrow R{-}M_{i+1}{}^\bullet \tag{2.9}$$
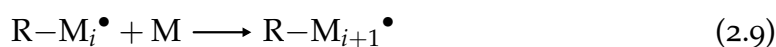
Again, R denotes a rest-group, which may be an initiator fragment I. If a multifunctional monomer, i.e., a monomer with multiple attached acrylate groups, is used, the R group may also be another acrylate group, leading to highly crosslinked polymers.

Chain Termination

The chain propagation can be terminated by one of several processes. In the *radical-radical recombination*, two radical groups react with each other and yield

a nonreactive product. This process is more likely for high concentrations of radicals.

$$R-M_i{}^\bullet + R^\bullet \longrightarrow R-M-R \tag{2.10}$$

Alternatively, two radicals can *disproportionate* if a hydrogen atom is transferred from one radical to another. However, the thereby created double-bond is prone to subsequent radical attacks [85].

$$R-M_i-M^\bullet + R-M_j-M^\bullet \longrightarrow R-M-M + R-M_j{=}M \tag{2.11}$$

The radical propagation can also be inhibited or terminated in a *radical scavenging* process by a scavenger molecule X (also referred to as quencher). These molecules may then yield a stable radical which does not propagate further [85]. One prominent scavenger is oxygen [88], which scavenges radicals at a diffusion-limited rate in typical viscous monomers [88]. In fact, the scavenging reaction is so fast that during a polymerization induction period, the chain initiation and propagation reactions are inhibited until all scavengers are locally consumed [88]. In the oxygen scavenging process, peroxy radicals are formed, which tend to not re-initiate the polymerization, but recombine readily [89].

$$R-M_i{}^\bullet + X \longrightarrow R-M_i-X^\bullet \tag{2.12}$$

The polymerization threshold directly depends on the concentration of scavengers present in the photoresin [60], which may lead to the conclusion that scavengers should be removed to obtain a low polymerization threshold. However, it was observed that scavenger-free photoresins lead to a loss of resolution in 3D laser nano- and microprinting [60, 81].

Part I

MULTI-FOCUS 3D MICROPRINTING

3

A Setup for Multi-Focus Multi-Photon 3D Microprinting
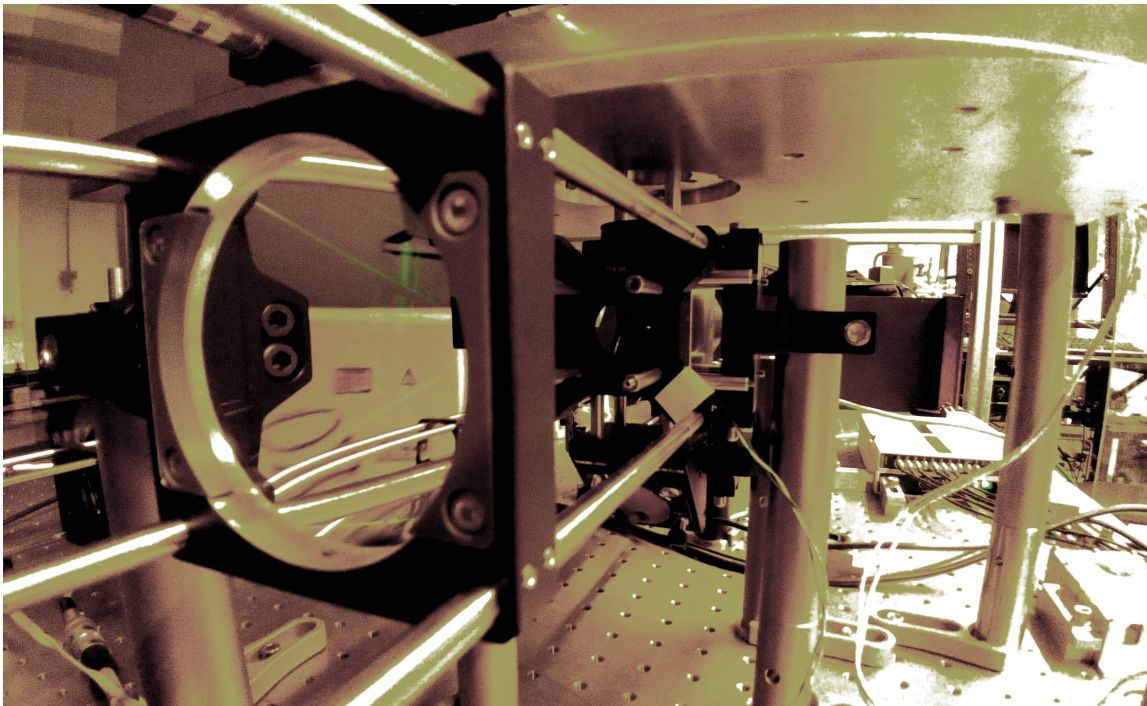
Close-up view of the tube lens, mounted in the multi-focus multi-photon 3D microprinting setup.

In this chapter, a multi-focus multi-photon 3D microprinter is presented. First, I will review different methods of laser beam splitting, including diffractive beam splitting. Next, the design, fabrication, and characterization of a diffractive beam splitter is discussed in detail. Finally, a setup specifically tailored for multi-focus 3D microprinting is described, including the electronic control of its components.

3.1 Power Scaling in Multi-Photon 3D Printing

One central aim in multi-photon 3D printing, as in other 3D printing methods, is to achieve high printing rates. To achieve high printing rates, two strategies have emerged: rapid scanning of the laser focus and printing with multiple foci in parallel. In the comparison of the total peak printing rate of different 3D printing methods in Figure 2.1, several multi-focus multi-photon 3D printing techniques are compared [16, 18, 23, 34, 35, 44, 49, 90]. Noteworthy, all of them are slower than the fastest single-focus multi-photon 3D printer [41]. At this point, one could dismiss this finding as a result of a technique that, in contrast to its single-focus pendant, is not yet fully optimized. However, the lower printing rates can also be explained by a more fundamental cause – the power scaling in multi-photon 3D printing.

For the model of multi-photon absorption 3D printing presented in section 2.3 and for fixed focusing conditions, the threshold dose D_{th} deposited in the photoresin is proportional to product of the exposure time t_{exp} times the threshold laser power P_{th} to the power of the nonlinearity exponent N, i.e.,

$$D_{th} \propto t_{exp} P_{th}^{N} = \text{const.} \tag{3.1}$$

For a canonical two-photon absorption process, $N = 2$ (see section 2.6). For multi-photon absorption, N may be even larger than 2 [91, 92]. By substituting the exposure time with the inversely proportional scan speed v_{scan} and solving for the threshold power, one obtains

$$P_{th} \propto \sqrt[N]{v_{scan}}. \tag{3.2}$$

When printing with K foci in parallel, the total power $P_{\Sigma} = KP_{th}$ becomes

$$P_{\Sigma} \propto K \sqrt[N]{v_{scan}}. \tag{3.3}$$

The total printing rate p is also directly related to the scan speed via

$$p = K \frac{v_{scan}}{d_{FWHM}}, \tag{3.4}$$

where d_{FWHM} is the voxel size.

Equation 3.3 has a profound consequence on the power scaling in multi-photon 3D printing, which is illustrated by the following example. Consider the case of single-focus two-photon 3D printing, i.e., $N = 2$, and fixed focusing conditions, i.e., $d_{FWHM} = \text{const.}$ To increase the printing rate p by a factor of 100, one can either scan 100 faster or print with 100 foci in parallel. When increasing v_{scan} by a factor of 100, the total laser power P_{Σ} increases, but only by a factor of 10.
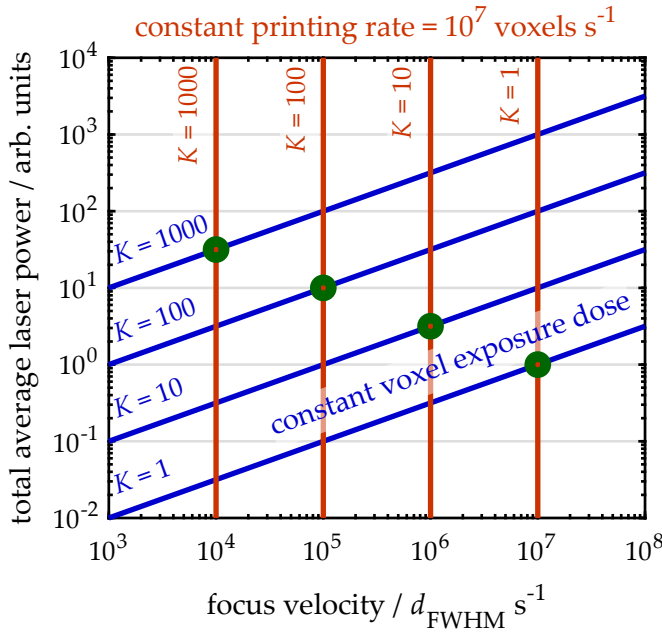
Figure 3.1: **Double-logarithmic plot of the total laser power versus the focus velocity in two-photon absorption 3D printing.** The series of blue lines (red lines) indicate a constant voxel exposure dose (constant printing rate of 10^7 voxels s^{-1}) for different integer numbers K of foci scanned in parallel. The crossings of a blue and a red line for a given K are highlighted by green dots. The solution for single-focus scanning ($K = 1$) yields the largest required scan speed, but also the lowest total power. This Figure is adapted from Ref. [83] (CC BY 4.0).

In contrast, when printing with $K = 100$ foci in parallel, the total laser power P_Σ increases by a factor of 100. Thus, for two-photon 3D printing at given voxel printing rate, it is more power economic to scan a single laser rapidly than to scan several foci slowly.

The nonlinear power scaling is also illustrated for a nonlinearity exponent $N = 2$ in the double-logarithmic diagram shown in Figure 3.1. There, the total (average) laser power is plotted versus the scan speed in voxels per second. For four different numbers of foci K, lines of constant exposure are drawn in blue. Additionally, vertical lines of the constant total printing rate 10^7 are drawn in red. The crossings of lines for a given K are highlighted by green dots, which show that the lowest total average laser power is required when scanning with one focus at the maximum scan speed. The values are calculated for *two*-photon absorption. For yet higher orders of absorption, the advantage of scanning with a single focus becomes yet more drastic.

However, there is an upper limit for the single focus printing rate, imposed by the pulsed laser's repetition rate. Each single voxel must be exposed to at least one laser pulse, which is emitted every 12.5 ns by typical 80 MHz repetition rate laser oscillators. For the condition of a single-pulse exposure, a threshold laser power of 110 mW can be extrapolated from the point exposure experiments shown in Fig. 3c in Ref. [77]. This is almost 30 times lower than the 3 W output power of typical femtosecond-pulsed Ti:Sa lasers used in multi-photon 3D printing [48, 83]. Thus, since the voxel printing rate is currently not limited by the laser power but by the laser scan speed, parallelized multi-photon printing is an attractive avenue

for faster multi-photon 3D printing.

3.2 BEAM SCANNING

While the voxel printing rate is ultimately limited by the pulse repetition rate, a more practical limit to the maximum scan speed is imposed by the used scanning method, which can be either sample scanning or focus scanning.

In the sample scanning method, the printing substrate is actuated and scanned along a trajectory by a stage. While nanometer-precision stages achieve scan speeds of some decimeters per second, due to the inertia of the sample and the stage, these speeds are only reached after comparably long acceleration times. These long acceleration times are an overhead, leading to long printing times.

In the beam scanning method, the laser beam is deflected by an angle α. The deflected beam is then focused by a lens of focal length f, resulting in a displaced laser focus position d

$$d = \tan{(\alpha)}\, f \approx \alpha f. \tag{3.5}$$

The small-angle approximation is justified by the maximum scan angle of $\pm 4.3°$ at the entrance pupil of the microscope objective lens[1]. By this equation, the angular scan rate $\dot{\alpha}$ can be converted to a spatial scan speed.

However, the voxel printing rate not only depends on the scan speed, but also on the focus diameter (see section 2.5), which in turn depends on the NA. This dependency is taken into account in the comparison of the scan rates of several types of beam scanners in Ref. [93]. The scan rate is calculated by dividing the angular scan rate $\dot{\alpha}$ by the angular $1/e^2$ beam radius (i.e., the beam divergence). To obtain a voxel print rate that is comparable to the values in Figure 2.1, the angular $1/e^2$ beam radius θ_{e^2} of the truncated and focused Gaussian beam is converted to the FWHM angular diameter θ_{FWHM} by [94]

$$\theta_{\text{FWHM}} = 1.24\theta_{e^2}. \tag{3.6}$$

Beam deflection methods can be classified into two categories: periodic deflectors and random-access deflectors [93]. Periodic deflectors, like rotating polygon mirrors and resonant scanners, continuously deflect the beam with a fixed angular amplitude and frequency and achieve scan rates of up to $2 \cdot 10^7$ voxels s^{-1} [93, 95]. The high scan speed is contrasted by three disadvantages. First, due to the fixed scanned amplitude, the laser focus is always scanned across the entire field of view [96]. Hence, when printing a 3D object with narrow lateral dimensions, a

---

[1] Calculated for Zeiss objectives with a field number of 25.

periodic scanner unnecessarily scans the void periphery of the scan field. Second, the variable scan speed of resonant scanners along each scanned line complicates the printing with uniform voxel size and material properties [41]. And third, periodic deflectors fix the hatching axis. In a typical periodic deflector 2D beam scanner, only one of the two scan axes, the hatching axis, is a periodic deflector, whereas the other axis is scanned by a slower scanner. In multi-photon 3D printing, the hatching direction is a pivotal degree of freedom. For instance, one would rarely like to print a line grating with the hatching axis oriented perpendicular to the ruling. Thus, periodic scanners can be useful for certain applications in multi-photon 3D printing [41], but their fixed amplitude and frequency constrain the 3D printing flexibility.

The second category of beam deflectors, random-access deflectors, can be steered to and halted at arbitrary positions within the scan field. Thereby, the scan field size can be adjusted to the 3D printed structure's dimensions and the hatching direction in 2D scanners is arbitrary. Random-access deflectors can be divided further into two types, which are scanners with and without moving mass.

Acousto-optic and electro-optic deflectors belong to the type of scanners without moving mass, reaching large printing rates of almost 10^8 voxels s^{-1} [93]. This rate is comparable to the repetition rate of typical mode-locked lasers, which ultimately limits the printing rate. Both, acousto-optic and electro-optic deflectors, have one major drawback: their limited resolution, i.e., the number of voxels that fit inside the scan field. In Ref. [93], the acousto-optic deflector with the largest scan field encompasses 322 voxels, i.e., the scan field is 322 times larger than the voxel FWHM. Electro-optic deflectors have a yet lower resolution of 80 voxels [93]. For comparison, the scan field of a numerical aperture NA = 1.4 microscope objective lens (FWHM spot-size 324 nm [94] at 800 nm wavelength) with a aberration-corrected field of view diameter of 625 μm offers a resolution 625 μm/0.324 μm voxel^{-1} = 1930 voxels of resolved FWHM spots[2].

Besides the low resolution, acousto-optic deflectors are not ideally suited for ultrashort pulsed laser beams. In an acoustic-optic deflector, the laser beam is diffracted by a photoelastic material, whose refractive index is spatially modulated by an acoustic wave with variable frequency. This has three consequences. First, the diffractive nature of the deflectors leads to an angular dispersion of the longitudinal modes of the finite-bandwidth laser beam [97], whereby deflected beams smear out when focused. Second, as a direct consequence of the angular dispersion, the pulse front of the laser beam is tilted [65], which increases the pulse length and decreases the effective numerical aperture of the focused beam. Third, the group velocity dispersion of the photoelastic material leads to a chirped

---

[2] This calculation neglects the nonlinear excitation. For a two-photon process, the resolution would be larger by a factor $\sqrt{2}$.

Figure 3.2: Photograph of a galvanometer scanner. The mirror (right) is attached to the shaft of the motor. The base of the scanner contains electronic connectors for the connection to the driver board. For scale, a metric centimeter-scaled ruler is placed in front of the scanner.

pulse and thereby to an increased pulse length. Thus, due to the low resolution of electro-optic deflectors and the dispersive function of acousto-optic deflectors, both are of limited use in multi-photon absorption 3D printing – despite their fast printing rate.

Galvanometer scanners belong to the second type of random-access deflectors, the moving-mass scanners. Figure 3.2 shows a photograph of a galvanometer scanner, which consists of as deflection mirror mounted on the shaft of a motor [96]. The motor contains a magnetic rotor [98] which is mounted within an electromagnetic stator. Electrical currents in the stator coils change the stator's magnetic field and drive the rotor to a controlled rest position. Galvanometer mirrors were used already in the early days of laser-scanning 3D micro- and nanofabrication [99, 100].

Compared to acousto-optic and electro-optic scanners, galvanometer scanners and moving-mass deflectors offer lower scan rates, with peak printing rates of approximately 10^6 voxels s^{-1} [93]. However, the field of view of galvanometer scanners has a resolution of more than 10^4 voxels [93], exceeding the field of view of high-end microscope objective lenses. Since galvanometer mirrors offer the largest field of view and the largest scan rates of current moving-mass deflectors [93], they are the beam deflection method of choice for multi-photon 3D printing of arbitrary structures.

3.3 BEAM SPLITTING

The maximum printing rate of galvanometer scanners can be directly converted to a voxel exposure time of $t_{exp} = 1\,\mu s$. At such short exposure times and for focusing with an NA of 1.4, the polymerization threshold power of sensitive multi-photon photoresin is approximately $30\,mW$ [83]. This threshold laser power is two orders of magnitude lower than the output power of femtosecond-pulsed Ti:Sa lasers used in multi-photon 3D printing [48, 83], leaving plenty of laser power for printing with multiple foci in parallel.
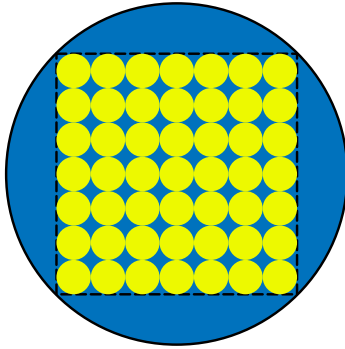
Figure 3.3: Packing of a square microlens array into a circular beam. For an infinite number of microlenses (illustrated by the yellow disks), only 50 % of the homogenized, round laser beam wavefront (blue) is covered. While more microlenses could be fitted in the beam area, stitching then becomes problematic.

To print with multiple foci in parallel, the laser beam must be split into individual beamlets. From the available passive beam splitting approaches [101], the two most commonly used ones for multi-focus multi-photon 3D printing are microlens arrays [16] and diffractive beam splitters [18, 23, 34, 35, 44, 49, 90]. In the following, the strengths and weaknesses of both approaches are discussed.

3.3.1 Refractive Beam Splitting

In a microlens array beam splitter, the wavefront of a laser beam is sampled in the transverse propagation direction by an array of, typically refractive, microlenses, which focus the beam to individual spots. The thereby created spot array is then imaged and tightly focused into the liquid photoresin for multi-focus multi-photon 3D printing.

Compared to diffractive beam splitters, the ultrashort pulses of the laser beam are not affected by refractive microlens arrays, which is desired in multi-photon 3D printing. However, microlens arrays have several weaknesses. First, if the microlens array is illuminated by a Gaussian-shaped laser beam profile, the intensity of the generated spots will vary across the aperture of the laser beam. Ideally, the spot intensity is uniform. To overcome this, the diameter of the laser beam can be increased, such that only the center portion of the beam profile is used [16]. This, of course, goes along with significant power losses. Alternatively, the laser beam can be converted from a Gaussian to a flat-top profile before reaching the microlens array [102, 103]. Nowadays, such beam shapers are available off-the-shelf as refractive telescopes. But even when using a homogenized beam, power losses have to be taken into account due to the limited packing density of the microlenses. For instance, consider the array of microlens arranged on a square lattice in Figure 3.3. Half of the input power is focused by the microlenses when neglecting any reflection and absorption losses.

3.3.2 *Diffractive Beam Splitting*

A diffractive beam splitter works by locally modulating the wavefront's amplitude, the phase, or both. The wavefront modulation for beam splitters is a periodic pattern, i.e., a grating, across the wavefront. The efficiency of diffractive beam splitters, that is the fraction of the total power which is diffracted into the desired spot array, can be as large as 90 % [104]. Such high efficiencies are achieved by phase masks, i.e., diffractive optical elements (DOEs) in which only the phase is modulated.

In multi-photon 3D printing, ultrashort pulsed lasers with a finite spectral bandwidth are used. For instance, the spectral bandwidth of a transform-limited 85 fs long pulse at 800 nm central wavelength wavelength has a spectral bandwidth of 8 nm. When diffracted by a DOE with grating constant g, the finite bandwidth of the laser leads to a spatially broadened angular diffraction pattern since the first-order diffraction angle α is proportional to the wavelength λ (see Figure 3.4a):

$$\frac{\lambda}{g} = \sin(\alpha) \approx \alpha. \tag{3.7}$$

Hence, when focusing a diffracted pulsed laser beam, the spread-out angular pattern translates into a spatially spread-out PSF, as illustrated in Figure 3.4b. According to Equation 3.5, the width Δd of the spread-out PSF is

$$\frac{\Delta d}{d} = \frac{\Delta \lambda}{\lambda}, \tag{3.8}$$

where d is the displacement of the focus from the optical axis. Of course, the value of Δd is only meaningful in comparison with the diffraction-limited PSF diameter d_{FWHM}. By expressing the displacement d in units of d_{FWHM}, one obtains

$$\frac{\Delta d}{d_{\mathrm{FWHM}}} = \frac{\Delta \lambda}{\lambda} M. \tag{3.9}$$

Here, M is a unit-less number, denoting distance of the diffracted laser focus from the optical axis, measured in the FWHM voxel diameter. Taking again the above example with $\lambda = 800$ nm and $\Delta \lambda = 8$ nm, then $\Delta d = d_{\mathrm{FWHM}}$ for $M = 100$. In other words, when the focus is diffractively deflected by 100 voxels, the effect of the angular dispersion is as large as the diffraction-limited PSF size.

In addition to the angular dispersion, the DOE induces also a pulse front tilt [65], which is illustrated by the dashed black lines in Figure 3.4a. The pulse front tilt has two consequences. First, the pulse front tilt temporarily stretches the pulse in the focal plane. This stretched pulse decreases the two-photon absorption rate.
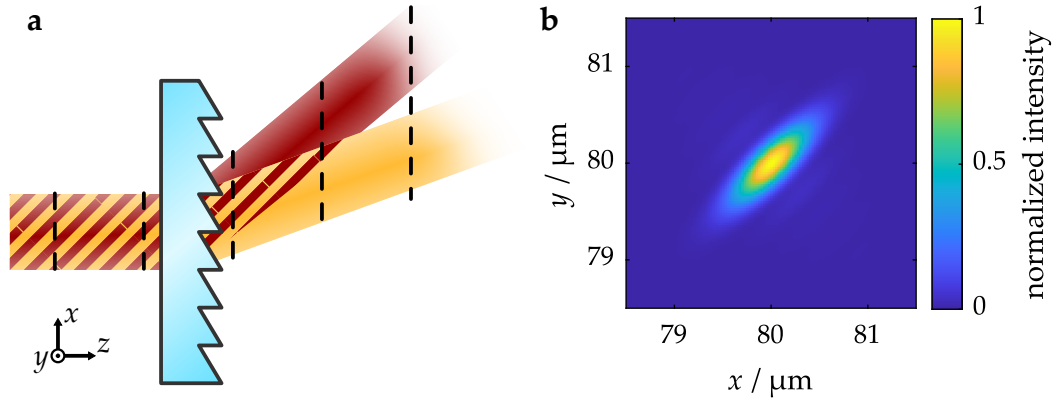
Figure 3.4: Angular dispersion of a diffracted laser beam. a, Schematic illustration of the angular dispersion, exemplified by two longitudinal modes of a broadband laser beam, diffracted at a blazed grating. The diffraction angle is proportional to the wavelength, which is represented by the beam colors. The dashed lines indicate the pulse front, which is tilted with respect to the diffracted beam wavefronts. For clarity, the drawn dimensions and angles are not to scale. **b**, False-color intensity diagram of a calculated, *lateral*-cut PSF with a spectral FWHM of $\Delta\lambda = 8\,\mathrm{nm}$, diffracted with $M = 250 \cdot \sqrt{2}$ and focused with a lens of NA 1.4 and a focal length $f = 4.12\,\mathrm{mm}$. The PSF-computations are obtained from the algorithm presented in Ref. [105]. The algorithm was implemented by Joachim Fischer.

For constant pulse energy, the two-photon absorption rate is proportional to the inverse of the pulse length [106]. The second consequence of the pulse front tilt is an effectively decreased NA of the laser focus. The tilted pulse front scans across the entrance pupil of the objective lens, filling only a fraction of the pupil at a time. In fact, tilted pulse fronts are exploited in temporal-focusing multi-photon 3D printing [47, 52, 66].

3.3.2.1 *Angular Dispersion Compensation*

The angular dispersion and hence the spread-out PSF can be compensated by a refractive Keplerian telescope, which was originally presented by Hu et al. in Ref. [97]. The telescope is designed to have a magnification inversely proportional to the wavelength λ [97]. This intended chromatic aberration is achieved by four lens-doublets, consisting of glasses with high and low dispersion [97]. The angular dispersion compensation is then converted to a transverse-spatially chirped beam, i.e., the wavelength varies transversely across the pulse front, which can again lead to a tilted pulse front by propagating through group velocity dispersive media [65]. However, from ray tracing calculations it can be seen that for a laser beam with a spectral bandwidth of 8 nm, the spatial displacement of the longitudinal modes is less than 150 μm, which is small compared to the later used laser beam diameter of 6 mm.

In summary, the combination of a DOE and the dispersion-compensating telescope offers an efficient method of laser beam splitting. The authors of the publication [97] kindly provided two sets of anti-reflection coated telescopes for the setup presented below. Next, the design, fabrication, and characterization of a suitable DOE is discussed.

3.3.2.2 Resolution of Diffractive Beam Splitters

When splitting the laser beam into beamlets and hence separated foci, it is important to space them sufficiently apart for two reasons. First, if the focused beamlets are in close proximity, interference effects arise in the form of Talbot planes along the optical axis [63, 64]. Second, a sufficient spacing allows a higher resolved unit cell, that is, more voxels fit (laterally) inside one unit cell. The lateral unit cell resolution can be conveniently expressed by the fraction of the focus spacing d_{focus} and the voxel FWHM diameter via

$$M = \frac{d_{\text{focus}}}{d_{\text{FWHM}}}. \tag{3.10}$$

In this equation, d_{focus} can be expressed by the grating constant g, the center wavelength λ and the focal length f using Equation 3.7 and Equation 3.5 as

$$d_{\text{focus}} = \frac{\lambda}{g} f. \tag{3.11}$$

Furthermore, λ and the NA determine the FWHM focus diameter [94] by

$$d_{\text{FWHM}} = 0.567 \frac{\lambda}{\text{NA}}. \tag{3.12}$$

Inserting both expressions into Equation 3.10 yields

$$M = \frac{\text{NA}f}{0.567g}, \tag{3.13}$$

which can be further simplified with the relation for the pupil diameter $D_{\text{pupil}} = 2\,\text{NA}f$ [96] to

$$M = 0.88 \frac{D}{g}. \tag{3.14}$$

Thus, the focus spacing and hence the lateral unit cell resolution is directly related to the number of grating periods in the (conjugate) objective lens pupil D_{pupil}/g. As an example, for a focus spacing of $M = 250$ voxels, the objective lens pupil must span 284 grating periods.
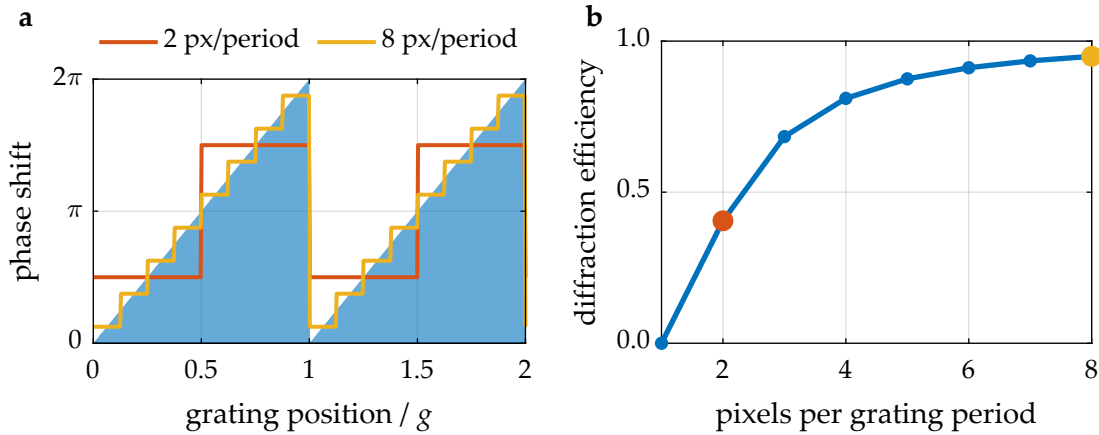
Figure 3.5: Diffraction efficiency of stepped blazed gratings. a, Phase profile of an ideal blazed grating (blue) and pixelated approximations thereof (red and yellow). **b**, Plot of the first-order diffraction efficiency, i.e., the fraction of the total power diffracted into the first order, versus the pixels per grating period. These results are based on the calculations in Refs. [107, 108]

Equation 3.14 imposes a first resolution criterion for the DOE. To obtain an efficient beam splitter, a second resolution criterion for DOEs is derived. Typically, a phase-only DOE approximates a locally phase-modulated wavefront profile by an array of pixels, which is exemplified in Figure 3.5a. There, a simple blazed grating is approximated by individual pixels, i.e., discrete steps. This discretization affects the diffraction efficiency, i.e., the fraction of power diffracted into the first order [108]. The calculated diffraction efficiency of the pixelated blazed grating is plotted in Figure 3.5b. For the grating with only two steps per period, the efficiency is only 40 % [108]. For higher resolved gratings, the diffraction efficiency increases. This example illustrates that a finer pixel-sampling of the DOE yields higher diffraction efficiencies.

In summary, a high pixel-resolution of the DOE is desired in order to achieve high diffraction efficiencies and large deflection angles. Previous instances of multi-photon 3D printing employing diffractive beam splitter either used spatial light modulators (SLMs) [23, 34, 35, 90] or static phase masks (DOEs) [18, 49]. A SLM consists of an array of electronically addressable pixels, e.g., liquid crystal cells or deformable mirrors, with variable adjustable phase retardance [108]. While the phase profile of common liquid crystal SLMs can be adjusted within milliseconds, they have four key disadvantages. First, state-of-the-art devices offer a pixel resolution of up to 2160 px across the diameter of a round laser beam[3]. Second, due to their limited fill factor of about 90 %, a significant portion of light is unaffected by the applied phase pattern and diffracted into the zeroth

---

[3] The reflective EXOLUS-4K1 from Thorlabs GmbH is used as exemplary device.

order. Third, owed to the reflectance of approximately 65 %, the throughput is comparably low. And finally, the phase profile of most SLMs jitters temporarily due to the time-modulated voltage with which pixels are addressed. Thereby, the diffracted beamlet intensities I vary temporally, which is especially critical in multi-photon 3D printing, where the deposited dose is proportional to I^N. All four aspects currently make SLMs unattractive for beam splitting applications in multi-focus multi-photon 3D printing.

In static phase masks, the phase of a wavefront is modulated by wavelength-scale height variations on the surface of an optical element. Within the thin-element approximation [109], the phase $\Delta\phi$ is assumed to change proportionally to the local height h_{DOE} of the surface profile and the difference of the refractive index Δn of the DOE and the surrounding:

$$\Delta\phi = \frac{2\pi}{\lambda}\, h_{\mathrm{DOE}}\, \Delta n. \tag{3.15}$$

The height profile of DOEs is commonly manufactured in a photolithographic layer-by-layer process [96]. Therefore, the phase profile of a DOE is static and cannot be updated within milliseconds, in contrast to the phase profile obtained by SLMs. However, DOEs can be fabricated with centimeter-large apertures and micrometer-small pixel sizes, hence offering an exceedingly large pixel resolution [110]. Furthermore, a high pixel filling fraction and a low material absorption ensure a high transmittance. And, finally, in contrast to SLMs, DOEs do not suffer from pixel jitter, and hence diffract with a constant temporal beamlet intensity. In conclusion, for multi-focus multi-photon 3D microprinting, DOEs are more attractive beam splitters than SLMs.

3.4 DESIGN AND FABRICATION OF A DIFFRACTIVE OPTICAL ELEMENT

Commercial DOEs are fabricated by lithographic methods, relying on costly sets of electron beam written chrome masks, which is cost-efficient only for large-scale productions. An alternative production method for small batches is given by laser direct-writing[4], in which a power-modulated laser beam scans over a photoresin-coated substrate and locally changes the photoresin's solubility [111]. The height of the surface profile is modulated either by varying the laser power (grayscale laser writing) [111] or by printing several binary layers, stacked on top of each other. The latter can be achieved by multi-photon 3D printing, where the nonlinear absorption locally confines the excitation.

---

[4] In the past, the term "laser direct-writing" has been used for one-photon and multi-photon absorption printing. Here, both are implied.

As outlined above, to achieve high diffraction efficiencies at large deflection angles, a large DOE pixel count, i.e., resolution, is required. The high DOE resolution can be either achieved by printing small pixels or by printing a large-area DOE, both of which have technical limits. The DOE diameter directly affects the fabrication time since laser direct-writing is a serial process. On the other hand, the voxel size of the focused direct-writing laser beam places a constraint on the lateral resolution and hence the pixel size. A set of feasible printing parameters is found in preliminary multi-photon DOE printing trials. For a focus NA of 1.4 and a scan velocity of $10\,\mathrm{mm\,s^{-1}}$, a $30\,\mathrm{mm^2}$ large eight-layer DOE was printed in less than $50\,\mathrm{h}$. With the used pixel size of $2\,\mathrm{\mu m} \times 2\,\mathrm{\mu m}$, the DOE has a resolution of $3000\,\mathrm{px}$ across its diameter.

To compute the phase profile, an iterative Fourier transform algorithm based on Ref. [112] is implemented. In this algorithm, the far-field diffraction pattern is obtained from an initially (randomly) guessed phase profile by computing its Fourier-transform. Then, the amplitude of the far-field pattern is replaced by the target amplitude, whereas the phase is retained. The coerced far-field pattern is then propagated back to the DOE plane by computing the inverse Fourier transform. The amplitude is replaced by a uniform amplitude in the DOE plane while retaining the phase profile. This cycle is repeated until a satisfactory DOE efficiency and fidelity is obtained. During the optimization, the phase is gradually coerced to eight discrete levels [113].

The target far-field intensity distribution for the diffractive beam splitter is shown in Figure 3.6a. The $2.1°$-spaced 3×3 square array of beamlets is computed for the center wavelength $\lambda = 790\,\mathrm{nm}$, which is also used in the later experiments. Note that the far-field is computed for few DOE periods ($M = 7$). Therefore, the size of the diffracted spots is pixelated and exaggerated in the figure. With the DOE diameter of $6\,\mathrm{mm}$, the targeted diffraction angle corresponds to $M = 240$. Hence, the focused beamlets are spaced by 240 times their FWHM focus diameter. This value is a compromise between the finite field of view of the dispersion-compensating telescope and a high unit cell resolution. In fact, at the targeted diffraction angles, the dispersion-compensating telescope already introduces noticeable aberrations on the diffracted beamlets and thereby reduces the focused peak intensity. To counteract these aberrations, the designed intensity of the diffracted beamlets increases proportionally to the diffraction angle.

Figure 3.6b displays a DOE, which is calculated for the target distribution. The DOE consists of eight individual levels and a $11 \times 11\,\mathrm{px}$ large unit cell (white-dashed outline). The corresponding far-field intensity distribution is shown in Figure 3.6c, plotted on a logarithmic color scale on which also higher diffraction orders are visible. While the target intensity distribution has a four-fold rotational
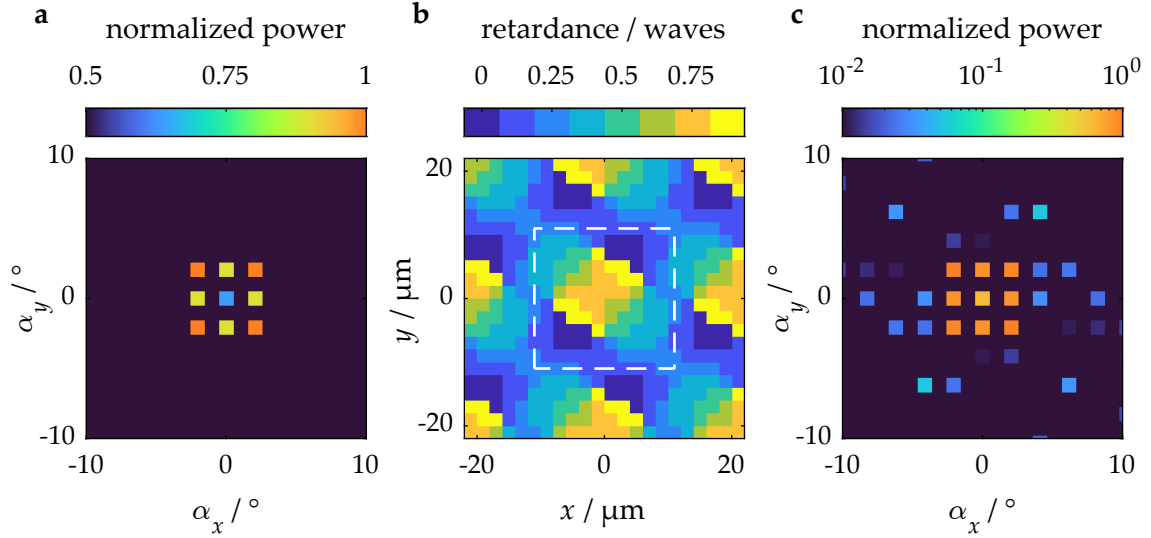
Figure 3.6: Design of the diffractive optical element (DOE). a, False-color diagram of the normalized target power distribution. To pre-compensate aberrations in the periphery of the field of view caused by the dispersion-compensating telescope, the power is intentionally lower for the zero-order peak than for the higher orders. The angular scale is valid for a center wavelength $\lambda = 790\,\text{nm}$. **b,** Designed DOE. The white dashed line outlines a single unit cell. **c,** Far-field diffraction pattern of the DOE shown in **b**. In contrast to the linear colormap in panel a, a logarithmic colormap is chosen, such that the power diffracted into higher orders becomes visible. The diffraction efficiency, that is, the fraction of power diffracted into the nine target orders versus the incident power, is 89 %.

symmetry, this symmetry is not present in the DOE and in the computed far-field intensity diagram. While it is possible to enforce the four-fold symmetry during the iterative Fourier-transform algorithm, the diffraction efficiency of symmetric solutions is significantly lower.

The DOE is fabricated by multi-photon printing in a multi-photon 3D printer (Photonic Professional GT, Nanoscribe GmbH). A silanized $22 \times 22\,\text{mm}$ large, $170\,\mu\text{m}$ thick borosilicate-glass coverslip serves as printing substrate. To avoid photoresin run-off during the print job, a polydimethylsiloxane (PDMS)-ring is placed on the coverslip, into which a droplet of photoresin (IP-L, Nanoscribe GmbH & Co. KG) is dispensed. This photoresin is designed for oil-immersion printing (Immersol 518F, Carl Zeiss AG) and used with a high-NA microscope objective lens (Plan-Apochromat $63\times$/NA1.4, Carl Zeiss AG). The printing speed is set to $10\,\text{mm}\,\text{s}^{-1}$ and the laser power to $17\,\text{mW}$, measured at the objective lens entrance pupil. Furthermore, a hatching distance of $143\,\text{nm}$ is used.

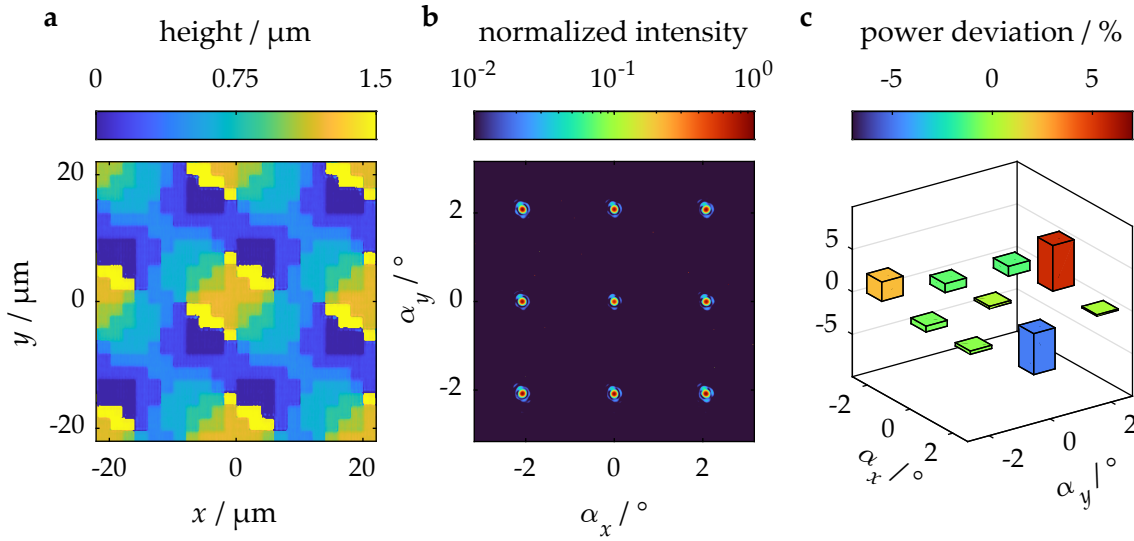While the multi-photon printed DOEs are highly reproducible, it is not trivial

Figure 3.7: Characterization of the fabricated diffractive optical element (DOE). a, Height profile of the multi-photon printed DOE, measured in a confocal profilometer with a NA of 0.9. **b,** Diffraction intensity pattern of a 790 nm wavelength laser beam, measured by collecting the diffracted light with a 50 mm focal length lens and a camera. **c,** Deviation of the measured beamlet-power from the corresponding target power (see Figure 3.6a). The root-mean-square (RMS) deviation is 2.6 %.

to obtain the desired intensity distribution for the nine beamlets. To print high-fidelity DOEs, two printing strategies proved to be essential. First, the stitching period must not be an integer multiple of the DOE grating period. Second, the ideal height profile must be found iteratively. Both strategies are now discussed.

The optics of the multi-photon printer offer a limited field of view in which structures can be printed accurately. However, even within this field, residual field curvature of the focal plane and vignetting of the laser beam occur. Hence, a 3D-printed nominally flat plane will exhibit some distortions. Moreover, two adjacent printing fields are typically not flush with each other. Uncertainties in the automatically detected interface position and stage movements lead to dislocations. Due to the stitching process, both artifacts are periodic and lead to a diffraction pattern with the lattice constant of the stitching period. If the stitching period and the DOE period are commensurable, crosstalk of both diffraction patterns is observed, leading to large errors in the diffracted beamlet intensities. Therefore, the stitching period (100 μm) and the DOE period (22 μm) are intentionally designed to be incommensurate. Even more, their least common multiple is large (1100 μm).

To optimize the height profile iteratively, the far-field diffraction pattern is measured at different wavelengths, ranging from 700 nm to 860 nm. Next, a global optimization routine numerically searches for a phase profile with modified height
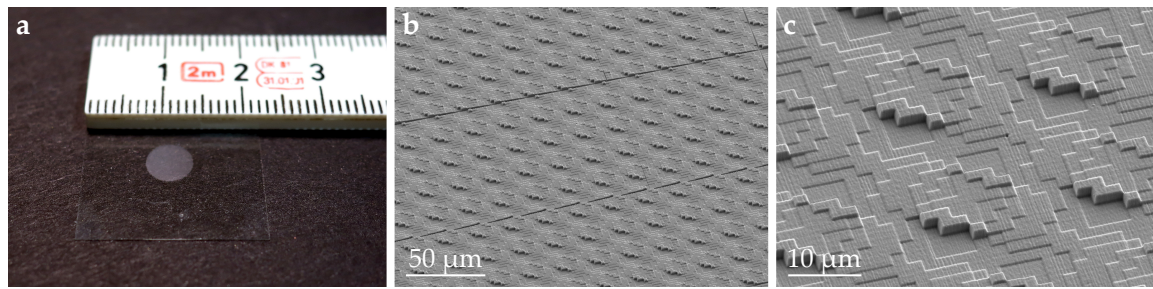
Figure 3.8: Images of the fabricated diffractive optical element (DOE). a, Photograph of the glass coverslip with the multi-photon printed DOE. **b**, Oblique-view scanning electron micrograph of several stitched printing fields of the DOE. The period of the DOE is intentionally different from the period of the stitching field. **c**,. Magnified view of the electron-micrograph, on which the eight printed layers and the hatching pattern are visible. This Figure is adapted from Ref. [48] (CC BY 4.0).

levels, whose far-field pattern matches the measured patterns. The deviation of the modified height level and the targeted height level is then compensated in the next fabrication iteration. This method converged after five iterations.

The final optimized DOE is characterized in Figure 3.7. Panel a shows the measured height profile, which qualitatively agrees well with the designed phase profile (see Figure 3.6b). On a closer look, the height of the levels does not linearly relate to the designed phase, which could be explained by an inhomogeneous refractive index of the polymer. This observation justifies the used optimization routine in which the DOE is optimized by its far-field diffraction pattern instead of the measured height profile. Panel b shows the measured far-field intensity distribution on a logarithmic color scale. To resolve the beamlets on a camera sensor, the beam diameter in front of the DOE is intentionally smaller than in printing experiments. The small beam diameter leads to a lower value of M and hence larger PSF diameters of the beamlets. A 2D Gaussian profile is fitted to each diffracted spot and the obtained beamlet power is compared to the targeted power in panel c. The RMS intensity deviation is 2.6 % and the largest deviation is 5 %. This deviation is tolerable with regard to the dynamic range offered by multi-photon 3D printing photoresins [91].

A photograph of the fabricated DOE is shown in Figure 3.8a. More details are revealed in the oblique-view scanning electron micrograph in panel b, on which also the stitching artifacts and the incommensurate stitching can be seen. The close-up electron micrograph in panel c reveals the eight printed layers and well-defined pixels, as well as the hatching pattern of the fabrication process.

3.5 COMPONENTS OF THE MULTI-FOCUS SETUP

Besides a beam splitting element, multi-focus multi-photon printing also requires a suitable, custom-built 3D printing setup. Commercial multi-photon printing instruments are typically not equipped with lasers powerful enough to allow for multi-focus printing at rapid speeds. Hence, in this section, a suitable setup is presented.

Figure 3.9 shows a sketch of the multi-focus multi-photon 3D printer, as it was assembled by the author with assistance of Pascal Kiefer, in the course of his Master's thesis. A 2.8 W output power, 80 MHz repetition rate Ti:Sa laser emits 90 fs long pulses (MaiTai HP, Spectra-Physics Inc). The tunable central emission wavelength is set to 790 nm, for which the DOE is designed.

The power of the laser beam is modulated by an acousto-optic modulator (AOM) (MT80-A1.5-IR, AA Opto Electronic). The first diffraction order of the AOM passes a pulse compressor, comprised of two N-SF10 prisms, separated by a 2 m long tip-to-tip distance [114, 115]. Thereby, about 30 000 fs^2 of group delay dispersion, which is acquired throughout the optical path, is pre-compensated (see Table 3.1).

Next, the laser beam is split by the DOE into an array of 3×3 beamlets. The unpatterned side of the DOE substrate is coated with a 140 nm thin MgF$_2$ anti-reflection coating. Importantly, to avoid vignetting of the beamlets, the DOE is located in a conjugate pupil plane of the high-NA objective lens. Therefore, the DOE is imaged first by the dispersion-compensating telescope (see section 3.3). In the conjugate pupil plane, the beam-array is transmitted by a polarizing beam splitter (PBS) (PBS252, Thorlabs GmbH) and demagnified by a relay telescope. Lens data for the first lens group (LG1) of this relay telescope is provided in Table A.1. The second lens group LG2 is identical in construction to the lenses of the *XY* scan relay presented in Ref. [117]. The demagnified beam-array is then deflected by a 6 mm clear-aperture galvanometer-mirror (6215H, Cambridge Technology Inc.). The galvanometer is imaged by a 1:1 telescope (scan relay *XY* from Ref. [117]) onto a second, perpendicular galvanometer mirror (same model). To avoid heating of the galvanometer mirrors during extended printing jobs, both mirrors are water-cooled. The galvanometer mirror is magnified fourfold using a scan lens LG5 and a tube lens LG6, which are identical in construction to the lenses SL and TL presented in Ref. [117], into the entrance pupil of a microscope objective (Plan-Apochromat 40×/NA1.4, Carl Zeiss AG). An achromatic quarter-wave plate is located near the entrance pupil of the objective lens (B. Halle Nachfl. GmbH).

A microscope *xy*-stage (Scan IM 120 × 100, Märzhäuser-Wetzlar) and a piezoelectric stage for axial movements (Q-545.140, Physik Instrumente GmbH & Co. KG)
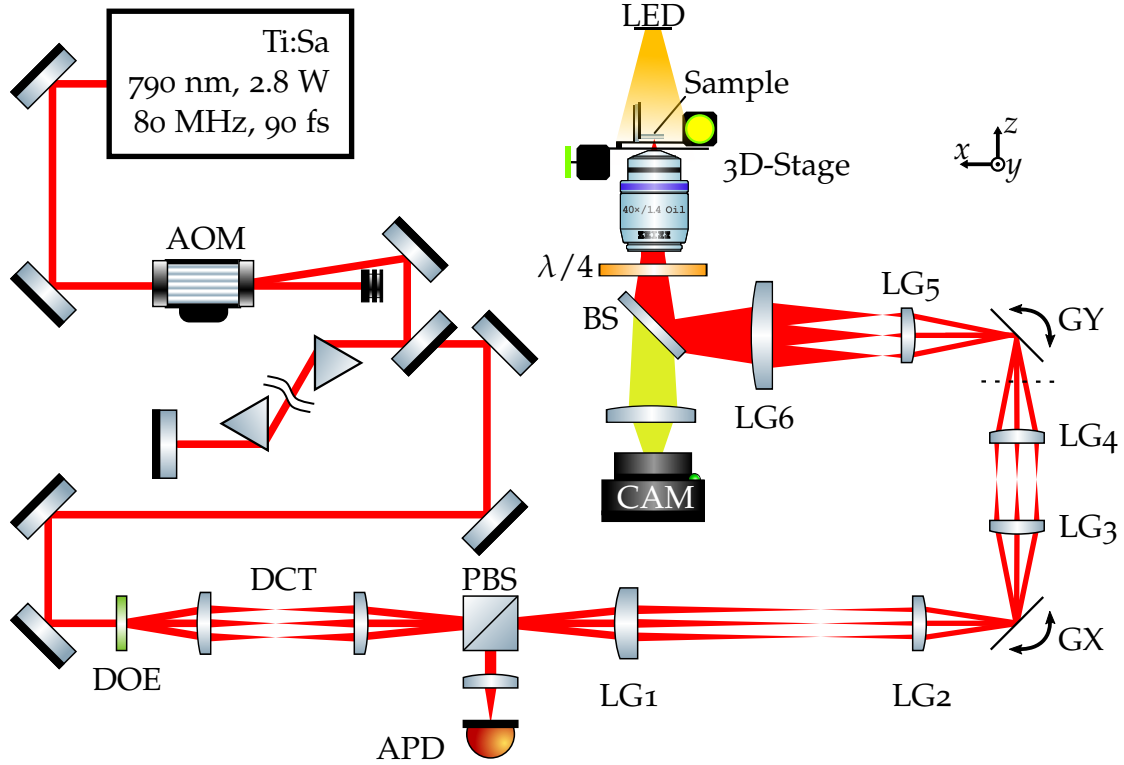
Figure 3.9: Scheme of the multi-focus multi-photon 3D printing setup. The beam of a femtosecond-pulsed Ti:Sa laser is modulated by an acousto-optic modulator (AOM). Next, the laser beam passes a prism-based pulse compressor, which compensates for the acquired group velocity dispersion. A diffractive optical element (DOE) splits the beam into an array of 9×9 beamlets, which are relayed by a dispersion compensation telescope (DCT). The DCT compensates the lateral chromatic dispersion caused by the finite pulse length and the DOE. After passing through a polarizing beam splitter (PBS), the beamlets are imaged onto a first galvanometric-actuated mirror (GX) by a telescope consisting of lens groups LG1 and LG2. A second telescope (LG3 and LG4) relay the beam onto a second galvanometric mirror (GY) with a perpendicular scanning axis. The dashed horizontal lines indicates a flip of the coordinate system. Mirror GY is imaged through a quarter-wave plate on the NA = 1.4 objective lens entrance pupil. The objective lens focuses the beamlets onto the sample, which is mounted on a motorized xy-stage and a piezo-actuated z-stage. The printing process is recorded by a camera (CAM). Back-reflected light is collected by an avalanche photodiode (APD). This Figure was created using "ComponentLibrary" [116] by Alexander Franzen (CC BY NC 3.0) and is adapted from Ref. [48] (CC BY 4.0).

element	GDD / fs^2	count
AOM	10180	1
DCT	9700	1
LG1	1529	1
LG2, LG2, LG3, LG4	1683	4
LG5	1362	1
LG6	818	1
objective lens	4245	1
Total	34566	

Table 3.1: **Overview of the acquired group delay dispersion (GDD) within the multi-focus multi-photon setup.** The used abbreviations are the same as in Figure 3.9. For the objective lens, the value is estimated from lens data disclosed in the patent application [118]. The GDD values are calculated for the chief ray of the central beam.

position the printing substrate in the setup. Back-reflected light is detected at an avalanche photodiode (APD), attached to the side-port of the PBS.

To control the AOM and the galvanometer mirrors with synchronous drive-signals, a real-time computer and an field-programmable gate array (FPGA) (7931R, NI Corp.) with a transceiver-module (5783, NI Corp.) is used. An initial version of the control-software was programmed by Pascal Kiefer in the scope of his Master's thesis. For the experiments in chapter 4, the software was further updated by the author. The FPGA is fed with points on a scan trajectory and laser power values. During printing, the coordinate points are linearly interpolated and output as an analog voltage signal. To account for the lag of the galvanometer mirrors, the power-modulation signal is delayed with respect to the position signal by 119 µs, a value empirically found.

3.6 SUMMARY

In this chapter, a setup for multi-focus multi-photon 3D printing was presented. Due to the setup's high degree of modularity, it has also been used in applications other than multi-focus printing [119]. The aim of multi-focus multi-photon 3D printing is to enhance the multi-photon 3D printing rate, which is limited by the scan speed of the laser beam scanner. Therefore, several beam splitting methods and their limitations were reviewed. A diffractive beam splitter was fabricated and characterized. Finally, an optical setup suitable for multi-focus 3D printing was presented. In the next chapter, structures 3D printed with the multi-focus multi-photon printer are presented and characterized.

4 Chapter 4

Multi-Focus
3D Printed Structures
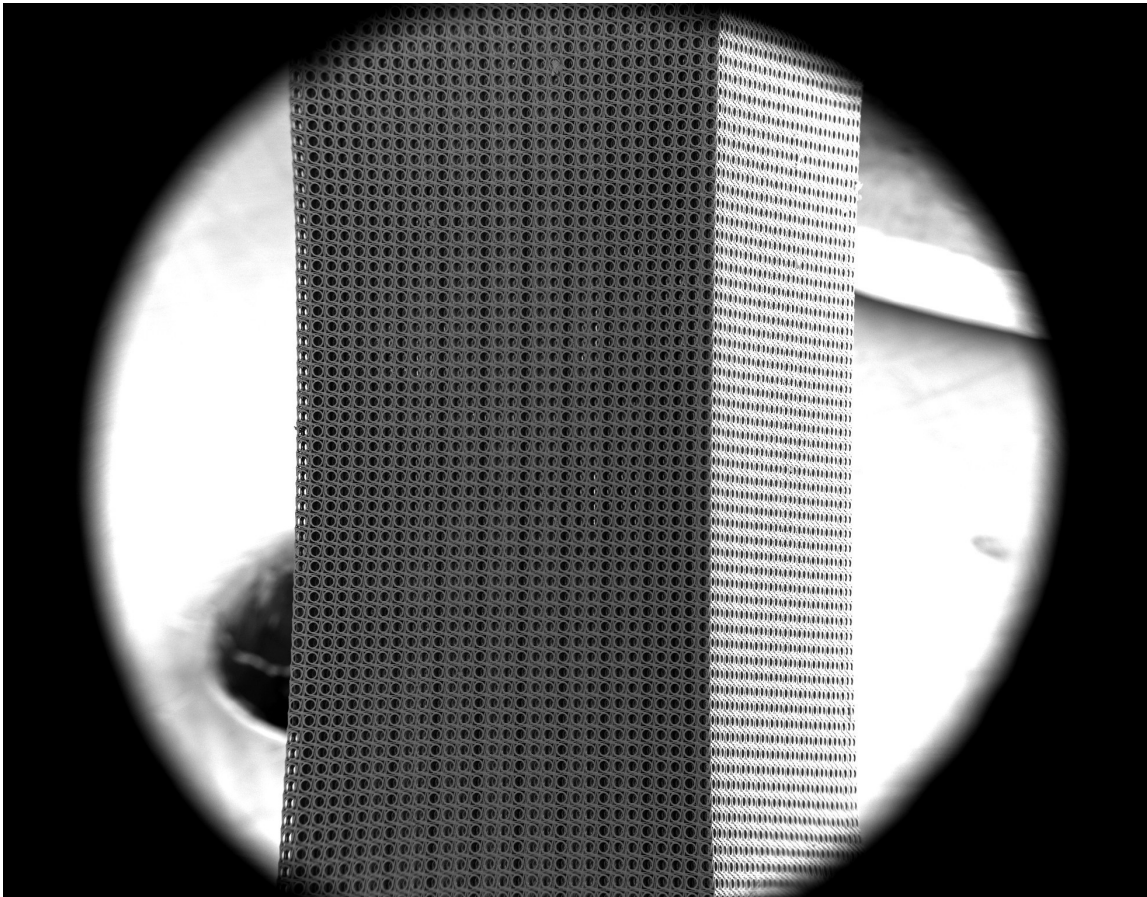
Electron micrograph of a multi-focus multi-photon 3D printed sample.

In this chapter, the presented multi-focus multi-photon 3D printing setup is used to 3D print centimeter-sized metamaterials at a peak voxel printing rate of over one million voxels per second.

4.1 VOXEL SIZE

For equal focusing conditions, the voxel size in the multi-focus setup does not differ from that of the single-focus 3D printing setup. However, the dispersion-compensating telescope is expected to introduce some optical aberrations. Therefore, isolated suspended lines are printed in order to characterize the minimum voxel size that can be achieved by the multi-focus multi-photon setup presented in chapter 3. Electron micrographs of square blocks, which are interconnected by lines, are shown in Figure 4.1. Averaged over one 3×3 array of lines printed in parallel, a lateral linewidth (and hence lateral voxel size) of $406 \pm 62\,\text{nm}$ and a line height (and hence axial voxel size) of $1.01 \pm 0.38\,\mu\text{m}$ are measured. The uncertainty denotes plus/minus one standard deviation.

These voxel dimensions are larger than the squared intensity distribution lateral and axial FWHM diameter (225 nm and 560 nm, respectively), which is used as reference in the benchmark graphic in Figure 2.1. While it is possible to print

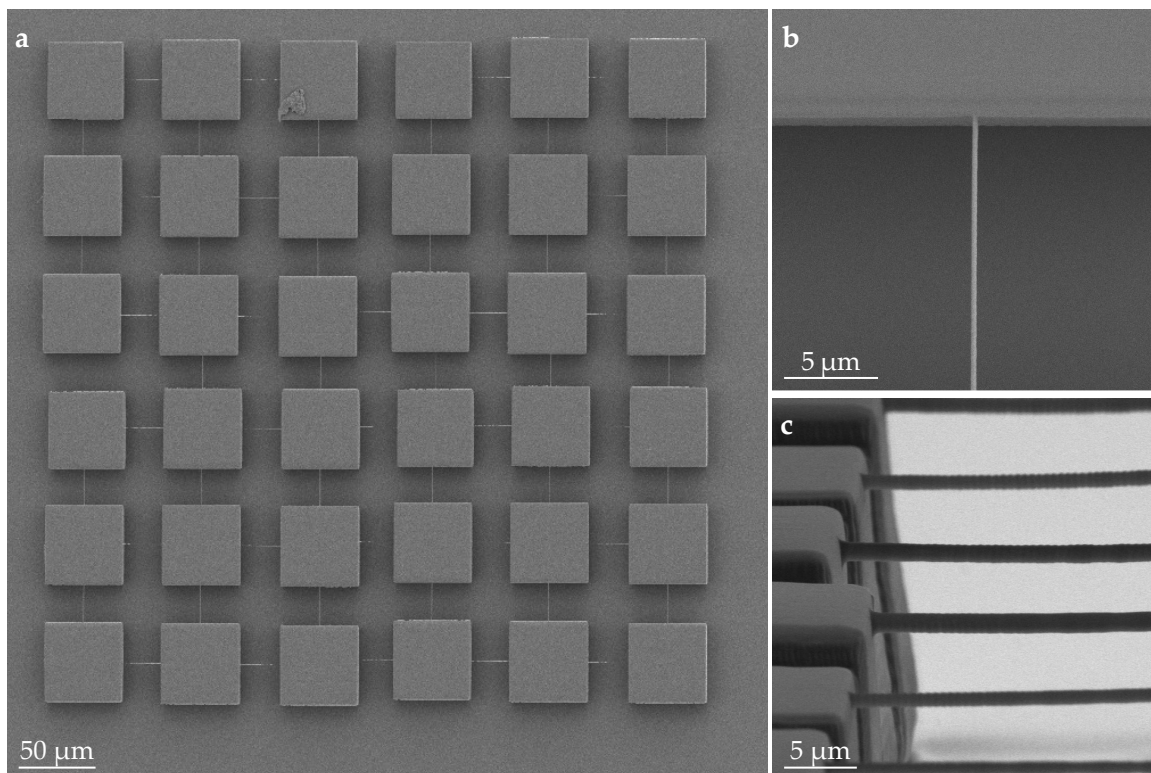**Figure 4.1: Scanning electron micrograph of the test patterns printed to determine the linewidth. a**, 3D printed block array. The blocks are connected by singly-scanned, suspended lines. **b**, Top-view zoom-in of a single suspended line. **c**, Oblique-view of several suspended lines. This Figure is adapted from Ref. [48] (CC BY 4.0).
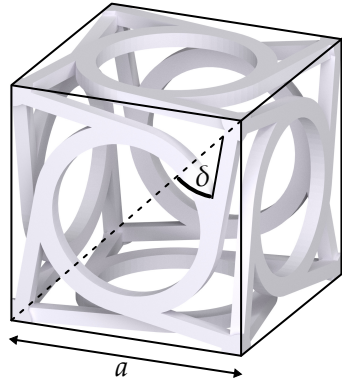
Figure 4.2: Chiral metamaterial unit cell from Ref. [120]. Depending on the value of δ, the cubic unit cell with side length a is either chiral ($\delta = 34.8°$, depicted) or achiral ($\delta = 0°$). This Figure is adapted from Ref. [48] (CC BY 4.0).

smaller voxel lines, the variation of the focus intensity causes some lines to break. The quoted measured linewidth is for one set of line simultaneously printed intact lines. A second reason for the enlarged voxel size is the limited field of view of the dispersion-compensating telescope, which deteriorates the peripheral foci.

4.2 LARGE CHIRAL METAMATERIAL CRYSTALS

To benchmark the presented multi-focus multi-photon 3D printer, a 3D mechanical metamaterial crystal is printed. A metamaterial is a rationally designed composite with tailored effective material parameters that can exceed the parameters of its constituent materials [121]. Metamaterial crystals are attractive benchmark structures for multi-focus 3D printing, since many metamaterials are fabricated by 3D additive manufacturing [27, 72, 122], yet the total number of crystal unit cells is typically limited by the fabrication time. For multi-focus 3D printing, however, the fabrication time of crystalline metamaterials decreases almost proportionally with the number of foci.

Recently, T. Frenzel et al. proposed a chiral mechanical metamaterial that is designed to twist when strained [120]. Figure 4.2 shows a blueprint of the cubic unit cell, which is characterized by the angle δ and the side length a. For multi-focus 3D-printing with the setup presented in chapter 3, the side length is set to $a = 80\,\mu m$, which is below the smallest side length of $a = 100\,\mu m$ presented in the original publication [120]. Furthermore, the index-matched photoresin IP-Dip (Nanoscribe GmbH & Co. KG) is used in conjunction with a $NA = 1.4$ objective, instead of IP-S (Nanoscribe GmbH) and a $NA = 0.8$ objective lens, which was used in the original publication [120]. The different photoresin and the larger objective NA also lead to decreased hatching and slicing distances, which are set to $200\,nm$ and $500\,nm$, respectively. Furthermore, printing large-scale objects requires a sufficient photoresin reservoir. However, without precautions, larger volumes of the IP-Dip photoresin gradually flow off the objective lens during
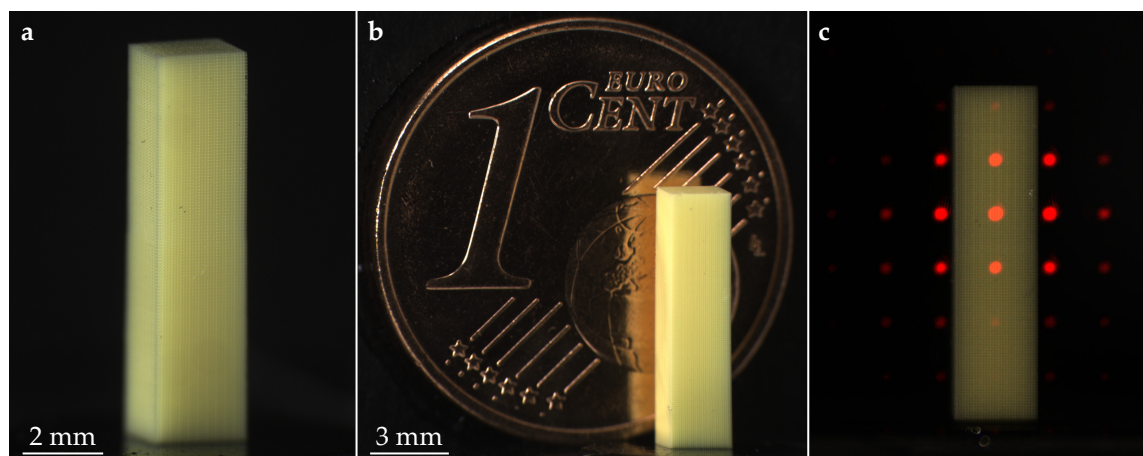
Figure 4.3: 3D printed chiral metamaterial crystal. a, Photograph of a 2.4 mm × 2.4 mm × 9.6 mm large 3D printed achiral structure, comprised of 30 × 30 × 120 = 108000 unit cells. The structure has a yellow tint, caused by residual photoinitiator molecules and fragments thereof in the polymerized material. **b**, Photograph of a metamaterial with the identical dimensions as the structure in a, however comprised of chiral unit cells, i.e., for $\delta = 34.8°$. A one-cent coin is depicted in the background for scale. **c**, Laue diffraction pattern of a helium-neon laser beam (wavelength 633 nm) at the metamaterial crystal. The recorded intensity of the diffraction pattern is intentionally saturated to reveal higher diffraction orders. For clarity, a photograph of the structure is shown in the background. Parts of this Figure are adapted from Ref. [48] (CC BY 4.0).

printing, which is why the resin is contained in a rubber O-ring, attached with non-permanent glue (Fixogum, Marabu GmbH & Co. KG) on top of the objective lens.

To achieve high peak printing rates, the laser-focus scan speed is set to $400 \, \text{mm s}^{-1}$, which is ultimately limited by the galvanometer mirror's resonance frequency. To attain a uniform scan speed along an exposed trajectory, the galvanometer scanned laser foci are accelerated on a 42 μm long run-up distance before each scanned line.

Photographs of two 3D printed metamaterial crystals, each comprised of 30 × 30 × 120 = 108 000 unit cells, are shown in panel a and b of Figure 4.3. The displayed structures differ in the geometry parameter δ, which is $\delta = 0°$ for the achiral structure (panel a) and $\delta = 34.8°$ for the chiral structure (panel b). The printing time for each 9.6 mm tall metamaterial crystal is about two days. For comparison, the printing of a 500 unit cell large structure took about one day in the original publication [123], which is a factor of 100 less. On the photographs, the metamaterial crystal looks almost homogeneous and the interior substructure is
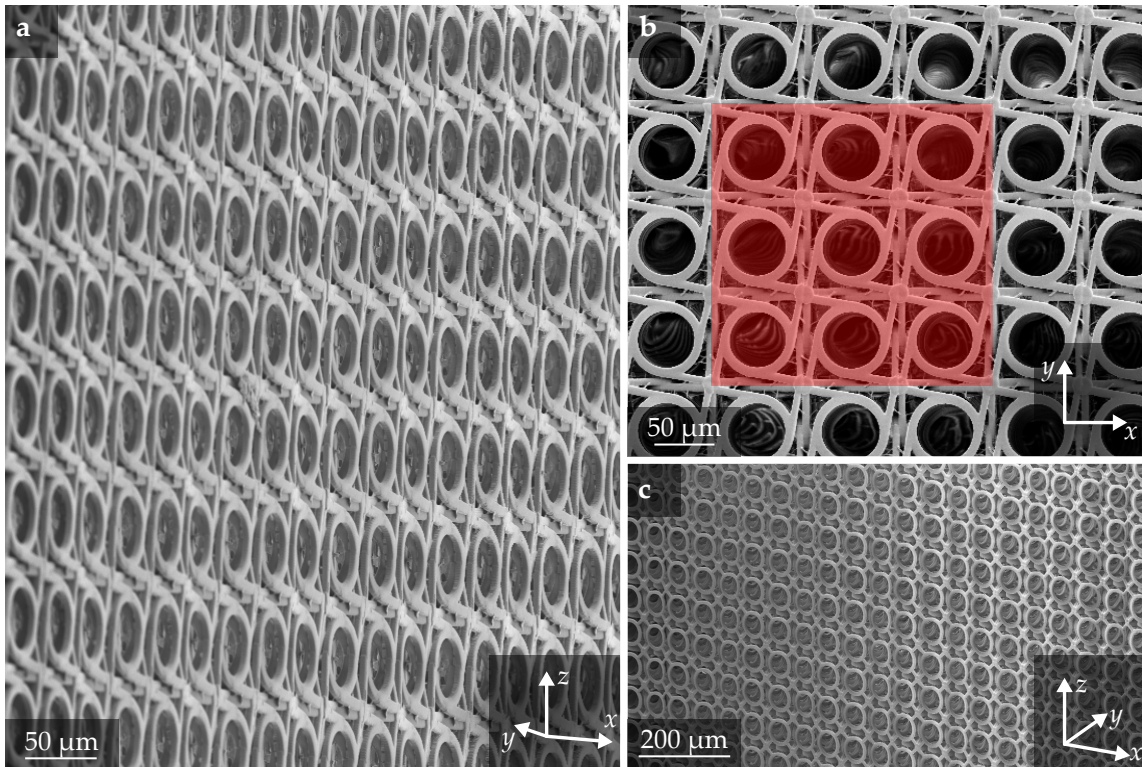
Figure 4.4: Scanning electron micrographs of metamaterial samples. a, Side view perspective of the chiral metamaterial crystal. **b**, Top view of the same sample with highlighted simultaneously printed array of 3×3 unit cells. Stitching in between adjacent foci or adjacent field of views causes small offsets. **c**, Side view of an achiral metamaterial structure ($\delta = 0°$). This Figure is adapted from Ref. [48] (CC BY 4.0).

not resolved. To confirm the crystalline nature of the structure, a Laue diffraction pattern is recorded with a camera by irradiating the structure with a helium-neon laser beam. Figure 4.3c shows a photograph of the diffraction pattern, exhibiting sharp peaks, which is indicative for an ordered crystal-structure.

More details of the printed metamaterial are revealed in the scanning electron micrographs shown in Figure 4.4. There, the stitching seams in between neighboring unit cells can be seen at the corners of the cubic unit cell. Note that two types of stitching occur in multi-focus multi-photon 3D printing: stitching between adjacent foci and stitching between adjacent writing fields. For both, only minor offsets can be seen in the electron micrographs.

At this point, it would be interesting to perform characterization experiments on the printed structure to see if the desired push-to-twist conversion can be observed. In their experiments, Frenzel et al. have quantified the strain-to-twist conversion,

Figure 4.5: Modified chiral metamaterial unit cell from Ref. [123]. Laterally adjacent unit cells are connected by the red-colored protruding bars, which are easily deformable. The tetragonal unit cell has an aspect ratio of $a_z/a_{xy} = 2/3$. The blue part is identical to the unit cell in Figure 4.2. The two colors are for illustration only and do not encode two different materials. This Figure is adapted from Ref. [123] (CC BY 4.0).
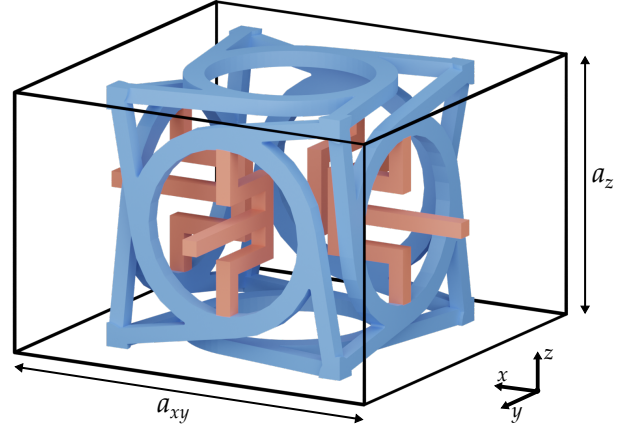
which was as large as 2% for a sample with a scale factor[1] $S = L/a = 1$ and an aspect ratio of 2 [123]. For large S and a constant aspect ratio, the twist per strain decays proportionally to $1/S$, i.e., reciprocally to the scale factor S [120]. The largest structure in Ref. [120] with $S = 5$ showed a twist per strain below 1%. Hence, a much lower twist per strain is expected for the metamaterial crystal with order of 10^5 unit cells. Hence, in order to obtain appreciable large twist per strain values also for large S, a modified, tetragonal metamaterial unit cell is presented in the next section.

4.3 A CHIRAL METAMATERIAL WITH A LARGE CHARACTERISTIC LENGTH

The decrease in twist angle for chiral metamaterials with large scale factors can be intuitively understood by the cancellation of the rotational displacement vectors of adjacent unit cells. Hence, the twist of adjacent unit cells cancels in the bulk and the overall twist is governed by unit cells on the surface of the metamaterial [120]. However, for small S, the twist per strain does not decrease monotonically. Instead, for a fixed sample aspect ratio, the twist angle per strain increases linearly up to a characteristic length $L_c = a \times S_c$ [123]. Only for samples larger than this characteristic length, the twist per strain decreases proportional to the sample's surface to volume ratio [123]. Thus, to obtain a significant twist per strain for large samples, this characteristic length must be increased accordingly.

Patrick Ziemke and Tobias Frenzel have designed chiral metamaterial unit cells with such large characteristic lengths. The underlying idea is to connect the chiral motifs in the unit cells by easily deformable elements [123, 124], such that the

---

[1] The symbol N is used in the original publication for the scale factor. To avoid confusion with the effective order of nonlinearity N of photoresins, the symbol S is used herein.

coupling strength between neighboring unit cells decreases. Figure 4.5 shows a modification of the original chiral unit cell, in which the unit cells are laterally connected by the red-colored bars. To make the bars yet more flexible, they recede into the unit cell and thereby allow each unit cell to rotate more freely around their own center of mass [125].

Figure 4.4 shows a gallery of micrographs of multi-focus 3D printed structures with different scale factor S. The structures were printed by Tobias Frenzel and the author and are part of a larger study, involving also single-focus multi-photon 3D printed structures [123]. Here, only multi-focus 3D printed results are presented. In contrast to the metamaterial crystal shown in section 4.2, the samples in this section were supercritically dried (see section 2.2). A 200 nm slicing distance and a 300 nm hatching distance are used. Note that in consistency with the structures printed in Ref. [120], a sample height-to-width aspect ratio of 2 is chosen. The tetragonal unit cell aspect-ratio of 2/3 leads to $S_z = 3S_x = 3S_y = 3S$. Furthermore, in contrast to the metamaterial crystal shown in section 4.2, here two equally dimensioned crystals of opposite handedness are printed on top of each other. Thereby, no sliding boundaries are required when compressing the sample in the twist angle measurements and one sample contains a total of $2 \times S_x \times S_y \times S_z = 2 \times 3 \times S^3$ unit cells. Protruding plates with attached markers are printed in between the crystals of opposite handedness. These markers are required to optically track the angular displacement. Using the multi-focus 3D printer, structures with $S = 3, 6, 9, 12, 15, 18, 21, 27$ are fabricated. The printing time for the largest structure with $S = 27$, containing $2 \times 27 \times 27 \times 81 = 118\,098$ unit cells, is about 30 h.

To fabricate these structures, three modifications are made to the setup presented in chapter 3. First, a motorized aperture is placed right behind the dispersion-compensating telescope. This aperture allows rapid switching between multi-focus printing with nine foci and single-focus printing, which is more convenient when printing the intermediate plates. Second, the two-prism pulse-compressor is replaced by a single-prism pulse compressor, with the prism made of highly-dispersive N-SF66 glass. The prism is Brewster-cut for 800 nm wavelength. In the single-prism compressor, the beam is folded by two hollow roof prism mirrors, which are coated with a low group-delay-dispersion coating (HRS1015-AG, Thorlabs GmbH) [126]. The effective tip-to-tip distance is 90 cm. Third, the lens spacing of the dispersion-compensating telescope is slightly increased, leading to a larger magnification and thereby to lower focus-spacing of $a_{xy} = 74\,\mu$m.

All samples were characterized by Tobias Frenzel in a dedicated setup, which is described in detail in Ref. [125]. In brief, the setup consists of a metal stamp which compresses the printed sample axially by a distance u_z. The sample strain
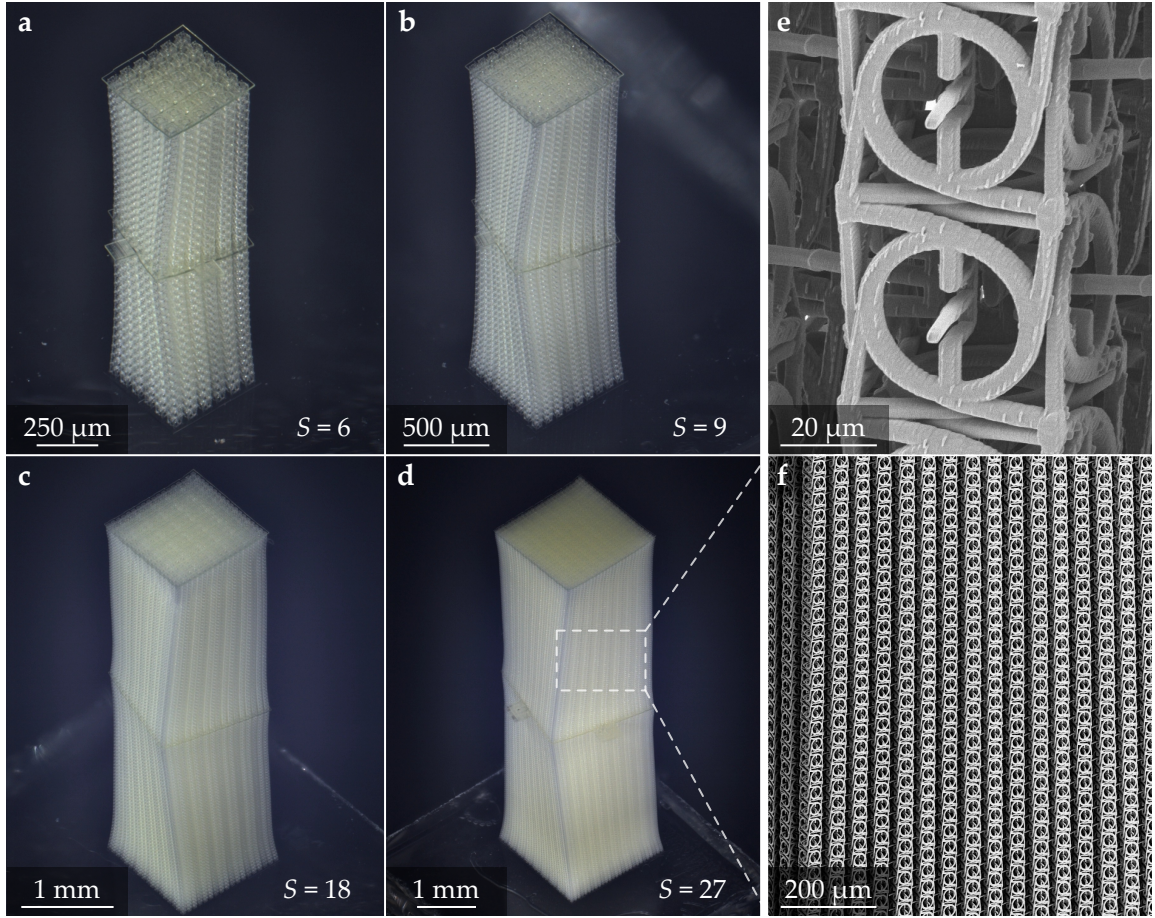
Figure 4.6: Micrographs of chiral metamaterial crystals with large characteristic lengths. Optical micrographs of metamaterials with **a**, $2 \times 6 \times 6 \times 18$, **b**, $2 \times 9 \times 9 \times 27$, **c**, $2 \times 18 \times 18 \times 54$, **d**, $2 \times 27 \times 27 \times 81$ unit cells. **e**, High-magnified electron micrograph of a printed crystal with $S = 3$. **f**, Electron micrograph of a crystal with $S = 27$. The optical micrographs were recorded by Tobias Frenzel and previously published in [123] (CC BY 4.0).

is computed by the fraction of the displacement and the sample length u_z/L_z, with negative strains corresponding to a compression. The twisting motion of the sample is captured by two cameras, one of which coaxially images the sample's middle plate. From these images, the displacement and hence the twist angle is computed via an image cross-correlation analysis [120].

Figure 4.7 shows the measured twist angles for prescribed strain values for the fabricated samples with different scale factors S. First, all twist angles per strain exceed the $2.0°$ maximum twist angle per strain observed for crystals comprised of the cubic unit cell in Ref. [123]. Second, the maximum twist angle per strain (for
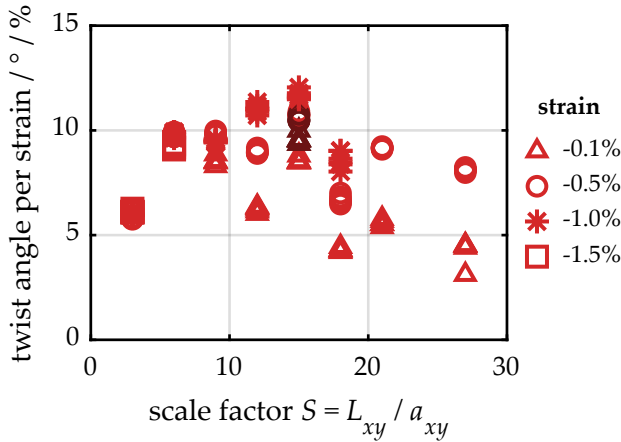
Figure 4.7: Measured twist per strain for samples of different scale factor. The twist per strain increases up to a characteristic length of $S_c \approx 7.2$. For large scale factors, the data points for different strain values scatter due to nonlinearities. For each scale factor S, the different color shades indicate measurements on different samples. The measurements were performed by Tobias Frenzel and published in Ref. [123] (CC BY 4.0).

small strains) is reached for a scale factor in the range of $S = 6$ and $S = 9$, which is in good agreement with the expected value of $S = 7.2$ obtained by finite-element calculations and a simple analytic model [123]. Finally, for large S, nonlinearities in the twist angle per strain can be observed. That is, for larger absolute strain values, the twist angle increases. Such nonlinearities have also been observed in numerical calculations. However, the numerical calculations performed by Tobias Frenzel and Patrick Ziemke in Ref. [123] were only possible up to a scale factor of $S = 20$, which is below the maximum scale factor $S = 27$ of the fabricated samples.

4.4 DISCUSSION

In this chapter, 3D metamaterial crystals were presented comprising more than 10^5 unit cells, fabricated by 3D additive manufacturing. This unit cell count surpasses previous demonstrations of large-scale 3D metamaterials of comparable complexity [31, 120]. Furthermore, the achieved peak printing rate of around 10^7 voxels s^{-1} is more than one order of magnitude above earlier multi-focus multi-photon 3D printing approaches and is at par with industry-scale ink-jet 3D printers. In the following, further routes to decrease the fabrication time of 3D printed structures are outlined.

One aspect frequently neglected when discussing 3D printing methods is the overhead, which is also not included in the voxel *peak* printing rate. Nevertheless, a significant amount of printing time is consumed by these overheads, which include sample preparation, signal processing and communication overhead, stage movement, acceleration distances, post-processing, and development. Or, in other words, in photopolymerization-based 3D printing techniques, any processing time in which the sample is not exposed to the laser beam or UV-light is overhead.

Indeed, for the tetragonal sample presented in section 4.3, substantial 70 % of the

scan time are spent on acceleration and deceleration tracks, and only in 30 % of the time the photoresin is actually exposed to the focused laser. This is accompanied by some minor overhead caused by z-stepping, xy-stitching, and data transfer. One option to eliminate the scan overhead is to incorporate the acceleration and deceleration tracks in the scan trajectory – at the expense of a uniform scan speed. In order to keep the scanner and the power modulation synchronized, precise knowledge of the galvanometer dynamics is required. Alternatively, the galvanometer mirrors can be operated in a closed-loop mode with continuous position-feedback.

A possibility to increase the peak printing rate is to decrease the excitation-laser wavelength. For instance, printing with a frequency-doubled laser-output [127, 128] at an identical focus NA halves the focus diameter and thereby increases the peak printing rate by a factor of two [93], with the additional benefit of a smaller voxel size. Furthermore, the undesired angular dispersion for a given focus displacement M and a fixed bandwidth-limited pulse-length τ decreases linearly for a blue-shifted excitation wavelength with spectral width $\Delta\lambda$, which can be seen by inserting the time-bandwidth product of a light pulse [129]

$$\tau \cdot \frac{\Delta\lambda}{\lambda^2} = \text{const.} \tag{4.1}$$

into Equation 3.9, resulting in

$$\frac{\Delta d}{d_{\text{FWHM}}} \propto M\lambda. \tag{4.2}$$

An alternative way to decrease the voxel diameter is given by stimulated emission-depletion (STED)-inspired multi-photon printing [22]. Therein, each focus is precisely superposed by a depletion focus with a different beam-mode, which suppresses the polymerization in the focus periphery. In laser-scanning and multi-focus 3D printing, the precise alignment of each focus-pair can be easily deteriorated by optical aberrations. In the course of this thesis, it was found that the STED-compatible photoinitiator 7-diethylamino-3-thenoylcoumarin (DETC) can be depleted using high-power cw laser beams at the same (fundamental) wavelength as it is excited (results not shown). Thereby, chromatic aberrations are absent by design.

Ultimately, the peak printing rate is limited by the repetition rate of the mode-locked laser, which is typically around 80 MHz.[2] With the (lateral) voxel diameter of 324 nm [94], a maximum scan-speed of 26 m s^{-1} can be achieved, resulting in

---

[2] Beam splitting and recombining allows to increase the repetition rate [78], at the expense of peak intensity.

each voxel being exposed to a single laser pulse. At this point, a further increase in the peak printing rate cannot be achieved by faster scanning anymore. However, parallelization, which does not necessarily imply multi-focus 3D printing, is still possible. An alternative parallelization method is to expose axially adjacent voxels simultaneously by dynamically increasing the voxel size (i.e., decrease the focus NA), which is also called two-photon grayscale lithography [130].

The herein presented multi-focus 3D printing approach with nine simultaneously scanned foci faces two limits. First, the available laser power is limited - not only by the laser source, but eventually also by the damage threshold of the used optics. Both limitations can be eliminated by finding more sensitive photoresin formulations, directions therefore are presented in a recent publication by P. Kiefer et al. [83]. Second, the used dispersion-compensating telescope limits the available aberration-free printing field. Technically it is possible to design and fabricate a dispersion-compensating telescope with an increased field of view. However, due to the exotic glasses and large radii of curvature, the manufacturing of such lenses becomes a costly endeavor. As alternative to improving the dispersion-compensating telescope, an optical arrangement which avoids the dispersion-compensating telescope altogether is presented in the next section.

4.5 AN OUTLOOK: HYBRID REFRACTIVE-DIFFRACTIVE BEAM SPLITTING

In section 3.3, beam splitting methods have been discussed. Diffractive beam splitters offer diffraction efficiencies of close to 90 %, but they suffer from angular chromatic dispersion, which needs to be compensated to obtain stigmatic foci. The used dispersion-compensating telescope has a transmittance of about 75 % and added a considerable fraction of group delay dispersion to the optical path. Lens arrays on the other hand do not suffer from chromatic aberrations, but losses due to vignetting have to be taken into account. By combining both methods, diffractive beam-splitting and lens array beam-splitting, the disadvantages of either method can be bypassed, enabling a highly efficient laser beam-splitting.

Figure 4.8 shows a schematic of the proposed beam splitting method. A diffractive optical element is located at the beam waist location of a Gaussian beam and split into separate beamlets. In contrast to the 9×9 DOE, for which $M \approx 250$, the DOE here diffracts the beams with a low M-value, ensuring little angular dispersion. A converging lens focuses each beamlet, such that the (conjugate) beam-waist is centered in the entrance pupil of one lens within the lens array [131]. The collimating lens also ensures that the chief ray of each beamlet propagates parallel to the optical axis, i.e., making the arrangement telecentric. The lens array
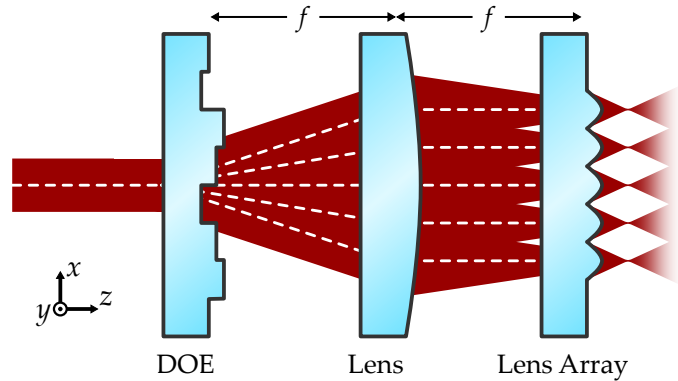
Figure 4.8: Schematic of the hybrid DOE plus lens-array beam splitter. The DOE splits the laser beam into an array of beamlets of small M-value, i.e. with little angular spacing. A converging lens with a long focal length f focuses the beamlet array into the entrance pupil of the lens array. The lens array tightly focuses each beam and thereby increases the M-value without introducing angular dispersion. The white dashed lines indicate chief rays. The drawn distances are not to scale.

focuses each beamlet individually, which effectively increases the M-value without introducing angular dispersion.

This arrangement of a DOE and a lens array is more power-efficient than the DOE or the lens array by itself. By illuminating the lens array with the matching beamlet-array, no power is lost due to vignetting. Reflection losses can be easily avoided by coating all three elements with an anti-reflection coating. The largest loss of power in this arrangement is caused by light diffracted into higher orders by the DOE. However, for a given DOE diameter and DOE pixel size, the diffraction losses decrease for low M-values (see Figure 3.5). For the same reason, no stitching is required when printing the DOE, eliminating cross-talk of the stitching period. As further benefit, the low M-value and hence small-diameter DOE can be printed in several minutes, which is significantly less than the two days printing time required to fabricate the 6 mm DOE presented in section 3.4.

Moreover, due to the very recent advances in two-photon grayscale lithography [130], tailor-made lens arrays can be 3D printed nowadays. The setup presented in chapter 3 has a high degree of modularity and allows the straightforward integration of the presented hybrid DOE plus lens array beam splitter.

Part II

TWO-STEP-ABSORPTION 3D PRINTING

5

One-Color Two-Step-Absorption Photoinitiation
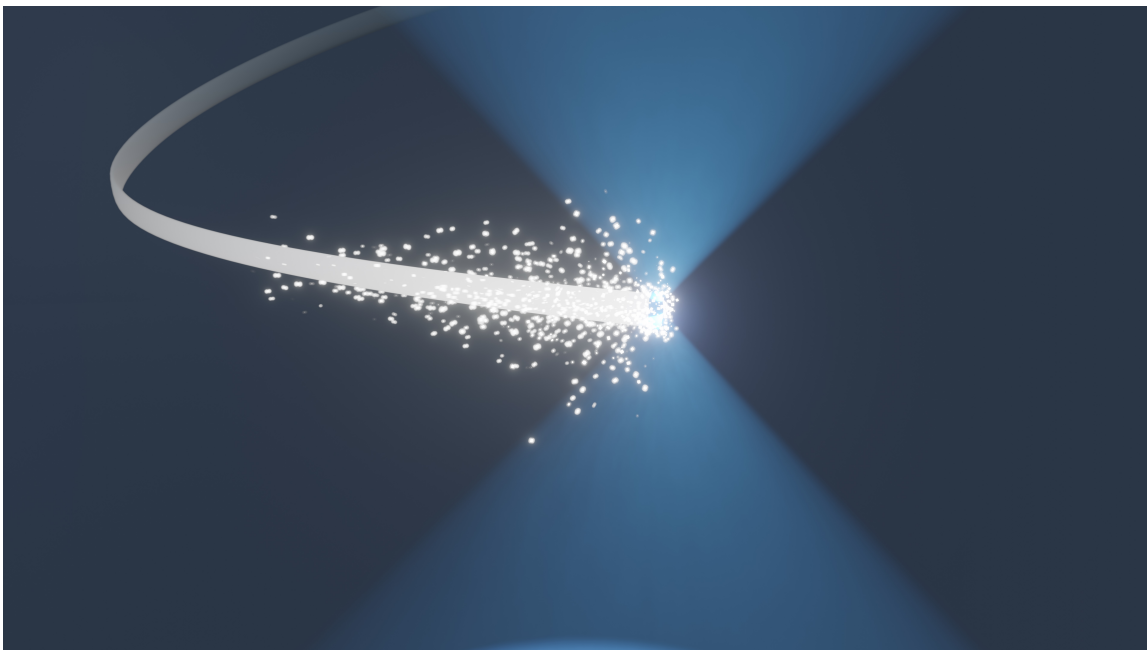
Artistic rendering of a laser-scanned trajectory.

The crucial optical nonlinearity in two-photon absorption 3D nanoprinting is provided by the two-photon absorption process. For efficient two-photon absorption, ultrashort pulsed laser sources are required. However, these laser sources are bulky and expensive and therefore hinder further parallelization of 3D nanoprinters. Two-step absorption, as alternative to two-photon absorption, does not require pulsed laser sources.

5.1 MOTIVATION

Two-photon absorption is at the heart of state-of-the-art polymer 3D nano- and microprinting. For 3D printing parts with voxel sizes below $1\,\mu m$ and at printing rates above $10^5\,\mathrm{voxels\,s^{-1}}$, there is currently no alternative to two-photon 3D printing. However, two-photon 3D nanoprinting has problems and limitations, many of which are caused by the use of femtosecond pulsed laser sources.

As discussed in section 4.4, the continuous demand for higher printing rates in two-photon 3D printing calls for high-power lasers. Femtosecond pulsed lasers with higher output powers than the one used for the experiments in Part I are commercially readily available nowadays. However, increasing the laser power entails new issues since the used optical components have to withstand these power levels, which is not granted. For example, at an incident laser power of almost $1\,W$, the body temperature of the objective lens used in the multi-focus 3D printing experiment (see chapter 4) slightly increased during prolonged 3D printing jobs.

Another common problem encountered in two-photon 3D printing are micro-explosions [132], which lead to micro-cavities that locally damage 3D printed structures. Micro-explosions are hard to avoid and occur when the focused laser beam is linearly absorbed by impurities within the photoresin [91]. Moreover, micro-explosions are also observed when exposing the photoresin with a laser power above the damage-threshold laser power. For typical photoresins and 3D printing conditions, the damage-threshold laser power is a factor of 3 above the polymerization-threshold power [91]. However, this dynamic range narrows for increasing peak powers [91], and hence for increased printing velocities.

Besides these technical challenges when 3D printing with high laser powers, there are two very practical problems with the femtosecond-pulsed lasers employed in two-photon 3D printers. These lasers are bulky and expensive. All components included, the Ti:Sa-laser employed for the multi-focus experiments has a volume of more than $100\,L$. At a price of approximately 10^5 Euro, it is the most expensive component in the multi-focus setup. Both aspects hinder a more widespread application of two-photon 3D printing and further parallelization.

In this chapter, the concept of two-step absorption photoinitiation is introduced. Two-step-absorption photoinitiators do not rely on ultrashort pulsed laser sources to obtain the quadratic nonlinearity, which is needed to tightly confine the deposited optical excitation. Instead, inexpensive cw laser sources are employed for 3D nanoprinting that do not trigger microexplosions. However, the nonlinearity in two-step absorption photoinitiation practically constrains the minimum voxel exposure time and hence the scan velocity, which we will discuss.
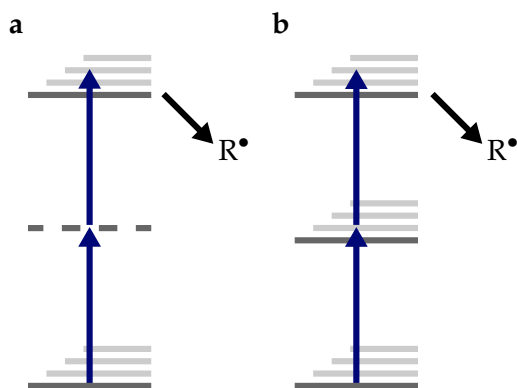
Figure 5.1: Two-photon absorption and two-step absorption. a, Schematic energy-level diagram for two-photon absorption in photoinitiator molecules. By simultaneous absorption of two photons via a virtual intermediate state (dashed line), the molecule is optically excited to an upper electronic state, whereof the initiator decays into free radicals R$^{\bullet}$. **b**, For two-step absorption, the virtual intermediate state is replaced by a *real* intermediate state, as indicated by the solid line. Adapted from Ref. [53] with permission from Springer Nature.

5.2 THE CONCEPT OF TWO-STEP ABSORPTION

Two-photon absorption describes the process in which a molecule in its electronic ground-state is excited optically by simultaneous absorption of two photons via a virtual intermediate state to a real electronic state [133]. The intermediate state is called "virtual" since it exists only in the presence of the strong external light field. From the excited electronic state, a photoinitiator molecule then decays into free radicals. Thus, the concentration of radicals [R$^{\bullet}$], which we identify with the relevant optical dose D, is proportional to the squared intensity I

$$D \propto I^N = I^2. \tag{5.1}$$

Here, N is the nonlinearity exponent, or effective order of absorption [78], which is $N = 2$ for canonical two-photon absorption. As discussed in section 2.6, a nonlinearity with $N > 1$ is essential in two-photon 3D printing to spatially confine the optical dose. Importantly, this local confinement cannot be provided solely by one-photon absorption, for which $N = 1$.

In two-step absorption, the *virtual* intermediate energy-level in two-photon absorption is replaced by a *real* intermediate energy-level, as illustrated by the schematic energy-level diagram in Figure 5.1. The lifetime $\tau = k_D^{-1}$ of the real intermediate state is independent of the light field pulse duration. In contrast, in two-photon absorption, the lifetime of the induced virtual state is governed by the laser pulse duration, which is typically on the order of a few hundred femtoseconds.

5.3 THE NONLINEARITY EXPONENT IN TWO-STEP ABSORPTION

The light-field-independent finite intermediate-state lifetime in two-step absorption directly affects the nonlinearity exponent N in a 3D printing experiment. To illustrate this, assume the intermediate-state lifetime was infinitely long. During optical excitation of the photoresin, photoinitiator molecules will be pre-excited to the intermediate state. This pre-excitation not only happens in the laser focus, but also in its tails. When scanning the laser focus, eventually all photoinitiator molecules in the photoresin are pumped to the intermediate state, from whereon the radical decay can be triggered by one-photon absorption, i.e., by a process with nonlinearity exponent $N = 1$. A unity nonlinearity exponent inevitably leads to a loss of resolution (see also section 2.6). On the other hand, for a very short intermediate-state lifetime, all pre-excited molecules rapidly return to the ground-state, lowering the chances for a second photon to excite the molecule further and trigger the polymerization reaction. Hence, as in two-photon absorption, high laser intensities are necessary to compensate for the low re-excitation probability. In summary, there is a tradeoff between resolution and photoresin sensitivity in two-step-absorption 3D printing.

The behavior of the nonlinearity in between those two extremes can be studied using a rate-equation model. A scheme of a rate model for two-step absorption is shown Figure 5.2. The model consists of a ground state A, which is the only populated state at time $t = 0$. Molecules can be optically excited from the ground state to the state B' with the rate coefficient $k_1 \propto \epsilon_1 I$, with ϵ_1 being the molar decadic extinction coefficient of ground state molecules and I the light intensity, both at the used wavelength λ. From state B', molecules decay rapidly and nonradiatively to state B, from whereon they may decay back to the ground state with a rate coefficient $k_D = \tau^{-1}$. τ is the intermediate-state lifetime. Alternatively, molecules can be re-excited from state B to state C with rate coefficient $k_2 \propto \epsilon_2 I$, where ϵ_2 is the molar decadic extinction coefficient of an intermediate-state excited molecule. State C decays immediately to state D, which corresponds to the relevant optical dose and is proportional to the radical concentration $[\text{R}^\bullet]$.

The governing rate equations are

$$\frac{\text{d}[\text{A}]}{\text{d}t} = -k_1[\text{A}] + k_\text{D}[\text{B}], \tag{5.2}$$

$$\frac{\text{d}[\text{B}]}{\text{d}t} = +k_1[\text{A}] - k_\text{D}[\text{B}] - k_2[\text{B}], \tag{5.3}$$

$$\frac{\text{d}[\text{C}]}{\text{d}t} = \frac{\text{d}D}{\text{d}t} = +k_2[\text{B}]. \tag{5.4}$$

Using the initial conditions $[\text{A}](0) = [\text{A}]_0$, and $[\text{B}](0) = [\text{C}](0) = D(0) = 0$,
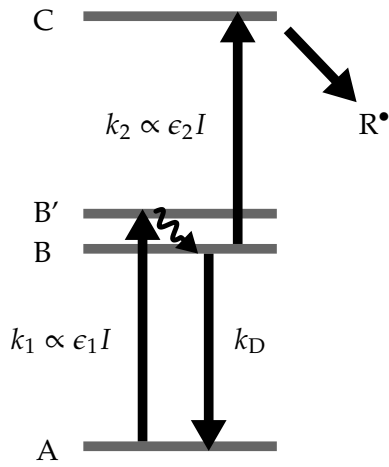
Figure 5.2: Energy-level model for a simple two-step absorption photoinitiation process. At time $t = 0$, only the photoinitiator ground state A is populated. Photoinitiator molecules are optically excited to state B' with the intensity-dependent rate coefficient $k_1 \propto \epsilon_1 I$, from whereon they rapidly and non-radiatively decay to state B. From state B, molecules either decay to the ground state with the rate coefficient $k_D = \tau^{-1}$. Alternatively, molecules are excited by the intensity-dependent rate coefficient $k_2 \propto \epsilon_2 I$ to state C, from where they immediately decay into state D, which is associated with the free radical concentration [R$^\bullet$]. Adapted from Ref. [53] with permission from Springer Nature.

this rate-equation system can be solved analytically (see section A.2). With these expressions at hand, the nonlinearity exponent N is derived in analogy to the nonlinearity exponent in two-photon absorption by

$$N(k_1, k_2, k_D, t) = \frac{\mathrm{d}\ln(D)}{\mathrm{d}\ln(I)} = \frac{I}{D}\frac{\mathrm{d}D}{\mathrm{d}I}. \tag{5.5}$$

Note that N is a function of k_1, k_2, k_D, and the time t.

Figure 5.3 shows the temporal evolution of the energy levels (thin lines and left-hand vertical axis) and the nonlinearity exponent (bold lines and right-hand vertical axis) for different sets of parameters k_1 and k_2. For time $t \to 0$, the nonlinearity exponent is $N = 2$, which can be seen by expanding the expression obtained for $D(k_1, k_2, k_D, t)$ in a Taylor series around $t = 0$, where the leading term of the dose is proportional to $I^2 t^2$. The nonlinearity decreases monotonically and approaches $N = 0$ once the ground state is fully depleted, i.e., [A] $= 0$. However, we assume that the polymerization-threshold is reached long before all photoinitiator is consumed [134] and define the following threshold condition:

$$D\left(t_{\mathrm{exp}}\right) = 10\,\%. \tag{5.6}$$

At the polymerization-threshold exposure-time t_{exp}, the nonlinearity exponent in all three cases is $N > 1$.

A more detailed understanding of the nonlinearity exponent can be derived from Figure 5.4. Panel a shows a false-color diagram of the exposure time in units of the intermediate-state lifetime $t_{\mathrm{exp}}\tau^{-1} = t_{\mathrm{exp}}k_D$ versus k_1/k_D and k_2/k_D. The exposure time decreases from the bottom left towards the top right, i.e., for
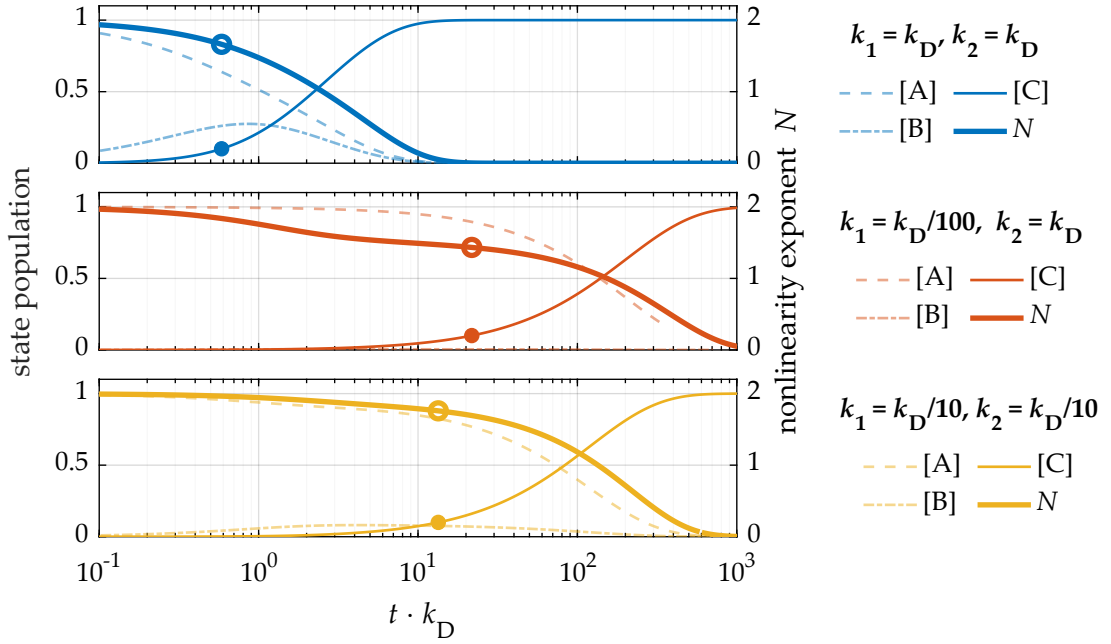
Figure 5.3: Temporal evolution of the energy-level population for different sets of rate coefficients. The values used for k_1 and k_2 are expressed in units of k_D and provided in the legend. Note that k_1 and k_2 are proportional to the light intensity. The state populations of [A], [B], and [C] are plotted using thin lines (left-hand vertical scale), whereas the nonlinearity exponent N is plotted using a bold line (right-hand vertical scale). The dots and circles indicate the time t_{exp} at which the threshold condition is met. Adapted from Ref. [53] with permission from Springer Nature.

increasing intensity I. Panel b shows a false-color diagram of the nonlinearity exponent N at time $t = t_{exp}$ plotted against k_1/k_D and k_2/k_D, i.e., the same axes as in panel a. The nonlinearity exponent approaches $N = 2$ if the conditions $k_1 < k_D$ and $k_2 < k_D$ are fulfilled. If either $k_1 > k_D$ or $k_2 > k_D$, the nonlinearity exponent decreases to $N = 1$. However, if both rate coefficients are balanced and larger than k_D, i.e., $k_1 \approx k_2 > k_D$, the nonlinearity exponent is $1 < N < 2$, even for high intensities or, equivalently, short exposure times. From this nonlinearity $N > 1$, one might get the impression that two-step-absorption 3D printing is possible with arbitrarily short exposure times, as long as k_1 equals k_2. However, the discussion above neglects the *temporal nonlinearity* $\widetilde{N}$, which is defined by

$$\widetilde{N}(k_1, k_2, k_D, t) = \frac{d \ln(D)}{d\ln(t)} = \frac{t}{D} \frac{dD}{dt}. \tag{5.7}$$

Panel c of Figure 5.4 shows a false-color diagram of the temporal nonlinearity $\widetilde{N}(t_{exp})$. For $k_1 \approx k_2 > k_D$, the temporal nonlinearity is $\widetilde{N} > 1$, i.e., the dose D
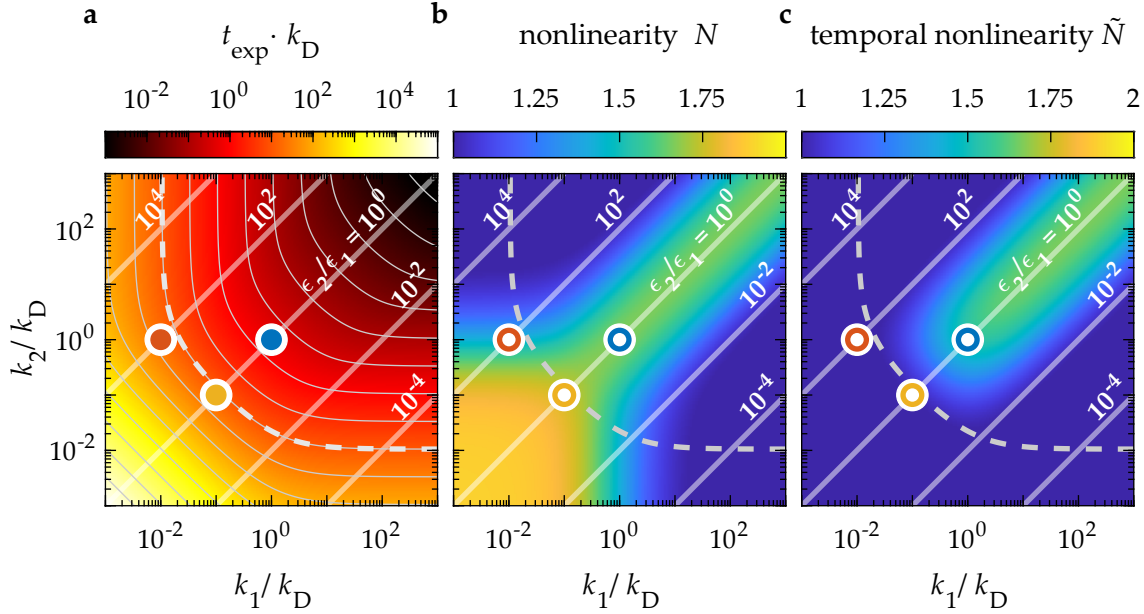
Figure 5.4: False-color diagrams of the exposure time, the nonlinearity, and the temporal nonlinearity. a, Normalized exposure time $t_{exp} k_D$ plotted on a double-logarithmic scale as a function of k_1/k_D and k_2/k_D. **b**, Nonlinearity exponent N at $t = t_{exp}$. **c**, Temporal nonlinearity $\tilde{N}$ at $t = t_{exp}$. In all panels, the white diagonals are lines of constant extinction coefficient ratio ϵ_2/ϵ_1. Moving along the diagonals from bottom left to top right corresponds to an increase in light intensity. The dots and circles correspond to the exposure conditions shown in Figure 5.3. The dashed contour indicates data points plotted in Figure 5.7. Adapted from Ref. [53] with permission from Springer Nature.

increases nonlinearly with time via

$$D \propto I^N\, t^{\tilde{N}}. \tag{5.8}$$

Figure 5.5 illustrates the consequences of $\tilde{N} > 1$ in a 3D printing scenario. The lower panel of Figure 5.5 shows a double-logarithmic diagram of the dose D plotted versus the intensity I, expressed in terms of $k_1/k_D = k_2/k_D$. The diagram shows solutions for logarithmically spaced exposure times t_{exp}/k_D. The dashed gray line indicates the threshold dose D_{th}. The upper panel shows the nonlinearity $N(t_{exp})$ (blue curve) and the temporal nonlinearity $\tilde{N}(t_{exp})$ (red curve). For low intensities, the nonlinearity is $N \approx 2$ and the temporal nonlinearity is $\tilde{N} \approx 1$, i.e., D_{th} depends nonlinearly on I_{th}, but linearly on t_{exp}. In contrast, for large intensities, $\tilde{N} = N \approx 1.7$, i.e., the dose depends nonlinearly on both, I_{th} and t_{exp}. Consider two exposure scenarios with equal deposited dose $D = D_{th}$. The first exposure has an exposure time of $t_{exp,1}/k_D = 10^1$ (filled blue square), and the second one a 100 times longer exposure time, i.e., $t_{exp,2}/k_D = 10^3$ (open blue
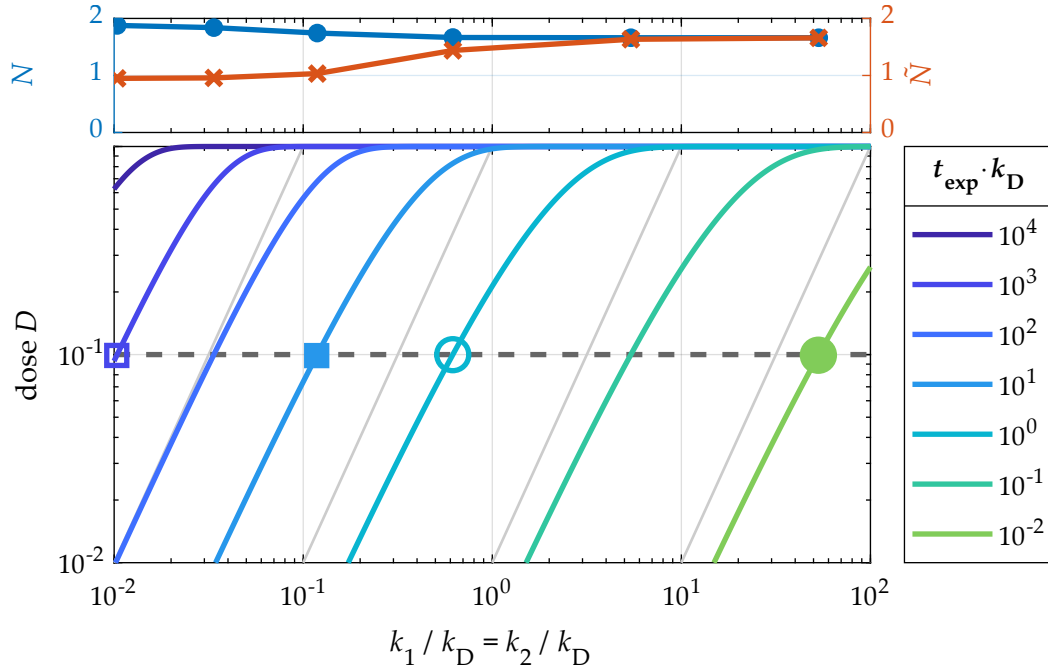
Figure 5.5: Comparing exposures with and without temporal nonlinearity. The lower panel shows a double-logarithmic diagram of the dose plotted versus the intensity for logarithmically scaled exposure times. The intensity is expressed in terms of $k_1/k_D = k_2/k_D$, i.e., for the case of $\epsilon_1 = \epsilon_2 = 1$. The gray dashed line indicates the threshold dose D_{th}, the gray diagonals have a slope of 2. For long exposure times (blue lines), the dose is $D \propto I^2 t_{exp}$. For short exposure times (green lines), the dose is $D \propto I^2 t_{exp}^2$. The upper panel shows the (intensity) nonlinearity N (blue curve) and the temporal intensity $\widetilde{N}$ (red curve).

square). In this regime, the ratio of the threshold intensities is $I_{th,1}/I_{th,2} \approx 10$, which is the same ratio as for canonical two-photon absorption (see section 3.1). Now, consider another pair of exposures using much shorter exposure times with $t_{exp,3}/k_D = 10^{-2}$ (filled green dot), and $t_{exp,4}/k_D = 1$ (open green circle). In this case, the ratio of the threshold intensities is $I_{th,3}/I_{th,4} \approx 100$, which is the same ratio as for canonical one-photon absorption.

Thus, if the dose scales nonlinearly with the exposure time, i.e., $\widetilde{N} > 1$, a nonlinearity $N > 1$ is, in general, insufficient to warrant the required nonlinearity for 3D printing (see section 2.6). This statement can be further refined. First, the false-color diagram of $\widetilde{N}(t_{exp})$ displayed in Figure 5.4c shows that the regime for which $\widetilde{N} > 1$ is limited to $k_1 \approx k_2 > k_D$. Second, $\widetilde{N}$ and the nonlinearity N are no global properties, but depend on the *local* intensity and on the *local* exposure history of the photoresin. Hence, it is possible that $\widetilde{N} \approx 2$ (or $N \approx 1$) in the focus
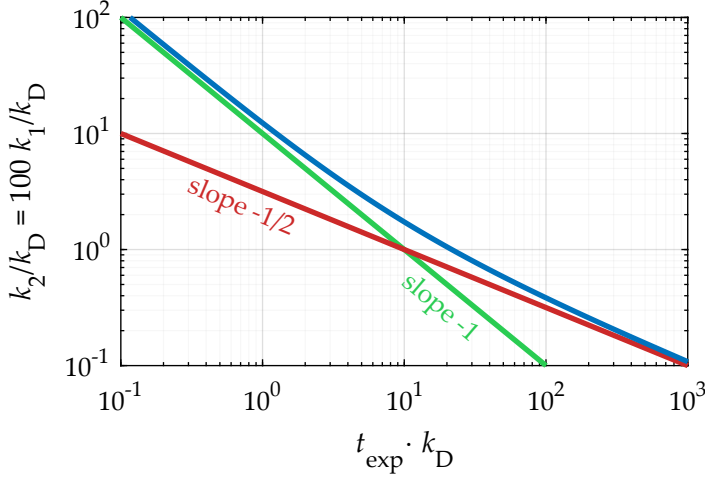
Figure 5.6: Plot of the threshold intensity versus the exposure time t_{exp}. The threshold intensity is proportional to k_2/k_{D}, which is plotted on the vertical axis. The ratio of the extinction coefficients is $\epsilon_2 = 100\epsilon_1$. At $t \cdot k_{\mathrm{D}} = t/\tau \approx 10$, the curve changes its slope from -1 to $-1/2$. Adapted from Ref. [53] with permission from Springer Nature.

of an intense laser beam, whereas $\widetilde{N} \approx 1$ (or $N \approx 2$) is obtained in the tails of the focused beam.

In summary, to obtain a nonlinearity exponent of $N > 1$ and a temporal nonlinearity $\widetilde{N} = 1$, one must ensure low rate coefficients $k_1 < k_{\mathrm{D}}$ and $k_2 < k_{\mathrm{D}}$. Using Figure 5.4a, this condition can be converted to an upper bound for the exposure time. For the case of $\epsilon_1 = \epsilon_2$, this bound is $t_{\mathrm{exp}} \gtrsim 2\tau$. In laser-scanning 3D nanoprinting, the exposure time is inversely proportional to the scan velocity v_{scan} and the voxel FWHM-diameter d_{FWHM}, i.e.,

$$v_{\mathrm{scan}} \propto \frac{d_{\mathrm{FWHM}}}{t_{\mathrm{exp}}}. \tag{5.9}$$

Thus, for a given voxel size, the maximum scan velocity at which $N > 1$ and $\widetilde{N} = 1$ is limited in two-step absorption and depends on the intermediate-state lifetime $\tau = k_{\mathrm{D}}^{-1}$. This limit is in sharp contrast to two-photon absorption 3D printing, where the nonlinearity exponent is independent of the scan velocity.

Experimentally, photoresins are characterized in point-exposure experiments, in which the threshold intensity I_{th} is measured for various exposure times t_{exp}. Figure 5.6 shows the threshold intensity I_{th}, expressed in terms of k_1/k_{D}, plotted against the exposure time $t_{\mathrm{exp}}/\tau = t_{\mathrm{exp}} k_{\mathrm{D}}$ with a ratio of the extinction coefficients of $\epsilon_2 = 100\,\epsilon_1$. This corresponds to the cut of Figure 5.4a along the diagonal labeled "10^2". The parameters are chosen for direct comparison with the results of the point-exposure experiments discussed in subsection 6.3.1. In the plot, the slope changes from -1 to $-1/2$ at $t_{\mathrm{exp}} \approx 10\tau$. From the relation $D_{\mathrm{th}} \propto I_{\mathrm{th}}^N t^{\widetilde{N}}$, it can be

seen that the slope of the curve indicates the negative fraction of $\widetilde{N}$ and N, i.e.,

$$\frac{\mathrm{d}\ln\left(I_{\mathrm{th}}\right)}{\mathrm{d}\ln(t_{\mathrm{exp}})} = -\frac{\widetilde{N}}{N}. \tag{5.10}$$

For the used pair of extinction coefficients, the temporal nonlinearity is $\widetilde{N} \approx 1$ (see Figure 5.4c) and the slope of the curve is equal to $-1/N$.

5.4 GOOD TWO-STEP-ABSORPTION INITIATORS

From the simple rate model proposed in section 5.3, we have learned that a two-step-absorption photoinitiator must have a sufficiently short intermediate-state lifetime. However, this condition is yet very vague and will be specified in more detail below. We will discuss five further criteria that a good two-step-absorption photoinitiator should fulfill.

5.4.1 Intermediate-State Lifetime

As discussed in section 5.3, the intermediate-state lifetime of the photoinitiator limits the maximum laser-focus scan velocity at which the desired nonlinearity exponent $N = 2$ is obtained. However, a short intermediate-state lifetime also implies a large polymerization threshold intensity. These two constants must be balanced for the target application.

Commercially available laser-scanning 3D nanoprinting setups currently achieve (single focus) peak printing rates on the order of $k_{\mathrm{scan}} = 3 \cdot 10^5$ voxels s^{-1} [9]. This printing rate corresponds to a voxel exposure time of $k_{\mathrm{scan}}^{-1} = 3\,\mu$s. From the rate-model calculations in section 5.3, we have learned that for two-step absorption, the voxel exposure time must remain well above the intermediate-state lifetime in order to obtain a nonlinearity exponent $N \approx 2$. Thus, for high-speed 3D laser printing, an intermediate-state lifetime of $\tau < 3\,\mu$s is desired.

So far, the nature of the intermediate-state was not further specified. With the constraint on the intermediate-state lifetime at hand, we can pick suitable transient molecular state candidates. Upon optical excitation, an organic molecule undergoes an electronic transition from the ground-state to a higher electronic singlet state. In general, the molecule is excited to a vibronically excited singlet state, from which it will relax to the lowest excited singlet state within picoseconds [135]. The lifetime of the lowest excited singlet state is on the order of nano- to microseconds for most organic molecules [135, 136]. Molecules in their first excited singlet state decay either to the singlet ground-state or, via intersystem crossing, to the triplet manifold. Energetically, the lowest triplet-state energy is located below the first

excited singlet-state and typical triplet-state lifetimes of organic molecules are on the order of micro- to milliseconds [135], but can even be seconds long [136]. However, quencher molecules like oxygen lower the triplet-state lifetime.

Therefore, excited singlet-states and triplet-states qualify as candidates for intermediate states in two-step absorption. On the one hand, the short intermediate-state lifetime offered by excited singlet-states allows for short exposure times, while on the other hand, such short intermediate-state lifetimes require high light intensity levels to reach the polymerization threshold. For the longer lived excited triplet-state molecules, the situation is the other way round. However, there the lifetime can be conveniently tuned using quencher molecules. Hence, we will focus on two-step photoinitiators with a triplet intermediate-state in the following.

Singlet and triplet states are not the only candidates for two-step absorption intermediate states. For instance, photochromic molecules have been suggested as two-step-absorption photoinitiators and employed in holography [137, 138]. The therein used photochromic molecule, a spiropyrane, undergoes a ring-opening reaction when excited with near-UV light. The isomer formed as an intermediate product by the ring-opening reaction can be further excited optically, or revert back to the original ring-closed form in a thermally or optically activated reaction. The intermediate-state lifetime of photochromic molecules ranges from microseconds to minutes [139] and is a topic of ongoing research.

5.4.2 *Ground-State and Excited-State Extinction*

As second criterion, a good one-color two-step photoinitiator must absorb light at one given wavelength λ in both, its ground-state and in its intermediate state. Otherwise, one-color two-step absorption is simply not possible. There are cases in which a two-step-absorption photoinitiator in its intermediate state is practically transparent at the wavelength λ. However, a nonzero transient-extinction may exist at a second, different wavelength λ_2. The latter case is referred to as *two-color* two-step-absorption photoinitiation and will be discussed in detail in chapter 7 and chapter 8. Within this chapter and chapter 6, two-step absorption refers to the case of *one-color* two-step absorption.

In two-photon absorption, the focused laser beam traverses the photoresin from the objective lens to the focal plane almost unattenuated. In contrast, in a two-step absorption photoresin, the focused laser beam is attenuated during propagation. After propagating a distance d in a photoresin with photoinitiator concentration c and a (linear) extinction coefficient ϵ_1, the incident chief-ray-power[1] P_0 is

---

[1] For objective lenses with a planar front-lens, the distance from the front-lens to the focal plane through the photoresin is longer for the marginal ray than it is for the chief ray.

Figure 5.7: The trade-off between a low threshold intensity and a high nonlinearity. For a fixed exposure time $t_\mathrm{exp} = 10\tau$ and ground-state extinction ϵ_1, the threshold intensity, expressed in terms of $k_{1,\mathrm{exp}}/k_\mathrm{D}$ (blue), decreases for large values of ϵ_2. The nonlinearity N (red) is maximal for $\epsilon_2 = \epsilon_1$. The gray diagonal lines have a slope of $-1/2$.
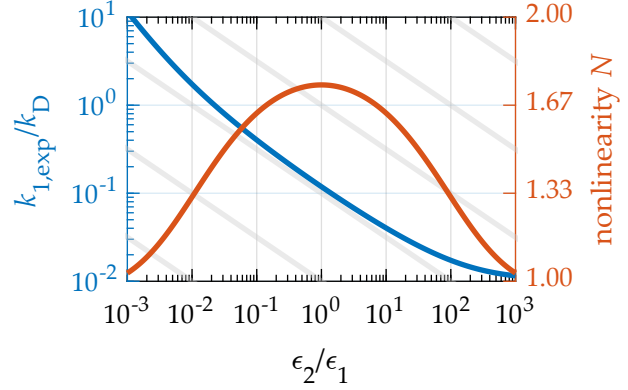
attenuated according to Beer's law by

$$P = 10^{-\epsilon_1 cd} P_0. \tag{5.11}$$

To illustrate the consequences of Beer's law, assume a photoresin with a photoinitiator concentration of 50 mM and a decadic extinction coefficient of $\epsilon_1 = 10^3\,\mathrm{M^{-1}\,cm^{-1}}$. These values yield a (decadic) extinction of $\epsilon_1 c = 50\,\mathrm{cm^{-1}}$. After a propagation distance of 300 μm, which is a typical microscope-objective free working-distance, the total power at the focal plane is reduced to a meager intensity $P = 3\,\%\,P_0$. The remaining power is absorbed within the resin, adding up to the accumulated dose. Hence, the photoresin's extinction at the wavelength λ must remain sufficiently low, i.e., below $\epsilon_1 c = 5\,\mathrm{cm^{-1}}$ when used with dip-in, high-NA objective lenses.

The constraint of a fixed ground-state extinction can be taken into account in the rate-model calculations discussed in section 5.3. Then, the exposure time t_exp and the transient extinction coefficient ϵ_2 alone determine the threshold intensity I_th. In Figure 5.7, the rate coefficient $k_{1,\mathrm{exp}}$, which is proportional to the threshold intensity I_th, is plotted versus the extinction coefficient ratio ϵ_2/ϵ_1 on a double-logarithmic scale for a fixed exposure time $t_\mathrm{exp} = 10\tau$. The threshold intensity decreases with increasing excited-state extinction coefficient. On the right vertical axis, the nonlinearity exponent N is plotted. N is maximal for equal extinction coefficients ϵ_2 and ϵ_1. Hence, for a two-step-absorption photoinitiator with a low polymerization threshold intensity, the transient extinction coefficient ϵ_2 should be large. Then again, to obtain a high nonlinearity exponent N at short exposure times, both extinction coefficients should be equal. Thus, in two-step absorption there is a compromise between photoresin sensitivity and maximum scan speed, which places an upper bound on ϵ_2. Note that in two-photon absorption, there is no upper bound for the two-photon absorption cross-section.

5.4.3 Inert Intermediate State

So far, we have assumed that no polymerization reactions are triggered from the intermediate state. If this requirement is not fulfilled, we are effectively dealing with a one-photon-absorption photoinitiator. In practice, an inert behavior can be encouraged by furnishing the intermediate state with little energy. For instance, typical bond-cleavage energies in photoinitiators are on the order of a $290\,\mathrm{kJ\,mol^{-1}} = 3.0\,\mathrm{eV}$ [84]. Ensuring that the intermediate-state energy is below this energy level ensures that bond-cleavage reactions are suppressed. However, other types of undesired reactions may well be triggered below this energy threshold, for instance intra- or intermolecular hydrogen abstraction. Hence, it is of prime importance to suppress any polymerization reaction triggered from the intermediate-state.

5.4.4 Solubility

As forth criterion, the two-step-absorption photoinitiator molecule should dissolve in adequate amount in the liquid acrylic monomer, otherwise the initiator is of little use. For instance, polycyclic aromatic hydrocarbons are notoriously difficult to dissolve in acrylic monomers. In contrast, compounds bearing extended aliphatic chains dissolve much easier [83]. To some extent, low solubility can be compensated by a large extinction coefficient.

5.4.5 Location of the Absorption Band

In 3D laser nanoprinting, a laser beam is tightly focused by high-NA microscope objectives. These refractive objectives consist of several glass-lens groups to correct for optical aberrations [140]. However, most glasses do not transmit UV-light well [141], hence limiting the usable excitation wavelength range to the near-UV, visible and, infrared. Therefore, two-step-absorption photoinitiators in which either the first or the second excitation-step requires deep-UV-excitation, are problematic. A UV absorption band is less problematic in two-photon absorption since the excitation happens at the fundamental wavelength, i.e., twice the wavelength of the absorption band.

5.4.6 Efficient Photoinitiation

So far, I have tacitly assumed that the final D state in our model triggers a (free-radical) polymerization. However, this behavior is not granted for two-step absorption compounds — processes like reverse intersystem crossing from the upper excited state C are well conceivable [135]. The vast majority of common

one-step photoinitiators are ketones and aldehydes, which incorporate at least one carbonyl group [84]. Ketones and aldehydes are able to initiate photopolymerization via a Norrish type I or Norrish type II reaction (see also section 2.7), which makes those compounds promising two-step-absorption initiator candidates.

It should be emphasized, however, that there are other two-step-absorption photoinitiator systems, that do not incorporate a carbonyl unit. For one, there are photochromic systems (see subsection 5.4.1). Moreover, the combination of an α-quinquethiophene as photosensitizer with 3,3'-diazidodiphenylsulfon as acceptor as two-step-absorption photoinitiator system was reported [142, 143]. In the latter system, however, the α-quinquethiophene suffers from poor solubility and the polymerization threshold intensity of the entire system is comparably large.

5.5 TWO-STEP-ABSORPTION PHOTOINITIATOR CANDIDATES

Table 5.1 lists a selection of aldehydes and ketones and their triplet energies E_T [136]. According to our third criteria, a low intermediate-state energy is preferred for a good two-step-absorption initiator. Furthermore, according to the fifth criterion, the two-step absorption initiator should have its absorption band in the visible - something that is true for the four candidates of lowest triplet-state energy. Fluorescine has been used extensively as fluorescent marker in microscopy, and as such, it has a high fluorescence quantum yield [144]. Furthermore, fluorescine consists of several aromatic rings, which do not dissolve well in acrylic monomers. Similarly, Fluorenone, which comprises two aromatic rings, can be expected to not dissolve well in acrylic monomers.

The next two candidates in Table 5.1 with low triplet-energy level are benzil (diphenylethanedione) and biacetyl (butane-2,3-dione), which both belong to the group of α-diketones. In the next chapter, we will see that they fulfill almost all criteria for good two-step-absorption photoinitiators. However, despite their low triplet-state energy, both molecules trigger reactions from their triplet state. Furthermore, whereas benzil with its overlapping ground-state and triplet-state absorption-spectra qualifies as one-color two-step-absorption photoinitiator, the ground-state and triplet-state spectra in biacetyl are well separated — hence making biacetyl a good two-color two-step-absorption photoinitiator.

Table 5.1: List of aldehydes and ketones and their triplet-state energies E_T. The entries are from Ref. [136].

Compound	E_T / eV	Compound	E_T / eV
Xanthone	3.2	Flavone	2.7
Acetophenone	3.2	Michler's ketone	2.6
Diisopropylketone	3.2	4-Acetylbiphenyl	2.6
Benzaldehyde	3.1	2-Acetonaphthone	2.6
1,2-Dibenzoylbenzene	3.0	1-Naphthylphenylketone	2.5
Benzophenone	3.0	1-Acetonaphthone	2.4
1,4-Diacetylbenzene	2.9	1-Naphthaldehyde	2.4
4-Cyanobenzophenone	2.9	**Biacetyl**	**2.4**
Thioxanthone	2.8	**Benzil**	**2.3**
Phenylglyoxal	2.7	Fluorenone	2.3
Anthraquinone	2.7	Fluorescine (acid)	2.2

6

One-Color Two-Step-Absorption 3D Nanoprinting
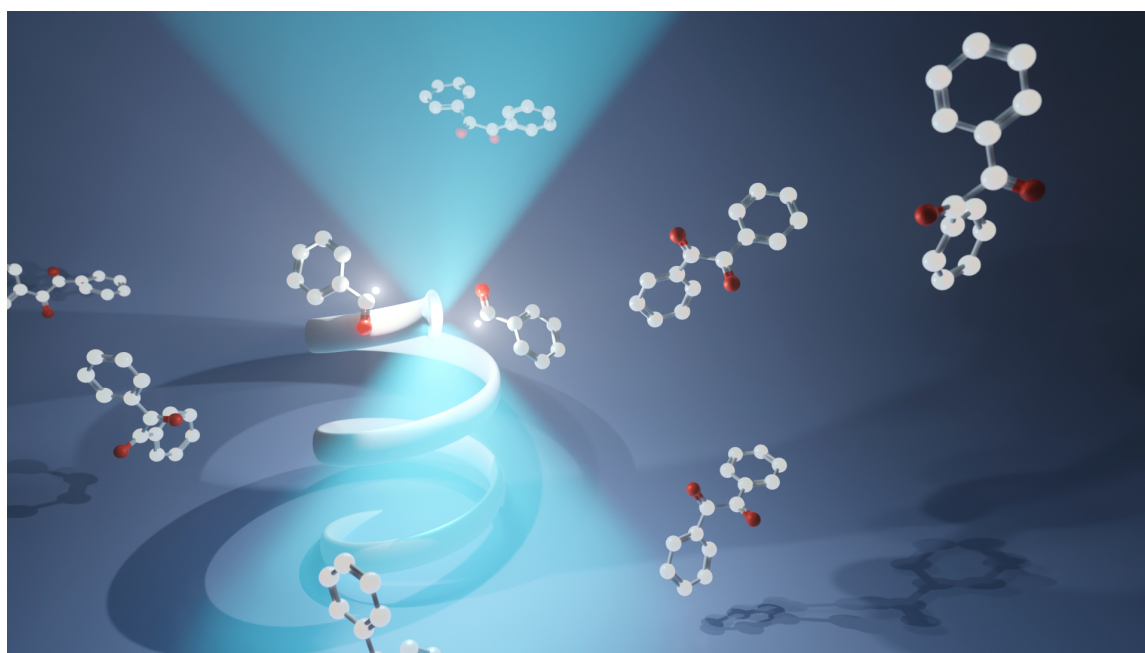
Artistic rendering of two-step-absorption 3D nanoprinting using benzil.

I have selected two potential two-step-absorption photoinitiator candidates in chapter 5. In this chapter, one candidate, benzil, is introduced in more detail and finally used in 3D nanoprinting experiments.

6.1 BENZIL AS TWO-STEP-ABSORPTION PHOTOINITIATOR

6.1.1 Structure and Electronic States

The 2D and 3D chemical structures of benzil are shown in Figure 6.1. Benzil consists of two adjacent carbonyl groups and hence belongs to the group of α-diketones. One phenyl ring is attached to each carbonyl. In its singlet ground-state, benzil has a skewed confirmation, meaning that the two carbonyl groups do not lie in a common plane but in planes that are twisted by a dihedral angle of 117° (see Figure 6.1b) [145]. However, without coinitiators, benzil is not known to be a good photoinitiator. In fact, benzil has been referred to as "[...] a relatively poor photoinitiator and is seldom used" [84].

Figure 6.2 shows a Jablonski-diagram for benzil in benzene, based on the work of Flamigni et al. [147]. Singlet ground-state benzil can be optically excited to the excited singlet-manifold by absorption of blue- or UV-light. From the lowest excited singlet state S_1, benzil fluoresces with a low quantum yield of less than 0.1 % [147]. The main relaxation pathway from the S_1 state is via intersystem crossing to the triplet manifold, which happens with a quantum yield of 92 % [148]. In the triplet state, benzil changes its conformation to a trans-planar form [149]. From the lowest triplet state T_1, the main deactivation pathway in an inert solvent is via reverse intersystem crossing to the singlet manifold [147]. While phosphorescence from the T_1-state is observed only with a low quantum yield of 3.1 %, the phosphorescence decay time in a deoxygenated benzene solution at a temperature of 20 °C is 80 µs [147].

6.1.2 Ground-State and Transient Spectra

The overlapping ground-state and intermediate-state spectrum is one important criterion for a two-step-absorption photoinitiator(see subsection 5.4.2). Figure 6.3 shows the ground-state and triplet-state spectra of benzil in acetonitrile and ben-

Figure 6.1: Molecular structure of benzil. a, Skeletal structure of benzil. **b**, 3D rendering of benzil in its ground-state, according to Ref. [146]. The skewed geometry is outlined by two planes.
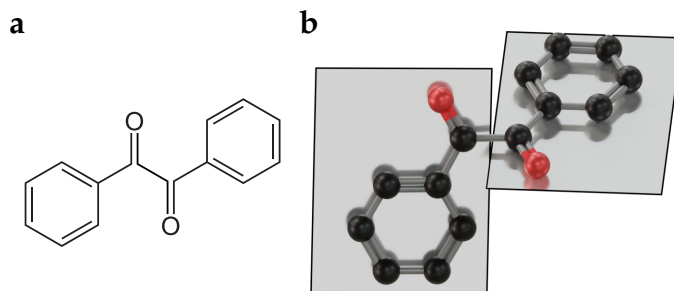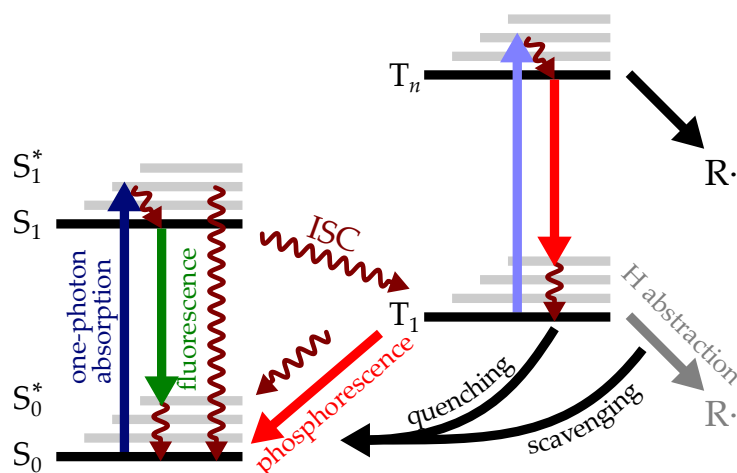
Figure 6.2: Jablonski-diagram of benzil, based on Ref. [147]. Ground-state molecules are optically excited to the upper singlet manifold and rapidly relax to the lowest excited singlet-state S_1. From S_1, intersystem crossing to the triplet manifold happens with a high quantum yield. From the lowest triplet-state T_1, molecules can either decay to singlet ground-state S_0 by reverse intersystem-crossing, by quenching, or by emitting phosphorescence. Alternatively, molecules in the T_1-state can be further optically excited to a higher triplet-state T_n, from where molecules readily dissociate into free radicals $R^\bullet$ [150]. Depending on the solvent, a bimolecular hydrogen-abstraction reaction is possible from the lowest triplet-state. Adapted from Ref. [53] with permission from Springer Nature.

zene, respectively. The data for the triplet-state spectrum are taken from Ref. [151]. The ground-state spectrum has a $n - \pi^*$ absorption band [149] at a wavelength of 380 nm, whose tails extent into the visible. At 405 nm wavelength, benzil has a molar decadic extinction coefficient of $40\,\mathrm{M}^{-1}\,\mathrm{cm}^{-1}$. The excited-state spectrum on the other hand shows characteristics of a $\pi - \pi*$ transition [136], with a peak extinction coefficient of $8 \cdot 10^3\,\mathrm{M}^{-1}\,\mathrm{cm}^{-1}$ at a wavelength of 480 nm. However, the absolute value of the triplet-state extinction coefficient must be considered to have a substantial uncertainty since another group has measured a peak extinction coefficient of $12 \cdot 10^3\,\mathrm{M}^{-1}\,\mathrm{cm}^{-1}$ [152]. At the wavelength 405 nm, the triplet-state extinction coefficient is approximately $4 \cdot 10^3\,\mathrm{M}^{-1}\,\mathrm{cm}^{-1}$ and hence 100 times larger than the ground-state extinction coefficient at the same wavelength.

6.1.3 *Intermediate-State Properties*

As listed in Table 5.1, the T_1-state of benzil lies at 2.3 eV and is hence below the bond-cleavage energy of ≈ 3 eV [153]. However, upon further optical excitation

Figure 6.3: Absorption spectra of benzil. Ground-state (dark-blue) and excited-state (light-blue) molar decadic extinction coefficient of benzil, measured in acetonitrile and benzene, respectively. Note that the excited-state spectrum is scaled by a factor 100. The data for the excited-state spectrum is taken from Ref. [151]. Adapted from Ref. [53] with permission from Springer Nature.
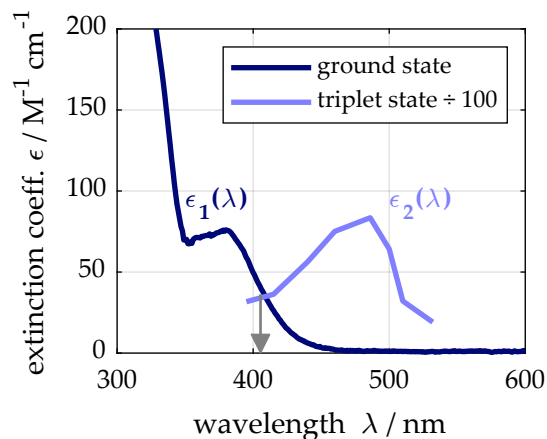
into an excited triplet-state, sufficient energy is provided to overcome this energy barrier and to fragment benzil into two radicals [150, 153, 154]. This energy barrier ensures the desired two-step photoinitiation behavior [150]. Having said that, benzil in its triplet ground-state is able to abstract hydrogen atoms from nearby susceptible groups, leading to the formation of free radicals [154]. This is a common and well-known reaction of ketones [136, 155], which is undesired for a two-step-absorption photoinitiator.

6.1.4 Triplet Quenching

One option to suppress the hydrogen-abstraction reaction is to employ triplet quenchers [136]. In a photoresin, a quencher molecule promotes the relaxation of triplet-state molecules to the singlet ground-state or another, nonradiative state. One quencher that is present in all photoresins at ambient conditions is solvated molecular oxygen [60, 88, 152]. In a carbon tetrachloride solution, oxygen quenches benzil at a considerable rate of $0.5 \cdot 10^9 \, \text{M}^{-1} \, \text{s}^{-1}$, somewhat below the diffusion-limited rate of $3 \cdot 10^{10} \, \text{M}^{-1} \, \text{s}^{-1}$ [156]. However, oxygen also scavenges free radicals to peroxy radicals, and is hence depleted in the course of the polymerization [60, 88].

Adjusting the oxygen concentration in a photoresin during 3D printing is cumbersome and challenging. Therefore, another quencher molecule, bis(2,2,6,6-tetramethyl-4-piperidyl-1-oxyl) sebacate (BTPOS), is introduced in the photoresin to counteract the intermediate-state reaction (see Figure 6.4). The molecular structure of BTPOS is shown in the inset of Figure 6.4. One molecule contains two linked (2,2,6,6-tetramethylpiperidin-1-yl)oxyl (TEMPO)-moieties.

TEMPO, which has an aminoxyl group and belongs to the group of hindered amine light-stabilizers [157], is a persistent, or stable, radical. A persistent radical
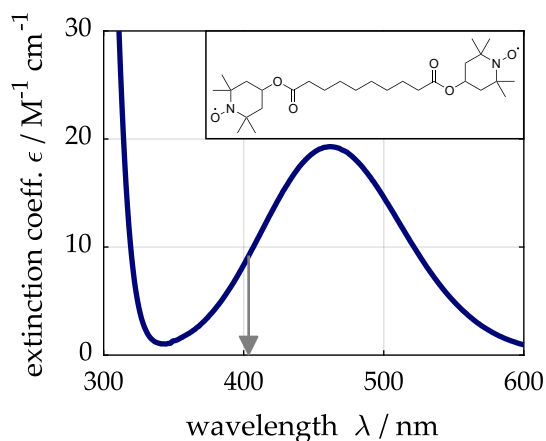
Figure 6.4: Molecular structure and optical extinction coefficient of the quencher and scavenger molecule BTPOS. Plot of the molecular decadic extinction coefficient of BTPOS in acetonitrile. Inset: Structure formula of BTPOS, which consists of two linked TEMPO-moieties. Adapted from Ref. [53] with permission from Springer Nature.

does not react with other radicals of the same kind, i.e., it does not self-terminate, yet it reacts with other free radicals. Nitroxide-mediated radical polymerization takes advantage of this effect [158]. In solution, TEMPO quenches benzil's triplet state at a rate close to the diffusion limit [159] and thereby favorably decreases benzil's effective triplet-lifetime. Furthermore, TEMPO can suppress hydrogen-abstraction reactions from its own excited state [160].

Thus, benzil in combination with a suitable quencher like BTPOS fulfills all criteria for a one-color good two-step-absorption photoinitiator. To confirm this finding, results of 3D nanoprinting experiments with benzil-containing photoresin are now presented.

6.2 METHODS

6.2.1 *Photoresin Compositions*

In the following, photoresin compositions used in the 3D nanoprinting experiments are listed. For simplicity, the photoresins are labeled as "PR1"–"PR4". Benzil, TEMPO, and Pentaerythritol triacrylate (PETA) are purchased from Sigma-Aldrich (now Merck KGaA). BTPOS is purchased from TCI Chemicals. Trimethylolpropane triacrylate (TMPTA) is purchased from Alfa-Aesar. IP-Dip NPI is purchased from Nanoscribe GmbH & Co. KG. Irgacure 369 is purchased from Ciba Speciality Chemicals (now IGM Resins B.V.). All photoresins are mixed and used in yellow-light conditions. For each of the below listed photoresins, variants containing less or no BTPOS are also prepared.

PR1 21.0 mg benzil and 25.6 mg BTPOS are dissolved in 1 mL of PETA. This composition corresponds to a final concentration of 1.7 wt% (100 mM) benzil and 2.1 wt% (50 mM) BTPOS. To dissolve all ingredients, the mixture is stirred on a hot plate at 45 °C for 4 h.

PR2 21.0 mg benzil and 25.6 mg BTPOS are dissolved in 1 mL mixture of 70 vol% IP-Dip NPI and 30 vol% PETA. The ratio of the two monomers is adjusted to obtain a diffraction-limited focus in dip-in printing mode [72] at 405 nm wavelength. This photoresin composition corresponds to a final concentration of 1.8 wt% (100 mM) benzil and 2.2 wt% (50 mM) BTPOS. To dissolve all ingredients, the mixture is stirred on a hot plate at 45 °C for 4 h.

PR3 21.0 mg benzil and 25.6 mg BTPOS are dissolved in 1 mL TMPTA. This composition corresponds to a final concentration of 1.8 wt% (100 mM) benzil and 2.2 wt% (50 mM) BTPOS. To dissolve all ingredients, the mixture is stirred on a hot plate at 45 °C for 4 h.

PR4 18.3 mg Irgacure 369 and 12.8 mg BTPOS are dissolved in 1 mL PETA. This composition corresponds to a final concentration of 1.5 wt% (50 mM) benzil and 1.1 wt% (25 mM) BTPOS. Due to its lower solubility, the absolute concentration of Irgacure 369 in PR4 is lower than the absolute concentration of benzil in PR1-PR3. The relative molar concentration of photoresin and quencher is kept constant. To dissolve all ingredients, the mixture is stirred on a hot plate at 45 °C for 4 h.

6.2.2 Focus-Scanning 3D Nanoprinting Setup

A custom 3D nanoprinting setup is used to characterize one-color two-step-absorption photoresins and to print 3D structures. Joachim Fischer originally assembled the setup [76], and since then, it has been rearranged several times. The setup in its most recent state, as schematically depicted in Figure 6.5, is enhanced with further cw lasers, a galvanometric beam-scanner and the corresponding optics and electronics by the author together with Tobias Messer.

Five different laser sources are installed in this setup, any two of which can be used simultaneously. The first laser is a Ti:Sa laser (Spectra-Physics MaiTai HP), whose emission wavelength is tunable in the range of 690 nm to 1040 nm. While this laser is designed to emit femtosecond pulses, it can be operated in a non-modelocked mode by reducing the pump power and by disabling the intracavity AOM. The Ti:Sa laser power is modulated by an (extracavity) AOM (AA Opto Electronic MTS-40-A3-750.850).

A second expanded laser beam is emitted by a 488 nm wavelength, fiber-coupled (Schäfter&Kirchhoff 60FC-4-M8-33), current-modulated, diode-laser (Toptica iBeam smart-488-S-HP). The beam is combined by a dichroic shortpass beam splitter (Edmund Optics 69-206) with the expanded Ti:Sa laser beam. Both beams pass the PBC in transmission.
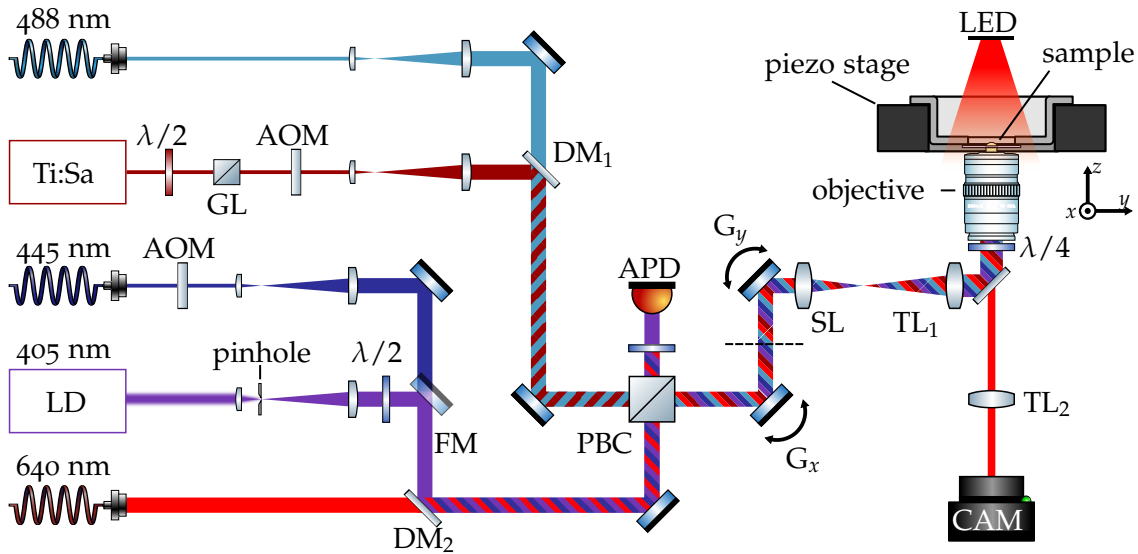
Figure 6.5: Scheme of the main components of the focus-scanning 3D nanoprinting setup. The setup consists of five beam paths, which are combined by dichroic mirrors (DM_1 and DM_2), a kinematic flip mirror (FM), and a polarizing beam combiner (PBC). Three lasers are fiber-coupled, whereas the deep-blue laser diode (LD) and the Titanium-Sapphire (Ti:Sa) laser emit into a free-space mode. The power of the Ti:Sa and LD beams is adjusted with a half-wave plate and a polarizer (PBC). For the Ti:Sa beam, a Glan-Laser polarizer (GL) is used. The power of the Ti:Sa beam is modulated by an AOM, all other lasers are current-modulated. Galvanometric mirrors (G_x and G_y) deflect the laser beams in the x- and y-direction. The dashed line located at the conjugated objective entrance-pupil indicates a $90°$ rotation of the drawing plane around the z-axis. A telescope formed by a scan lens (SL) and a tube lens (TL_1) images both galvanometer mirrors to planes close to the objective entrance-pupil. Circular polarization can be obtained by placing an apochromatic quarter-wave plate near the entrance pupil. The objective focuses the laser beams tightly through a coverslip into the photoresin, which is mounted on a piezoelectric-actuated stage. The piezo stage in turn is mounted on a motorized stage for coarse positioning (not shown). In point-exposure experiments, an APD monitors the pulse lengths of the filtered light of the 405 nm wavelength laser diode. A camera (CAM) is used to observe the sample plane, which is illuminated by a red light-emitting diode (LED). Created using "ComponentLibrary" [116] by Alexander Franzen (CC BY NC 3.0).

Third, the expanded beam of a fiber-coupled (Schäfter&Kirchhoff PMC-400Si-2.3-NA014 3-APC-300-P, Schäfter&Kirchhoff 60SMS-1-4-M12-33) 445 nm wavelength diode-laser (Picoquant LDH D-C-440), whose power is modulated by an AOM (AA Opto Electronic MT80-1.5-400.442), is used.

Alternatively, the 445 nm wavelength beam can be replaced by a kinematic mirror for a 405 nm wavelength beam, emitted by a current-modulated laser-diode (Thor-

labs L405P150), mounted on a thermoelectrically cooled (TEC) laser-diode driver (Thorlabs LDM56/M). The laser diode nominally emits in a single spatial-mode. However, the emitted beam is elliptic and astigmatic. Hence, the beam profile is cleaned by a 10 µm-diameter pinhole (Thorlabs P10C), which is mounted in a Keplerian telescope. The maximum laser power of the 405 nm wavelength laser diode is adjusted using a half-wave plate (Thorlabs WPHSM05-405) in combination with the subsequent PBC.

Finally, the deep-blue laser beam is combined by a longpass dichroic mirror (Thorlabs DMLP 567) with the beam of a current-modulated, fiber-coupled 640 nm wavelength diode-laser (Toptica iBeam smart PT-640). The combined beams are reflected in the PBC and combined with the Ti:Sa laser beam and the 488 nm-wavelength laser beam.

After passing the PBS, all beams are deflected by a pair of galvanometric mirrors (Pangolin Laser Systems, Saturn 5B 56S). In contrast to the setup proposed in chapter 3, where either axis of the galvanometric mirror-pair is imaged onto the other, the mirrors in this setup are mounted tightly spaced around the conjugated pupil plane.

The galvanometric mirrors are mounted near the rear entrance-port of a microscope body (Leica DM IRB), where the mirrors are imaged by a pair of achromatic lens-doublets (Thorlabs ACL254-100-A and ACL-254-150-A) to planes near the objective entrance-pupil. The oil-immersion microscope-objective (Leica HCX PL APO 100×/1.4-0.7 Oil CS, Leica type F immersion liquid) tightly focuses the laser beams through a glass coverslip (Paul Marienfeld, #1.5H) into the liquid photoresin. The sample with the glass coverslip is mounted on a pizoelectric-actuated three axis stage (Physik Instrumente P-527.3CL), which in turn is mounted on a motorized stage (Märzhäuser-Wetzlar Scan IM 120 × 100). For 3D printing experiments of 3D structures that exceed an axial extent of 20 µm, the piezo-actuated stage is replaced by one with an extended travel range (Physik Instrumente P563.3CD).

Laser powers are measured using a semiconductor power sensor (Coherent TP86) at the objective pupil plane. Furthermore, an APD (Thorlabs APD410A/M) is mounted at the idle exit port of the PBS. The APD is used to monitor the pulse shape emitted by the 405 nm laser diode during point-exposure experiments.

The movements of the piezo-actuated stage, the motorized stage, the galvanometric mirrors, and the electronic power modulation is concerted by two computer-controlled high-speed digital-analog boards (National Instruments PCI-6731, National Instruments PCI-MIO-16XE-10). These boards also acquire analog voltage signals, e.g., the voltage signal of the APD. The control software originally written by Joachim Fischer, Jonathan Müller, and Patrick Müller was further enhanced, e.g., to address the galvanometric laser-scanners.
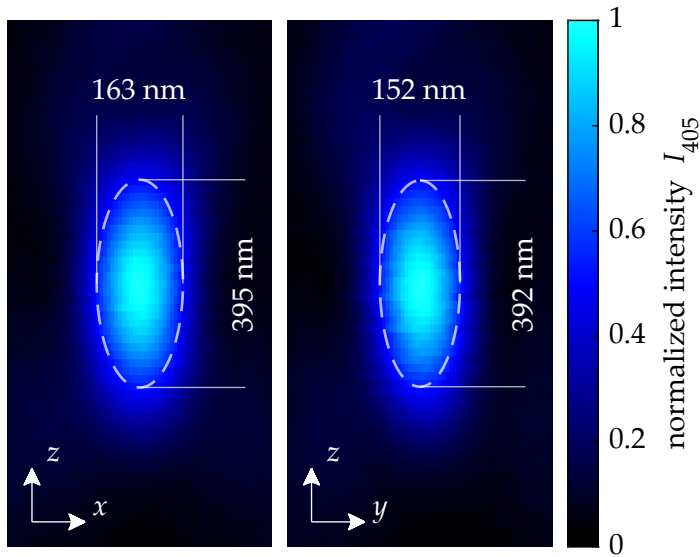
Figure 6.6: Measured laser focus intensity distribution for the $405\,nm$ **wavelength laser beam.** The left panel shows a cut in the xz-plane, the right panel a cut in the yz-plane. The FWHM-diameter is obtained by fitting a two-dimensional Gaussian distribution on the measured data. The intensity profiles are measured for a linearly polarized laser beam, i.e., without the quarter-wave plate in front of the objective lens pupil. Hence, the lateral FWHM-values differ [76]. Adapted from Ref. [53] with permission from Springer Nature.

6.2.2.1 Focus Characterization

Although the objective lens is nominally aberration-corrected for parallel ray-bundles, i.e., "collimated beams", a diffraction-limited focus is only obtained for slightly convergent or divergent beams. The optimum divergence depends on the beam wavelength and hence must be optimized for each laser beam individually, using the corresponding telescope or fiber-coupler. To assess the focus quality, a glass coverslip, spin-coated with $80\,nm$ gold-beads, which are embedded in a layer of cured optical adhesive, is scanned through the laser focus. The backscattered signal is collected by a semiconductor photodiode (not depicted) and recorded by the computer [76]. With the setup, the foci of two laser beams can be analyzed simultaneously, which is important to precisely superimpose both foci in all three dimensions for two-color excitation experiments [76]. However, in general, it is not possible to overlay two entirely aberration-free foci of different laser wavelengths despite the apochromatic objective lens.

Figure 6.6 shows two false-color diagrams of measured focus intensity profiles for the $405\,nm$ wavelength laser beam. A two-dimensional Gaussian intensity-profile is fitted to the data. The resulting axial and lateral FWHM-diameters are highlighted by a dashed ellipse and the obtained values for the (squared) intensity FWHM in x, y, and z are $163\,nm$ ($120\,nm$), $152\,nm$ ($113\,nm$) and $393\,nm$ ($288\,nm$). The axial values are averages from both measured intensity profiles. The difference in the lateral intensity profiles is caused by the linearly polarized laser beam used for this measurement [76]. From these values, a voxel aspect ratio of 2.5 can be inferred, indicating a diffraction-limited focus.

6.2.3 Sample Preparation

For an improved substrate adhesion of 3D printed objects, the glass coverslips are cleaned and silanized. First, the glass coverslips are cleaned in an 2 vol% aqueous solution of Hellmanex III (Hellma GmbH & Co. KG) at 55 °C for 15 min. Next, the cleaned substrates are washed three times in de-ionized water and dried in a stream of nitrogen gas. The surface of the substrates is activated for 20 min in an air-plasma. Finally, the substrates are vapor-silanized for 2 h in an exsiccator, which is evacuated to an ambient pressure of 100 mbar. There, the substrates are placed next to a Petri dish containing a droplet of pure 3-(trimethoxysilyl)propyl methacrylate (Merck KGaA).

During 3D printing in non-dip-in-mode [72], 25 μL of photoresin are contained in a 5 mm internal diameter PDMS-ring. This is especially important to avoid low-viscosity photoresins from flowing off the substrate, and to ensure a comparable photoresin-film height throughout experiments. Furthermore, the PDMS-ring is sealed by a second coverslip if the photoresin contains volatile ingredients.

6.2.4 Sample Development

After 3D printing, the remaining liquid photoresin is removed from the sample in a development process. Therefore, the sample is immersed in acetone for 3 min. Afterwards, the sample is washed for a few seconds in isopropyl alcohol, before it is dried in a stream of nitrogen gas. 3D printed photonic crystal samples are developed for 3 min in a solution of acetone and then transferred for supercritical drying (see section 2.2). Supercritically drying samples preserves filigree 3D printed structures, which would collapse in the conventional development process due to capillary forces.

6.2.5 Microscopy

3D nanoprinted samples are easiest characterized under an optical microscope. However, brightfield optical microscopes cannot resolve the finest features and surface quality of 3D nanoprinted structures. Scanning-electron microscopes can resolve features down to the single-digit nanometer scale. To avoid charging effects during the analysis, the samples are sputter coated with a 10 nm thick gold layer (Cressington 108 Auto, TESCAN GmbH). The analysis is performed with a Zeiss Supra 55VP (Carl Zeiss AG) at a primary-electron voltage of 5 kV. Since the polymers used for 3D printing are opaque to the electron beam, the interior of a 3D printed volume cannot be inspected in a scanning electron microscope (SEM) without further ado.

By using ultramicrotomy, information about the volume of 3D printed structures can be obtained. The following ultramicrotomy procedure was performed by Ernest Ronald Curticean, Dr. Irene Wacker, and Prof. Dr. Rasmus Schröder according to Ref. [53] on a set of 3D printed photonic woodpiles, which were printed by the author. In ultramicrotomy, a sample is first incubated for 2 h in a solution of 2 % of osmium tetroxide, a contrasting agent, dissolved in acetone. The acetone solution is replaced by a 50 % acetone-Epon solution, in which the sample is infiltrated for 3 h. Epon is an epoxy resin, comprised of 42.6 g glycid ether 100, 29.6 g dodecenylsuccinic acid anhydride, 18.4 g methyl-5-norbornene-2,3-dicarboxylic anhydride, and 2.4 g benzyldimethylamine. Finally, the sample is embedded in pure Epon and polymerized for 2 d at 62 °C. The printing substrate, a glass coverslip, is removed in liquid nitrogen and the cured epoxide-block is trimmed down to reveal the target structure.

Ultrathin slices with a thickness of 80 nm are cut from the epoxide-block using a diamond blade (RMC Boeckeler PowerTome PC ultramicrotome) and placed on silicon wafers. SEM-images of the slices are taken in a field-emission scanning electron-microscope (Carl Zeiss Microscopy Ultra 55) using a primary-electron energy of 1.5 keV.

6.3 3D NANOPRINTING RESULTS

6.3.1 Point-Exposure Experiments

To check if benzil exhibits the expected two-step absorption characteristics, point-exposure experiments are performed using photoresin PR3 and a laser wavelength of 405 nm. Figure 6.7 shows a double-logarithmic plot of the threshold laser powers P_{405} for exposure times in the range of $3 \cdot 10^1$–10^5 µs. The course of the data points follows the results obtained using the rate-model calculations (see Figure 5.6). For exposure times $t_{\exp} < 8 \cdot 10^2$ µs, the points lie on a line with a slope of -1. For longer exposure times, the behavior changes and the measured values lie on a line of slope $-1/2$, until they flatten even further for exposure times $t_{\exp} > 10^4$ µs. The plateau at long exposure times is not reproduced in the rate-model calculations, but has been observed many times in ordinary two-photon resists before and is attributed to in-diffusion of oxygen into the exposed voxel volume [60, 77].

The comparison with Figure 5.6 obtained by the rate-model yields an estimate of the intermediate-state lifetime $\tau \approx 80$ µs, which is in good in agreement with the intermediate-state lifetime of benzil measured in (quencher-free) solution (see section 6.1).
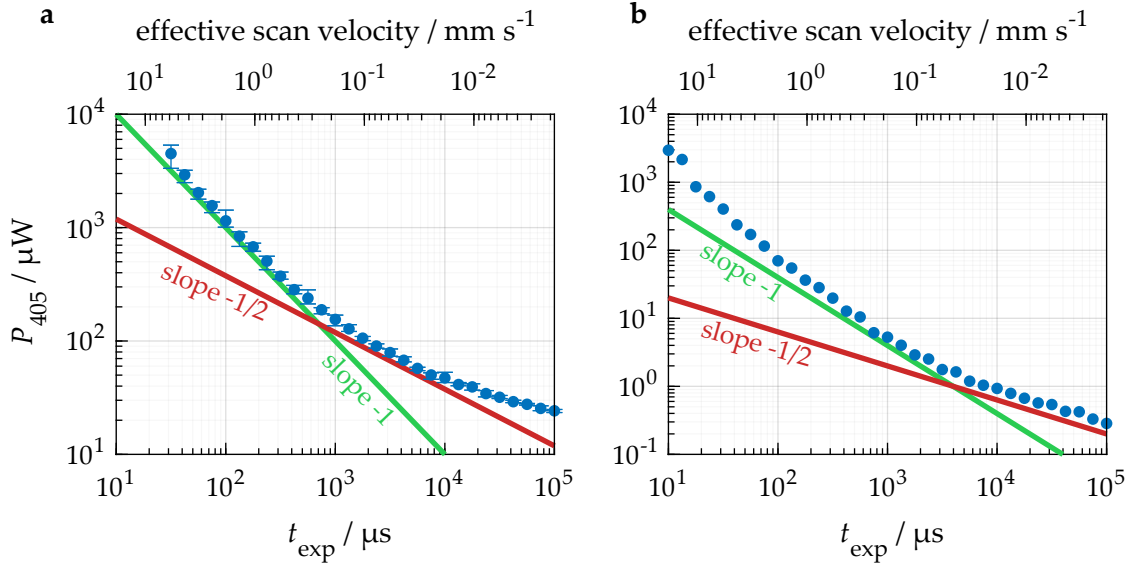
Figure 6.7: Double-logarithmic plot of the threshold laser power for point-exposure experiments using the photoresin PR1 (a) and PR4 (b). a, For short exposure times $t_{exp} < 8 \cdot 10^2$ µs, the data points lie on a line with slope -1 (green line), whereas for longer exposure times 10^4 µs $> t_{exp} > 8 \cdot 10^2$ µs, the data points follow a line with slope $-1/2$ (red line). Each measurement is repeated at least three times and the error bars mark the minimum and maximum measured value. **b,** Control experiment (single measurement) using photoresin PR4, which contains the photoinitiator Irgacure 369, for which a one-photon absorption behavior is expected at 405 nm wavelength. For long exposure times, a slope < 1 is found. Note the different vertical scale in the two panels. Adapted from Ref. [53] with permission from Springer Nature.

In control experiments, the point-exposure experiment is repeated under comparable conditions but using the photoresin PR4. Photoresin PR4 contains the one-photon-absorption photoinitiator Irgacure 369, for which a slope of -1 is expected in the double-logarithmic plot. However, even for the polymerization threshold of PR4 (see Figure 6.7b), a slope different from -1 is observed. Again, this apparent nonlinear behavior can be attributed to chemical nonlinearites [60, 77]. Hence, the observed slope of $-1/2$ alone does not warrant a two-step absorption behavior.

At this point, one might be tempted to think that chemical nonlinearities suffice to obtain the desired nonlinearity necessary for 3D nanoprinting. In fact, other groups have exploited these chemical nonlinearities and successfully printed 3D microstructures using cw lasers [161–163]. These chemical nonlinearities can be obtained by in-diffusion of quencher-species into the printing voxel [163]. In the course of the printing process, these quenchers are irreversibly consumed - not only locally, but also in the tails of the laser focus and eventually, by molecular diffusion,
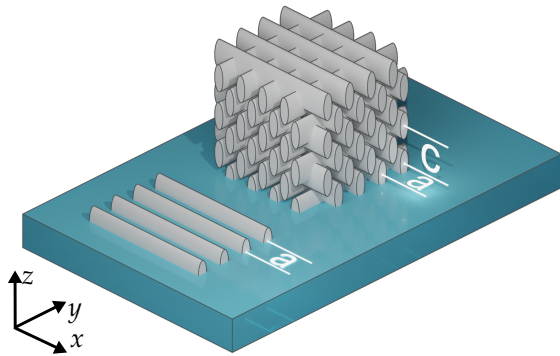
Figure 6.8: Artistic rendering of a line grating and a woodpile photonic crystal. Rendering of a 2D line grating (left) with line spacing a. The grating is printed directly on the glass-photoresin interface. Rendering of a face-centered cubic (fcc) woodpile photonic crystal (right), which consists of axially stacked, rotated, and shifted layers of line gratings. Adapted from Ref. [53] with permission from Springer Nature.

also in a larger volume around the printed object [60, 77, 81]. Thereby, the maximum scan speed for 3D printing is limited or large quencher concentrations are necessary which demand for high optical powers. A comparison of these and other works is provided in section 6.4.

6.3.2 Resolution Benchmarks

As explained in the previous section, the point-exposure experiments are of limited use to securely differentiate between a two-step absorption process and a process exploiting chemical nonlinearities. By going from point-exposures to more intricate structures, a more secured conclusion on the underlying process can be made. In section 2.6, the 3D printing results for nonlinearity exponents $N = 2$ and $N = 1$ are compared. While it is still possible to print individual lines by employing a printing process with $N = 1$, dense line patterns are already problematic. In 3D structures, the different behavior of processes with $N = 2$ and $N = 1$ becomes even more pronounced (see section 2.6).

As benchmark, line gratings and woodpile photonic crystals are printed. Figure 6.8 shows 3D renderings of a line grating with lattice constant a and a woodpile photonic crystal. The latter is an established benchmark for the printing resolution in three dimensions. A face-centered cubic (fcc) woodpile photonic crystal consists of axially stacked layers with lateral lattice constant a and axial lattice constant $c = \sqrt{2}a$. Each layer is rotated by $90°$ with respect to the preceding layer and shifted by $a/2$ with respect to the previous layer of same grating orientation.

6.3.2.1 Line Gratings

Scanning electron micrographs of actual 3D nanoprinted line gratins are shown in Figure 6.9. The photoresin PR1 and a piezo-stage scan speed of $100\,\mu m\,s^{-1}$ is used. Well separated line gratings can be obtained down to a lattice constant of
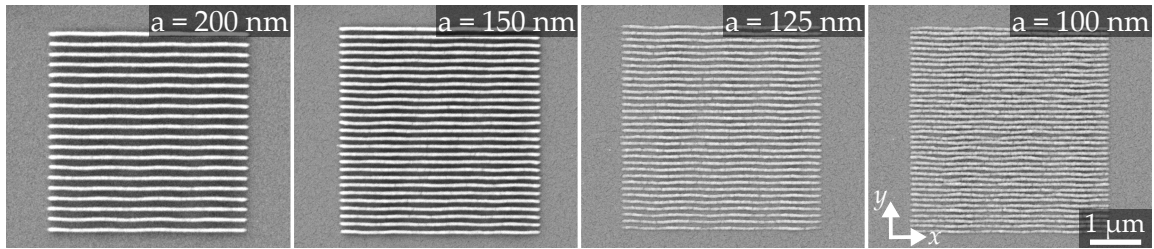
Figure 6.9: Electron micrographs of 2D line gratings. The $4 \times 4 \, \mu m^2$ large gratings are printed in photoresin PR1 at a scan speed of $100 \, \mu m \, s^{-1}$. Grating periods of below 150 nm are resolved. Adapted from Ref. [53] with permission from Springer Nature.

$a = 125$ nm. For even lower lattice constants, the lines appear separated. However, a clear assessment is difficult from the scanning electron micrograph.

Let us compare the two-step absorption printed line gratings with results obtained in two-photon absorption 3D printing. Systematic results are available for line gratings printed at twice the wavelength used herein, i.e., 810 nm [22]. In fact, these results published by Joachim Fischer et al. were obtained at the same printing setup. The minimal resolved lattice constant in his experiments was 200 nm [22]. However, when using STED as resolution-enhancement technique, line gratings down to 175 nm could be resolved [22]. Using a pulsed 405 nm wavelength diode laser, Patrick Müller et al. demonstrated line gratings with a lattice constant of $a = 110$ nm [164]. The minimal grating constant is governed by the laser wavelength, limiting the dimensions of the diffraction limited laser focus and hence also the resolution as determined by the two-photon (or two-step) absorption Sparrow's criterion (see section 2.5). For the nonlinearity of $N = 2$, the free-space wavelength $\lambda = 405$ nm, and NA = 1.4, the lateral resolution according to Sparrow's criterion is $\Delta y = 102$ nm. The well-resolved gratings and the good agreement of the expected minimal grating constant with the measured one further indicates a two-step absorption process.

6.3.2.2 *Woodpile Photonic Crystals*

Printing woodpile photonic crystals is more challenging than printing flat line gratings. For woodpiles, variations on the order of 1 % of the laser power can make the difference between a resolved and an overexposed structure [22]. As a result, all woodpile structures are printed using the piezo-stage rather than the galvanometer mirrors, resulting in longer printing times. Thus, power variations across the scan field are avoided. However, the piezo scan-mode limits the maximum scan velocity to $100 \, \mu m \, s^{-1}$.[1]

---

[1] In principle, faster scan speeds are possible. However, faster scanning requires a longer run-up distance to ensure a uniform scan speed across the entire area of the printed structure. Also, scan lag times increase and must be pre-compensated.

When printing a woodpile photonic crystal at a constant laser power value, the total dose accumulated at the edge of each woodpile is lower than in the center. In the worst case, the nonuniform dose distribution can lead to underexposed or collapsed edges of the 3D structure. Therefore, the laser power is intentionally increased in a linear ramp towards the edges of each structure. The length of the power ramp is set to $8 \cdot a$. The laser power is increased by 18 % at the edge for the woodpile with $a = 450$ nm and 13 % for the woodpile with $a = 200$ nm. Both values are found empirically. Intermediate power ramp values are found by interpolation. In contrast to previous published results on woodpile photonic crystals [22, 165], the laser power is kept constant in the z-direction and there is no need to pre-compensate the shrinkage to obtain the proper axial lattice constant.

Furthermore, the optimum laser power depends on the lattice constant a of the woodpile. By reducing the laser power, the rod heights can be decreased until the rods are too short to connect adjacent layers. When increasing the laser power on the other hand, neighboring rods eventually come in contact. To find the optimum parameters, an exposure-dose test is performed for an array of 24-layer tall woodpile photonic crystals with lattice constant a in the range of 225–450 nm. Figure 6.10a shows a true-color reflection-mode optical microscope image of such an array. The laser power is increased from left to right in 5 % steps and the lattice constant a is decreased from bottom to top. The observed color is due to Bragg reflections from the woodpile and serve as an indicator for a good sample quality [76]. The woodpiles on the left side of the image, i.e., for low laser powers, are underexposed. For increasing power, the woodpiles become colorful and their color gradually changes due to an increasing filling fraction [166]. The woodpile color also changes for lower lattice constants a [167]. For low lattice constants < 300 nm, the laser power range for which woodpiles of good structural quality are obtained becomes narrow. Still, it is possible to 3D print colorful woodpiles with a lattice constant of $a = 225$ nm.

Figure 6.10b shows a top-view scanning electron micrograph of the woodpile with $a = 300$ nm, which is encircled in Figure 6.10a. No signs of strong proximity effects can be observed and the magnified view shown in the inset reveals well-separated rods. However, proximity effects would be most prominent in the volume of a woodpile. Therefore, ultrathin cuts of woodpile samples are analyzed in the scanning electron microscope. Figure 6.10c shows a micrograph of a cut through a woodpile with $a = 300$ nm. The cutting plane is tilted at an angle of $1.7°$ with respect to the printing yz-plane. The cut reveals four aspects. First and foremost, no signs of proximity or overexposure can be observed in the volume. The rod dimensions do not differ at the surface of the woodpile from those measured in the volume. Second, the measured voxel diameter and height are $d_{\mathrm{voxel}} = 110$ nm and $h_{\mathrm{voxel}} = 302$ nm, respectively. Those values agree well with the FWHM voxel
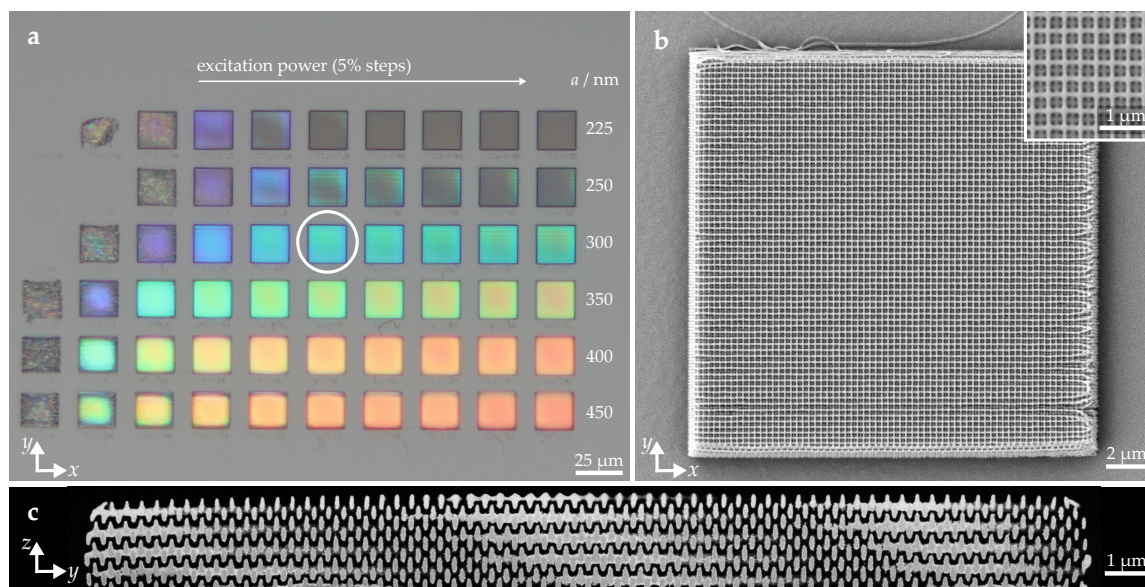
Figure 6.10: Microscope images of woodpile photonic crystals. **a**, True-color reflection-mode optical microscope image (observed with NA = 0.4) of an array of woodpile photonic crystals. The 3D nanoprinting laser power is increased in 5 % steps from left to right and the lattice constant decreases from bottom to top. **b**, Scanning electron micrograph of the woodpile photonic crystal highlighted in panel **a** with lattice constant $a = 300$ nm. The inset shows the same woodpile structure at a higher magnification level. **c**, Scanning electron micrograph of an ultrathin section of a woodpile with $a = 300$ nm along the axial direction. The cutting plane is rotated by 1.7° with respect to the yz-plane of the 3D printing coordinate system. Adapted from Ref. [53] with permission from Springer Nature.

dimensions obtained from the squared laser focus intensity measurements (see subsubsection 6.2.2.1). In fact, the aspect ratio of $h_{\text{voxel}}/d_{\text{voxel}} = 2.36$ inferred from the micrograph is even slightly lower than the aspect ratio obtained by the measurement of the gold-bead backscattered intensity signal. Third, a filling fraction of 55 % is obtained by digitizing the scanning electron micrograph with a threshold value obtained through Otsu's method [168]. Fourth, the measured axial lattice constant $c_{\text{measured}} = 428$ nm deviates only by 1 % from the target axial lattice constant $c = \sqrt{2}a = 424$ nm – without any applied shrinkage pre-compensation.

Finally, it is interesting to compare the results obtained for two-step-absorption 3D laser nanoprinting with literature results on two-photon absorption 3D laser nanoprinting. In general, woodpile photonic crystals are excellent benchmark structures since they were printed numerous times [22, 164, 167, 169–173]. Using a femtosecond laser at 810 nm wavelength, Joachim Fischer et al. [22] were able to print colorful woodpile photonic crystals down to lattice constants of 375 nm. Again, these results were achieved using the same objective lens as the

results presented herein. Using STED-inspired 3D laser nanoprinting, colorful woodpiles were printed at a yet smaller lattice constant of $a = 275\,\text{nm}$ [22]. Using a nanosecond-pulsed 405 nm diode laser, Patrick Müller et al. were able to print resolved woodpiles with a lattice constant of 250 nm in a photoinitiator-free photoresin. In a similar fashion, Andreas Wickberg et al. used a frequency-doubled femtosecond laser to print woodpiles 405 nm wavelength [127]. There, the smallest lateral rod distance printed is $a = 675\,\text{nm}$ and an axial rod distance of $c \approx 540\,\text{nm}$ [165]. However, that work did not target for the minimal achievable lattice constant. In comparison, the woodpile photonic crystals presented herein have smaller lattice constants than the woodpiles presented in the above listed literature. However, according to Sparrow's criterion (see section 2.5), the minimal resolvable axial lattice constant is $c_{\min} = \Delta z = 256\,\text{nm}$, corresponding to a minimal lateral lattice constant of $a_{\min} = 181\,\text{nm}$. Currently, it is unclear whether it is possible to resolve such high-resolution woodpile structures under the used focusing conditions and with photoresin PR1.

In conclusion, the successfully 3D printed woodpile structures further confirm the two-step absorption behavior of PR1. Furthermore, the achieved woodpile lattice constants are on the edge of the current state-of-the-art in photopolymerization 3D printing.

6.3.3 3D-Printed Microstructures

To showcase the versatility of two-step-absorption 3D laser nanoprinting, a set of 3D microstructures is printed. Scanning electron micrographs are shown in Figure 6.11, the used printing parameters, i.e., hatching, slicing, laser power, scan speed, photoresin, and used development procedure are listed in Table 6.1. Panel **a** shows four helices with an axial pitch of 800 nm and a radius of 800 nm. The three Buckyballs shown in panel **b** are 15 µm, 10 µm, and 5 µm in diameter. The printed structure is of high fidelity; on close inspection, even the discretization artifacts from the slicing and hatching procedure can be seen. This is also the case for the stack of dip-in printed five chiral metamaterial unit cells [120] shown in panel **c**. The 16 µm lattice constant is five times smaller than the lattice constant used in the multi-focus experiments presented in chapter 4, yet there are no signs of proximity effects. Even in two-photon absorption experiments it is challenging to ensure that the vertical rings within the side-walls and the horizontally lying rings at the unit cell bottom and top face remain separated. No such difficulties could be observed for two-step-absorption 3D laser nanoprinting. Panel **d** shows an upright-standing model of the KIT logo. Finally, panel **e** shows a $16 \times 12 \times 8\,\text{µm}^3$ large #3DBenchy[2] boat, which is more challenging to print. The large filling fraction of the boat's hull

---

[2] 3DBenchy.com
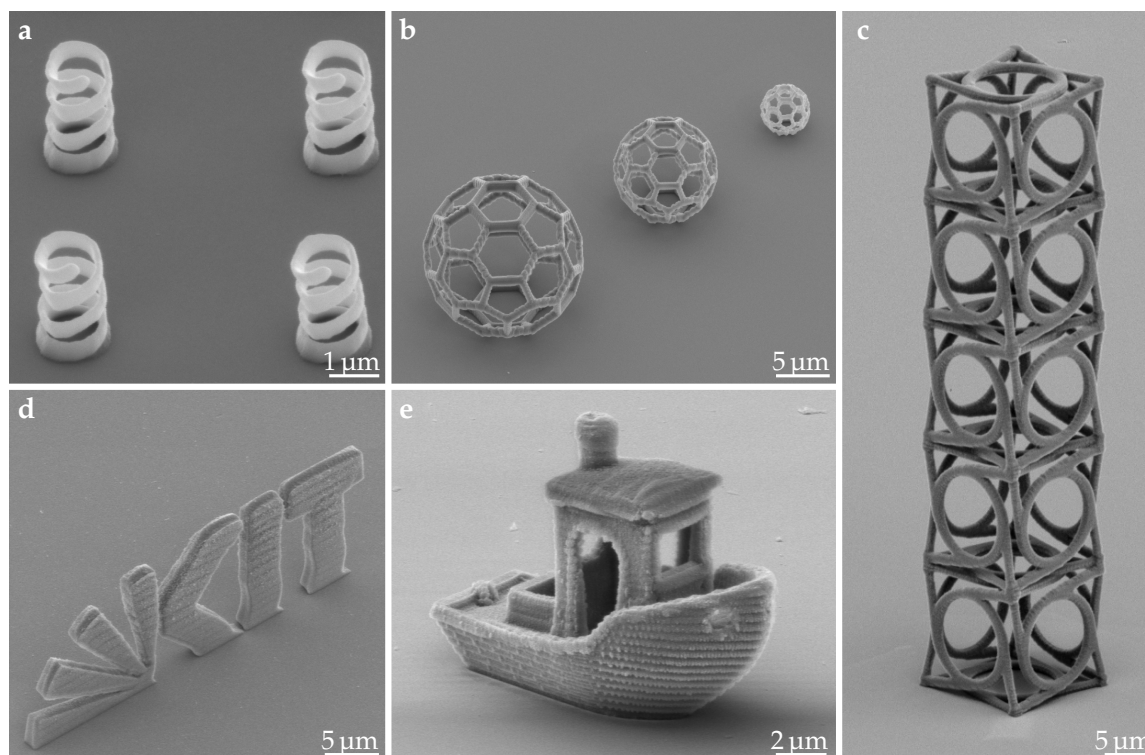
Figure 6.11: 3D nano- and microstructures printed by two-step-absorption 3D laser nanoprinting. a, Helices with an axial pitch of 800 nm and a radius of 800 nm. **b**, Buckyball models with diameters of 15 µm, 10 µm, and 5 µm. **c**, Five stacked unit cells of the chiral metamaterial proposed in Ref. [120]. The lattice constant is 16 µm. **d**, A 3D model of the KIT logo. **e**, Miniaturized #3DBenchy boat-structure. Adapted from Ref. [53] with permission from Springer Nature.

leads to noticeably dose accumulation in subsequent layers. Therefore, the boat is printed using the less viscous photoresin PR3 in which the quencher diffusion rate is increased. Again, slicing and hatching artifacts are well reproduced in the 3D nanoprinted structure. The 3D microstructures are printed with scan speeds of 0.5–4.0 mm s^{-1}, corresponding to a printing rate of 2400–19 400 voxels s^{-1}.

6.4 DISCUSSION AND CONCLUSION

The results obtained for two-step-absorption 3D laser nanoprinting are compared to published results of (quasi-)cw laser 3D laser nanoprinting in the double logarithmic diagram in Figure 6.12. On the horizontal axis, the maximum scan speed is plotted, the vertical axis shows the used laser power. A good 3D nanoprinting approach would be located at the bottom right, whereas slow and power-intensive methods are at the top left. The data points for two-step-absorption 3D laser

Table 6.1: Printing parameters used for the printing of the line gratings, woodpile photonic crystals, and 3D microstructures. The column "Power" denotes the used laser power, measured at the entrance pupil of the objective lens. SCD: supercritical drying.

Fig.	Hatching	Slicing	Power	Scan Speed	Resist	Dip-In	SCD
6.9	variable	-	66 µW	0.1 mm s^{-1}	PR1	no	no
6.10c	(300 nm)	(106 nm)	$\sim$ 45 µW	0.1 mm s^{-1}	PR1	no	yes
6.11a	-	-	500 µW	0.5 mm s^{-1}	PR1	no	no
6.11b	30 nm	100 nm	320 µW	1.0 mm s^{-1}	PR1	no	no
6.11c	50 nm	100 nm	270 µW	3.0 mm s^{-1}	PR2	yes	no
6.11d	30 nm	100 nm	320 µW	4.0 mm s^{-1}	PR1	no	no
6.11e	50 nm	100 nm	400 µW	1.0 mm s^{-1}	PR3	no	no

nanoprinting [53] are highlighted by an ellipse, showing that the achieved scan speeds are faster by up to three decades, but also lower peak laser powers by more than three decades, when compared to the other published results.

In summary, two-step-absorption 3D laser nanoprinting is an attractive alternative to multi-photon absorption 3D laser nanoprinting. Still, there are two restrictions for the general applicability of two-step-absorption 3D laser nanoprinting.
First, bulky structures with high-filling fraction are difficult to print, which is probably caused by the irreversible consumption of quencher molecules in the printing surrounding. Detailed analytical insights into the underlying photochemical processes can help in finding improved photoresin formulations.
Second, the maximum scan speed is limited by the photoinitiator's intermediate-state lifetime. At the expense of higher threshold laser powers, the benzil triplet-state lifetime can be decreased further. A shorter intermediate-state lifetime can be achieved by increasing the quencher concentration or employing smaller, faster diffusing quencher molecules like TEMPO. In addition, molecules that are not consumed in a radical scavenging process but act only as triplet quencher can be added to the photoresin mixtures. One candidate for such a triplet quencher is 1,4-diazabicyclo[2.2.2]octane (DABCO). Alternatively, photoinitiator molecules with intrinsically short intermediate-state lifetimes can be employed. As outlined in subsection 5.4.1, the singlet state of organic molecules typically decays within nanoseconds and hence qualifies as short-lived intermediate state.

Two-step absorption opens the gate for massive parallelization in 3D nanoprinting. The laser diode used for two-step-absorption 3D nanoprinting has a maximum optical output power of 150 mW. Neglecting transmission losses, this output power is in theory sufficient for more than 400 foci scanned at a speed of

Figure 6.12: Comparison of published results on cw laser 3D nanoprinting. The double logarithmic chart compares the used scan speeds (horizontal axis) and laser powers (vertical axis) of published results on (quasi-)cw laser 3D nanoprinting. The results obtained using two-step absorption [53] are highlighted by an ellipse. The numbers in brackets are literature references. Adapted from Ref. [53] with permission from Springer Nature.
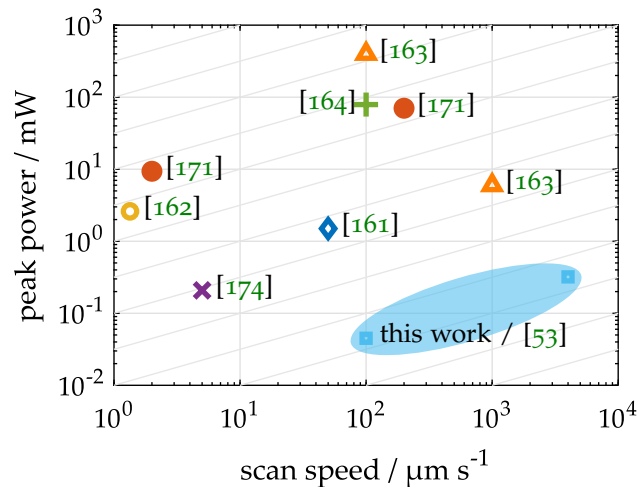
$4\,\mathrm{mm\,s^{-1}}$ (compare Table 6.1), resulting in a considerable total peak printing rate of $19\,400\,\mathrm{voxels\,s^{-1}} \cdot 400 = 7.8 \cdot 10^6\,\mathrm{voxels\,s^{-1}}$. Moreover, by employing powerful vertical-cavity surface-emitting laser (VCSEL) arrays [175] the number of laser foci can be increased yet further.

Furthermore, no micro-explosions are observed in the described experiments. When increasing the laser power, the size of the resulting voxel increases accordingly, offering a large dynamic range for 3D printing. Dynamically tuned voxel sizes have been recently employed in two-photon grayscale lithography to rapidly print microoptical elements with smooth surfaces and little staircasing artifacts [130]. There, the voxel size is increased in areas of high filling fraction, which can also be considered a form of parallelization. However, for two-photon absorption, the dynamic range of the voxel size is limited by the onset of micro-explosions.

The spatial resolution obtained by two-step-absorption 3D nanoprinting already surpasses the results obtained by conventional two-photon absorption 3D nanoprinting. Yet, there is room for conceptual improvement. The achieved resolution in two-photon absorption is enhanced by superimposing the 3D printing focus with a second, donut- or bottle-beam shaped laser focus, which depletes the pre-excited photoinitiator population tightly around the printing focus [22]. Such a STED-inspired 3D printing scheme is also conceivable for two-step-absorption 3D nanoprinting. Therefore, photoinitiator molecules need to be found for which an optically induced back-reaction to the ground state is possible. For example, an initiator that possesses a large fluorescence quantum yield could be depleted via STED [176]. Alternatively, a photoinitiator could be deactivated via an inert excited triplet-state by reverse-intersystem crossing and rapid relaxation to the ground state.
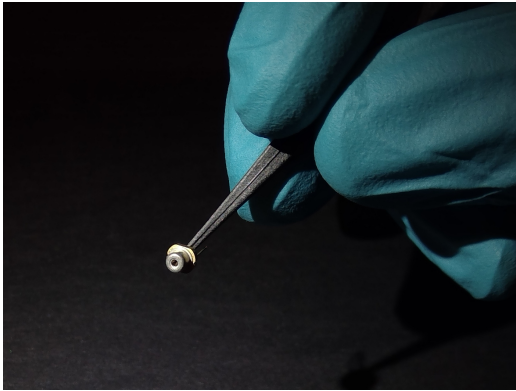
Figure 6.13: Photograph of the packaged laser diode used for two-step-absorption 3D nanoprinting. The yet smaller actual laser diode is mounted in the 3.8 mm diameter transistor outline (TO) housing. The compact form factor enables miniaturized 3D laser nano printers. Adapted from Ref. [53] with permission from Springer Nature.

One major advantage coming along with two-step-absorption 3D laser nanoprinting is the compact form factor of the employed laser diode, a photograph of which is shown in Figure 6.13. The housing of the actual diode has about the size of a needle pin and the diode consumes 500 mW of electrical power, which is a fraction of the power that a smartphone display consumes [177]. The compact size and the low driving power of laser diodes open the gate for drastic miniaturization in 3D nanoprinting. Replacing the suitcase-sized laser system in two-photon absorption nanoprinters by a compact laser diode allows for a portable 3D nanoprinting system which could be powered by a battery.

7

Two-Color Two-Step-Absorption Photoinitiation
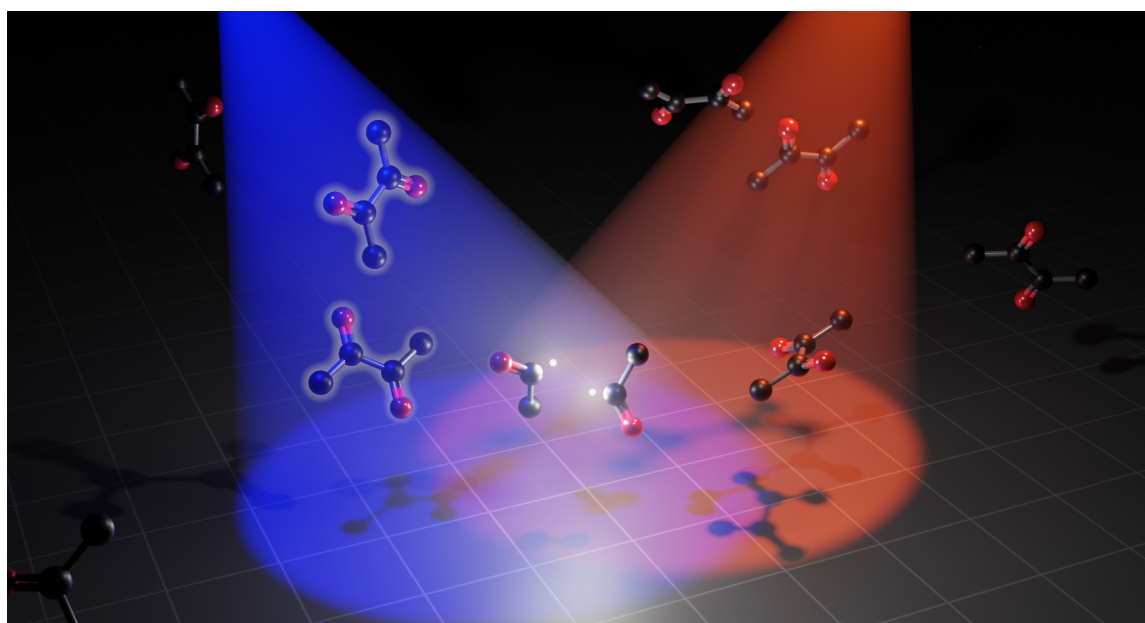
Excited biacetyl molecules.

In this chapter, the idea of light-sheet 3D printing is presented and suitable photoresins therefore are characterized.
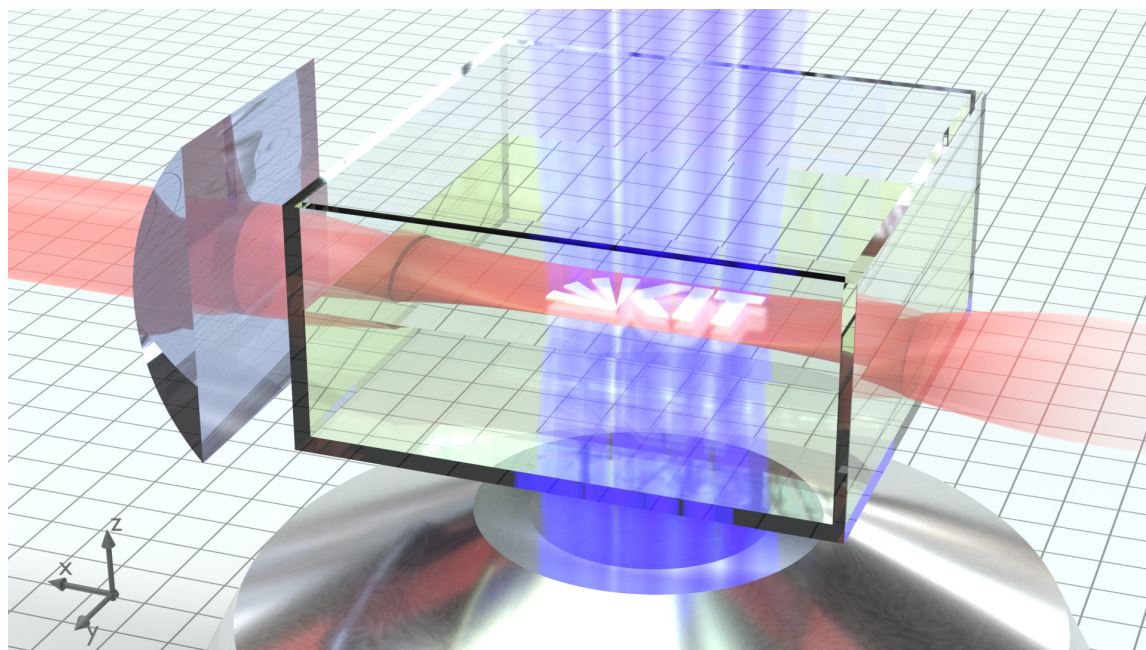
Figure 7.1: Rendering of light-sheet 3D printing. Adapted from Ref. [12] with permission from Springer Nature.

7.1 TWO-COLOR TWO-STEP ABSORPTION FOR LIGHT-SHEET 3D PRINTING

In the previous chapter 6, we have learned that the low polymerization threshold powers in one-color two-step-absorption 3D nanoprinting opens new avenues for parallelization in 3D printing. These low laser powers invite to the idea, that instead of scanning a single laser-focus, one could simply use a projector to project entire layers of a 3D object at once into the liquid photoresin. However, this approach has one issue. Consider the case of an extended plane that should be printed. When projecting the image of this plane into the photoresin, the laser intensity below and above the focal plane is effectively constant over a large distance. However, with slightly modified conditions on the two-step-absorption photoinitiator, one can instead use *two-color* two-step absorption photoresins and print 3D objects in a layer-by-layer fashion by light-sheet 3D printing.

An artistic illustration of light-sheet 3D printing is shown in Figure 7.1. In light-sheet 3D printing, a 3D object is sliced into layers, which are then projected with light of a first wavelength λ_1 (here blue) and focused into a photoresin vat. In the rendering, the sliced layer is exemplified by the KIT logo. A second laser beam of another wavelength λ_2 (here red) propagates orthogonally to the blue laser beam. The red laser beam is focused along only one axis by a cylindrical

Figure 7.2: Schematic of two-color two-step absorption. By sequential absorption of two photons a photoinitiator molecule is stepwise excited to an upper electronic state, from where the molecule decays into free radicals R•. Importantly, the two photons must be of different wavelengths.

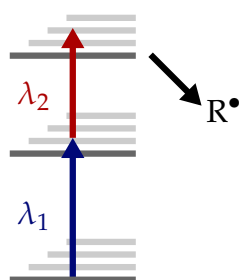lens into the shape of a light-sheet, which intersects the focal plane of the blue laser beam. Importantly, the liquid photoresin is a two-color two-step-absorption photoresin, which polymerizes only in those areas which are exposed to light of both wavelengths, λ_1 and λ_2, simultaneously. In regions below and above the focal plane, no polymerization occurs, i.e., only negligible optical dose is accumulated.

The idea of the two-color two-step-absorption process is illustrated in Figure 7.2. A photoinitiator molecule in its ground state absorbs light of wavelength λ_1 to get excited to an idle, intermediate state. From the intermediate state, the pre-excited initiator can decay back to the ground state. In contrast to one-color two-step absorption however, the pre-excited photoinitiator does not absorb photons of wavelength λ_1. However, it readily absorbs light at a second wavelength λ_2 to get excited to a state of sufficient energy to trigger a polymerization reaction.

In chapter 5, several conditions for a "good" (one-color) two-step-absorption photoinitiator were proposed. While most of the proposed conditions apply also to the case of a good two-color two-step-absorption photoinitiator, the first two conditions need to be adjusted.

The first condition for a good two-step-absorption photoinitiator says that from the pre-excited state, the photoinitiator must decay back to the ground state in due time. This condition also holds for two-color two-step absorption. Again, "due time" can be specified more precisely for the target application. For one-color two-step absorption, the intermediate-state lifetime sets a lower bound on the voxel exposure time, for which the accumulated dose scales nonlinearly with the photoinitiator concentration. Similarly, for two-color two-step absorption, the intermediate-state lifetime limits the minimal layer exposure time. To illustrate this limit, consider the exposure of an extended plane. The blue-laser beam of wavelength λ_1 promotes photoinitiator molecules along the entire optical track into the intermediate state. For the case of an infinitely long intermediate-state lifetime, all molecules remain in the intermediate state, even after progressing with the exposure to the next layer. Now, the light-sheet beam alone suffices to polymerize the liquid photoresin by an effective one-photon absorption. Hence, the intermediate-state lifetime ultimately limits the achievable printing rate or the

Figure 7.3: Molecular structure of biacetyl. **a**, Skeletal structure of biacetyl. **b**, Ball-and-stick (H-atoms omitted) model of biacetyl in its ground state, according to Ref. [179]. The cis-planar geometry is outlined by a plane.
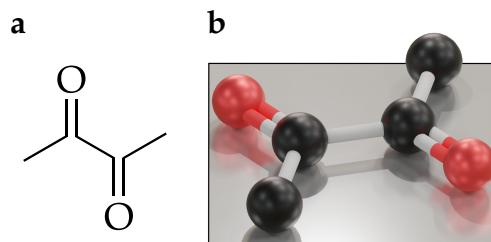
printing resolution.

Technically, the exposure rate is also limited by maximum frame rate of projector systems, which are on the order of $1\,\mathrm{kHz}$ for modern liquid crystal on silicone (LCOS) displays [178]. Therefore, from a practical viewpoint, the intermediate-state lifetime should also be on the order of $1\,\mathrm{kHz}^{-1} = 1\,\mathrm{ms}$. As before in the case of one-color two-step absorption, this lifetime falls into the regime of triplet-state lifetimes of organic molecules [136].

The second condition states that a two-step-absorption photoinitiator must absorb, ideally visible, light in its ground state, but also in the intermediate state. For one-color two-step absorption, the absorption spectra of both states must overlap. Conversely, in the special case of two-color two-step absorption, the spectra must not overlap. Photoinitiators obeying the former condition of overlapping spectra are useful in one-color two-step-absorption 3D printing. Photoinitiators which obey the latter condition of nonoverlapping spectra can be employed in light-sheet 3D printing.

7.2 BIACETYL AS TWO-COLOR TWO-STEP-ABSORPTION INITIATOR

One photoinitiator candidate that fulfills the modified set of conditions for a good two-color two-step-absorption photoinitiator is biacetyl, which was already singled-out in section 5.5 for its low triplet-state energy.

7.2.1 Molecular Structure and Electronic States

Figure 7.3a shows the chemical structure of biacetyl, also known as diacetyl or butane-2,3-dione, which is the simplest diketone molecule. At room temperature, biacetyl is a pale-yellow colored liquid [180]. The molecule is not a common photoinitiator but is a well-known flavoring agent, due to its buttery odor [180]. In it's ground-state, biacetyl takes a cis-planar conformation (Figure 7.3b), which sets it apart from the skewed ground-state conformation of benzil.

Starting in the 1940s, research interest in biacetyl emerged due to biacetyl's room-
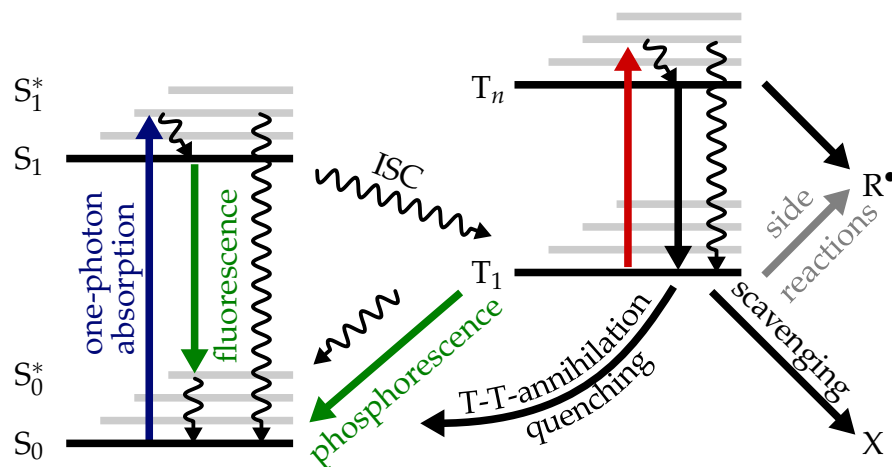
Figure 7.4: Jablonski-diagram of biacetyl. Molecules are optically excited by blue or ultraviolet light from the singlet ground-state S_0 to the upper singlet manifold, where they rapidly relax to the lowest excited singlet-state S_1. From S_1, molecules undergo intersystem crossing to the triplet manifold with nearly unity quantum yield. From the lowest triplet-state T_1, molecules can either decay to singlet ground-state S_0 by triplet-triplet annihilation, reverse intersystem-crossing, quenching, or by emitting phosphorescence. Alternatively, molecules in the T_1-state can be further optically excited by red or ultraviolet light to a higher triplet-state T_n [190], providing sufficient energy for bond-dissociation $R^\bullet$. Depending on the solvent, a bimolecular hydrogen-abstraction reaction is possible from the lowest triplet-state [155]. Adapted from Ref. [12] with permission from Springer Nature.

temperature observable phosphoresence [181]. Since then, the photochemistry of biacetyl has been reviewed several times [182–184]. Figure 7.4 shows a Jablonski diagram for biacetyl. From its ground-state, biacetyl is excited optically to the excited singlet-manifold by absorption of a blue- or ultraviolet photon. From there, biacetyl undergoes intersystem crossing to the triplet-manifold with nearly unity quantum yield [185]. The lowest triplet-state has an energy of 2.4 eV [185–187] and in solution, the triplet-state lifetime is 200 µs [188]. The latter can be measured conveniently via the emitted phosphorescence, which is spectrally located around 550 nm wavelength and has a phosphorescence quantum yield of approximately 15 % in the vapor and a few percent in the liquid phase [188, 189].

Biacetyl's triplet-state energy is well below it's lowest bond cleavage energy of 3.2 eV [191, 192]. Hence, a Norrish type I reaction does not occur from the energetically lowest triplet state. However, similar to benzil and other diketones, biacetyl in its triplet state is able to abstract hydrogen atoms from nearby susceptible groups [155]. This hydrogen-abstraction reaction can lead to radicals being generated from the lowest triplet-state. The hydrogen-abstraction reaction is not

Figure 7.5: Extinction spectra of bi-acetyl. Ground-state (blue) and excited-state (red) molar decadic extinction coefficient of biacetyl in acetonitrile and benzene, respectively. The absolute value of the triplet-state molar decadic extinction coefficient ϵ_2 is estimated from Refs. [190, 193]. The red arrows indicate the wavelengths $\lambda_1 = 440\,$nm and $\lambda_2 = 660\,$nm used in the light-sheet 3D printing experiments. Adapted from Ref. [12] with permission from Springer Nature.
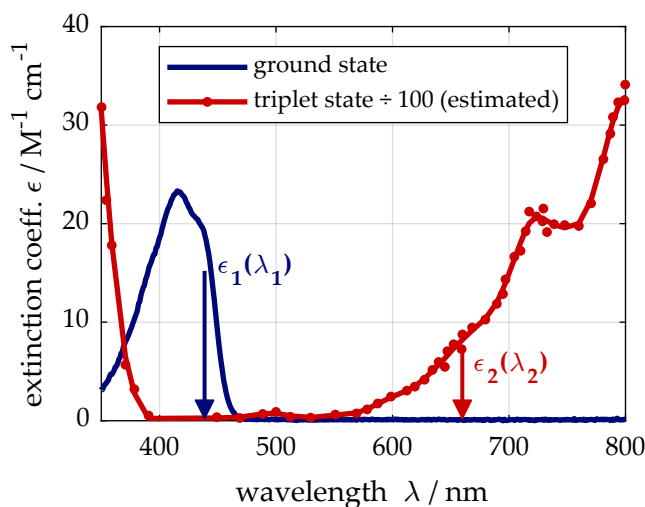
desired since it follows an ordinary one-photon absorption process and adds to the accumulated dose also in locations exposed to the light of only one wavelength. Hence, to suppress these side-reactions, the quencher and radical-scavenging molecule TEMPO is employed (see subsection 6.1.4).

7.2.2 *Ground-State and Transient Absorption-Spectra*

To overcome the bond-cleavage activation-energy barrier in the triplet manifold, biacetyl can be optically excited from the lowest triplet-state to an excited triplet-state. Figure 7.5 shows the ground-state and triplet-state molar decadic extinction spectra of biacetyl in acetonitrile and benzene, respectively. The absorbance data for the triplet-state spectrum is taken from Ref. [190], which is scaled to yield an absolute extinction coefficient by the data provided in Ref. [193]. In the ground state, biacetyl absorbs light in the visible region at a wavelength of 415 nm with a peak extinction coefficient of $\epsilon_1\,(415\,\mathrm{nm}) = 23\,\mathrm{M}^{-1}\,\mathrm{cm}^{-1}$, which is characteristic for an n-π^*-transition [136]. At wavelengths longer than 460 nm, biacetyl is transparent. In the triplet-state, on the other hand, biacetyl does not show a strong absorbance in the wavelength interval from 400–550 nm. For longer wavelengths however, a series of strong absorption peaks with estimated peak extinction coefficients of $\epsilon_2 > 1000\,\mathrm{M}^{-1}\,\mathrm{cm}^{-1}$ are observed.

7.3 METHODS

The substrate preparation and sample development procedure described for one-color two-step-absorption 3D nanoprinting in section 6.2 are the same as for the biacetyl characterization experiments.

7.3.1 Focus-Scanning 3D Printing Setup

The focus-scanning 3D nanoprinting setup used to characterize biacetyl photoresins is depicted in Figure 6.5 and described in detail in subsection 6.2.2. For the experiments in which the red laser beam wavelength is varied (see subsection 7.4.4), the 640 nm laser wavelength beam is replaced by laser diodes of different wavelengths (Thorlabs HL6545MG, Thorlabs HL6750MG).

7.3.2 Photoresin Compositions

In the following, photoresin composition used for the two-color two-step absorption 3D printing experiments are listed. For simplicity, the photoresins are labeled as "PRA"–"PRC". Biacetyl, TEMPO, PETA, and pentaerythritol tetraacrylate (PETTA) are purchased from Sigma-Aldrich (now Merck KGaA). TMPTA is purchased from Alfa-Aesar (now Thermo Fisher (Kandel) GmbH). Dipentaerythritol hexaacrylate (DPEHA) is purchased from abcr GmbH. All photoresins are mixed and used in yellow-light conditions. For each of the below listed photoresins, several variants will be discussed in the experiments further below.

PRA 1.8 mg TEMPO are dissolved in 1 mL of TMPTA. To dissolve TEMPO in the monomer, the mixture is stirred on a hot plate at 45 °C for 4 h. Then, 10 μL biacetyl is added to the mixture, which is stirred for another hour at room temperature. This photoresin composition corresponds to a final concentration of 1.1 wt% (110 mM) biacetyl and 0.2 wt% (11 mM) TEMPO.

PRB Same as PRA, but using PETA as monomer instead of TMPTA.

PRC DPEHA is heated to 50 °C until completely molten and all crystallites are dissolved. Then, 1.8 mg TEMPO are dissolved in 1 mL of DPEHA. To dissolve TEMPO in the monomer, the mixture is stirred on a hot plate at 45 °C for 4 h. Then, 10 μL biacetyl is added to the mixture, which is stirred for another hour at 45 ° °C. This photoresin composition corresponds to a final concentration of 1.1 wt% (110 mM) biacetyl and 0.2 wt% (11 mM) TEMPO.

7.4 Point-Scanning Experiments on Biacetyl as Photoinitiator

To characterize the photoresin threshold behavior, the two-color point-scanning polymerization-threshold is measured for the photoresins PRA-PRC and further variants thereof. In these measurements, two laser beams are co-focused by a NA = 1.4 objective lens into the liquid photoresin. While printing dashed line patterns, the laser powers of the two superposed foci are independently varied.

After developing the sample, for each red laser-focus intensity I_2 the minimal blue laser-focus intensity I_1, for which a polymerized dash in the darkfield microscope image is visible, is recorded. By default, a scan speed of $v_{\text{scan}} = 100\,\mu\text{m s}^{-1}$, a blue laser-wavelength $\lambda_1 = 440\,\text{nm}$, and a red laser-wavelength $\lambda_2 = 640\,\text{nm}$ are used.

7.4.1 *Exposure Time*

In order to see if PRA shows the expected two-color two-step-absorption behavior, the two-color polymerization threshold intensity is measured for the reference scan speed $v_{\text{scan}} = 100\,\mu\text{m s}^{-1}$. Using the measured (blue) laser focus diameter of $d_{\text{FWHM},1} = 187\,\text{nm}$ (not shown), this scan speed corresponds to an effective exposure time of $t_{\text{exp}} = d_{\text{FWHM},1} \cdot v_{\text{scan}}^{-1} \approx 2\,\text{ms}$.

The thick line in Figure 7.6 shows the two-color polymerization-threshold diagram for the reference scan speed $v_{\text{scan}} = 100\,\mu\text{m s}^{-1}$. In the double-logarithmic diagram, the blue laser-intensity I_1 is plotted on the vertical logarithmic axis versus the red laser-intensity on the horizontal axis. The intensities I_1 and I_2 are derived from the measured laser powers P_1 and P_2, which are plotted on the right and top axis, and the measured focus FWHM-diameters ($d_{\text{FWHM},1} = 187.5\,\text{nm}$ and $d_{\text{FWHM},2} = 282.5\,\text{nm}$ for the blue and red beam, respectively). The individual data points are connected by lines.

At a reference scan speed of $v_{\text{scan}} = 100\,\mu\text{m s}^{-1}$ and low red laser-intensities I_2, the curve starts at $I_1(I_2 = 0\,\text{mW}\,\mu\text{m}^{-2}) = 31\,\text{mW}\,\mu\text{m}^{-2}$ (or, equivalently, a blue laser power $P_1 = 1\,\text{mW}$). For increasing red laser-intensities I_2, the blue threshold power I_2 decreases in a sigmoid fashion and starts to plateau at an intensity $I_1(I_2 = 30\,\text{mW}\,\mu\text{m}^{-2}) = 0.16\,\text{mW}\,\mu\text{m}^{-2}$ ($P_2 = 4.6\,\mu\text{W}$). The ratio of the two extremal blue laser-intensities defines the threshold contrast

$$\gamma = \frac{31\,\text{mW}\,\mu\text{m}^{-2}}{0.16\,\text{mW}\,\mu\text{m}^{-2}} \approx 200. \tag{7.1}$$

For an ideal two-color two-step-absorption photoresin, γ approaches infinity.

The sigmoid curve shape and the large threshold contrast γ confirm the synergistic effect of the two laser beams and thereby the two-color two-step-absorption polymerization behavior for the photoinitiator biacetyl. Notably, when exposing the photoresin only with red light, no polymerization is observed within the probed range, even for long voxel exposure times, as expected for an ideal two-color two-step-absorption photoinitiator. There is, however, a polymerization reaction also triggered when the photoresin is irradiated only with blue light. To better understand the dynamics of the single-color triggered polymerization, the two-color polymerization-threshold experiment is repeated for scan speeds
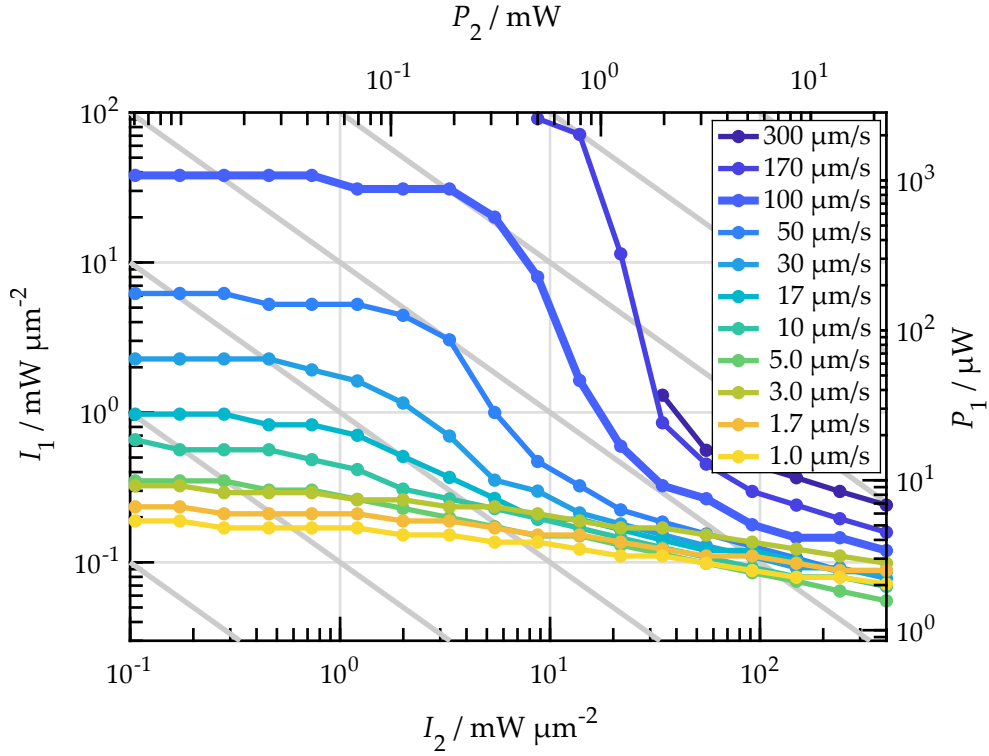
Figure 7.6: Two-color polymerization threshold of photoresin PRA at different scan speeds v_{scan} and hence different voxel exposure times. The curve for $v_{\text{scan}} = 100\,\mu\text{m s}^{-1}$ is highlighted by a thicker line. The blue laser threshold-intensity I_1 decreases in a sigmoid fashion with increasing red laser-intensity I_2. The diagonal lines have a slope of -1 and are a guide for the eye.

in the range of 1–$300\,\mu\text{m s}^{-1}$, which are plotted in Figure 7.6 using thin lines. The sigmoid curve shape can also be observed for these scan speeds. However, with decreasing scan speed, the curves shift downwards, i.e., to lower I_1, and leftwards, i.e., to lower I_2. Thereby, the sigmoid curve-shape becomes flatter and the threshold contrast decreases to $\gamma_{\text{threshold}} \approx 6$ for $v_{\text{scan}} = 1\,\mu\text{m s}^{-1}$. For yet faster scanning than $v_{\text{scan}} = 100\,\mu\text{m s}^{-1}$, the blue threshold-intensity (and hence the blue threshold power) at low red laser-intensities is above the experimentally maximum accessible laser power of $P_{1,\text{max}} = 1.6\,\text{mW}$.

7.4.2 Acrylic Monomer

Aiming for a deeper understanding of the photoresin behavior, the two-color polymerization-threshold experiments are performed for a fixed scan speed of $v_{\text{scan}} = 100\,\mu\text{m s}^{-1}$ and for photoresins with different monomers, namely TMPTA (PRA), PETA (PRB), PETTA, and DPEHA (PRC). These monomers differ in their viscosity, which is $\eta_{\text{tmpta}} \approx 0.1\,\text{Pa s}$ at $T = 20\,^\circ\text{C}$ [194], $\eta_{\text{peta}} \approx 1.1\,\text{Pa s}$ at $T = 20\,^\circ\text{C}$ [194],
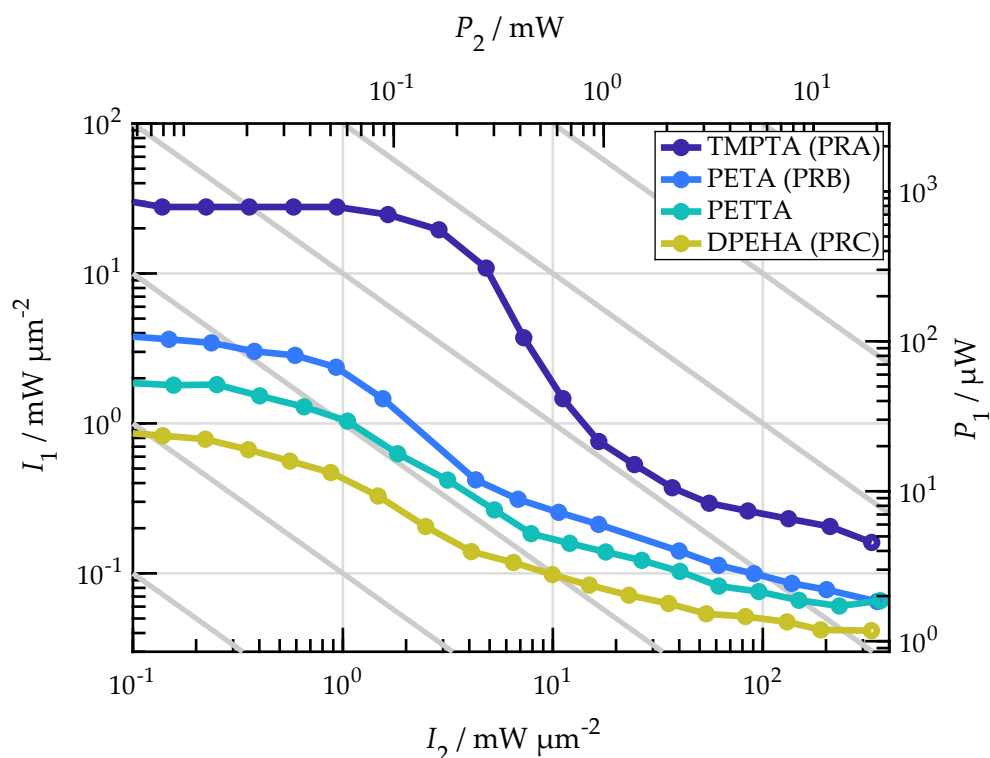
Figure 7.7: Two-color polymerization threshold of photoresins containing different acrylic monomers. All experiments are performed using a scan speed $v_{\text{scan}} = 100\,\mu\text{m}\,\text{s}^{-1}$. The blue threshold-intensity I_1 decreases with increasing monomer viscosity. Note that the monomers have different degrees of functionality. TMPTA and PETA have three, PETTA has four, and DPEHA has six acrylate groups per monomer molecule. Adapted from Ref. [12] with permission from Springer Nature.

and $\eta_{\text{dpeha}} \approx 6.2\,\text{Pa}\,\text{s}$ at $T = 25\,°\text{C}$ (vendor specification). No room-temperature viscosity data was found for PETTA [1]. Additionally, the monomers differ in the number of acrylate-groups per monomer. TMPTA and PETA are triacrylates, PETTA is a tetraacrylate, and DPEHA is a hexaacrylate.

Figure 7.7 shows the two-color polymerization-threshold diagram for the four photoresin formulations. Generally, the blue polymerization threshold-intensity I_1 decreases for the more viscous photoresins PRB and PRC, and, similar to the case for low scan speeds, also shifts towards lower red laser intensities I_2. Furthermore, the polymerization threshold-contrast $\gamma_{\text{threshold}}$ also decreases. For PRC with the monomer DPEHA, the contrast is $\gamma_{\text{threshold}} \approx 20$.

The observed effect of a decreasing polymerization threshold in more viscous

---

[1] At $T = 38\,°\text{C}$, the viscosity is specified to be $\eta_{\text{petta}} = 0.34\,\text{Pa}\,\text{s}$. At room temperature, the viscosity of PETTA is expected to lie between the viscosity of PETA and DPEHA.
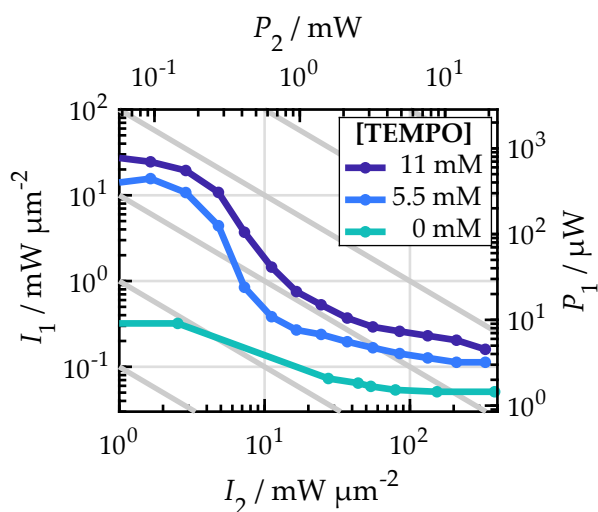
Figure 7.8: Two-color polymerization-threshold experiments for different TEMPO concentrations. All measurements are performed at a scan speed $v_{\text{scan}} = 100\,\mu\text{m}\,\text{s}^{-1}$. Due to strong proximity effects in the point-exposure experiments for the TEMPO-free photoresin, some data points could not be measured accurately and are hence excluded from the plot. The threshold contrast increases with increased TEMPO concentration. Likewise, the blue threshold-intensity increases.

photoresins was already observed in multi-photon-absorption photoresins, where it was attributed to the decreased diffusion rate of quencher and scavenger molecules [61]. In the experiments on two-photon-absorption photoresins, the main quencher and radical scavenger present was molecular oxygen. Here, the photoresins PRA, PRB, and PRC contain TEMPO as additional quencher and radical scavenger molecule.

7.4.3 Quencher Concentration

So far, the role of the quencher and radical scavenger molecule TEMPO in the photoresin is not clear. Therefore, two variations of photoresin PRA which contain either no TEMPO, or half the TEMPO-concentration of PRA are prepared. These photoresins are then characterized in two-color polymerization-threshold experiments, the results of which are shown in Figure 7.8. As a reference, the results for the pristine photoresin PRA are also plotted.

As expected, the polymerization threshold decreases for lower TEMPO concentrations. Interestingly, however, the threshold contrast also decreases. When printing without any quencher at all, the threshold contrast is $\gamma_{\text{threshold}} \approx 6$. However, the measurements on the TEMPO-free photoresin at low red laser-intensities are subject to considerable proximity effect and hence it is difficult to accurately measure the threshold laser power. For the photoresin with the intermediate quencher concentration (5.5 mм), a threshold contrast of $\gamma_{\text{threshold}} \approx 166$ is found in the two-color polymerization-threshold experiment.

This measurement shows that TEMPO is an essential ingredient in the two-color two-step-absorption photoresins, increasing the threshold contrast by more than 30-fold. Or, in other words, with increasing quencher concentration, the blue-

Figure 7.9: The two-color polymerization threshold of photoresin PRA and for a variable red laser-beam wavelength λ_2. Left panel: Stacked chart of two-color polymerization-threshold diagrams. To each set of data points, a logistic function is fitted and the midpoint is highlighted by a large dot. The curves are vertically stacked with their midpoints spaced according to the wavelength λ_2. The black curve connecting the midpoints shows the same characteristic spectral features as the triplet-triplet absorption spectrum (right panel) [190, 193]. Adapted from Ref. [12] with permission from Springer Nature.
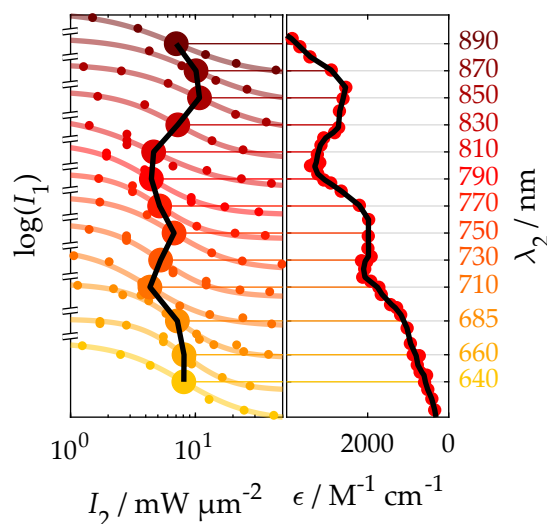
color threshold $I_1(I_2 = 0\,\mathrm{mW\,\mu m^{-2}})$ increases more rapidly than the two-color threshold $I_1(I_2 = 30\,\mathrm{mW\,\mu m^{-2}})$.

Naively, one might be tempted to increase the threshold contrast even further by increasing the TEMPO-concentration. Unfortunately, the available laser power at 440 nm is limited and does not allow the measurement of the blue-light only exposure threshold. In similar experiments using a more powerful 405 nm laser (not shown), the threshold contrast does not increase further in the probed range, but rather decreases slightly. Whereas the blue-only threshold changed only little with an increased quencher concentration, the threshold for high red-laser powers increased. At the moment, the reason for this optimal quencher concentration are unclear.

7.4.4 Wavelength

The synergistic behavior of simultaneous red- and blue-light exposure of the photoresin suggests a two-step absorption mechanism. To further prove the two-step character, the red laser beam wavelength λ_2 is tuned within the absorption band of biacetyl's triplet state (Figure 7.5). A stacked plot of the two-color polymerization-threshold curves is shown in the left panel of Figure 7.9. A logistic function is fitted to each curve, and the midpoint red laser beam intensities are highlighted by large dots. The midpoints are used to space the measurements according to the secondary wavelength λ_2. The black line connecting the midpoints is a polymerization action spectrum [195].

For comparison, the triplet-triplet absorption spectrum of biacetyl [190, 193] is plotted next to the spectral polymerization-threshold curve in the right panel of
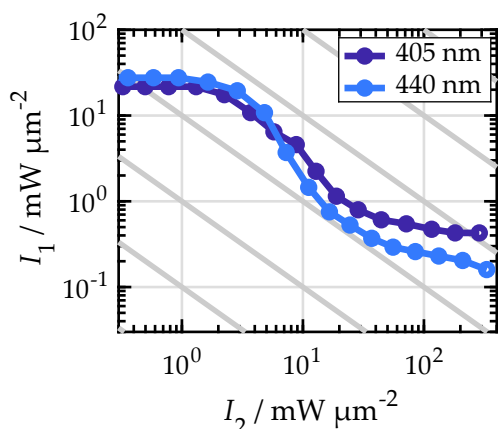
Figure 7.10: The two-color polymerization threshold of photoresin PRA for different primary wavelengths λ_1. For low red laser beam intensities I_1, the threshold intensity is lower for the beam with wavelength 405 nm. For high red laser beam intensities, the situation is reversed, and the threshold intensity is lower for the beam with wavelength 440 nm. Adapted from Ref. [12] with permission from Springer Nature.

Figure 7.9. The local maxima and local minima observed in the triplet-triplet absorption spectrum are well reproduced in the action spectrum, further confirming the two-step absorption character. Interestingly, the relative heights of the extinction maxima do not agree with the relative heights of the peaks in the action spectrum, which has been observed also for other photoinitiators [195]. In the action spectrum, peaks at smaller secondary wavelengths λ_2 are larger than expected. This trend towards lower polymerization threshold intensities can be attributed to the decreased overlap of the red and blue laser foci towards longer red laser-laser beam wavelengths, which cause a larger diffraction-limited focus FWHM-diameter.

Furthermore, the two-color polymerization-threshold experiment in photoresin PRA are repeated with an alternative blue laser beam wavelength of $\lambda_1 = 405$ nm. The threshold diagram is shown in Figure 7.10. As reference, the experiment at the wavelength $\lambda_1 = 440$ nm is also depicted. Both experiments were done with a red laser beam wavelength of 640 nm and at a scan speed $v_{\text{scan}} = 100\,\mu\text{m}\,\text{s}^{-1}$. The intensities plotted in the diagram are calculated from the respective laser-focus FWHM-diameter measurements. The double-logarithmic diagram shows also for $\lambda_1 = 405$ nm a sigmoid polymerization-threshold curve. Towards low red laser beam intensities I_2, the threshold intensity I_1 is slightly below the threshold intensity measured for the wavelength $\lambda_2 = 440$ nm. For increased red laser beam intensities I_2, the blue laser beam threshold-intensity I_1 for the wavelength $\lambda_1 = 405$ nm is larger than the threshold-intensity at $\lambda_1 = 440$ nm. The two-color threshold-contrast is $\gamma_{405} = 41$ (which compares to $\gamma_{440} \approx 200$ at $\lambda_1 = 440$ nm wavelength).

From the linear absorption spectrum of biacetyl in acetonitrile (see Figure 7.5), a lower polymerization threshold is expected since the extinction coefficient at the wavelength $\lambda_1 = 405$ nm is larger than at $\lambda_2 = 440$ nm. This is in accordance with the observation at low red laser powers I_2. This interpretation does not

hold for large I_2, where the threshold intensity for 405 nm wavelength is higher than for 440 nm. Since the triplet-triplet-spectrum is low at both wavelengths, excited-state absorption is not probable for light of either wavelength. However, owed to the smaller wavelength, the diffraction-limited FWHM focus diameter for the 405 nm wavelength laser beam is smaller than for the 440 nm wavelength laser beam. Thereby, the photoresin volume in which photoinitiator molecules are excited and hence quencher molecules become depleted, decreases. Furthermore, also the spatial overlap of the red laser beam and the blue laser beam decreases for a smaller focus diameter, or in other words, a larger fraction of the red laser beam is "unused".

7.4.5 Pulse-Train

As discussed in section 7.1, in 3D light-sheet printing, the photoinitiator intermediate-state lifetime limits the maximum printing rate and the resolution. While lifetime data in organic solvents are available [155, 188], the lifetime in the final photoresin mixture may well be different from that. Quencher molecules like oxygen and TEMPO affect the triplet-state lifetime and the bimolecular quenching rate constant depends on the monomer viscosity. Therefore, it is interesting to measure biacetyl's triplet lifetime.

Pump-probe phosphorescence-lifetime experiments in which biacetyl is excited by a short, intense laser pulse are not suitable to obtain a realistic estimate for the triplet-state lifetime in the photoresin. In such experiments, a large fraction of photoinitiator molecules is excited, leading locally to a high concentration of triplet-state biacetyl molecules. Thereby, the probability for a triplet-triplet annihilation reaction (see subsection 7.5.2) increases, which in turn reduces the intermediate-state lifetime. Therefore, to measure the triplet-state lifetime under more realistic conditions, pulsed-excitation two-color point-scanning experiments are performed. Again, dashed-line patterns are printed by the two co-focused laser beams of wavelengths $\lambda_1 = 440$ nm and $\lambda_2 = 640$ nm. However, the power of both lasers is modulated by a square-wave modulation with a duty cycle D and a frequency f. The phase-delay $\Delta\varphi$ of the two power-modulated laser beams is swept in the range $\Delta\varphi = 0$–2π, which is equivalent to a time delay between the square-wave pulse-burst

$$\Delta t = \frac{\Delta\varphi}{2\pi f}. \tag{7.2}$$

Figure 7.11 shows the measured polymerization threshold-intensity I_1 plotted versus the phase-delay $\Delta\varphi$. On the lower horizontal axis, $\Delta\varphi$ is converted to the time-delay Δt and on the right vertical axis, the intensity I_1 is converted to the corresponding laser power P_1. Panel a shows results for the experiment
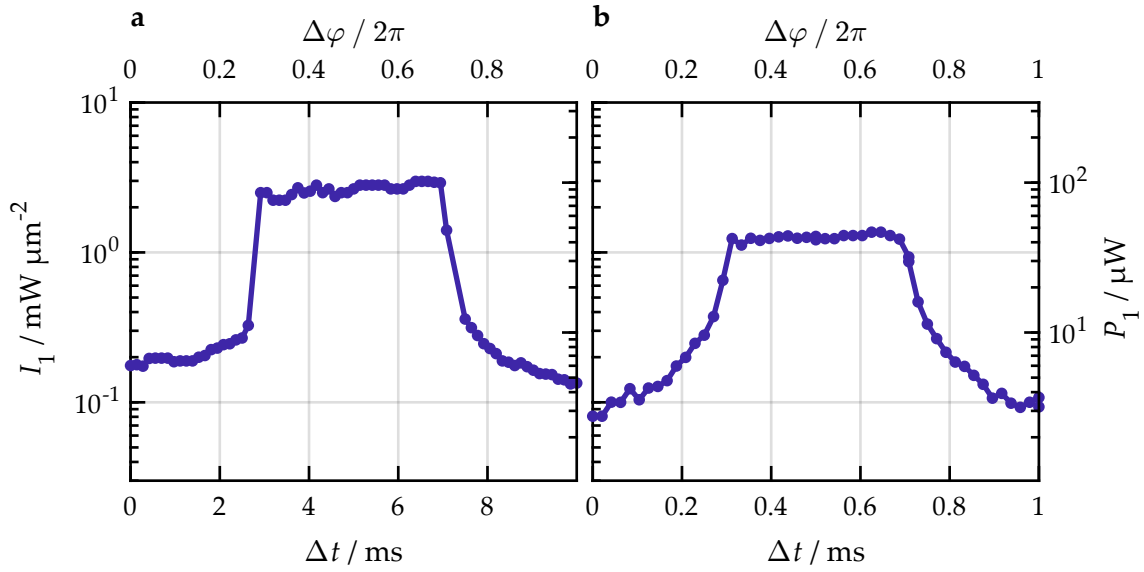
Figure 7.11: Intermediate-state lifetime measurements using a phase-shifted pulsed excitation. Two-color point polymerization intensity I_1 (left vertical axis) plotted versus the time delay Δt (lower horizontal axis) and phase delay (upper horizontal axis). On the right vertical axis, the polymerization laser power P_1 is calculated using the averaged FWHM beam-diameter of 209 nm. **a**, Results for photoresin PRA, a scan speed $v_{scan} = 10\,\mu m\,s^{-1}$, a frequency $f_A = 100\,Hz$, and a duty cycle of $D = 30\,\%$. **b**, Same plot as in a, however with $v_{scan} = 50\,\mu m\,s^{-1}$ and a frequency $f_C = 1\,kHz$. Note the different lower horizontal axis scaling. Adapted from Ref. [12] with permission from Springer Nature.

using photoresin PRA, $D = 30\,\%$, $v_{scan,A} = 10\,\mu m\,s^{-1}$, $f_A = 100\,Hz$, and the peak red laser beam power of $\hat{P}_2 = 19\,mW$, corresponding to a peak intensity of $\hat{I}_2 = 300\,mW\,\mu m^{-2}$. For the results plotted in panel b, the more viscous photoresin PRC is used at a higher pulse frequency $f_C = 1\,kHz$ and a higher scan speed $v_{scan,C} = 50\,\mu m\,s^{-1}$.

In both cases, the blue laser beam threshold intensity I_1 is minimal at $\Delta\varphi = 0$ and $\Delta\varphi = 2\pi$, i.e., for completely overlapping pulses. The threshold intensity increases with increasing pulse phase-delay and plateaus in both cases for $\Delta\varphi = 2\pi \cdot 0.3$, i.e., for completely non-overlapping pulses. For $\Delta\varphi = 2\pi \cdot 0.6$, the pulses start overlapping again and the threshold intensity I_1 decreases.

From these experiments, an upper limit of the effective intermediate-state lifetime can be deduced. First of all, if the lifetime in either photoresin were significantly longer than the period f^{-1}, the threshold intensity I_1 would be independent of $\Delta\varphi$. Furthermore, if the lifetime in photoresin PRA τ_A were longer than D/f_A, the observed plateaus in Figure 7.11 would appear smeared out. Hence, the

intermediate-state lifetime in photoresin PRA $\tau_A < 3\,\text{ms}$ and, using the same arguments, the lifetime in PRC $\tau_C < 300\,\mu\text{s}$.[2]

7.5 THE SINGLE-COLOR TRIGGERED POLYMERIZATION

For an ideal two-color two-step photoresin, the two-color threshold contrast γ approaches infinity. In the point-scanning experiments at $v = 100\,\mu\text{m}\,\text{s}^{-1}$, the photoresins PRA and PRC have a threshold contrast of $\gamma_A \approx 200$ and $\gamma_C \approx 30$, respectively. The limited factor for the polymerization threshold is a blue-light triggered polymerization reaction. In this section, the nature of the single-color triggered polymerization in the photoresins PRA, PRB, and PRC are discussed, based on the focus-scanning characterization experiments and on triplet-state reactions of biacetyl that are reported in the literature.

7.5.1 Exposure-Time Characteristics

To understand the behavior of the *single*-color polymerization in biacetyl photoresins, focus-scanning experiments with variable scan speed are performed. Figure 7.12 shows a double logarithmic diagram with the threshold intensity I_1 plotted on the vertical axis and the scan speed v_{scan} plotted on the horizontal axis. I_1 and v_{scan} are converted to the laser power P_1 (right vertical axis) and the effective exposure time t_{exp} (top horizontal axis) using the laser focus FWHM-diameter. The measured threshold intensities for photoresin PRC show an almost linear behavior and lie on a line with a slope slightly lower than 1. A slope below 1 is also observed for the threshold intensities of photoresin PRA and PRB at slow scan speeds v_{scan}. For scan speeds $v_{\text{scan}} > 30\,\mu\text{m}\,\text{s}^{-1}$, however, the situation changes and the threshold intensities lie on lines with a slope of about 2. The nonlinear behavior observed in the less viscous photoresins PRA and PRB indicate that the single-color polymerization is suppressed for very long and very short exposure times. Furthermore, the viscosity dependence of this nonlinear behavior suggests that diffusion processes are involved.

For long exposure times, the radical polymerization is inhibited by the in-diffusion of quenchers and scavengers into the exposed voxel volume [60, 61, 77]. This effect was previously observed in multi-photon absorption 3D printing and is referred to as "Schwarzschild effect", in reference to the Schwarzschild effect in photography [60, 61, 77]. The in-diffusion rate is faster in low-viscosity monomers (as in photoresin PRA), consequently, the Schwarzschild effect is most pronounced

---

[2] Since photoresin PRA is less viscous and hence, the bimolecular diffusion-rate for TEMPO is larger in PRA than in PRC, the lifetime in photoresin PRA can also be expected to be $\tau_a < 300\,\mu\text{s}$.
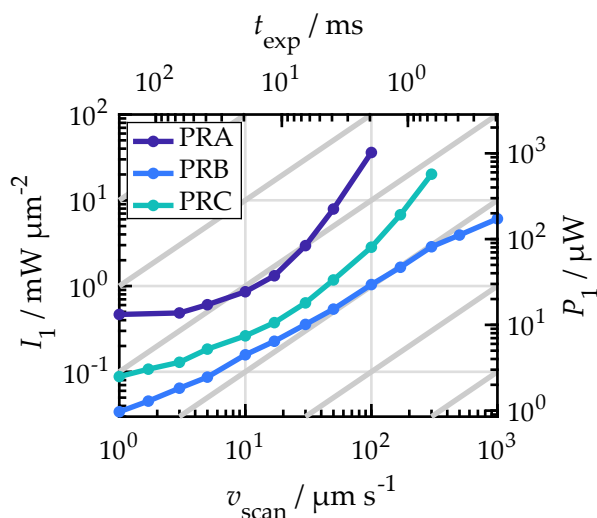
Figure 7.12: Single-color exposure point-scanning experiments with variable scan speed v_{scan} for the photoresins PRA, PRB, and PRC. The gray diagonals with a slope of 1 are a guide for the eye. On the right vertical axis, the plotted laser power P_1 is derived from the intensity I_1 using the laser focus FWHM-diameter. Similarly, the exposure time t_{exp} is obtained by dividing the laser focus FWHM-diameter (average of all measurements) by v_{scan}. For low v_{scan}, the curves have a slope < 1, whereas at large v_{scan}, the slope is > 1 for PRA and PRB. Adapted from Ref. [12] with permission from Springer Nature.

there. However, the Schwarzschild effect cannot explain the nonlinear behavior at short exposure times, which will be discussed in the context of triplet-triplet annihilation.

7.5.2 *Triplet-Triplet Annihilation*

Biacetyl molecules in their triplet ground-state are quenched in a triplet-triplet annihilation reaction [196]. From gas-phase experiments on biacetyl, Badcock et al. [196] concluded that the triplet-triplet annihilation of two triplet-state biacetyl molecules leads to one ground-state biacetyl molecule and one molecule which gets promoted to the second excited singlet state S_2. In vapor, biacetyl molecules in the S_2-state rapidly decay into free radicals [196]. In contrast, Richard et al. [197] found that in solution, biacetyl molecules in the S_2 state do not decay into radicals, but rapidly decay to the S_1 state. From these findings, it can be concluded that biacetyl is effectively quenched by the triplet-triplet annihilation. It should be pointed out, that this conclusion is in variance with the interpretations of Wolf [198], who attributes the measured second-order triplet-decay to a triplet-triplet annihilation and consequently concludes that observed radicals are generated in this process. However, no quantum yield measurement for the observed radicals is presented.

Since the triplet-triplet annihilation is a bimolecular process, its rate increases nonlinearly with the population of the T_1 state. If the process were to yield radicals, the radical concentration and hence the dose D would be proportional to the exposure time t_{exp} times the squared triplet ground-state population $[T_1]^2$,

which in turn is proportional to the squared blue laser beam intensity I_1^2:

$$D \propto [T_1]^2 t_{\text{exp}} = I_1^2 t_{\text{exp}} \propto I_1^2 v_{\text{scan}}^{-1}. \tag{7.3}$$

Therefore, a line with a slope of

$$\frac{d \log(I_1)}{d\log(v_{\text{scan}})} = 1/2 \tag{7.4}$$

is expected in the double-logarithmic plot of the single-color threshold intensity I_1 versus the scan speed. However, in Figure 7.12 the opposite, a slope of 2, is observed for short exposure times. This observation is in better accordance with a quenching reaction triggered by the triplet-triplet annihilation. There, large populations of the T_1-state lead to a more efficient quenching. This interpretation is further confirmed by the rate-model calculations in section 7.6.

7.5.3 Hydrogen Abstraction

Furthermore, a hydrogen-abstraction reaction was described many times in the literature for biacetyl in its triplet state [155, 199]. Therefore, chemical groups bearing labile hydrogen atoms must be available in the vicinity of the triplet-excited molecule. Typically, tertiary amines, alcohols, ethers, thiols, but also esters serve as hydrogen donor groups [84]. Thus, in the photoresin, the acrylic monomer can provide abstractable hydrogens. Since intramolecular hydrogen abstraction is unlikely due to biacetyl's geometry, the hydrogen abstraction in the discussed photoresins is a bimolecular process, which is retarded in more viscous monomers.[3] Hence, this process competes with the quenching and scavenging reaction of TEMPO and oxygen.

Thus, it is very likely that a hydrogen-abstraction reaction happens in the optically excited photoresins PRA, PRB, and PRC. Interestingly, Wolf [198] has observed acetyl-radicals being generated in degassed benzene solutions of biacetyl, which were irradiated with light at the wavelength 440 nm. Unfortunately, no radical quantum yield was calculated. The observation of radicals in this experiment is surprising since benzene does not participate in hydrogen-abstraction reactions. In another room-temperature photolysis experiment of degassed solutions containing biacetyl, biacetyl did not decay at all [200].

7.5.4 Reactions with Molecular Oxygen

In free radical polymerization, oxygen is generally considered a polymerization inhibitor since oxygen is a triplet state quencher but also reacts with propagating

---

[3] Assuming that the rate is diffusion-limited.

radicals to nonreactive peroxy-radicals [88]. However, this inhibiting effect is not necessarily true for reactions initiated by α-diketones. For instance, the α-diketone camphorquinone polymerizes faster in some monomers in the presence of oxygen than under an inert atmosphere [201]. Similarly, biacetyl also reacts with dissolved oxygen [155, 202]. Therefore, it is possible that the single-color polymerization in the photoresins PRA, PRB, and PRC is triggered by the oxidation of excited biacetyl molecules.

However, Wolf [198] has irradiated biacetyl with light at the wavelength 440 nm in a nominally degassed benzene solution. Despite the lack of available oxygen, radical formation was detected. Moreover, Pascal Rietz has repeated the two-color point-scanning threshold power experiments in photoresin PRA, once under an argon atmosphere, and once under an oxygen enriched atmosphere [12]. In both cases, the single-color polymerization-threshold power remained constant, whereas the two-color polymerization threshold was indeed affected by the atmosphere. Therefore, it can be assumed that the single-color polymerization in PRA, PRB, and PRC is not triggered by an oxidation of excited biacetyl molecules.

7.5.5 Thermally-Activated Norrish Type I Reaction

Biacetyl was intentionally selected as two-step-absorption photoinitiator because of its low triplet-state energy of 2.4 eV, which does not allow for a bond-cleavage reaction. The α-carbon bond cleavage energy for biacetyl is approximately 3 eV. This energy gap is confirmed by Concheanainn and Sidebottom, who measured an activation energy of $E_A = 0.65$ eV for the bond-cleavage reaction from the triplet ground-state of biacetyl in the gas phase [192]. However, the pre-exponential factor in the derived Arrhenius equation is as large as $A = 2 \cdot 10^{11}\,\mathrm{s}^{-1}$. Hence, the absolute (unimolecular) bond-cleavage rate coefficient at room temperature is

$$k_{\mathrm{scission}}(297\,\mathrm{K}) = A \exp\left(E_A\right) = 1.9\,\mathrm{s}^{-1}. \tag{7.5}$$

This rate coefficient is too small to yield significant bond-cleavage, especially in comparison with biacetyl's lifetime (see section 7.2). At this point, one could argue that the temperature within the laser focus is likely well above the room temperature. To attain a considerable bond-scission rate constant of $k_{\mathrm{scission}} = 10^3\,\mathrm{s}^{-1}$, the local temperature must reach $T = 394\,\mathrm{K} = 121\,°\mathrm{C}$. Assuming no highly absorbing transient species are generated, an estimate for the temperature in the laser focus can be made based on an analytical formula, which takes the heat conduction in two dimensions into account [106]. Assuming the monomer thermal-conductivity of $k_{\mathrm{thermal}} = 1.4 \cdot 10^{-1}\,\mathrm{W\,K^{-1}\,m^{-1}}$ [203], a monomer mass-density of $\rho_{\mathrm{monomer}} = 1.1\,\mathrm{kg\,L^{-1}}$ (vendor specification), a specific heat of $c_{\mathrm{p,monomer}} = 1.89\,\mathrm{J\,g^{-1}\,K^{-1}}$ (vendor specification), an incident laser power of $P_1 = 1\,\mathrm{mW}$, and

an exposure time of $t_{\text{exp}} = d_{\text{FWHM}} \cdot v_{\text{scan}}^{-1} = 2\,\text{ms}$, a temperature increase of

$$\Delta T(t_{\text{exp}}) = \frac{\epsilon_1(\lambda_1)c\ln(10)P_1}{4\pi k_{\text{thermal}}} \ln\left(\frac{8t_{\text{exp}}k_{\text{thermal}}}{w_0^2 c_{\text{p,monomer}}\rho_{\text{monomer}}} + 1\right) = 2.8\,\text{K} \qquad (7.6)$$

can be estimated. Here, c is the photoinitiator concentration and w_0 is the $1/e^2$ beam radius. A further increase of the local temperature is caused by the exothermic polymerization reaction itself [132], [4] which of course occurs only after the initiation. Thus, it is unlikely that the single-color polymerization is a thermally activated Norrish type I reaction, originating from the lowest triplet state. However, a local increase in temperature lowers the viscosity, which affects diffusion-limited processes.

7.5.6 Other Triplet-State Reactions

Similar to benzil, one-color two-step absorption could also happen in biacetyl. However, the triplet-triplet absorption spectrum of biacetyl does not show any absorption band at the wavelength $\lambda_1 = 440\,\text{nm}$. Still, if there were some low triplet-state absorption at 440 nm, the expected threshold laser-intensity would be much higher than for the red laser beam in the two-color exposure. Thus, at the used wavelength λ_1 and the used intensities I_1, one-color two-step absorption is unlikely responsible for the single-color polymerization threshold.

Yet another mechanism by which biacetyl's lowest triplet-state can react is a photoenolization reaction. A photoenolization reaction is a phototautomerization reaction, in which a proton is relocated from a carbon atom to an oxygen atom. This reaction was observed for biacetyl in solution, which was irradiated with light at the wavelength 435.8 nm [204]. However, under these conditions, appreciable photoenolization quantum yields were obtained only at a temperature of 100 °C.

Pre-excited biacetyl molecules could also reabsorb the emitted phosphorescence of surrounding biacetyl molecules [148]. In contrast to triplet-triplet annihilation, which happens nonradiatively, this process is mediated by emission and absorption of radiation. Incidentally, biacetyl's red phosphorescence emission overlaps with its triplet-triplet-absorption band [188, 190], which is a pre-condition for reabsorption of radiation. However, the local intensities reached by the phosphorescence are far off the necessary red laser beam intensities observed in the two-color polymerization experiments (see Figure 7.6). These low phosphorescence intensities have two reasons. First, for biacetyl, the phosphorescence quantum yield in the absence of any quencher is on the order of a few percent [188]. Second, due to the

---

[4] The temperature increase caused by the polymerization reaction was estimated to be a few Kelvins for the monomer PETA and two-photon absorption [132].

(by design) low extinction of the photoresin, only a small fraction of the incident blue photons are absorbed within the exposed voxel volume. Thus, despite the overlapping spectra, photon reabsorption is unlikely to cause the single-color triggered polymerization.

7.6 Numerical Modeling of the Photoinitiation Process

Numerical rate models can be used to better understand the interplay of the involved different processes in the two-color two-step photoinitiation. For the free radical polymerization, rate-equation models were already developed for single voxel exposure experiments [60, 77] and for the case of global illumination [88]. There, the behavior of the initiation, the free radical propagation, and the termination were successfully modeled. While in those models, the initiation step is a simple unimolecular, irreversible reaction, the initiation step in two-step absorption is more complex. Therefore, a rate model which focuses on the photoinitiation and neglects the downstream processes, i.e., radical propagation and termination, is presented .

7.6.1 Model Design and Parameters

Figure 7.13 shows a sketch of the energy-level diagram used to model the two-color two-step photoinitiation of biacetyl. State A is the ground state and is populated at time $t = 0$ s. Molecules are excited by a blue-light intensity-dependent rate coefficient k_1 to state B′, from where molecules rapidly decay to state B, which is identified with the intermediate state. Thereof, molecules can be further excited by a red-light intensity-dependent rate coefficient k_2 to state C, whose population either decays back to the state B by a rate constant k_{D2}, or the population decays into the state D by a rate constant k_{R2}. State D is identified with the radical concentration and hence the accumulated dose. As in the rate model for benzil (see section 5.3), the polymerization threshold is reached once state D is populated with 10 % of the total initial photoinitiator population, i.e.,

$$[D]_{th} = 10\,\%[A](0). \tag{7.7}$$

Furthermore, four other decay processes are allowed from state B. First, the population of state B decays in an unimolecular decay with the rate constant k_{D1} to the ground state A. Second, [B] decays to the ground state in a bimolecular reaction with other molecules in state B, i.e., with the rate $k_{TTA}[B]^2$. The latter decay models the triplet-triplet annihilation. Third, the population decays to an nonreactive species X with the rate $k_Q[Q][B]$, where [Q] is the population of the
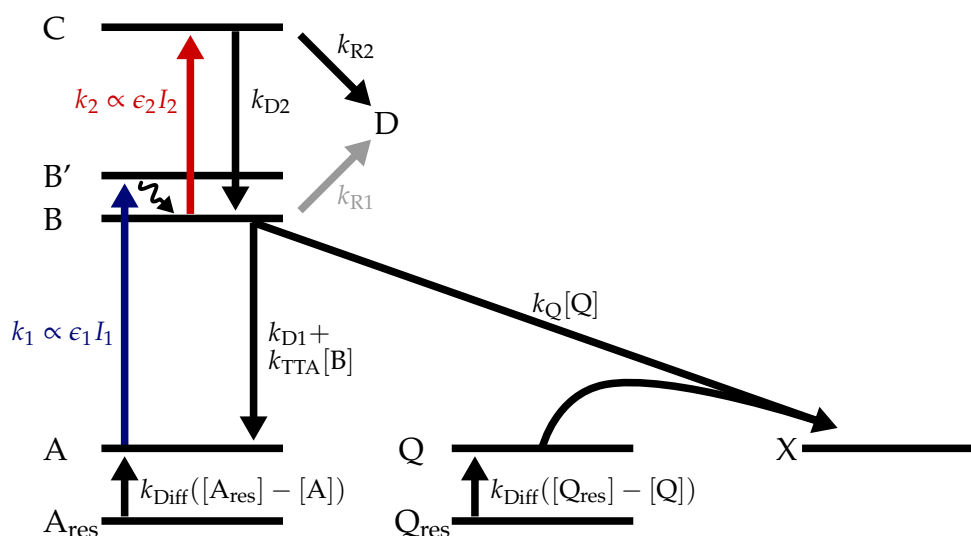
Figure 7.13: Sketch of the kinetic rate-model for biacetyl. Photoinitiator molecules are optically excited from the ground state A to state B' with rate coefficient $k_1 \propto \epsilon_1 I_1$, with ϵ_1 being the ground-state extinction coefficient and I_1 the intensity at wavelength λ_1. From B', molecules relax rapidly to the intermediate state B. Five reaction pathways exist from the intermediate state. First, molecules relax to the ground-state via an unimolecular decay with the rate coefficient k_{D1}. Second, the population of state B decays via a triplet-triplet annihilation reaction with bimolecular rate coefficient k_{TTA}. Third, intermediate-state molecules are quenched by a quencher Q in a bimolecular reaction with rate coefficient k_Q, yielding an inert state X. Fourth, molecules decay to state D, which is identified with the deposited dose, by a rate constant k_{R1}. Fifth, molecules can be excited optically with a rate coefficient $k_2 \propto \epsilon_2 I_2$ to state C. From state C, molecules either decay back to state B with rate k_{D2} or they decay to state D with the rate coefficient k_{R2}. Due to the irreversible quenching and radical-decay processes, photoinitiator and quencher molecules are consumed in the reaction. The ground-state populations of these molecules are repopulated with the rate coefficient k_{Diff} from the reservoirs A_{res} and Q_{res}. Adapted from Ref. [12] with permission from Springer Nature.

quencher state.[5]. And, finally, the population may decay directly to state D with the rate constant k_{R1}.

In the quenching reaction, photoinitiator- and quencher-molecules are removed from the system. In the model, both populations are replenished from infinite reservoirs A_{res} and Q_{res} with the diffusion rates $k_{Diff}([A]_{res} - [A])$ and $k_{Diff}([Q]_{res} - [Q])$. The assumption of infinite reservoirs simplifies spatial variations and diffusion processes of the molecules. In more rigorous treatments, the diffusion processes are taken into account by solving the diffusion equation [77].

---

[5] The terms scavenging and quenching are used interchangeably within this chapter.

Table 7.1: Rate coefficients used for the two-color two-step polymerization rate model. The molar decadic extinction coefficients are $\epsilon_1 = 20\,\text{M}^{-1}\,\text{cm}^{-1} = 2\,\text{m}^2\,\text{mol}^{-1}$ and $\epsilon_2 = 700\,\text{M}^{-1}\,\text{cm}^{-1} = 70\,\text{m}^2\,\text{mol}^{-1}$. The wavelengths are given in m (meters) and the intensities in $\text{W}\,\text{m}^{-2}$. The pre-factor $1.92\,\text{mol}^{-1}\,\text{J}^{-1}\,\text{m}^{-1}$ results from the conversion from a molar decadic extinction coefficient to an absorption cross section. The viscosity η is given in Pa s. R is the ideal gas constant, T the thermodynamic temperature, which is set to $T = 296\,\text{K}$ in the calculations. The resulting bimolecular rate coefficients k_{TTA}, k_{Diff}, and k_{Q} are in units of $\text{M}^{-1}\,\text{s}^{-1}$. The remaining rate coefficients are in units of s^{-1}.

rate coeff.	value	source
k_1	$0.1 \cdot 1.92\,\text{mol}^{-1}\,\text{J}^{-1}\,\text{m}^{-1} \cdot \epsilon_1 \lambda_1 I_1(t)$	fit
k_{D1}	$5 \cdot 10^3$	fit, based on Ref. [188]
k_{TTA}	$8000RT/(3\eta)$	experiment (diffusion limited)
k_{Diff}	$10^6/\eta$	fit, based on Ref. [60]
k_{R1}	$5 \cdot 10^2$	fit
k_2	$1.92\,\text{mol}^{-1}\,\text{J}^{-1}\,\text{m}^{-1} \cdot \epsilon_2 \lambda_2 I_2(t)$	experiment
k_{D2}	10^6	fit
k_{Q}	$8000RT/(3\eta)$	experiment (diffusion limited)
k_{R2}	10^3	fit

For this model, the following rate-equations are derived:

$$\frac{\mathrm{d}[A]}{\mathrm{d}t} = -k_1[A] + k_{\text{D1}}[B] + k_{\text{TTA}}[B]^2 + k_{\text{Diff}}([A_{\text{res}}] - [A]), \tag{7.8}$$

$$\frac{\mathrm{d}[B]}{\mathrm{d}t} = +k_1[A] - (k_{\text{D1}} + k_{\text{R1}} + k_2)[B] - k_{\text{TTA}}[B]^2 + k_{\text{D2}}[C] - k_{\text{Q}}[B][Q], \tag{7.9}$$

$$\frac{\mathrm{d}[C]}{\mathrm{d}t} = +k_2[B] - (k_{\text{D2}} + k_{\text{R2}})[C], \tag{7.10}$$

$$\frac{\mathrm{d}[D]}{\mathrm{d}t} = +k_{\text{R1}}[B] + k_{\text{R2}}[C], \tag{7.11}$$

$$\frac{\mathrm{d}[Q]}{\mathrm{d}t} = -k_{\text{Q}}[B][Q] + k_{\text{Diff}}([Q_{\text{res}}] - [Q]), \tag{7.12}$$

$$\frac{\mathrm{d}[A_{\text{res}}]}{\mathrm{d}t} = 0, \tag{7.13}$$

$$\frac{\mathrm{d}[Q_{\text{res}}]}{\mathrm{d}t} = 0. \tag{7.14}$$

State [B'] is not included in the coupled differential equations because it decays to state [B] instantaneously. The initial conditions for the coupled differential equations are given by $A(0) = A_{\text{res}}(0) = 100\,\text{mM}$ and $Q(0) = Q_{\text{res}}(0) = 10\,\text{mM}$.

Figure 7.14: Two-color polymerization threshold obtained by rate-model calculations. The intensities I_1 and I_2 (lower horizontal and left vertical axis) are converted to laser powers P_1 and P_2 using the focus FWHM-diameters $d_{\text{FWHM},1} = 187\,\text{nm}$ and $d_{\text{FWHM},2} = 283\,\text{nm}$. The calculated curves agree with the corresponding point-scanning experiments shown in Figure 7.7. Adapted from Ref. [12] with permission from Springer Nature.
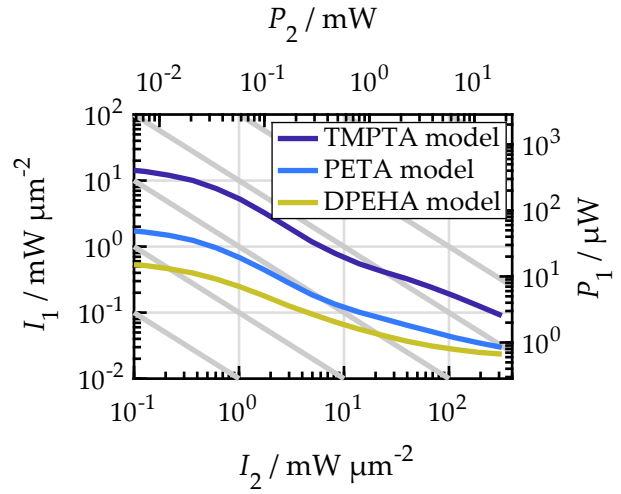
All other states are initially unpopulated. The parameters used in the computations are listed in Table 7.1.

In the characterization experiments, the laser is scanned in dashed line patterns. Hence, a single point on the scanned line is exposed to a temporally variable intensity. The model reproduces the temporal intensity profile by a Gaussian profile with a (temporal) FWHM-diameter of $t_{\text{FWHM},i} = d_{\text{FWHM},i} v_{\text{scan}}$, where $d_{\text{FWHM},i}$ is the spatial (measured) laser-focus FWHM-diameter and v_{scan} the scan speed. For the blue laser beam, $d_{\text{FWHM},1} = 187\,\text{nm}$ and for the red laser beam, $d_{\text{FWHM},2} = 283\,\text{nm}$. The temporal Gaussian profiles are both centered at $t = 2t_{\text{FWHM},i}$, to avoid a cut-off of the musicians' tails at $t = 0\,\text{s}$. For the same reason, the calculation is only stopped at the time $t_{\text{end}} = 5t_{\text{FWHM},2}$.

The coupled differential equations are solved using Matlab's "ode23s"-solver [205]. Furthermore, the threshold-intensity is obtained by numerically searching for the minimal blue intensity I_1 which fulfills the threshold condition (see Equation 7.7) for the given set of parameters.

7.6.2 Results

The rate-model parameters are derived by manually fitting calculated curves to the experimental polymerization-threshold data shown in Figure 7.7, Figure 7.11, and Figure 7.12, i.e., to the threshold data obtained for different monomer viscosities, for the pulsed excitation experiments, and for blue-light only exposure experiments. The results for the three modeled experimental data-sets are shown in Figure 7.14, Figure 7.15, and Figure 7.16.

First, the trend of the threshold-curves for different monomer viscosities plotted
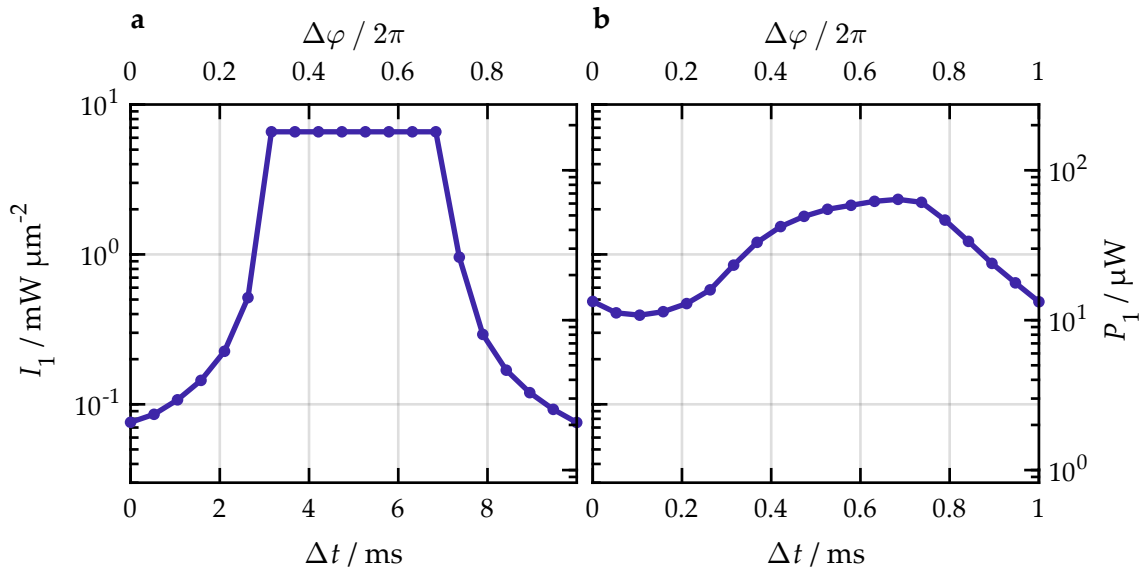
Figure 7.15: Rate-model calculations of the polymerization threshold-intensities for a phase-shifted pulsed two-color excitation scheme. The corresponding results of point-scanning experiments are shown in Figure 7.11. **a**, Results for photoresin PRA, a simulated scan speed $v_{scan} = 10\,\mu m\,s^{-1}$, a frequency $f_A = 100\,Hz$, and a duty cycle of $D = 30\,\%$. **b**, Same plot as in a, however for $v_{scan} = 50\,\mu m\,s^{-1}$ and a frequency $f_C = 1\,kHz$. Note the different lower horizontal axis scaling. Adapted from Ref. [12] with permission from Springer Nature.

in the two-color polymerization-threshold diagram in Figure 7.14 agree well with the experimentally obtained curves. For the high-viscosity monomer DPEHA, the polymerization threshold is lower than for the lower-viscosity monomers PETA and TMPTA.[6] Furthermore, all curves show a sigmoid behavior with a plateau for larger scan speeds. More importantly, the computed curves also agree with the experimentally obtained curves, in that the threshold-contrast also increases for the less viscous monomers.

The modeled results for the pulsed-light excitation experiments are shown in Figure 7.15. For both conditions, i.e., a pulse repetition rate of $f_A = 100\,Hz$ in photoresin PRA (panel a) and a pulse repetition rate of $f_C = 1\,kHz$ in photoresin PRC (panel b), the model reproduces the experimentally observed curve shapes. In panel a, the modeled curve shows a flat plateau for non-overlapping pulses (i.e., $7\,ms > \Delta t > 3\,ms$). Outside this range, the threshold intensity rapidly decays and is minimal for $\Delta t = 0\,s$ and $\Delta t = 10\,s$. However, the absolute threshold-intensities only agree with the order of magnitude with the experimen-

---

[6] No threshold-curve is calculated for the monomer PETTA, due to missing room-temperature viscosity data.

Figure 7.16: Polymerization threshold-intensities obtained by rate model calculations for a blue-light only exposure of photoresins PRA, PRB, and PRC at different scan speeds. The corresponding results point-scanning experiments are shown in Figure 7.12. The gray diagonal lines have a slope of 1 and are a guide for the eye. For low scan speeds (long exposure times), the threshold intensity plateaus with a slope < 1, whereas for high scan speeds (short exposure times), the threshold intensity increases quadratically with the scan speed, i.e., $I_1 \propto v_{scan}^2$. Adapted from Ref. [12] with permission from Springer Nature.
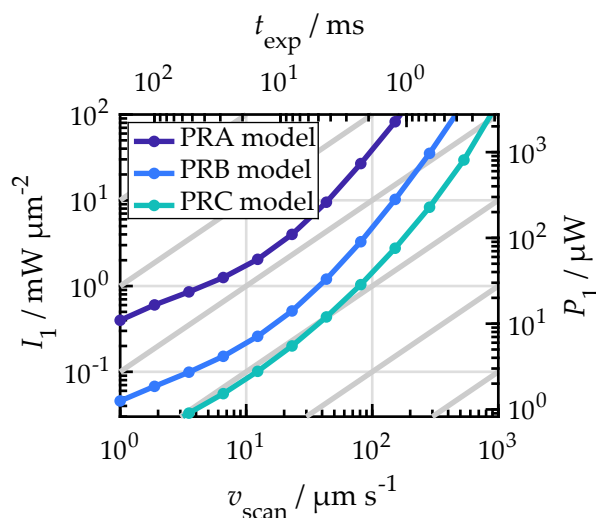
tally observed threshold-intensities.

Similarly, the results shown in Figure 7.15b overall agree with the experimental results. For overlapping pulses, the computed absolute threshold-intensity value overestimates the measured values by a factor of five. For non-overlapping pulses, the intensity-thresholds differ only by a factor of ≈ 1.5. In contrast to the curve in Figure 7.15a, however, the plateau in the computed curve in panel b appears smoothed. Also the computed slopes at $\Delta t = 300\,\mu s$ and $\Delta t = 700\,\mu s$ are less steep than in the experiment. This smoothed appearance of the threshold curve is expected, if the effective lifetime of state B becomes comparable to the pulse period. Consider again the extreme case for an infinite intermediate-state lifetime. In this case, the intermediate-state population is irrespective of the pulse delay Δt and no plateau is expected for the curves shown in Figure 7.15. Hence, it can be directly concluded that the rate-model slightly overestimates the effective intermediate-state lifetime.

Finally, the modeled data for the blue-light only exposure at different scan speeds are shown in Figure 7.16. Again, the trend towards lower polymerization thresholds for an increased monomer viscosity is reproduced accurately by the model. As expected from the experiment, at scan speeds below $10\,\mu m\,s^{-1}$, the curves start to plateau. This plateau is caused by the diffusion of quencher and photoinitiator molecules from the reservoirs A_{res} and Q_{res} into A and Q. For large scan speeds, the slope of the curves increase, which is expected from the triplet-triplet annihilation of the intermediate-state molecules. However, in the experiments for the monomer DPEHA (PRC), this increase in slope is not observed.

7.6.3 Discussion

Overall, the proposed rate model qualitatively reproduces the experimental findings of the polymerization threshold for photoresins of different monomer viscosity, for a pulsed laser excitation, and for a single-color exposure at scan speeds spanning more than two orders of magnitude. Yet, some discrepancies between the computed and experimentally-obtained results exist. These discrepancies are understandable since the model simplifies the polymerization process. These simplifications are discussed in the following paragraphs.

First of all, in the model, the polymerization threshold condition is reached, once state D is sufficiently populated. In reality, the polymerization threshold can be linked to the degree of monomer conversion [79], which could be modeled by a radical propagation and termination reaction, starting from state D. In the course of the polymer propagation reaction, the monomer viscosity increases and hence bimolecular reactions slow down. However, expanding the proposed rate model by these reactions adds further unknown rates and leads to an overall more complex rate model. Therefore, the radical propagation and termination are not included in the rate model.

Furthermore, the proposed model contains only the quencher (or scavenger) state Q. In reality, several photoresin ingredients are known to be biacetyl triplet quenchers, for instance TEMPO, oxygen, and the acrylic monomer itself [152, 156, 206, 207]. No biacetyl quenching rate constant for TEMPO could be found in the literature. However, data is available for di-tert-butyl-nitroxide [206], which can be expected to quench the biacetyl triplet at a diffusion-limited rate in the acrylic monomer. Similarly, oxygen is an infamous biacetyl triplet quencher [156], which is, under ambient conditions, also dissolved in photoresins [88]. In fact, (irreversible) oxygen quenching was already recognized in the first photochemical investigations on biacetyl [181]. The quenching rate constant of oxygen is diffusion-limited in the viscous monomers [152, 156, 208]. While oxygen is a small molecule with a high diffusion coefficient compared to TEMPO, the absolute concentration of oxygen is approximately 10 times lower than that of TEMPO. Hence, TEMPO is expected to govern the quenching of biacetyl triplets and oxygen is neglected in the model. Finally, for the quenching of the used acrylic monomers, no data is available. However, the quenching rate constant of other acrylic monomers is well below the diffusion limit and hence, monomer quenching is neglected as well in the model.

In the model, quenching is assumed to transfer biacetyl molecules from the B state to an inert state X. However, also reversible quenching, i.e., by transferring molecules from state B to state A, is conceivable. For the biacetyl quenching by oxygen, available data indicates that reversible and irreversible quenching hap-

pens at comparable rates [181, 209], leading ultimately to a depletion of oxygen. From the literature, it is unclear whether quenching by TEMPO is primarily reversible or irreversible. It is likely that TEMPO is regenerated for some quenching reactions [157]. However, TEMPO also participates in irreversible radical scavenging [198]. Unfortunately, quantitative measurements of the quenching mechanism of TEMPO in the used acrylic monomers are scarce. Hence, reversible quenching is neglected in the model.

The single-color polymerization reaction in the model proceeds with the unimolecular rate coefficient k_{R1} from the B state. From the discussion on the characteristics and mechanism of the single-color induced polymerization (see section 7.5), it was concluded that radicals are likely generated in a bimolecular hydrogen-abstraction reaction. Again, no measurements of the rate of hydrogen abstraction by biacetyl in the used acrylic monomers were found in the literature. Also, the most likely substrate for hydrogen abstraction, the acrylic monomer itself, is available in abundance. Hence, a this process is simplified by a unimolecular rate coefficient.

To understand the photochemical processes in the two-color two-step photoresins better, analytical quantitative experiments, focusing on the interplay of TEMPO and biacetyl, should be performed. Open key questions are, whether the quenching of biacetyl is of physical (i.e., reversible) or chemical (i.e., irreversible) nature. Moreover, to understand how to increase the two-color polymerization threshold contrast γ, the single-color polymerization reaction should be studied in more depth. One option is to use perfluorinated chemicals to suppress the hydrogen-abstraction reaction. In summary, despite some open questions, the presented rate model reproduces the experimental results and provides a starting point for future investigations.

8 Chapter 8
Light-Sheet 3D Microprinting
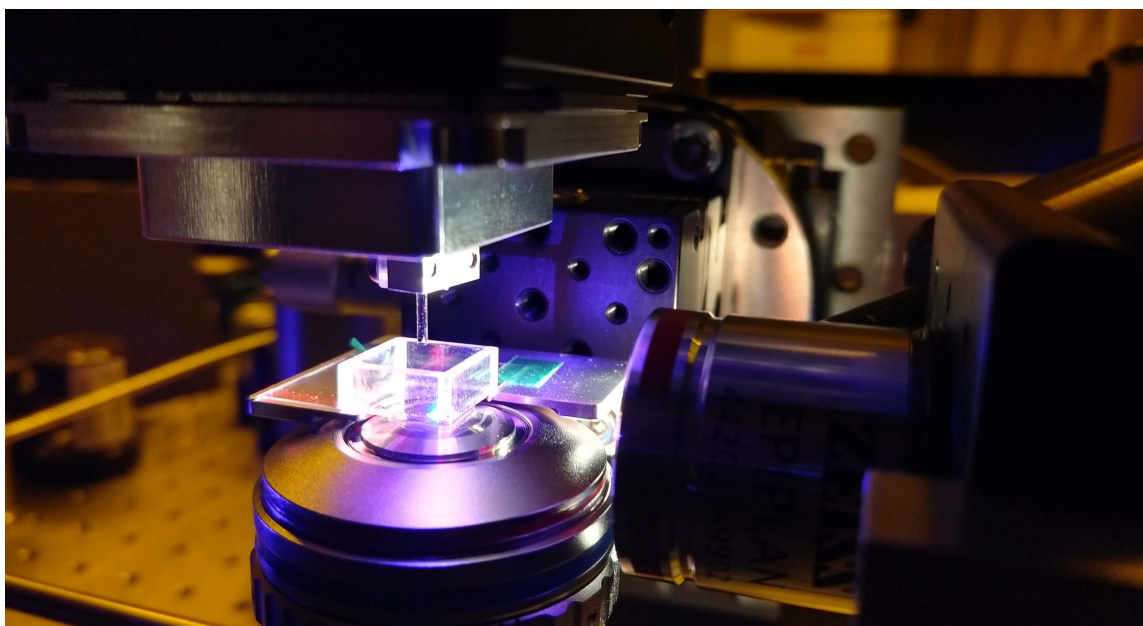
Close-up photograph of the light-sheet 3D microprinting setup.

In this chapter, a light-sheet 3D microprinting system, which is tailored to the two-color two-step-absorption photoinitiator biacetyl, is presented. With this setup, 3D microstructures printed in the blink of an eye are fabricated.

8.1 A SETUP FOR LIGHT-SHEET 3D MICROPRINTING

Light-sheet 3D microprinting is a novel technique [9–11] and, as such, there are no fully engineered, technologically-matured general-purpose 3D light-sheet printers yet that can be bought off the shelf. Hence, for printing experiments with the photoresins presented in chapter 7, a light-sheet 3D microprinter is custom designed and built. In this section, critical design aspects of a 3D light-sheet microprinter are discussed. Similar to the process of commercial product design, we will first define very general requirements for the microprinter. Next, we will discuss features of the technical implementation. Finally, the assembled setup is presented alongside with an evaluation of its optical performance.
The following discussion will take up the general introduction on light-sheet 3D microprinting, which was presented in section 7.1.

8.1.1 Design Considerations and Requirements

The trend in 3D printing is clearly towards higher printing rates [48], which also sets the design objective for a light-sheet 3D microprinter. At this point, one might already ask the question, why one should build a light-sheet 3D printer for micrometer-sized structures instead of a light-sheet 3D printer with more macroscopic voxel sizes. There are two reasons to do so. First, a higher printing resolution allows 3D printing for numerous exciting applications, like micro-optics or cell-scaffolds [74, 210]. The second reason is more pragmatic. To polymerize one voxel, a certain amount of energy must be absorbed by the photoinitiator within the voxel volume. Large voxels require more energy than small voxels. Since the total available laser power is limited, a higher voxel printing rate can be achieved for smaller voxel volumes. Thus, in light-sheet 3D microprinting, we make a virtue out of necessity and aim for both, high printing rates and micrometer-sized voxels.

Generally, high printing rates require either a high degree of parallelization, i.e., a large number of simultaneously exposed voxels, or a short voxel exposure period. While light-sheet 3D microprinting allows for parallelization, there are still three reasons, to make a short voxel exposure time a priority. First, we have seen in section 7.4 that short exposure times lead to triplet-triplet annihilation, resulting in a large polymerization threshold contrast γ, which is ideal in light-sheet 3D microprinting. While this photoresin behavior might not hold true for any two-color two-step photoinitiator, there is a second good reason to stick to short exposure times. In the course of the polymerization, the refractive index of the polymerized material increases by as much as $\Delta n \approx 0.02$ [60]. This local increase in refractive index within the focal plane entails disturbing aberrations and scattering of the light-sheet beam. Fortunately, the polymerization is not
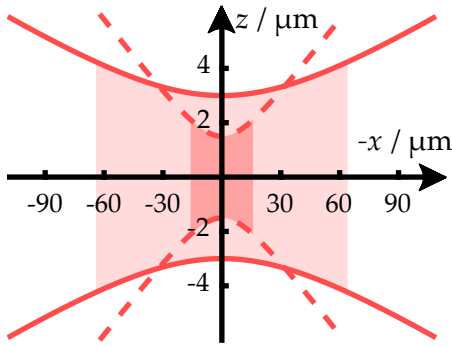
Figure 8.1: For a Gaussian beam, the Rayleigh length and the beam waist are inherently linked. The dashed line outlines the $1/e^2$-diameter of a Gaussian beam profile, propagating in the $-x$-direction, with a beam waist of $1.5\,\mu m$. The continuous line outlines a Gaussian beam with larger beam waist of $3\,\mu m$. Consequently, the Rayleigh length, shaded in red, of the wider beam is longer. In the calculations, a wavelength of $\lambda_2 = 660\,nm$ and a refractive index of $n = 1.5$ is used. Adapted from Ref. [12] with permission from Springer Nature.

instantaneous. In acrylic photoresins, the crosslinking reaction starts only after an induction period, in which quencher molecules are consumed, and proceeds for a few hundred microseconds up to a millisecond, depending on the photoresin viscosity [60, 88]. Thus, to avoid scattering of the light-sheet beam during the polymerization, exposure times on the order of a few hundred microseconds are desirable.[1] To understand the third reason why short exposure times are preferable over a high degree of parallelization, one must consider how the length of the projected layer limits the axial voxel size.

In light-sheet 3D microprinting, the axial voxel size, that is the voxel size in the propagation direction of the projection beam (z-direction), is defined by both, the light-sheet beam and the projected image. The projected image is focused with a certain NA into the photoresin (refractive index n). The larger the NA is, the faster the intensity decays on either side of the focal plane, at least for one isolated focused beam. However, when a large area is exposed, i.e., many densely packed focused beams, the projected intensity does not decay axially and the projection optics does not define the axial voxel size (see section 2.6).

In any case, the axial voxel size is defined by the perpendicular propagating light-sheet beam with wavelength λ_2 and beam waist w_0. Ideally, one wants the w_0 to be as small as possible. As illustrated in Figure 8.1, for a Gaussian beam, a small beam waist implies a small Rayleigh length l_R [129], i.e., a narrow depth of focus,

$$l_R = \frac{\pi w_0^2 n}{\lambda_2} \propto d_z^2. \tag{8.1}$$

Here, d_z is the light-sheet height (see Figure 8.2). If, however, l_R is very small compared with the length of the projected image along the light-sheet propagation axis d_x, then the axial voxel size at the edge of the projected image is much larger

---

[1] Scattering of the light-sheet beam is addressed again below.

Figure 8.2: Light-sheet dimensions.
The light-sheet propagates in the $-x$ direction. The light-sheet height d_z is the dimension along the projection propagation axis. The light-sheet length d_x is the dimension along the light-sheet propagation axis. The light-sheet span d_y is perpendicular to the light-sheet and projection propagation axes.
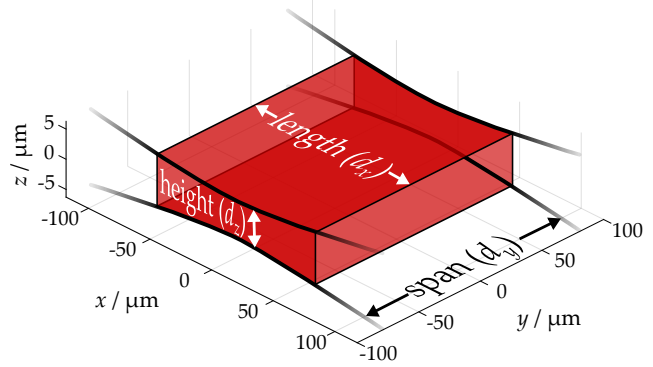
than in the center. This is clearly not desired. Hence, for an uniform axial voxel size across the projected field of view, the Rayleigh length l_R must be larger than d_x, i.e., $l_R \gtrsim d_x$. Thereby, the light-sheet beam waist w_0, and hence the axial voxel size, limits the projected length d_x, leading to a trade-off between (axial) voxel size and printing rate. This marks the third reason why short exposure times are favored over a high degree of parallelization, i.e., a large field of view, in light-sheet 3D microprinting.

8.1.2 Implementation

There is, however, a technical lower limit for the exposure time imposed by the frame rate of the projection system. At a $1920 \times 1080\,\text{px}$ resolution, state of the art digital micromirror device (DMD)-type microdisplays achieve black-and-white frame rates of up to $20\,\text{kHz}$, or $1\,\text{kHz}$ when displaying grayscale images [211]. High speed LCOS displays achieve frame rates of $720\,\text{Hz}$ [178]. While DMD-type microdisplays offer excellent intensity contrast, the micro-mirrors within one display have some tilt angle variance, making DMDs incompatible with the demagnifying optics used for 3D light-sheet microprinting [212]. For this reason, slices are projected using an LCOS display with a minimum exposure time of $1.4\,\text{ms}$.

Available high frame-rate microdisplays are fabricated for video projectors and hence these displays typically have a widescreen aspect ratio of $R_A = 16/9 = 1.7\overline{7}$. If the entire display area is to be projected, this leaves the design choice of the orientation of the projected display with respect to the light-sheet beam, i.e., either the long or the short display side is coaligned with the light-sheet propagation axis. Several arguments need to be considered in this regard. First, the intensity I_2 of the light-sheet beam is larger, when the long side of the display is coaligned with the light-sheet propagation axis. This can be understood by the following calculation. The intensity is inversely proportional to the light-sheet height d_z and

the light-sheet span d_y (see Figure 8.2),

$$I_2 \propto d_y^{-1} d_z^{-1}. \tag{8.2}$$

Equation 8.1 relates the light-sheet height d_z to the Rayleigh length by

$$d_z \propto \sqrt{l_R} \propto \sqrt{d_x}. \tag{8.3}$$

Inserting Equation 8.3 into Equation 8.2 for a constant projection area $A = d_x d_y$ yields

$$I_2 \propto \frac{\sqrt{d_x}}{A}. \tag{8.4}$$

Hence, for a fixed projection area, the light-sheet intensity is higher if the display's long side is parallel to the light-sheet propagation axis.
On the other hand, this alignment leads to a larger light-sheet height d_z and hence a larger voxel aspect ratio, i.e., the ratio of the voxel's axial and lateral width. Furthermore, as discussed above, changes in the refractive index during polymerization lead to a scattering and hence an extinction of the light-sheet beam along its propagation axis. This scattering increases for larger d_x. For these two reasons, the LCOS is aligned with its short side collinear to the light-sheet propagation axis – despite the lower intensity, which can be compensated by higher laser powers.

In the design of a light-sheet 3D microprinter, one pivotal degree of freedom affecting most design decisions downstream is the assignment of the light wavelength to either the light-sheet beam or the projection beam. For either choice, there are several pros and cons. If biacetyl is used as photoinitiator, one beam must be blue-colored and the other beam must be red-colored. Let us first consider the argument for a blue-colored light-sheet beam.

For a Gaussian beam, the Rayleigh length is inversely proportional to the wavelength (see Equation 8.1). That means, that for a given beam waist and medium, a Gaussian beam of blue-color has a longer Rayleigh length than a beam of red color. Therefore, a blue-colored beam enables a longer projected field of view, and hence more simultaneously exposed voxels.
Conversely, for a constant Rayleigh length, the beam waist of a Gaussian beam decreases proportional to the square root of the wavelength (again, see Equation 8.1). A small light-sheet beam waist is particularly interesting to achieve isotropic voxels.

However, there are several reasons for a red light-sheet beam. For the two-color two-step-absorption photoresins, we have observed also single-color exposure polymerization. This undesired polymerization happens when exposing the

photoresin intensely or for an extended period with only blue light, hence both conditions must be avoided. The light-sheet beam is focused with low NA, and accordingly, the intensity does not decrease rapidly in the focused light cone. Moreover, the light-sheet beam is switched on constantly. On the other hand, the intensity of the tightly focused projection beam decays rapidly outside the focal plane, at least when projecting sparse layers. Only when exposing layers with high filling fractions, the axial intensity profile decays slowly. Still then, since the exposed patterns change for each layer, the out-of-focus intensity distribution also changes. Thus, the photoresins shortcomings favor a light-sheet 3D microprinting setup in which the blue light is used for projection.

Above all, the most pressing argument for a blue projection beam is the necessary laser power. While the projection beam exposes a two-dimensional area, the light-sheet beam exposes only a single line since its propagation direction is within the focal plane. Therefore, for a given wavelength, more laser power is needed for the projection beam than for the light-sheet beam. However, the readily available laser powers are limited. From the point-scanning experiments on photoresin PRC, we know that the voxel threshold intensity for the red laser beam is two orders of magnitude larger than for the blue laser beam. Hence, in order to keep the necessary red laser power at a manageable level, also in regard to the damage threshold of optical components, a red light-sheet beam is used.

The choice of the exact light-sheet beam wavelength is flexible, due to the broad triplet-triplet absorption spectrum of biacetyl. While the triplet-triplet extinction increases in the infrared spectral range (see Figure 7.5), a smaller light-sheet wavelength leads to a tighter focused beam (for a given NA) and hence to a higher local intensity, compensating the lower triplet-triplet extinction. A good compromise is found at a wavelength of 710 nm. However, currently, no high power, high beam-quality lasers are available at this wavelength. The nearest practical laser wavelength is 660 nm, which lies also close to the used 640 nm characterization wavelength used in chapter 7. Hence, this wavelength is chosen for the light-sheet beam.

More wavelength-options are available for the blue projection-beam, which, in contrast to the light-sheet beam, does not rely on a high beam-quality. The absorption spectrum of ground-state biacetyl ranges from 380 nm to 450 nm. Two common high-power gallium-nitride laser diode wavelengths fall in this range, 405 nm and 445 nm. From a resolution point-of-view, the smaller wavelength is favored for its smaller diffraction-limited PSF. However, the used LCOS display absorbs near-UV light, making a 445 nm projection beam preferable. Moreover, the excitation of biacetyl by 445 nm wavelength is also close to the zero-phonon line of biacetyl [187]. An excitation at this wavelength hence provides less excess vibrational energy for undesired photoresin heating or other reactions triggered from the lowest excited state (see section 7.5).

So far only lasers have been considered. Recently high power LEDs have become available in the blue spectral region. However, their radiance, that is the emitted power per projected area and per solid angle, is insufficient to expose the photoresin. For instance, consider a state-of-the art LED[2] emitting almost $10\,\mathrm{W}$ of power in a Lambertian emission profile from an area of $1.86\,\mathrm{mm^2}$. This LED has a basic radiance, which is a conserved quantity in ideal optical systems [213], of $L_{e,0}^* = 1.7\,\mathrm{W\,sr^{-1}\,mm^{-2}}$. In the characterization experiment for photoresin PRC, a blue laser beam threshold intensity (i.e., irradiance in the language of radiometry) of $I_\mathrm{th} = 0.1\,\mathrm{\mu W\,\mu m^{-2}}$ was found. When focused with a $\mathrm{NA} = n\sin(\theta) = 1.2$ in a photoresin of refractive index $n = 1.5$, the basic radiance at the polymerization threshold is

$$L_{e,1}^* = \frac{I_\mathrm{th}}{2\pi\left(1 - \cos\left(\theta\right)\right)n^2} = 18\,\mathrm{W\,sr^{-1}\,mm^{-2}},\tag{8.5}$$

which is 10 times larger than the basic radiance of the LED. Thus, even when neglecting any transmission and polarization losses in the beam path, LEDs are *currently* an inadequate illumination source for rapid light-sheet 3D microprinting with the proposed two-color two-step photoresins, no matter how large (or small) the projected area is.

Next, the beam-shaping options are discussed. The blue projection beam should evenly illuminate the rectangular LCOS microdisplay. There are two power economic, commonly used techniques for laser beam shaping [214]. In the first method, the "field mapping" method, a single spatial-mode laser beam, typically of Gaussian shape, is formed to a flat top beam by a phase element, e.g., refractive optics [102, 103]. The beauty of this method lies in the resulting flat wavefront, which is hence free of speckles. Moreover, the polarization state of the input beam is preserved. However, a nonnegotiable prerequisite is a clean spatial mode profile at the input. For the laser powers needed in light-sheet 3D microprinting, single-mode laser diodes do not exist.

A multi-mode compatible alternative to field mapping homogenizers are beam integrators, which work by superimposing many plane waves [214]. This is achieved by microlens arrays or by channel integrators, e.g., homogenizer rods or multi-mode optical fibers. They do, however, produce speckle patterns, which can be reduced for instance by temporally incoherent light sources [215].

Since only diode lasers with a spatial multi-mode emission are available with sufficient laser power for light-sheet 3D microprinting, we will resort to a multi-mode fiber as beam homogenizer in the setup presented below. Speckles are reduced by using an array of laser diodes, effectively increasing the spectral width. Again, if LEDs with sufficient radiance were available, speckle patterns could be
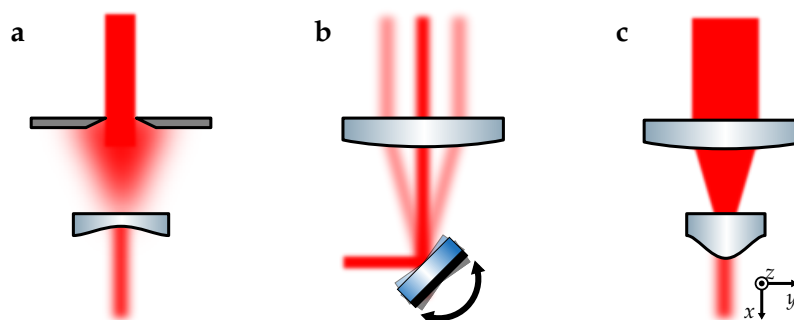
Figure 8.3: Three ways of forming a uniform light-sheet beam. a, A circular Gaussian beam expanded by a cylindrical lens and clipped at an aperture. **b**, A Gaussian beam is rapidly scanned along one axis, forming a *virtual* light-sheet. **c**, An aspheric lens forms a divergent line, which is then "collimated" by a lens. In all examples, the light-sheet beam propagates in the $-x$ direction.

easily suppressed.

Similarly, there are several ways in which a light-sheet beam can be formed from a (circular) Gaussian beam. In the most primitive form, a cylinder lens focuses the beam along only one axis. In this configuration, the beam intensity profile across the unfocused axis retains its Gaussian profile and hence, the intensity in the center of the light-sheet is higher than at the edge. Figure 8.3 shows three ways to achieve a more uniform lateral beam profile.

First, the Gaussian beam can be clipped by an aperture. This, of course, leads to significant power losses and is only feasible if sufficient optical power is disposable. In the second option, a circular laser beam is scanned rapidly along the span of the light-sheet [216], enabling variable light-sheet widths. In this configuration, the line-scan frequency must be larger than the frame rate. Moreover, if the light-sheet beam excites the second step of a two-step absorption process, the line-scan frequency must also exceed the decay rate of the photoinitiator's intermediate state. Otherwise, photoinitiator molecules are pre-excited numerous times from the ground-state to the intermediate state, before they eventually get excited by the light-sheet beam. This unnecessary photoinitiator cycling requires an increased blue laser power and favors undesired side-reactions from the intermediate-state. For the biacetyl photoresins, we estimate an intermediate-state decay-rate of approximately 1 kHz, which is just at the edge of what fast galvanometric scanners achieve.

Finally, a circular Gaussian beam can also be transformed to a uniform, stationary light-sheet beam in a laser-power economic fashion by shaping the wavefront, e.g., with a Powell lens, which is a cylindrical aspheric lens [217, 218]. A detailed description of an according optical arrangement is given below in subsection 8.1.3.

---

[2] Osram Ostar Projection Power LE D P0MQ.

Let us discuss a further, elegant way of obtaining a light-sheet beam using spatial multi-mode laser diodes. By design, edge-emitting laser diodes emit beams with a single transverse-mode and multi longitudinal-mode beam profile, which is exactly the beam profile needed in a light-sheet. Hence, one only needs to image the facet of the laser diode with appropriate transverse and longitudinal magnifications to obtain a light-sheet beam. Modern single-emitter laser diodes emit up to 1.3 W cw radiation in the red and near-infrared spectral range[3]. When focused to a light-sheet with a 3.5 µm FWHM waist and 160 µm span[4], a peak intensity of 2.3 mW µm^{-2} can be achieved. This is just short of the necessary red laser beam threshold intensity of $\approx$ 6 mW µm^{-2} obtained in the single-point characterization experiments (see Figure 7.7). Hence, with the two-step photoresins at hand, laser diodes are *not yet* a feasible option for light-sheet generation. This might change with the development of more sensitive photoresins or higher-powered laser diodes.

The purpose of light-sheet 3D microprinting is to print rapidly, which allows large structures to be printed within an acceptable time. So far, we have discussed the exposure of only a single layer. There, the lateral extent of light-sheet printed objects is limited by the LCOS field of view and the axial extent by the light-sheet. To print 3D structures, several printing fields must be stacked axially on top of each other, and, for increased lateral structure dimensions, stacks can be stitched laterally next to each other. Conceptually, two options exist to do so: Either the already 3D printed part is moved with respect to the projection and light-sheet optics, or vice versa. This choice can be made for each axis. For the lateral axes, it is easiest to actuate the 3D printed object instead of the entire bulky optical train. The situation is different for the axial dimension, not the entire optical track would need to be moved since modern microscope objective lenses are designed for a conjugate image at infinity, i.e., for collimated beams at the entrance pupil. However, the free working-distance of high NA objectives is only a few hundred micrometers, which again would limit the axial printing range. Moreover, if the projection objective is moved, also the light-sheet beam must be tracked accordingly, requiring precise synchronization of both systems. No such difficulties arise when moving the printed object.

In volumetric printing, it has become common to actuate the 3D printed object by moving the photoresin container [5, 6, 11]. Thereby, the 3D printed object floats in the photoresin and no solid printing substrate is needed, which can be considered an advantage for some applications. However, for light-sheet 3D microprinting, this approach has four disadvantages. First, to avoid inertial drifts of the printed structure within the liquid, no rapid accelerations must be

---

[3] e.g., Thorlabs L637G1

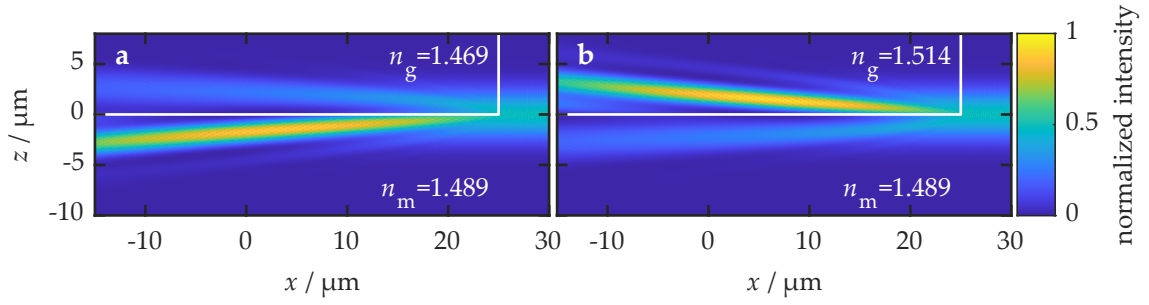[4] These are the actual dimensions of the light-sheet used below.

Figure 8.4: Diffraction of the light-sheet beam at the photoresin-substrate interface. The false-color diagrams show the time-averaged, globally-normalized absolute value of the Poynting vector obtained in finite-element calculations using the Comsol Multiphysics software package (using the Paradiso solver, a maximum mesh element size $0.2\lambda_2/n$, and perfectly matched layers at all boundaries except at the beam input plane). The refractive index of the photoresin monomer is $n_m = 1.489$ and of the glass substrate, which is highlighted by the white frame, is n_g. In accordance with the coordinate system of the light-sheet 3D printing setup below, the Gaussian beam is propagating in $-x$-direction, the beam is polarized in the y-direction (TE-polarization) and its geometrical focus is located at the origin, i.e., $x = z = 0\,\mu m$. **a**, $n_g = 1.4691$. **b**, $n_g = 1.514$.

made to the photoresin container. This prohibits fast stitching. Second, extended printing sessions are problematic since the printed structure sediments within the photoresin container due to its higher density. Third, the limited working-distance of the projection objective lens limits the maximum axial extent of the printed structure. And finally, a movement of the photoresin container implies that the distance the projection beam propagates in the photoresin changes for every layer. Accordingly, due to the photoresin's extinction, the intensity in the focal plane changes and, due to the changing propagation length in media with different refractive indices, aberrations occur. In conclusion, substrate-free printing entails several disadvantages in light-sheet 3D microprinting.

The previous paragraph outlined the necessity for a 3D printing substrate. Next, the substrate geometry and material requirements are discussed. The flat glass substrates commonly used in 3D nanoprinting are not practical in light-sheet 3D microprinting since their large surface area leads to drag within the viscous photoresin. Preferably, the substrate should be small in diameter and sufficiently long, such that it can be dipped into the photoresin container. Since both laser beams are focused to high intensities, the substrate should not substantially absorb light, to avoid heating or burning, nor should the substrate strongly reflect light, to avoid interference effects and polymerization in undesired locations. These conditions have led to the choice of glass rods as 3D printing substrate. Transparent plastic 3D printing filament is an alternative substrate.

The refractive index mismatch of the substrate and the photoresin is important to actually *see* the substrate and to position it in the photoresin cuvette. However, the mismatch also leads to reflection and diffraction effects of the laser beams. For the projection beam, whose chief ray impinges almost perpendicular on the substrate, only little intensity is reflected and no pronounced interference effects are observed. The situation is different for the light-sheet beam. The result of 2D finite-element calculations of the local intensity of a light-sheet beam, propagating through the photoresin, and being diffracted at the edge of a glass substrate with refractive index n_G is shown in Figure 8.4. The calculations are performed for two different substrate refractive indices. The laser beam intensity vanishes in locations close to the substrate surface, which is clearly undesired since the photoresin would not polymerize in those locations. Therefore, 3D structures would not adhere to the substrate.

To overcome this problem, the substrate surface is angled relative to the incident light-sheet beam (see Figure 8.5). Thereby, the light-sheet does not propagate through the substrate before arriving at the actual printing location. Still, the large angle of incidence leads to a strong reflection at the photoresin-glass interface, despite the nearly matched refractive indices. The reflected waves lead to an interference pattern of the light-sheet beam in the photoresin. Again, for small angles, the intensity close to the interface becomes zero (see panel Figure 8.5a). However, the period of the intensity modulation decreases for smaller angles of incidence and a nonzero light-sheet intensity is obtained close to the interface (Figure 8.5d). Therefore, the substrates used in 3D light-sheet microprinting must be mounted at an angle relative to the light-sheet plane (*xy*-plane).

In light-sheet 3D microprinting, the choice of objective lenses is more challenging than in focus-scanning 3D laser nanoprinting since two objectives lenses must be brought in close proximity to superpose their focal planes under a right angle. However, for most objective lenses, a compact housing is no design requirement. Therefore, objectives with long working distances are required. Many long working-distance microscope lenses exist for the light-sheet objective since it is focused with a low NA. For the projection objective lens, which needs to have a higher NA, the choice is limited. Moreover, to avoid spherical aberrations due to the refraction at the interfaces between the immersion oil, the photoresin container, and the photoresin itself, an objective lens comprising an immersion medium correction collar is preferable. For this purpose, a suitable $63\times/\text{NA}1.2$ immersion microscope objective with a free working distance of 660 μm was identified. Since this is an immersion lens, it should be mounted in vertical orientation to avoid runoff of the immersion fluid.

Finally, we discuss the requirements for the photoresin container. Both, the pro-
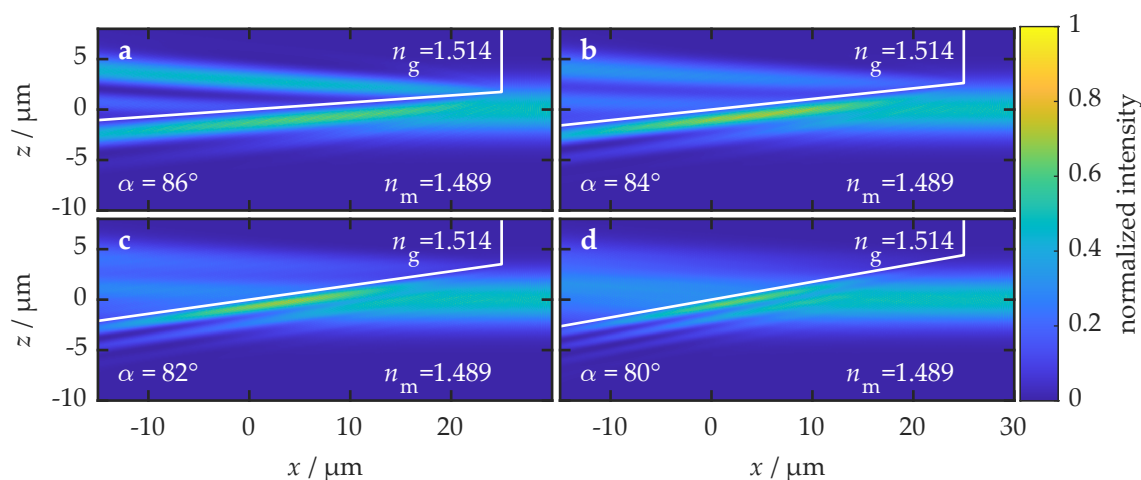
Figure 8.5: Diffraction of the light-sheet beam at the angled photoresin-substrate interface. The parameters in this figure are the same as in Figure 8.4b, except for the angle of incidence α, which is varied in the range 86–80°. The pivot point is located at the origin. Adapted from Ref. [12] with permission from Springer Nature.

jection and the light-sheet beam, must be superimposed in the liquid photoresin, which hence must be contained in a transparent vat with optically clear sides. Spectroscopy cuvettes are the natural choice for this purpose. However, the base plate of common cuvettes is not polished. This is problematic since the vertically mounted, high-NA objective needs to focus through the base plate into the cuvette. Thus, plastic cuvettes are used, whose base plate is sawed off and replaced by a thin microscope glass coverslip.

8.1.3 Elements of the Setup

Figure 8.6a shows a schematic of the assembled light-sheet 3D microprinting setup. It consists of four elements: the light-sheet beam path, the projection beam path, the photoresin container, and the substrate. In this section, the materials and devices used for the light-sheet path, the projection path, the cuvette, the substrate, and the electronics are presented.

The light-sheet beam path consists of a 6 W output power, 660 nm emission-wavelength solid-state laser (Laser Quantum GmbH, axiom). The 0.85 mm $1/e^2$-diameter laser beam is shaped by a 1° fan-angle Powell lens (Laserline Optics Canada Inc, LOCP-8.9R01-1.0), which is an aspheric lens with a large conic constant. The beam is then focused and collimated by a set of spherical and cylindrical lenses (Thorlabs GmbH, LA1131-A-ML, LJ1629RM-A, and LJ1267RM-A), before it is focused into the photoresin container by a microscope objective (Carl
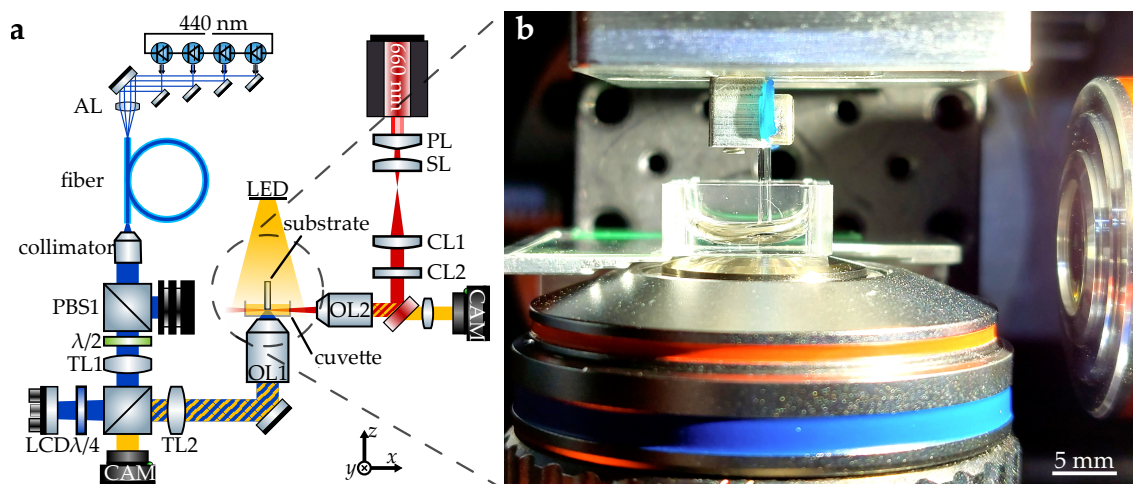
Figure 8.6: The light-sheet 3D microprinting setup. a, Schematic of the light-sheet setup. The following abbreviations are used: AL: aspheric lens, PBS: polarizing beam splitter, BD: beam dump, TL: tube lens, LCD: liquid crystal display, CAM: camera, OL: objective lens, CL: cylindrical lens, SL: spherical lens, PL: Powell lens. **b,** Photograph of the encircled area of **a**. The photoresin cuvette is mounted atop of the high-NA immersion-objective. The substrate is dipped from the top into the photoresin and the light-sheet beam is focused by the objective lens at the right. Created using "ComponentLibrary" [116] by Alexander Franzen (CC BY NC 3.0) and adapted from Ref. [12] with permission from Springer Nature.

Zeiss AG, Epiplan $5\times/0.13$). The light-sheet beam is polarized in the y-direction. A more detailed list of the optical path is supplied in Table A.2.

The projection beam path consists of four 6 W output power, 440 nm wavelength multi-mode laser diodes (Lasertack GmbH, PD-01231), which are coupled into a 1 m long rectangular-core fiber (Ceramoptec GmbH, NA 0.22, $810 \times 405\,\text{mm}^2$ core dimensions). The homogenized beam at the output of the fiber is collimated by a microscope objective (Carl Zeiss AG, EC-Epiplan-Neofluar $20\times/0.5$). Next the collimated beam is polarized by a polarizing beam splitter (Thorlabs GmbH, PBS251) and its polarization axis is rotated by a zero-order half-wave plate (Thorlabs GmbH, WPH10M-445). A 150 mm focal-length achromatic doublet (Thorlabs GmbH, AC254-150-A-ML) focuses the collimated beam, which is reflected at a second polarizing beam splitter[5] (Thorlabs GmbH, PBS251) and transmitted through a zero-order quarter-wave plate (Thorlabs GmbH, WPQ10M-445). The latter converts the linear polarization to a circular polarization. The focused beam is reflected at the $1920 \times 1080\,\text{px}$ resolution, 720 Hz frame-rate LCOS display (Holo-

---

[5] The combination of two polarizing beam splitters is needed to illuminate the display with light of a high degree of polarization. The extinction ratio of the polarizing beam splitters in the reflected beam is only 20 : 1.

eye GmbH, HED4552). Light being reflected by nominally white pixels changes the handedness of the circular polarization state, whereas light being reflected by black pixels retains its handedness. The reflected light passes again through the quarter-wave plate, converting the circular polarization to linear polarization with perpendicular polarization axes for black and white pixels. At the second polarizing beam splitter, beams from nominally white pixels are transmitted and collimated by a tube lens (Thorlabs GmbH, ITL200). At this location, the measured contrast ratio between white and black pixels is 314. The collimated beam is then focused by a high-NA objective lens (Carl Zeiss AG, LD LCI Plan Apochromat $63\times/1.2$ Imm Corr DIC). This objective lens comprises a correction collar to minimize spherical aberrations caused by mismatched immersion media. The correction collar is set to a refractive index of $n \approx 1.5$. The objective lens focuses the beam through a thin layer of immersion fluid (Carl Zeiss AG, Immersol 518F) into the photoresin container. A more detailed list of the optical path is supplied in Table A.3.

The photoresin container consists of an UV-transparent, solvent-resistant, square plastic cuvette (Brand GmbH & Co KG) with an internal wall distance of 1 cm. The cuvette is cut to a height of 5 mm, with its base plate removed. A $\approx 100\,\mu m$ thin microscope glass coverslip (Thorlabs GmbH, CG00C) is glued by an UV-curable adhesive (Norland Products Inc., NOA63) to the bottom of the plastic cuvette. For a precise alignment of the cuvette within the light-sheet 3D printing setup, the cuvette is mounted on goniometric and linear-translation stages.

Finally, the 1 mm diameter cylindrical glass rods (Hilgenberg GmbH) are cut to a length of 13 mm. To obtain a flat printing substrate, the glass rods are manually polished by grinding them on wetted sandpaper (Starcke GmbH & Co KG, Matador series) at an angle of $\approx 8°$. For aligning the light-sheet, a 45° angled glass rod is prepared. The glass rod substrates are positioned by a set of precision stages. For coarse z-positioning, a 13 mm travel-range stepper-motor actuated stage (Physik Instrumente GmbH & Co KG, L-306.011112) is used. For rapid stitching within the xy-plane, a voice-coil actuated stage (Physik Instrumente GmbH & Co KG, V-528.1AA) with a 20 mm travel-range is employed. Finally, the sample is rapidly actuated and positioned in the z-direction by a low-inertia piezo-stage (Physik Instrumente GmbH & Co KG, P-622.ZCD). The travel-range of the latter is limited to 250 μm. All stages are stacked vertically on top of each other. The stack is mounted hanging from a breadboard, which is mounted on an optical table.

The LCOS display is controlled by an FPGA, which receives the display image sequence via a high-definition multimedia interface (HDMI) connector. The image sequence is encoded in a 4K resolution ($3840 \times 2160\,px$) color frame video stream with 60 Hz frame rate. At the FPGA, each frame of the video-stream is

decoded into 12 separate $1920 \times 1080\,\text{px}$ grayscale frames. The frame display at the LCOS display and the movement of the stages is concerted by a dedicated software, programmed in C++, and running on a stock Debian GNU/Linux operating system on a computer equipped with a graphics processing unit (NVidia GeForce GTX970). The programming of the software interface and the setup of the computer was done by Frank Hermann, details of the implementation can be found in his Bachelor's thesis.

8.1.4 Optical Performance

In this section, the optical performance of the designed 3D light-sheet printer is evaluated.

8.1.4.1 Projection Focus Characterization

The focus quality of the projection beam is characterized by ray tracing calculations in an optical design software (Zemax LLC, OpticStudio). Therein, the output of the homogenizing fiber is modeled as a Gaussian apodized ray bundle with an NA of 0.22 and the wavelength $\lambda_2 = 440\,\text{nm}$. The rays are then propagated through the setup, according to the lens data provided in Table A.3. Three components of the setup are proprietary compound lenses however. The first compound lens, the Zeiss $20\times$ objective, is substituted by a thin paraxial lens with focal length $f = 165\,\text{mm}/20 = 8.25\,\text{mm}$.[6] The second compound lens is a model ITL200 tube lens, which is substituted by the similar model TTL200 (both Thorlabs GmbH), for which a ray tracing model exists. Finally, the high-NA objective lens is substituted by lens data from a Zeiss patent for an objective lens with matching characteristics [219].

For the ray tracing, all pixels of the LCOS display are assumed to be in the "white" state, which allows the display to be modeled by a perfect mirror surface. Let us briefly consider the opposite case, in which a beam is reflected only at a small area of white pixels and all remaining pixels are in the black state. In this case, the display acts as a pinhole, diffracting the reflected beam, and thereby increasing the NA of the beam.

Thus, in the ray-tracing model, the NA in the photoresin is effectively limited to $4.3 \cdot 0.22 = 0.95$ by the $4.3\times$ magnified NA of 0.22 of the optical fiber. In contrast, for arbitrary displayed LCOS-patterns, the NA can be larger than this value and is ultimately limited by the NA of the objective lens.

Figure 8.7 shows numerically calculated PSF data of the projected beams in the

---

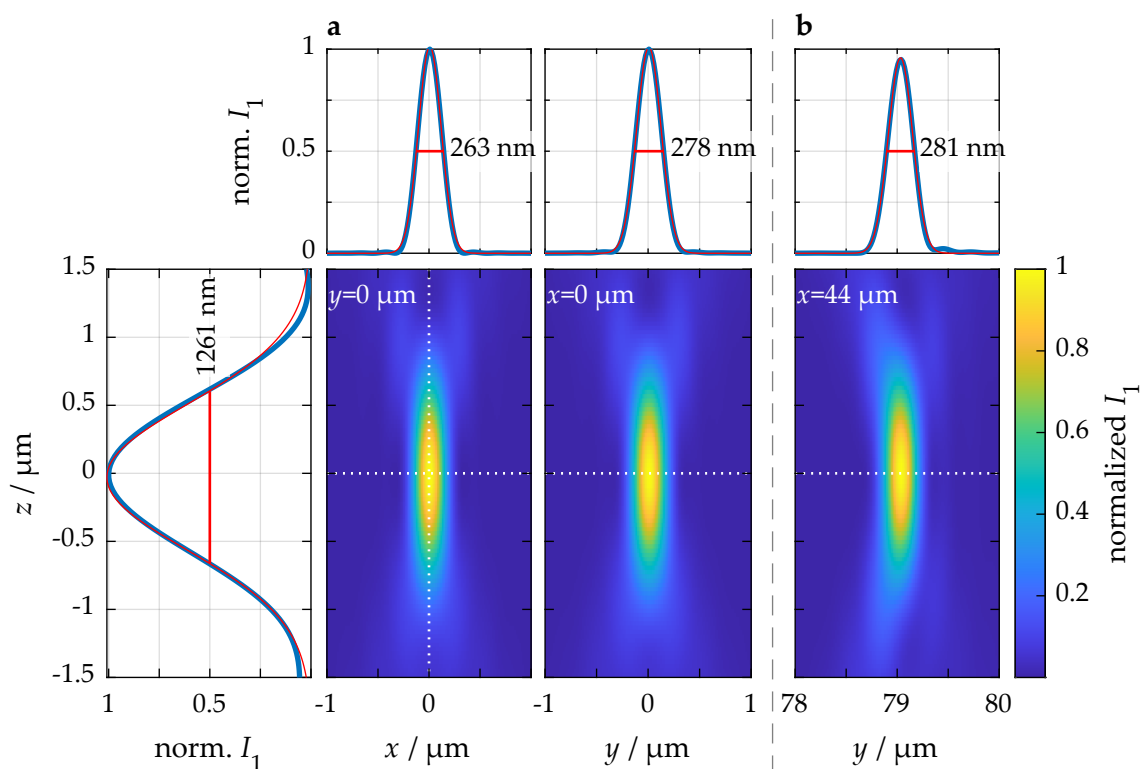[6] The Zeiss tube length reference focal length is 165 mm [140].

Figure 8.7: Calculated PSF of the projection path. The PSF data is computed in the software Zemax OpticStudio using the Huygens-PSF function, which computes the coherent, amplitude-weighted superposition of plane waves, taking into account the light's polarization-state. In the false-color intensity diagrams, the white dashed lines indicate the axis used in the 1D intensity cuts. In the 1D intensity cuts, a Gaussian distribution (red line) is fitted to the calculated data. **a**, Data for the focus located at $x = y = 0\,\mu m$, i.e., which is centered in the projected field of view. The difference in the lateral PSF-diameters results from the linear polarization along the y-axis. **b**, Data for the focus located in the corner of the projected field of view, i.e., at $x = 44\,\mu m$ and $y = 79\,\mu m$. The same colorbar is used for all false-color diagrams. The field shown in panel **b** is also normalized to the maximum intensity of the PSF in panel **a**. Adapted from Ref. [12] with permission from Springer Nature.

photoresin (refractive index $n_m = 1.489$). The central focus shown in panel a has a mean lateral FWHM-diameter of 270 nm. The lateral FWHM area covers the area of 8.5 projected pixels. This means, that of the $1920 \times 1080\,\text{px} = 2.1 \cdot 10^7\,\text{px}$ projected by the LCOS, only $2.5 \cdot 10^6\,\text{px}$ are optically resolved in the photoresin. Thereby, pixelation artifacts are smoothed at the expense of a lower voxel printing rate. The axial FWHM-length of the isolated PSF is 1261 nm and hence approximately three times smaller than the light-sheet height (see below). However, for larger exposed areas, the axial FWHM-height increases rapidly, leading to a better overlap with the light-sheet beam. In panel b, PSF data for a focus in the corner of the projected

area is shown. While some coma-like aberrations can be seen in the false-color intensity diagram, the peak intensity (see 1D cut) is only slightly below the peak intensity of the on-axis focus shown in panel a. Moreover, the lateral FWHM-diameter is only 1 % larger than the corresponding diameter of the on-axis focus. This consistency of the PSF data is important to achieve uniform print results across the entire projected field.

8.1.4.2 *Light-Sheet Characterization*

To characterize the light-sheet beam, a complementary metal-oxide-semiconductor (CMOS) camera (Teledyne FLIR LLC, BFLY-PGE-31S4M-C) is scanned along the x-axis, which is the propagation direction of the light-sheet beam. Since the light-sheet beam-height is of similar size as the camera's pixel size ($3.45 \times 3.45\,\mu m^2$), the camera is also scanned with sub-pixel accuracy along the z-direction, i.e., along the focused axis. At each location, an image of the intensity distribution is recorded. The sub-pixel-shifted images are then interleaved and stacked to a 3D array. To obtain the light-sheet FWHM height at each x- and y-coordinate, a Gaussian distribution is fitted to the intensity profile along the z-direction. However, the thereby obtained beam height is convoluted by the camera's pixel size. To correct for the finite pixel size, the measured light-sheet height is corrected by a factor derived from a calibration curve (see Figure A.1). This calibration curve is obtained from Gaussian curve fits on Gaussian distributions, which are convoluted with a 3.45 μm-wide square function.

Figure 8.8 shows the results of the measured 3D intensity array and the parameters obtained in the fitting procedure. The total optical power of the light-sheet in the focal plane is 3.6 W. At a laser output power of 6 W, this value corresponds to a 60 % transmission. In Figure 8.8a, the FWHM-intensity is plotted versus the beam propagation direction x. In the focus of the light-sheet, a local intensity of $6\,mW\,\mu m^{-2}$ is reached. At the edge of the red-shaded area, which is at $x = \pm 45\,\mu m$, the intensity decays to approximately $4\,mW\,\mu m^{-2}$. Note that in the photoresin, the Rayleigh range is longer by a factor n than in air (see Equation 8.1) and therefore, the intensity at the edge of the field of view is underestimated. These intensities can be compared directly to the threshold-intensities obtained in the point-scanning experiments (Figure 7.7). In the point-scanning experiments at the scan speed $v = 100\,\mu m\,s^{-1}$, the two-color polymerization curves of the screened monomers plateaued above $10\,mW\,\mu m^{-2}$. Figure 8.8b shows a cut of the light-sheet beam's intensity profile at $x = 0\,\mu m$. The profile is flat at the most part of the projected image. Towards the edges, the intensity decays to approximately 50 % of the plateau intensity. The light-sheet FWHM-height versus x is shown in Figure 8.8c. The profile agrees well with the profile of an ideal Gaussian beam
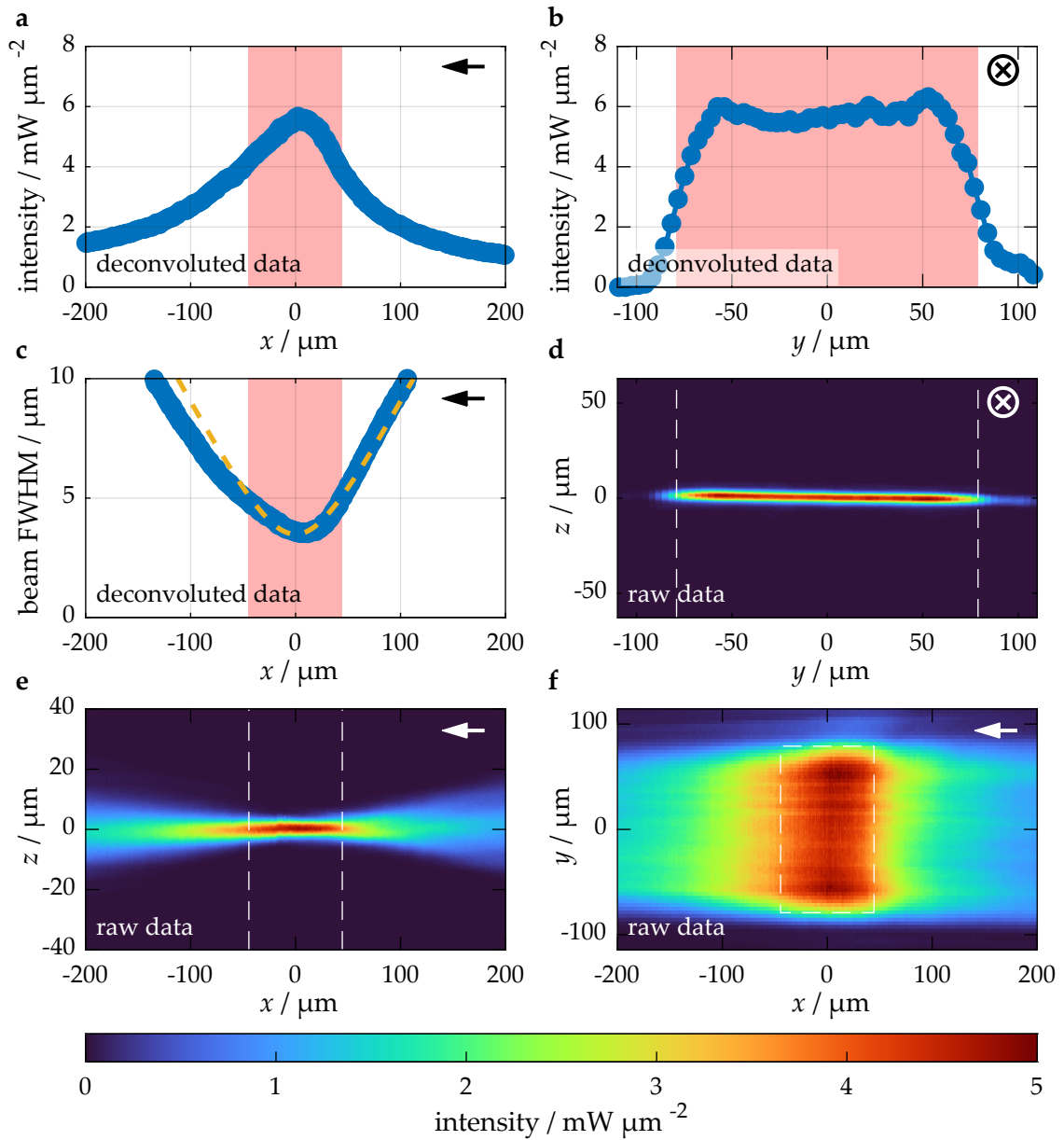
Figure 8.8: 3D characterization of the light-sheet beam. The intensities are measured in air at a reduced laser power. The absolute values are derived by scaling the data for a laser power of $P_2 = 6\,\text{W}$. "Deconvoluted data" refers to parameters obtained from a Gaussian curve fit along the z-direction of the 3D dataset. The light-red shaded area and the white dashed lines highlight the projected image area *in air*, which is centered at $x = y = z = 0$. The arrows in the upper right corner of the panels indicate the beam propagation direction. **a**, Intensity I_2 at $y = z = 0$. **b**, Peak intensity I_2 at $x = 0\,\mu\text{m}$. **c**, Light-sheet FWHM-height plotted against x. The orange dashed line outlines the profile of a Gaussian beam with a FWHM-height of $3.5\,\mu\text{m}$. **d**, Measured intensity at $x = 0\,\mu\text{m}$. **e**, Measured intensity at $y = 0\,\mu\text{m}$. **f**, Maximum intensity projection along the z-direction. Adapted from Ref. [12] with permission from Springer Nature.

with a 3.5 μm FWHM beam-height and a Rayleigh range of 85 μm in air. While the Rayleigh range is longer in photoresin than in air (a refractive index of $n = 1.48$ results in a Rayleigh range of 125 μm), the beam height is not affected by a change of refractive index. The figures Figure 8.8d, Figure 8.8e, and Figure 8.8f show 2D false-color intensity diagrams at $x = 0$ μm, $y = 0$ μm, and $z = 0$ μm respectively. The latter depicts the maximum intensity projection. Overall, these data show that the Powell lens is suitable for shaping a uniform light-sheet beam.

8.2 LIGHTSHEET 3D MICROPRINTED STRUCTURES

Ultimately, the capabilities of a 3D printer can only be assessed by actually printing 3D structures. First, the 3D printing workflow is presented, then the voxel size is characterized by printing line arrays, and finally, results of exemplary 3D printed structures are shown.

8.2.1 3D Printing Workflow

The 3D light-sheet microprinting setup is prepared by pipetting 150 μL of photo-resin into the cuvette. The cuvette is then positioned in the setup with the help of cameras. To precisely align the light-sheet to the focal plane of the substrate, a 45° wedged-end glass rod is mounted in the setup such that the low-powered light-sheet beam is reflected at the wedge-photoresin interface into the high-NA objective lens. The collected light-sheet beam is observed using a camera mounted at the idle port of PBS2 in a plane conjugate to the LCOS display. The light-sheet is positioned by an adjustment mirror mounted near the entrance pupil of the light-sheet objective lens. After the light-sheet alignment, the 45° wedged-end glass rod is replaced by the printing substrate.

Right before printing, the light-sheet laser output power is increased to 6 W (3 W for the suspended line gratings). Then, the job file is loaded on the real-time computer. This step takes a few seconds to load the image sequence, the stage movement commands, and the laser trigger commands from the hard disk into the memory. Once these prerequisites are finished, the exposure is initiated. First, the light-sheet shutter is opened. Then, the blue laser is switched on, and, after a few milliseconds, the image sequence is displayed on the LCOS display. Due to the inertia of the piezo-stage and the thereon mounted sample, the piezo-stage accelerates on a run-up distance of 6 μm. If multiple structures are stitched next to each other, the blue laser is switched off during sample repositioning, whereas the slower shutter of the light-sheet beam remains open. A few milliseconds after the exposure is finished, the blue laser is switched off, and the light-sheet shutter closes.

After printing, no time-consuming post-exposure by a UV lamp [11, 52] is required. The substrate is developed by dipping it into acetone for 30 s and subsequently dried in air. The suspended line gratings shown below are developed by supercritical drying in acetone to ensure structural integrity. The cuvette with the remaining liquid photoresin is cleaned by washing it for 15 min in spectroscopy-grade isopropyl alcohol and subsequently rinsing it with isopropyl alcohol before it is dried in a gentle nitrogen stream.

8.2.2 *Voxel Size and 3D Printing Rate*

To measure the voxel printing rate, suspended lines are printed with a variable nominal linewidth in the range of 0.5–2.0 μm. Figure 8.9a shows a scanning electron micrograph of an array of 3D printed lines. Sets of four 30 μm long lines, spaced by 6 μm, are printed by exposing a single layer for 5 ms at an intensity of 160 mW μm^{-2}. Two parallel 5 μm thick walls serve as support structure. The light-sheet laser is set to an emission power of 3 W to avoid saturation effects.

High-resolution scanning electron micrographs are used to measure the width and height of more than 150 printed lines. The measured width (height) is plotted as blue points (orange crosses) in Figure 8.9b. Small icons represent individual measurements, and large icons average values. The linewidth increases monotonically with an increasing target linewidth. However, the measured averaged widths are all below the targeted width (blue line), which can have several causes. First, acrylic monomers are known to shrink upon polymerization and development, with typical linear shrinkage ratios on the order of 10 % [220]. Shrinkage alone is unlikely the only effect since the observed linewidth deviation is larger than 15 %, especially towards small linewidths. A second cause for the reduced linewidth is the limited modulation transfer function of the LCOS projection system, smearing out the nominally rectangular spatial excitation profile. In the threshold model, the binarization of the smoothed profile leads to a reduced linewidth. The extent of this smoothed profile can be estimated from the calculated lateral PSF profile shown in Figure 8.7. Finally, diffusion effects can also explain the reduced linewidth. Before the polymerization reaction in the optically excited volume sets in, quencher and scavenger molecules must be sufficiently depleted [60, 88]. In the periphery of the exposed volume, the concentration of the polymerization inhibiting molecules can be replenished by in-diffusion from the unexposed surrounding, leading to a faster polymerization in the center of the exposed volume. The observed taper of the lines towards the bulky walls indicates that diffusion-based proximity effects occur within the photoresin.

The smallest shown lines are printed with a 6 px wide projected profile and
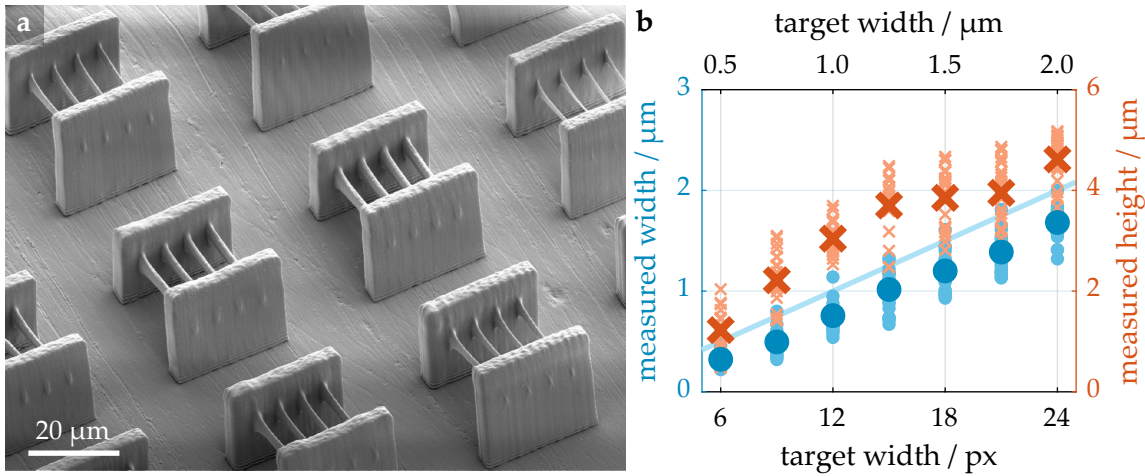
Figure 8.9: 3D light-sheet microprinted lines to measure the voxel size. a, Electron micrograph of 3D printed suspended lines, which are spaced by 6 μm within each set. The used blue laser beam intensity is set to 160 mW μm^{-2} and the light-sheet laser power is set to 3 W. **b**, Plot of the measured linewidths (points, left vertical axis) versus targeted linewidth (horizontal axis), and the measured line heights (crosses, right vertical axis). The small icons indicate individual measurements, whereas the large icons indicate averaged values. For data points on the blue line, the target width equals the measured width. Adapted from Ref. [12] with permission from Springer Nature.

result in, on average, 320 nm wide lines. However, one third of these lines broke, either during printing or during development. Hence, the smallest reproducibly printed lines are $d_{vx} = 500$ nm wide and are printed with a target linewidth of 750 nm (or 9 px). The corresponding line height, and hence voxel height, is $h_{vx} = 2.2$ μm, from which the voxel aspect ratio of $h_{vx}/d_{vx} = 4.4$ and a voxel volume of $(0.5\,\mu m)^2 \times 2.2\,\mu m = 0.55\,\mu m^3$ are derived. For larger target linewidths, the light-sheet beam height confines the line height to a value of approximately 4 μm.

From these measurements, a voxel peak printing rate can be calculated [48]. From the $\tilde{d}_{vx} = 9$ px wide projected voxel diameter, a voxel area of $\pi \tilde{d}_{vx}^2/4 = 63.6$ px^2 is calculated (assuming a round voxel shape). Hence, of the $2.1 \cdot 10^6$ projected pixels, $3.3 \cdot 10^4$ lead to resolved voxels. With the line grating exposure time of 5 ms, a peak voxel printing rate of $7 \cdot 10^6$ voxels s^{-1} is obtained and thereby a volume printing rate of $3.85 \cdot 10^6$ μm^3 s^{-1}.

8.2.3 3D Structures

To showcase the flexible 3D printing capabilities of the light-sheet 3D microprinter, several 3D structures are printed, which are shown in the SEM gallery in Fig-
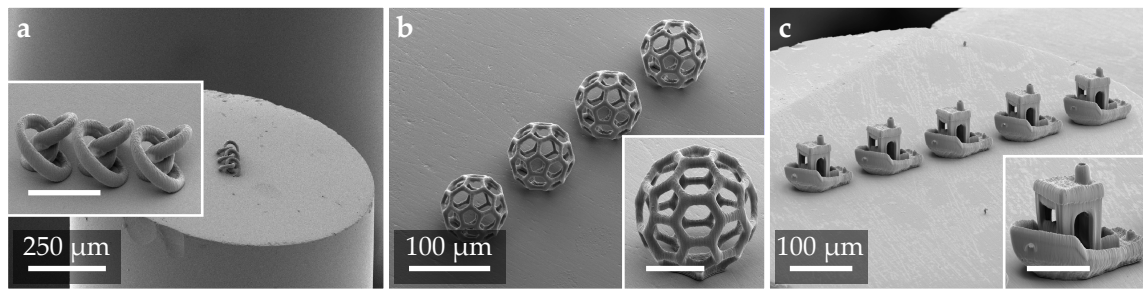
Figure 8.10: Scanning electron micrographs of 3D light-sheet microprinted structures. All inset scale bars are 50 µm long. **a**, Three knot-like structures printed in parallel on the slanted glass rod substrate. **b**, Four buckyballs with a diameter of 80 µm. **c**, A fleet of five #3Dbenchy boats. Each boat is 3D printed by stitching one boat behind the other. All parts are printed with a substrate z-velocity of approximately 350 µs. Adapted from Ref. [12] with permission from Springer Nature.

ure 8.10. Panel a shows three knot-like structures on the slanted glass rod substrate. All three structures are printed simultaneously within 153 ms. For comparison, in multi-photon 3D nanoprinting experiments of the same structure, a *single* knot is printed in 2 s (not shown). Panel b shows a series of 80 µm buckyballs, each printed in 250 ms. The bucky balls show a good reproducibility and overall structural quality. Finally, in panel c, a stitched fleet of five #3DBenchy[7] boats is printed, which allows for comparison with many other 3D printing approaches. Each boat fits into one printing field and is printed within 266 ms. At the base of the boat, a rippled structure can be seen, which is attributed to the standing wave pattern generated by the reflected light-sheet (compare Figure 8.5). Overall, the boat is more challenging to print than the other presented structures since its bulky hull has a filling fraction of 100 %, leading to proximity effects in adjacent layers. To pre-compensate this over-exposure, the blue laser beam intensity is reduced in areas of high filling fraction by displaying gray-scaled slices on the LCOS display. This proximity effect prohibits also the printing of larger structures, for which parts of the photoresin outside the focal plane start to polymerize, distorting the projected image.

Examples of 3D printed metamaterial structures are shown in the scanning electron micrographs in Figure 8.11. Panel a shows three stacked pairs of a chiral metamaterial unit cell, which are printed in one printing field, i.e., without stitching. The projected pattern of the two neighboring unit cells is 155 µm wide, covering almost the entire field of view. Despite the homogeneities observed in the light-sheet characterization (see Figure 8.8), no irregularities are observed in the 3D printed structure. The inset reveals the overall good structure quality, with little proximity
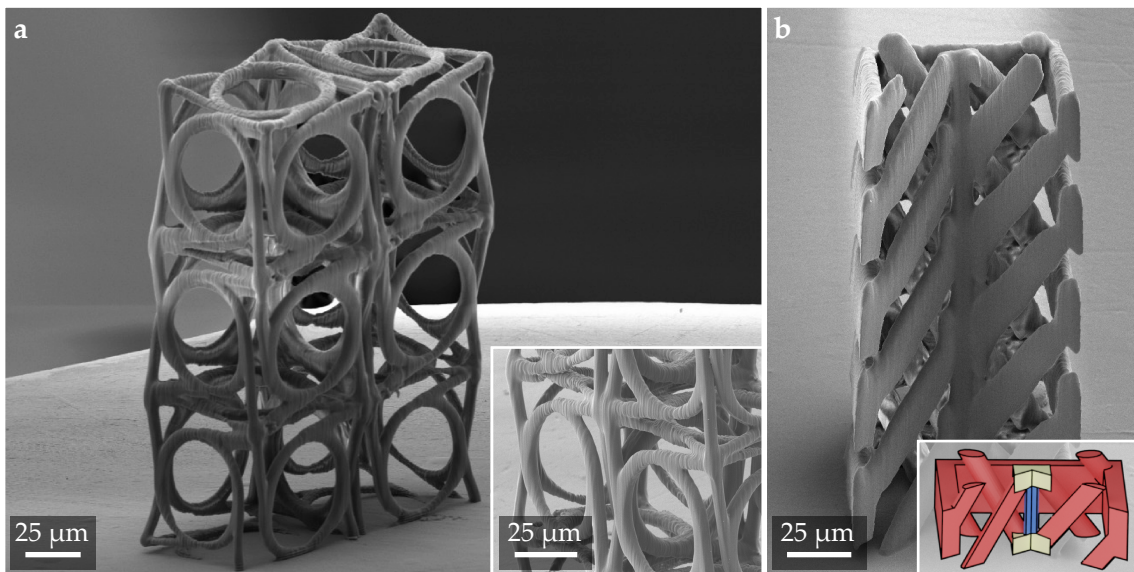
---

[7] www.3dbenchy.com

Figure 8.11: Scanning electron micrographs of 3D light-sheet microprinted metamaterial unit cells. a, Chiral metamaterial unit cells [120]. The inset shows a magnified view. **b**, Five stacked quarter-cut metamaterial unit cells, which were designed to yield a roton-like acoustical dispersion [221]. The inset shows a colored rendering of the unit cell for visual assessment. Adapted from Ref. [12] with permission from Springer Nature.

in locations of high filling fraction. Each unit cell has a side length of 78 µm, making it comparable with the results shown for the multi-focus multi-photon 3D nanoprinting (see chapter 4). In contrast to the *parallelized* multi-photon 3D printing results, where a single unit cell took approximately 1.6 s, all six unit cells shown here are printed in 1.4 s, or 117 ms per unit cell, albeit at the expense of spatial resolution. On further inspection, striation-like artifacts can be observed on the 3D printed structure. This artifact can be speculatively attributed to the static speckle-pattern caused by the multi-mode fiber beam-homogenization.

Panel b shows a stack of five quarter-cut metamaterial unit cells which were originally designed to yield a roton-like acoustic dispersion [221]. This structure is challenging to fabricate by other 3D printing methods like, for instance, multi-photon 3D printing since it contains overhanging structures (see rendered inset), which tend to drift off in the liquid photoresin. These overhanging parts are unproblematic for the presented 3D light-sheet microprinter. The entire stack is printed within 583 ms, offering little time for parts to drift away.

8.3 DISCUSSION

In this chapter, I have presented and characterized a light-sheet 3D microprinter. Starting from initial requirements and design considerations, a complete setup was designed and assembled from scratch. The optical performance of the setup was characterized in ray tracing calculations and in beam measurements. Finally, 3D structures were fabricated to benchmark the 3D printer's spatial resolution, peak printing rate, and versatility.

As can be seen from the benchmark diagram in Figure 2.1, the achieved voxel printing rate of $7 \cdot 10^6 \, \mathrm{voxels\, s^{-1}}$ stands in the forefront with other high-speed 3D printing approaches, and the obtained voxel size of $0.55 \, \mu m^3$ is two orders of magnitude smaller than that of the only other presented light-sheet 3D printer [11].

The primary objective of light-sheet 3D microprinting is a high printing rate. Starting from the existing setup, there are two general options to increase the printing rate further. Either each voxel is exposed shorter, or more voxels are exposed in parallel. Both options are discussed.

The first option, a decreased exposure time, is currently limited by the available light-sheet laser power. Hence, either higher laser intensities are necessary, or the photoresin must become more sensitive, i.e., possess lower threshold intensities. As discussed in subsection 8.1.2, powerful lasers in the red spectral region are scarce, especially with a single-transverse-mode beam. Hence, a better way to decrease the exposure time might be to increase the sensitivity of the photoresin. In this regard, the quencher molecule TEMPO introduced in the photoresin is an unfortunate necessity. On the one hand, it reduces the one-photon triggered side reaction and increases the resin's threshold contrast. On the other hand, it leads to a higher polymerization threshold intensities. Therefore, finding a two-color two-step initiator that suffers less from the one-photon triggered reaction could indirectly lead to a more sensitive photoresin.
Furthermore, the sensitivity of the photoresin can be raised by modifying the photoinitiator in order to obtain an increased excited-state extinction coefficient. Conversely, the excited-state absorption spectrum of the two-color two-step photoinitiator can be shifted to a wavelength where more powerful lasers are readily available, e.g., to the wavelength $532 \, \mathrm{nm}$. Directions on shifting the excited-state spectrum can be taken from the literature [222].
Finally, the photoresin can be sensitized by increasing the intermediate-state lifetime. Ideally, the excited-state lifetime should equal the voxel exposure time. From the characterization experiments in section 7.4, it is known that the intermediate-state lifetime is lower than $300 \, \mu s$ and hence more than a magnitude shorter than the voxel exposure time.

For the second option, i.e., increasing the amount of simultaneously exposed voxels, again, either a more sensitive photoresin or more powerful lasers are needed. Moreover, the optics need to be adapted. In the presented projection path, one resolved projected laser focus covers the area of nine pixels. This can be easily changed by decreasing the magnification of the projection telescope. However, a lower magnification is only half the share since the voxel size that is resolved by the photoresin is yet larger and covers the area of 64 pixels in the presented setup. Improved photoresin formulations that are less prone to proximity effects could help, for instance by going to less viscous photoresin formulations, for which it is known from multi-photon printing, that higher resolutions can be achieved [61].

To really benefit from a high printing rate, the printing time itself should represent the largest share of processing time. As with every 3D printing approach, there is overhead: setting up the printer, positioning of the sample holder, and development. Currently, this overhead takes 15 min, which is much longer than the typical second-long printing time itself. Thus, these processing steps should be automated.

Finally, the presented photoresin effectively limits the maximum size of the printed structures. After prolonged printing times, the photoresin polymerizes in out-of-focus locations due to proximity effects, which are caused by a single-color triggered polymerization reaction. Ideally, a two-color two-step photoinitiator with a completely inert intermediate state can be identified. Therefore, the nature of this reaction should be clarified (see section 7.5). However, there is also a pragmatic solution to avoid the out-of-focus dose accumulation by adding a microfluidic photoresin flushing system to the setup [223]. Yet a further way to suppress the intermediate state reaction in out-of-focus areas could be achieved by using selectively activated photoinhibitors or by replacing the glass coverslip at the cuvette base by an oxygen-permeable window as is the case in CLIP [37, 224]. The in-diffusing oxygen scavenges radicals in out-of-focus planes and thereby suppresses proximity effects [225].

Two-color two-step photoinitiators could also be useful in applications besides light-sheet 3D microprinting, for instance in CAL, where a photoresin is exposed to projections of the printed object from many angles. Exposing the photoresin simultaneously with beams of two different wavelengths incident from different directions can be used to decrease the voxel size and hence to increase the resolution [226].

9 | Chapter 9
CONCLUSIONS AND OUTLOOK

In the scope of this thesis, I have conceived and demonstrated concepts for fast and affordable additive manufacturing of 3D structures on the micro- and nanoscale. Starting from the original goal for the thesis, "conceptual development of 3D laser lithography", aiming at a parallelized multi-photon 3D nanoprinting, the ideas of two-step absorption and light-sheet 3D printing evolved.

In **chapter 2**, I have reviewed different state-of-the-art 3D printing technologies in terms of voxel size and voxel printing rate. Based on these two figures of merit, various 3D printing approaches can be universally benchmarked in terms of printing resolution and printing speed. From this benchmark, two aspects became clear. First, despite the serial voxel exposure in focus-scanning 3D printing methods, they are not inferior in their voxel printing rate compared to projection- or tomography-based 3D printing techniques. Second, so far, instances of *multi-focus* multi-photon 3D printing have been slower in their voxel printing rate than the fastest single-focus multi-photon printer.
Next, I introduced the threshold model and the accumulation model. Together, both models describe the photoresin response in photopolymerization 3D printing. I then defined the voxel size using the threshold, the accumulation model, and the generalized Sparrow resolution criterion.

In **chapter 3**, I have explained that the parallelization in previous works in multi-focus multi-photon 3D printing was at the expense of drastically reduced focus scan speeds. I further argued that for fixed laser power, a maximum printing rate is achieved by single-focus scanning. However, for galvanometer-based scanning, the printing rate is limited by the scan speed and not by the available laser power, allowing some degree of parallelization. Hence, a custom multi-focus multi-photon 3D printing setup comprising water-cooled high-speed galvanometer mirrors and a field-programmable gate array (FPGA) control unit was built. In this setup, a multi-photon-printed diffractive optical element (DOE) was used to split the laser beam into an array of 3×3 beamlets. Importantly, the angular dispersion of this diffractive beam splitter was compensated using a refractive

telescope.

In **chapter 4**, I have presented centimeter-scale chiral 3D metamaterial crystals containing more than 10^5 large cubic unit cells printed on the multi-focus 3D printing setup. In comparison, previous studies achieved less than 10^3 unit cells in a comparable printing time. The combination of the achieved printing rate approaching 10^7 voxels s^{-1} and the sub-micrometer voxel sizes exceed previous best figures of merit. Furthermore, metamaterial crystals comprised of modified unit cells, which are tailored to yield large twist angles, were printed. Characterization experiments showed the expected twist behavior upon compression, even for the largest samples.

The fabrication throughput of the multi-focus 3D printed crystals was limited by three factors: available laser power, scan speed, and the diffraction-limited field of view of the used optical components. In an outlook, I have presented an idea for a simple power-efficient beam splitter, which can be used to increase the number of simultaneously scanned laser foci further. However, the damage threshold of the used optical components ultimately limits the laser power and thus the throughput.

In **chapter 5**, I have presented the idea of one-color two-step-absorption 3D printing as an alternative to multi-photon 3D printing. In contrast to multi-photon 3D printing, two-step-absorption 3D printing does not depend on bulky and expensive ultrashort pulsed laser sources but is compatible with compact and affordable semiconductor diode lasers. Two-step-absorption 3D printing relies on the sequential absorption of two photons by a suitable photoinitiator molecule. Based on rate-model calculations, I have derived a condition for the required nonlinear optical response of two-step-absorption photoinitiators. One central result was that the intermediate-state lifetime must be shorter than the voxel exposure time. Based on this criterion and five further criteria, two photoinitiator molecule candidates were pre-selected.

In **chapter 6**, I have introduced the two-step-absorption photoinitiator candidate benzil. I have explained that benzil violates one of the six criteria for good two-step-absorption initiators, leading to an undesired one-photon-triggered reaction in a photoresin. To suppress this side reaction, a suitable quencher molecule was identified and added to the photoresin mixtures. Using a 405 nm laser diode, I characterized the benzil-containing photoresins in point-exposure threshold power experiments. The measured threshold power behavior was in good agreement with the expected threshold power behavior of the rate-model calculations, from which I have derived an intermediate-state lifetime of approximately 80 μs.

To quantify the 2D printing resolution of the two-step absorption photoresin, I have printed line gratings. The printed gratings were well resolved, even below $a = 125$ nm lattice constant. However, line gratings are of limited use to assess the

3D resolution. In contrast, woodpile photonic crystals consisting of densely spaced rods in all three dimensions are a genuine 3D printing challenge and an established resolution benchmark in 3D nanoprinting. Therefore, I have printed an array of woodpile photonic crystals with lateral rod spacings in the range of $a = 225\,\text{nm}$ to $a = 450\,\text{nm}$. We have seen that even the most demanding printed woodpile with $a = 225\,\text{nm}$ appeared bright and colorful in optical microscope images, indicating well-resolved 3D structures. Electron micrographs of ultrathin cuts were prepared to confirm that the structure's interior is well resolved. No signs of proximity were observed in the electron micrographs. Finally, I have fabricated a variety of 3D microstructures to showcase the flexibility of the approach. Remarkably, buckyball structures with $5\,\mu\text{m}$ diameter were excellently resolved, and also, the cubic chiral metamaterial structure could be printed with a lattice constant of $16\,\mu\text{m}$. However, some proximity effect was observed for rapidly scanned of voluminous structures. The structures were printed at printing rates of close to $2 \cdot 10^4$ voxels s^{-1} and with laser powers of a few hundred microwatts. Notably, these results were attained with a pinhead-sized continuous-wave (cw) laser diode, the price of which is a thousandth of the price of an ultrashort pulsed Ti:Sa laser used in multi-photon 3D printing.

The orders of magnitude lower polymerization laser powers necessary in two-step absorption than in multi-photon absorption 3D printing offer the possibility for drastic parallelization, for example, using projection-based approaches. I have argued that projecting large areas into a one-color two-step-absorption photoresin leads to a loss of the axial intensity confinement and thereby to a loss of axial resolution. As a solution to this problem, I have introduced the concept of light-sheet 3D printing in [chapter 7](). Light-sheet 3D printing relies on two-color two-step-absorption photoinitiators with non-overlapping ground-state and intermediate-state spectra. I have explained why a two-color two-step-absorption photoinitiator with short intermediate-state lifetime is necessary for high-resolution 3D printing with high voxel printing rates.

I have characterized the two-step photoinitiator candidate biacetyl in photoresin mixtures in comprehensive two-color polymerization-threshold experiments. One central finding was that, as for benzil, an intermediate-state triggered polymerization reaction exists. This reaction has less impact during short exposures, in low-viscous monomers, and for photoresins that contain the quencher molecule (2,2,6,6-tetramethylpiperidin-1-yl)oxyl (TEMPO). I have confirmed the two-color two-step absorption behavior by measuring the two-color polymerization threshold for different red laser beam wavelengths. We found that the measured polymerization threshold spectrum contains the characteristic features of the excited-state spectrum of biacetyl. Furthermore, I have derived the upper bound of $300\,\mu\text{s}$ for biacetyl's intermediate-state lifetime in the photoresin by performing pulsed-excitation experiments.

From this data and literature reports, I have discussed the possible mechanisms for the single-color-triggered polymerization, concluding that radicals are formed most likely in a hydrogen-abstraction reaction. Based on our observations, I have argued that the triplet-triplet-annihilation reaction does not lead to the formation of radicals but effectively acts as a quenching mechanism.

Finally, I have presented a rate model which reproduced the measured polymerization threshold behavior and agreed with the interpretations of the single-color polymerization mechanism.

In chapter 8, I have laid out the design considerations for a light-sheet 3D microprinting setup tailored for the biacetyl two-color two-step photoresins. I have explained the compromise between a thin light-sheet and a large printing area. Next, I have presented the components of the light-sheet 3D microprinter and subsequently characterized the light-sheet beam, for which a full-width half-maximum (FWHM) thickness of 3.5 μm was measured. Finally, 3D microstructures were printed using this light-sheet printer. I have first characterized the attainable voxel size by printing suspended line arrays. Based on the measured lateral voxel size of 0.55 μm, a voxel printing rate of $7 \cdot 10^6$ voxels s^{-1} was derived. To demonstrate the versatility of the light-sheet 3D printer, I have printed several 3D microstructures. For most structures, the exposure of one stitching block was finished in a few hundred microseconds. Entire jobs, comprised of several stitched printing fields, were printed in about a second.

Outlook

In the discussions in chapter 4, chapter 6, and chapter 8, I have provided perspectives for future developments of multi-focus multi-photon 3D microprinting, two-step-absorption 3D nanoprinting, and light-sheet 3D microprinting, respectively. Here, I discuss the impact on possible future applications, challenges and adoptions.

Using advanced beam splitting methods and improved photoresin formulations, fast multi-photon 3D printing with as many as 49 foci is imminent, allowing for voxel printing rates well beyond ten million voxels per second at sub-micrometer voxel sizes. The fabrication of large-scale metamaterials will naturally profit of multi-focus 3D printers, bringing metamaterials closer to real-world applications. But it is also the field of 3D printing which profits by metamaterial research. While the material palette in 3D printing has grown steadily, it is admittedly still limited [1]. One possibility to enhance the material palette is pointed out in the review on 3D metamaterials by Kadic et al. [121]. Since metamaterials allow to achieve effective material parameters beyond the properties of the ingredient materials, dissimilar material properties can be obtained by the substructure of

the printed part.

However, when printing with yet higher printing rates, the photoresin becomes rapidly depleted of oxygen, which is critical for high-resolution 3D printing [60]. In-situ microfluidic photoresin replenishment can help to elude this problem [223]. Alternatively, oxygen-insensitive photoresin formulations might become an attractive alternative to the acrylic photoresins used herein [227, 228].

Printing with yet more foci requires new, more sensitive photoresin formulations [83]. Importantly, finding photoinitiators with large multi-photon-absorption cross sections is insufficient. Rather, the the entire polymerization process must be taken into account [195].

The concept of two-step-absorption 3D nanoprinting results in a massive reduction in the cost and size of 3D nanoprinters, which leads to a democratization of the field [229]. Admittedly, it is currently not expected that 3D nanoprinters find their way into many private households. It is very likely, however, that more research institutes will adopt 3D nanoprinting due to the more affordable device cost. In fact, most laser scanning microscopes already contain the suitable laser sources and optics for two-step-absorption 3D printing. Through the broad dissemination of the technique, new, yet unforeseen ideas and applications will emerge.

Furthermore, the affordable device cost also fosters conceptual developments in two-step-absorption 3D nanoprinting. One route could be the development of photoresins suitable for diffraction-unlimited printing via stimulated emission-depletion (STED), enabling yet finer 3D nanoprinting.

Using light-sheet 3D microprinting, competitive 3D printing rates have been demonstrated from the beginning. Looking ahead, this technology has the potential to boost 3D printing rates well beyond the current state-of-the-art. Currently, the printing rate is not limited by the photoinitiator's intermediate-state lifetime anymore, but by the necessary threshold laser powers. If this bottleneck is eliminated, the presented setup allows for printing rates of up to $1920 \times 1080 \times 720 \, \text{voxels} \, \text{s}^{-1} = 1.5 \cdot 10^9 \, \text{voxels} \, \text{s}^{-1}$. Translated to the chiral meta-material crystal made of 10^5 unit cells, this printing rate reduces the two day long printing time that the multi-focus multi-photon 3D printer needed to less than 30 minutes.

For small samples, the fabrication time is dominated by sample handling and setup of the 3D printer. Automating these process steps allows light-sheet 3D printing to compete with the manufacturing times in injection molding.

Another barrier for widespread application of light-sheet 3D printing are proximity effects. With improved photoresin formulations, the impact of proximity effects will be reduced. Alternatively solutions include in-situ monitoring of the printing process and machine learning to predict and pre-compensate proximity effects.

Similar to Moore's law for the transistor density in semiconductor chips, a group proposes a biannually doubling of the printing rate in 3D printing [230], bringing additive manufacturing closer to mass production and a new industrial revolution. Ultimately, the vision for scalable additive is being able to rapidly print micro- or nanostructured parts on the meter scale and beyond. However, even with orders-of-magnitude boosted 3D printing rates, this goal is not in reach for any 3D printing technique in the near future. Consider the example of a $1\,\text{m}^3$ large part printed with $100\,\text{nm}$-sized voxels, which contains 10^{21} voxels – equivalent to the information content of one zettabit [83]. Appropriate data storage and transfer solutions for this amount of data are currently elusive. Combining additive manufacturing with controlled self-assembly is one suggested solution [83].

Looking back at the time when I started working with multi-photon 3D micro- and nanoprinting, I had the impression that the field was completely developed and that there was little left to be discovered. As I have learned firsthand, the opposite is true, and we are just at the beginning of fascinating advancements.

A Appendix A

A APPENDIX

A.1 Lens Data for the Multi-Focus Setup

Table A.1: Lens data for the lens group LG1 in Figure 3.9. The column "lens name" indicates the lens name of the Thorlabs GmbH lens catalog. Column r denotes the radius of curvature, d is the thickness. This table is adapted from Ref. [48] (CC BY 4.0).

#	lens name	r / mm	d / mm	material
1	LC1093-B	-51.46	4.00	N-BK7
2		infinity	6.71	
3	LC1093-B	-51.46	4.00	N-BK7
4		infinity	2.73	
5		-119.32	7.29	N-BK7
6	LE1418-B	-47.87	0.00	
7		infinity	6.18	N-BK7
8	LA1979-B	-103.01	1.19	
9		infinity	8.22	N-BK7
10	LA1384-B	-64.38	150.00	
11	LA1727-B	386.31	3.83	N-BK7

A.2 Solutions of the One-Color Two-Step-Absorption Rate-Equation System

The differential equation system 5.2, 5.3, and 5.4 are solved using the software Wolfram Mathematica. All rate coefficients are expressed in units of k_D, the time t is in units of k_D^{-1}.

$$[\mathrm{A}]\,(k_1, k_2, t) = \frac{e^{-\frac{1}{2}t(k_1+k_2+k_\mathrm{X}+1)}}{2k_\mathrm{X}}$$
$$\cdot \left(e^{k_\mathrm{X}t} \left(-k_1 + k_2 + k_\mathrm{X} + 1\right) + k_1 - k_2 + k_\mathrm{X} - 1 \right), \tag{A.1}$$

$$[\mathrm{B}]\,(k_1, k_2, t) = \frac{e^{-\frac{1}{2}t(k_1+k_2+k_\mathrm{X}+1)}}{k_\mathrm{X}} \left(k_1 e^{k_\mathrm{X}t} - k_1 \right), \tag{A.2}$$

$$[\mathrm{C}]\,(k_1, k_2, t) = \frac{e^{-\frac{1}{2}t(k_1+k_2+k_\mathrm{X}+1)}}{2k_\mathrm{X}}$$
$$\cdot \left(e^{k_\mathrm{X}t} \left(-k_1 - k_2 - k_\mathrm{X} - 1\right) + k_1 + k_2 - k_\mathrm{X} + 1 \right) + 1, \tag{A.3}$$

with the substitution

$$k_\mathrm{X} = \sqrt{(k_1 + k_2 + 1)^2 - 4k_1 k_2}. \tag{A.4}$$

A.3 LENS DATA FOR THE LIGHT-SHEET SETUP

Light-Sheet Path

Table A.2: Optical path of the light-sheet beam. The value of α denotes the angle between the toroidal lens's cylinder-axis rotation and the y-axis of the system. Note that the light-sheet beam propagates in the $-x$ direction. The radius and the thickness of the elements are given by the values of r and d, respectively. The distances between the lenses are obtained by optimizing the light-sheet uniformity since the optimal distances highly depend on the laser beam diameter. The column "conic" denotes the conic constant of the element. This table is adapted from Ref. [12].

#	type	component	α / °	r / mm	d / mm	material	conic
1	toroidal	LOCP-8.9R01-0.8	90	23.0	7.62	N-BK7	−2 700
2	standard		90	infinity	120		0
3	standard	LA1131-A-ML	0	25.7	5.34	N-BK7	0
4	standard		0	infinity	160		0
5	toroidal		90	infinity	4.46	N-BK7	0
6	toroidal	LJ1629RM-A	90	−77.5	90		0
7	toroidal		0	infinity	6.53	N-BK7	0
8	toroidal	LJ1267RM-A	0	−129.0	120		0

Projection Path

Table A.3: Optical path of the projection beam. The values of r and d are defined as in Table A.2. In ray-tracing calculations, the Zeiss 20× objective is substituted by a paraxial (thin) lens with a focal length $f = 8.25\,\text{mm}$. For the Zeiss 63× objective, lens data from a patent text of a lens with matching characteristics is used [219]. All distances are optimized in the software Zemax OpticStudio. This table is adapted from Ref. [12].

| #	type	component	r / mm	d / mm	material
1	standard	fiber facet	infinity	8.25	
2	paraxial	Zeiss 20×/0.5	—	8.25	proprietary
3	standard	PBS1	infinity	25.40	N-SF1
4	standard		infinity	22.00	
5	standard	$\lambda/2$	infinity	1.76	quartz
6	standard		infinity	110.00	
7	standard	TL1	91.62	5.70	N-BK7
8	standard	TL1	−66.68	2.20	SF5
9	standard		−197.70	10.34	
10	standard	PBS2	infinity	25.40	N-SF1
11	standard		infinity	31.50	
12	standard	$\lambda/4$	infinity	1.75	quartz
13	standard		infinity	88.54	
14	mirror	LCD	infinity	0.00	
15	standard		infinity	88.54	
16	standard	$\lambda/4$	infinity	1.75	quartz
17	standard		infinity	31.50	
18	standard	PBS2	infinity	25.40	N-SF1
19	standard		−77.50	11.00	
20	standard	ITL200	—	28.00	proprietary
21	standard		infinity	246.36	
22	paraxial	Zeiss 63×/1.2	—	45.00	proprietary

A.4 LIGHT-SHEET HEIGHT
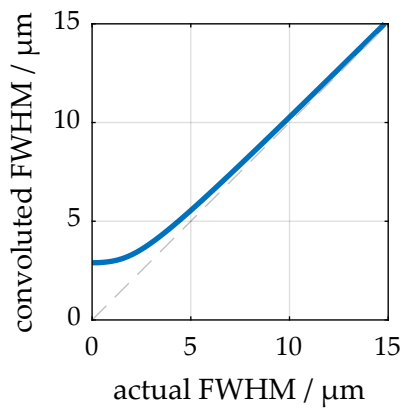
Figure A.1: Calibration curve for the measured light-sheet FWHM-height. The measured (i.e. convoluted) FWHM-height is plotted on the vertical axis against the actual FWHM-height of a gaussian light-sheet beam. The dashed line with slope 1 is a guide for the eye. Due to the camera's finite pixel size of $3.45 \times 3.45\,\mu m^2$, the light-sheet beam height is overestimated, especially for small actual light-sheet heights. Adapted from Ref. [12] with permission from Springer Nature.

Bibliography

[1] I. Gibson, D. Rosen, B. Stucker, and M. Khorasani, *Additive Manufactur-ing Technologies* (Springer International Publishing, Cham, 2021) (cited on pages 5, 6, 158).

[2] C. W. Hull, "Apparatus for Production of Three-Dimensional Objects by Stereolithography", U.S. pat. 4575330 A (Uvp, Inc., Mar. 11, 1986) (cited on pages 5, 14).

[3] W. Associates, ed., *Wohlers Report 2021: 3D Printing and Additive Manu-facturing State of the Industry Annual Worldwide Progress Report* (Wohlers Associates, Fort Collins (Colo.), 2021) (cited on pages 5, 6, 15).

[4] F. Willème, "Photographing Sculpture", U.S. pat. 43822A (Aug. 9, 1864) (cited on page 5).

[5] B. E. Kelly, I. Bhattacharya, H. Heidari, M. Shusteff, C. M. Spadaccini, and H. K. Taylor, "Volumetric Additive Manufacturing via Tomographic Reconstruction", Science **363**, 1075 (2019) (cited on pages 5, 10, 15, 17, 137).

[6] D. Loterie, P. Delrot, and C. Moser, "High-Resolution Tomographic Volu-metric Additive Manufacturing", Nature Communications **11**, 1–6 (2020) (cited on pages 5, 10, 15, 137).

[7] K. L. Agnew, "Photographic Reproduction by Discrete Intersecting Rays with Compression in the Third Dimension", U.S. pat. 3544402A (Battelle Development Corp, Dec. 1, 1970) (cited on page 5).

[8] W. K. Swainson, "Verfahren Und Material Zur Herstellung Von Dreidimen-sionalen Figur", German pat. 1797599 (A1) (Swainson Wyn Kelly, Aug. 29, 1974) (cited on pages 5, 15).

[9] V. Hahn, F. Mayer, M. Thiel, and M. Wegener, "3-D Laser Nanoprinting", Optics and Photonics News **30**, 28–35 (2019) (cited on pages 5, 15, 72, 130).

[10] V. Hahn, P. Müller, E. Blasco, and M. Wegener, "Parallelisierte 3D-Lithogra-phie mittels mehrstrahliger, mehrfarbiger lichtinduzierter Polymerisation", European pat. 2019078557W (Karlsruher Institut für Technologie, June 25, 2020) (cited on pages 5, 15, 130).

[11] M. Regehly, Y. Garmshausen, M. Reuter, N. F. König, E. Israel, D. P. Kelly, C.-Y. Chou, K. Koch, B. Asfari, and S. Hecht, "Xolography for Linear Volumetric 3D Printing", Nature **588**, 620–624 (2020) (cited on pages 5, 10, 15, 17, 130, 137, 148, 152).

[12] V. Hahn, P. Rietz, F. Hermann, P. Müller, C. Barner-Kowollik, T. Schlöder, W. Wenzel, E. Blasco, and M. Wegener, "Light-Sheet 3D Microprinting via Two-Colour Two-Step Absorption", Nature Photonics, accepted for publication (2022) (cited on pages 5, 10, 15, 102, 105, 106, 110, 112, 113, 115, 117, 119, 122, 124–126, 131, 140, 141, 144, 146, 149–151, 163–165).

[13] B. Berman, "3-D Printing: The New Industrial Revolution", Business Horizons **55**, 155–162 (2012) (cited on pages 5, 6).

[14] S. Maruo, O. Nakamura, and S. Kawata, "Three-Dimensional Microfabrication with Two-Photon-Absorbed Photopolymerization", Optics Letters **22**, 132 (1997) (cited on pages 6, 11).

[15] ISO/ASTM 52900:2021, *Additive Manufacturing — General Principles — Fundamentals and Vocabulary*, Standard, Nov. 2021 (cited on pages 9, 20).

[16] J.-i. Kato, N. Takeyasu, Y. Adachi, H.-B. Sun, and S. Kawata, "Multiple-Spot Parallel Processing for Laser Micronanofabrication", Applied Physics Letters **86**, 044102 (2005) (cited on pages 10, 12, 30, 35).

[17] G. M. Gratson, F. García-Santamaría, V. Lousse, M. Xu, S. Fan, J. A. Lewis, and P. V. Braun, "Direct-Write Assembly of Three-Dimensional Photonic Crystals: Conversion of Polymer Scaffolds to Silicon Hollow-Woodpile Structures", Advanced Materials **18**, 461–465 (2006) (cited on pages 10, 13).

[18] X.-Z. Dong, Z.-S. Zhao, and X.-M. Duan, "Micronanofabrication of Assembled Three-Dimensional Microstructures by Designable Multiple Beams Multiphoton Processing", Applied Physics Letters **91**, 124103 (2007) (cited on pages 10, 30, 35, 39).

[19] H. Plank, C. Gspan, M. Dienstleder, G. Kothleitner, and F. Hofer, "The Influence of Beam Defocus on Volume Growth Rates for Electron Beam Induced Platinum Deposition", Nanotechnology **19**, 485302 (2008) (cited on page 10).

[20] Stratasys, Ltd., *Fortus 360MC*, 2008 (cited on page 10).

[21] J. Go, S. N. Schiffres, A. G. Stevens, and A. J. Hart, "Rate Limits of Additive Manufacturing by Fused Filament Fabrication and Guidelines for High-Throughput System Design", Additive Manufacturing **16**, 1–11 (2017) (cited on page 10).

[22] J. Fischer and M. Wegener, "Three-Dimensional Direct Laser Writing Inspired by Stimulated-Emission-Depletion Microscopy [Invited]", Optical Materials Express **1**, 614–624 (2011) (cited on pages 10, 58, 92–95, 98).

[23] S. D. Gittard, A. Nguyen, K. Obata, A. Koroleva, R. J. Narayan, and B. N. Chichkov, "Fabrication of Microscale Medical Devices by Two-Photon Polymerization with Multiple Foci via a Spatial Light Modulator", Biomedical Optics Express **2**, 3167–3178 (2011) (cited on pages 10, 30, 35, 39).

[24] Stratasys, Ltd., *Mojo*, 2012 (cited on page 10).

[25] X. Zheng, J. Deotte, M. P. Alonso, G. R. Farquar, T. H. Weisgraber, S. Gemberling, H. Lee, N. Fang, and C. M. Spadaccini, "Design and Optimization of a Light-Emitting Diode Projection Micro-Stereolithography Three-Dimensional Manufacturing System", Review of Scientific Instruments **83**, 125001 (2012) (cited on pages 10, 14, 15).

[26] X. Zheng, H. Lee, T. H. Weisgraber, M. Shusteff, J. DeOtte, E. B. Duoss, J. D. Kuntz, M. M. Biener, Q. Ge, J. A. Jackson, S. O. Kucheyev, N. X. Fang, and C. M. Spadaccini, "Ultralight, Ultrastiff Mechanical Metamaterials", Science **344**, 1373–1377 (2014) (cited on page 10).

[27] X. Zheng, W. Smith, J. Jackson, B. Moran, H. Cui, D. Chen, J. Ye, N. Fang, N. Rodriguez, T. Weisgraber, and C. M. Spadaccini, "Multiscale Metallic Metamaterials", Nature Materials **15**, 1100–1106 (2016) (cited on pages 10, 14, 51).

[28] M. Shusteff, A. E. M. Browar, B. E. Kelly, J. Henriksson, T. H. Weisgraber, R. M. Panas, N. X. Fang, and C. M. Spadaccini, "One-Step Volumetric Additive Manufacturing of Complex Polymer Structures", Science Advances **3**, eaao5496 (2017) (cited on pages 10, 15).

[29] 3D Systems Corporation, *ProJet 7000 HD, Vendor Information*, 2012 (cited on page 10).

[30] Nanoscribe GmbH & Co. KG, *Photonic Professional GT*, 2014 (cited on page 10).

[31] T. Bückmann, M. Thiel, M. Kadic, R. Schittny, and M. Wegener, "An Elasto-Mechanical Unfeelability Cloak Made of Pentamode Metamaterials", Nature Communications **5**, 4130 (2014) (cited on pages 10, 57).

[32] E. B. Duoss, T. H. Weisgraber, K. Hearon, C. Zhu, W. Small, T. R. Metz, J. J. Vericella, H. D. Barth, J. D. Kuntz, R. S. Maxwell, C. M. Spadaccini, and T. S. Wilson, "Three-Dimensional Printing of Elastomeric, Cellular Architectures with Negative Stiffness", Advanced Functional Materials **24**, 4905–4913 (2014) (cited on pages 10, 13).

[33] Stratasys, Ltd., *Objet 500 Connex1*, 2014 (cited on pages 10, 14).

[34] L. Yang, A. El-Tamer, U. Hinze, J. Li, Y. Hu, W. Huang, J. Chu, and B. N. Chichkov, "Parallel Direct Laser Writing of Micro-Optical and Photonic Structures Using Spatial Light Modulator", Optics and Lasers in Engineering **70**, 26–32 (2015) (cited on pages 10, 30, 35, 39).

[35] W. Yan, B. P. Cumming, and M. Gu, "High-Throughput Fabrication of Micrometer-Sized Compound Parabolic Mirror Arrays by Using Parallel Laser Direct-Write Processing", Journal of Optics **17**, 075803 (2015) (cited on pages 10, 30, 35, 39).

[36] Ultimaker BV, *Ultimaker 2 Extended*, 2015 (cited on page 10).

[37] J. R. Tumbleston, D. Shirvanyants, N. Ermoshkin, R. Janusziewicz, A. R. Johnson, D. Kelly, K. Chen, R. Pinschmidt, J. P. Rolland, A. Ermoshkin, E. T. Samulski, and J. M. DeSimone, "Continuous Liquid Interface Production of 3D Objects", Science **347**, 1349–1352 (2015) (cited on pages 10, 15, 153).

[38] EOS GmbH, *FORMIGA P 110 with PA 2200 Top Quality 1.0, Datasheet and Vendor Information*, 2016 (cited on pages 10, 13).

[39] EOS GmbH, *P 770 with PA 2200 Top Speed 1.0, Datasheet and Vendor Information.* 2016 (cited on pages 10, 13).

[40] Hewlett-Packard Company, *JetFusion 3D 4210*, 2017 (cited on page 10).

[41] B. W. Pearre, C. Michas, J.-M. Tsang, T. J. Gardner, and T. M. Otchy, "Fast Micron-Scale 3D Printing with a Resonant-Scanning Two-Photon Microscope", Additive Manufacturing **30**, 100887 (2019) (cited on pages 10, 30, 33).

[42] L. Keller and M. Huth, "Pattern Generation for Direct-Write Three-Dimensional Nanoscale Structures via Focused Electron Beam Induced Deposition", Beilstein Journal of Nanotechnology **9**, 2581–2598 (2018) (cited on pages 10, 12).

[43] W. Chu, Y. Tan, P. Wang, J. Xu, W. Li, J. Qi, and Y. Cheng, "Centimeter-Height 3D Printing with Femtosecond Laser Two-Photon Polymerization", Advanced Materials Technologies **3**, 1700396 (2018) (cited on page 10).

[44] Q. Geng, D. Wang, P. Chen, and S.-C. Chen, "Ultrafast Multi-Focus 3-D Nano-Fabrication Based on Two-Photon Polymerization", Nature Communications **10**, 2179 (2019) (cited on pages 10, 30, 35).

[45] A. Reiser, M. Lindén, P. Rohner, A. Marchand, H. Galinski, A. S. Sologubenko, J. M. Wheeler, R. Zenobi, D. Poulikakos, and R. Spolenak, "Multi-Metal Electrohydrodynamic Redox 3D Printing at the Submicron Scale", Nature Communications **10**, 1853 (2019) (cited on pages 10, 13).

[46] D. A. Walker, J. L. Hedrick, and C. A. Mirkin, "Rapid, Large-Volume, Thermally Controlled 3D Printing Using a Mobile Liquid Interface", Science 366, 360–364 (2019) (cited on pages 10, 15).

[47] S. K. Saha, D. Wang, V. H. Nguyen, Y. Chang, J. S. Oakdale, and S.-C. Chen, "Scalable Submicrometer Additive Manufacturing", Science 366, 105–109 (2019) (cited on pages 10, 12, 37).

[48] V. Hahn, P. Kiefer, T. Frenzel, J. Qu, E. Blasco, C. Barner-Kowollik, and M. Wegener, "Rapid Assembly of Small Materials Building Blocks (Voxels) into Large Functional 3D Metamaterials", Advanced Functional Materials 30, 1907795 (2020) (cited on pages 10, 31, 34, 44, 46, 50–53, 130, 149, 161).

[49] C. Maibohm, O. F. Silvestre, J. Borme, M. Sinou, K. Heggarty, and J. B. Nieder, "Multi-Beam Two-Photon Polymerization for Fast Large Area 3D Periodic Structure Fabrication for Bioapplications", Scientific Reports 10, 8740 (2020) (cited on pages 10, 30, 35, 39).

[50] G. Ercolano, T. Zambelli, C. van Nisselroy, D. Momotenko, J. Vörös, T. Merle, and W. W. Koelmans, "Multiscale Additive Manufacturing of Metal Microstructures", Advanced Engineering Materials 22, 1900961 (2020) (cited on pages 10, 13).

[51] W. Jung, Y.-H. Jung, P. V. Pikhitsa, J. Feng, Y. Yang, M. Kim, H.-Y. Tsai, T. Tanaka, J. Shin, K.-Y. Kim, H. Choi, J. Rho, and M. Choi, "Three-Dimensional Nanoprinting via Charged Aerosol Jets", Nature 592, 54–59 (2021) (cited on pages 10, 13).

[52] P. Somers, Z. Liang, J. E. Johnson, B. W. Boudouris, L. Pan, and X. Xu, "Rapid, Continuous Projection Multi-Photon 3D Printing Enabled by Spatiotemporal Focusing of Femtosecond Pulses", Light: Science & Applications 10, 199 (2021) (cited on pages 10, 12, 17, 37, 148).

[53] V. Hahn, T. Messer, N. M. Bojanowski, E. R. Curticean, I. Wacker, R. R. Schröder, E. Blasco, and M. Wegener, "Two-Step Absorption Instead of Two-Photon Absorption in 3D Nanoprinting", Nature Photonics 15, 932–938 (2021) (cited on pages 10, 12, 65, 67–69, 71, 81–83, 87, 89–92, 94, 96–99).

[54] D. K. Limberg, J.-H. Kang, and R. C. Hayward, "Triplet–Triplet Annihilation Photopolymerization for High-Resolution 3D Printing", Journal of the American Chemical Society, 10.1021/jacs.1c11022 (2022) (cited on pages 10, 12).

[55] T. Baldacchini, Three-Dimensional Microfabrication Using Two-Photon Polymerization (William Andrew, Oct. 31, 2019), 762 pp. (cited on page 11).

[56] J. H. Strickler and W. W. Webb, "Two-Photon Excitation in Laser Scanning Fluorescence Microscopy", in CAN-AM Eastern '90, Vol. 1398 (Apr. 1, 1991), pp. 107–118 (cited on page 11).

[57] M. Hippler, E. Blasco, J. Qu, M. Tanaka, C. Barner-Kowollik, M. Wegener, and M. Bastmeyer, "Controlling the Shape of 3D Microstructures by Temperature and Light", Nature Communications 10, 232 (2019) (cited on page 11).

[58] E. Blasco, J. Müller, P. Müller, V. Trouillet, M. Schön, T. Scherer, C. Barner-Kowollik, and M. Wegener, "Fabrication of Conductive 3D Gold-Containing Microstructures via Direct Laser Writing", Advanced Materials 28, 3592–3595 (2016) (cited on page 11).

[59] F. Kotz, A. S. Quick, P. Risch, T. Martin, T. Hoose, M. Thiel, D. Helmer, and B. E. Rapp, "Two-Photon Polymerization of Nanocomposites for the Fabrication of Transparent Fused Silica Glass Microstructures", Advanced Materials 33, 2006341 (2021) (cited on page 11).

[60] J. B. Mueller, J. Fischer, F. Mayer, M. Kadic, and M. Wegener, "Polymerization Kinetics in Three-Dimensional Direct Laser Writing", Advanced Materials 26, 6566–6571 (2014) (cited on pages 11, 17, 19, 25, 82, 89–91, 116, 121, 123, 130, 131, 148, 159).

[61] T. Zandrini, N. Liaros, L. J. Jiang, Y. F. Lu, J. T. Fourkas, R. Osellame, and T. Baldacchini, "Effect of the Resin Viscosity on the Writing Properties of Two-Photon Polymerization", Optical Materials Express 9, 2601–2616 (2019) (cited on pages 11, 111, 116, 153).

[62] B. W. Pearre, C. Michas, J.-M. Tsang, T. J. Gardner, and T. M. Otchy, "Fast Micron-Scale 3D Printing with a Resonant-Scanning Two-Photon Microscope", Feb. 26, 2018 (cited on page 11).

[63] A. Egner and S. W. Hell, "Time Multiplexing and Parallelization in Multifocal Multiphoton Microscopy", Journal of the Optical Society of America A 17, 1192 (2000) (cited on pages 12, 38).

[64] A. Egner, V. Andresen, and S. W. Hell, "Comparison of the Axial Resolution of Practical Nipkow-disk Confocal Fluorescence Microscopy with That of Multifocal Multiphoton Microscopy: Theory and Experiment", Journal of Microscopy 206, 24–32 (2002) (cited on pages 12, 38).

[65] S. Akturk, X. Gu, E. Zeek, and R. Trebino, "Pulse-Front Tilt Caused by Spatial and Temporal Chirp", Optics Express 12, 4399–4410 (2004) (cited on pages 12, 33, 36, 37).

[66] V. Hahn and M. Wegener, "Response to 'Comment on Rapid Assembly of Small Materials Building Blocks (Voxels) into Large Functional 3D Metamaterials'", Advanced Functional Materials 30, 2003402 (2020) (cited on pages 12, 20, 37).

[67] I. Utke, P. Hoffmann, and J. Melngailis, "Gas-Assisted Focused Electron Beam and Ion Beam Processing and Fabrication", Journal of Vacuum Science & Technology B: Microelectronics and Nanometer Structures Processing, Measurement, and Phenomena **26**, 1197–1276 (2008) (cited on page 12).

[68] L. Hirt, A. Reiser, R. Spolenak, and T. Zambelli, "Additive Manufacturing of Metal Structures at the Micrometer Scale", Advanced Materials **29**, 1604211 (2017) (cited on page 12).

[69] J. J. Beaman and C. R. Deckard, "Selective Laser Sintering with Assisted Powder Handling", U.S. pat. 4938816A (University of Texas System, July 3, 1990) (cited on page 13).

[70] G. M. Gratson, M. Xu, and J. A. Lewis, "Direct Writing of Three-Dimensional Webs", Nature **428**, 386 (2004) (cited on page 13).

[71] E. B. Duoss, M. Twardowski, and J. A. Lewis, "Sol-Gel Inks for Direct-Write Assembly of Functional Oxides", Advanced Materials **19**, 3485–3489 (2007) (cited on page 13).

[72] T. Bückmann, N. Stenger, M. Kadic, J. Kaschke, A. Frölich, T. Kennerknecht, C. Eberl, M. Thiel, and M. Wegener, "Tailored 3D Mechanical Metamaterials Made by Dip-in Direct-Laser-Writing Optical Lithography", Advanced Materials **24**, 2710–2714 (2012) (cited on pages 16, 51, 84, 88).

[73] T. Gissibl, S. Thiele, A. Herkommer, and H. Giessen, "Sub-Micrometre Accurate Free-Form Optics by Three-Dimensional Printing on Single-Mode Fibres", Nature Communications **7**, 11763 (2016) (cited on page 16).

[74] T. Gissibl, S. Thiele, A. Herkommer, and H. Giessen, "Two-Photon Direct Laser Writing of Ultracompact Multi-Lens Objectives", Nature Photonics **10**, 554–560 (2016) (cited on pages 16, 130).

[75] F. Klein, T. Striebel, J. Fischer, Z. Jiang, C. M. Franz, G. von Freymann, M. Wegener, and M. Bastmeyer, "Elastic Fully Three-dimensional Microstructure Scaffolds for Cell Force Measurements", Advanced Materials **22**, 868–871 (2010) (cited on page 16).

[76] J. Fischer, "Three-Dimensional Optical Lithography beyond the Diffraction Limit", Ph.D. thesis, 10.5445/IR/1000028704 (Karlsruhe Institute of Technology, Karlsruhe, 2012) (cited on pages 17, 21, 84, 87, 93).

[77] L. Yang, A. Münchinger, M. Kadic, V. Hahn, F. Mayer, E. Blasco, C. Barner-Kowollik, and M. Wegener, "On the Schwarzschild Effect in 3D Two-Photon Laser Lithography", Advanced Optical Materials **7**, 1901040 (2019) (cited on pages 17, 19, 31, 89–91, 116, 121, 122).

[78] N. Liaros and J. T. Fourkas, "Methods for Determining the Effective Order of Absorption in Radical Multiphoton Photoresists: A Critical Analysis", Laser & Photonics Reviews **15**, 2000203 (2021) (cited on pages 18, 58, 65).

[79] H. H. Winter and F. Chambon, "Analysis of Linear Viscoelasticity of a Crosslinking Polymer at the Gel Point", Journal of Rheology **30**, 367–382 (1986) (cited on pages 18, 127).

[80] M. Hippler, "3D Laser Lithography of Stimuli-Responsive Hydrogels" (Karlsruher Institut für Technologie (KIT), 2020), 152 pp. (cited on page 18).

[81] M. F. Mayer, "On Multi-Material 3D Laser Microprinting" (Karlsruher Institut für Technologie (KIT), 2020), 148 pp. (cited on pages 18, 25, 91).

[82] J. Fischer and M. Wegener, "Three-Dimensional Optical Laser Lithography beyond the Diffraction Limit: 3D Optical Lithography off Limits", Laser & Photonics Reviews **7**, 22–44 (2013) (cited on page 20).

[83] P. Kiefer, V. Hahn, M. Nardi, L. Yang, E. Blasco, C. Barner-Kowollik, and M. Wegener, "Sensitive Photoresists for Rapid Multiphoton 3D Laser Micro- and Nanoprinting", Advanced Optical Materials **8**, 2000895 (2020) (cited on pages 22, 31, 34, 59, 75, 159, 160).

[84] W. A. Green, *Industrial Photoinitiators: A Technical Guide* (CRC Press, Apr. 22, 2010), 306 pp. (cited on pages 23, 75, 76, 80, 118).

[85] B. Tieke, *Makromolekulare Chemie: eine Einführung*, 3. Aufl (Wiley-VCH, Weinheim, 2014), 392 pp. (cited on pages 24, 25).

[86] S. Beuermann and M. Buback, "Rate Coefficients of Free-Radical Polymerization Deduced from Pulsed Laser Experiments", Progress in Polymer Science **27**, 191–254 (2002) (cited on page 24).

[87] K. S. Anseth, C. N. Bowman, and N. A. Peppas, "Polymerization Kinetics and Volume Relaxation Behavior of Photopolymerized Multifunctional Monomers Producing Highly Crosslinked Networks", Journal of Polymer Science Part A: Polymer Chemistry **32**, 139–147 (1994) (cited on page 24).

[88] C. Decker and A. D. Jenkins, "Kinetic Approach of Oxygen Inhibition in Ultraviolet- and Laser-Induced Polymerizations", Macromolecules **18**, 1241–1244 (1985) (cited on pages 25, 82, 119, 121, 127, 131, 148).

[89] S. C. Ligon, B. Husár, H. Wutzel, R. Holman, and R. Liska, "Strategies to Reduce Oxygen Inhibition in Photoinduced Polymerization", Chemical Reviews **114**, 557–589 (2014) (cited on page 25).

[90] K. Obata, J. Koch, U. Hinze, and B. N. Chichkov, "Multi-Focus Two-Photon Polymerization Technique Based on Individually Controlled Phase Modulation", Optics Express **18**, 17193–17200 (2010) (cited on pages 30, 35, 39).

[91]   J. Fischer, J. B. Mueller, J. Kaschke, T. J. A. Wolf, A.-N. Unterreiner, and M. Wegener, "Three-Dimensional Multi-Photon Direct Laser Writing with Variable Repetition Rate", Optics Express **21**, 26244–26260 (2013) (cited on pages 30, 44, 64).

[92]   Z. Tomova, N. Liaros, S. A. G. Razo, S. M. Wolf, and J. T. Fourkas, "In Situ Measurement of the Effective Nonlinear Absorption Order in Multiphoton Photoresists", Laser & Photonics Reviews **10**, 849–854 (2016) (cited on page 30).

[93]   P. Bechtold, R. Hohenstein, and M. Schmidt, "Evaluation of Disparate Laser Beam Deflection Technologies by Means of Number and Rate of Resolvable Spots", Optics Letters **38**, 2934–2937 (2013) (cited on pages 32–34, 58).

[94]   H. Urey, "Spot Size, Depth-of-Focus, and Diffraction Ring Intensity Formulas for Truncated Gaussian Beams", Applied Optics **43**, 620–625 (2004) (cited on pages 32, 33, 38, 58).

[95]   C. Rensch, S. Hell, M. v Schickfus, and S. Hunklinger, "Laser Scanner for Direct Writing Lithography", Applied Optics **28**, 3754–3758 (1989) (cited on page 32).

[96]   M. Bass, C. DeCusatis, J. M. Enoch, V. Lakshminarayanan, G. Li, C. MacDonald, V. Mahajan, and E. Van Stryland, *Handbook of Optics, Volume 1.* (McGraw-Hill Professional Publishing, New York, USA, 2009) (cited on pages 32, 34, 38, 40).

[97]   Q. Hu, Z. Zhou, X. Lv, and S. Zeng, "Compensation of Spatial Dispersion of an Acousto-Optic Deflector with a Special Keplerian Telescope", Optics Letters **41**, 207–210 (2016) (cited on pages 33, 37, 38).

[98]   W. R. J. Benner, *Laser Scanners: Technologies and Applications*, 1st ed. (Pangolin Laser Systems, Inc., Nov. 27, 2016), 346 pp. (cited on page 34).

[99]   S. Maruo and K. Ikuta, "Three-Dimensional Microfabrication by Use of Single-Photon-Absorbed Polymerization", Applied Physics Letters **76**, 2656–2658 (2000) (cited on page 34).

[100] M. Farsari, G. Filippidis, K. Sambani, T. S. Drakakis, and C. Fotakis, "Two-Photon Polymerization of an Eosin Y-sensitized Acrylate Composite", Journal of Photochemistry and Photobiology A: Chemistry **181**, 132–135 (2006) (cited on page 34).

[101] N. Streibl, "Beam Shaping with Optical Array Generators", Journal of Modern Optics **36**, 1559–1573 (1989) (cited on page 35).

[102] J. L. Kreuzer, "Coherent Light Optical System Yielding an Output Beam of Desired Intensity Distribution at a Desired Equiphase Surface", U.S. pat. 3476463A (Perkin Elmer Corp, Nov. 4, 1969) (cited on pages 35, 135).

[103] D. Shafer, "Gaussian to Flat-Top Intensity Distributing Lens", Optics & Laser Technology **14**, 159–160 (1982) (cited on pages 35, 135).

[104] V. Arrizón and M. Testorf, "Efficiency Limit of Spatially Quantized Fourier Array Illuminators", Optics Letters **22**, 197–199 (1997) (cited on page 36).

[105] A. S. van de Nes, L. Billy, S. F. Pereira, and J. J. M. Braat, "Calculation of the Vectorial Field Distribution in a Stratified Focal Region of a High Numerical Aperture Imaging System", Optics Express **12**, 1281 (2004) (cited on page 37).

[106] W. Denk, D. W. Piston, and W. W. Webb, "Multi-Photon Molecular Excitation in Laser-Scanning Microscopy", in *Handbook Of Biological Confocal Microscopy*, edited by J. B. Pawley (Springer US, Boston, MA, 2006), pp. 535–549 (cited on pages 37, 119).

[107] H. Dammann, "Spectral Characteristic of Stepped-Phase Gratings", Optik **53**, 409–417 (1979) (cited on page 39).

[108] J. W. Goodman, *Introduction to Fourier Optics* (Roberts and Company Publishers, 2005), 520 pp. (cited on page 39).

[109] T. Grossmann, S. Schleede, M. Hauser, T. Beck, M. Thiel, G. von Freymann, T. Mappes, and H. Kalt, "Direct Laser Writing for Active and Passive High-Q Polymer Microdisks on Silicon", Optics Express **19**, 11451–11456 (2011) (cited on page 40).

[110] M. Bass, C. DeCusatis, J. Enoch, and Optical Society of America, *Optics: Vol. 2: Design, Fabrications and Testing, Sources and Detectors, Radiometry and Photometry.* (2009) (cited on page 40).

[111] M. T. Gale, M. Rossi, J. Pedersen, and H. Schuetz, "Fabrication of Continuous-Relief Micro-Optical Elements by Direct Laser Writing in Photoresists", Optical Engineering **33**, 3556–3566 (1994) (cited on page 40).

[112] R. W. Gerchberg and W. O. Saxton, "A Practical Algorithm for the Determination of Phase from Image and Diffraction Plane Pictures", Optik **35** (1972) (cited on page 41).

[113] F. Wyrowski, "Iterative Quantization of Digital Amplitude Holograms", Applied Optics **28**, 3864–3870 (1989) (cited on page 41).

[114] W. Dietel, J. J. Fontaine, and J.-C. Diels, "Intracavity Pulse Compression with Glass: A New Method of Generating Pulses Shorter than 60 Fsec", Optics Letters **8**, 4–6 (1983) (cited on page 45).

[115] R. L. Fork, O. E. Martinez, and J. P. Gordon, "Negative Dispersion Using Pairs of Prisms", Optics Letters **9**, 150–152 (1984) (cited on page 45).

[116] A. Franzen, *ComponentLibrary*, Feb. 14, 2012 (cited on pages 46, 85, 141).

[117] J. N. Stirman, I. T. Smith, M. W. Kudenov, and S. L. Smith, "Wide Field-of-View, Multi-Region, Two-Photon Imaging of Neuronal Activity in the Mammalian Brain", Nature Biotechnology 34, nbt.3594 (2016) (cited on page 45).

[118] R. Wartmann, "Hochaperturiges Immersionsobjektiv", German pat. 1020090-37743A1 (Zeiss Carl Microimaging Gmbh, Feb. 24, 2011) (cited on page 47).

[119] A. Münchinger, V. Hahn, D. Beutel, S. Woska, J. Monti, C. Rockstuhl, E. Blasco, and M. Wegener, "Multi-Photon 4D Printing of Complex Liquid Crystalline Microstructures by In Situ Alignment Using Electric Fields", Advanced Materials Technologies 7, 2100944 (2022) (cited on page 47).

[120] T. Frenzel, M. Kadic, and M. Wegener, "Three-Dimensional Mechanical Metamaterials with a Twist", Science 358, 1072–1074 (2017) (cited on pages 51, 54–57, 95, 96, 151).

[121] M. Kadic, G. W. Milton, M. van Hecke, and M. Wegener, "3D Metamaterials", Nature Reviews Physics 1, 198 (2019) (cited on pages 51, 158).

[122] J. K. Gansel, M. Thiel, M. S. Rill, M. Decker, K. Bade, V. Saile, G. von Freymann, S. Linden, and M. Wegener, "Gold Helix Photonic Metamaterial as Broadband Circular Polarizer", Science 325, 1513–1515 (2009) (cited on page 51).

[123] T. Frenzel, V. Hahn, P. Ziemke, J. L. G. Schneider, Y. Chen, P. Kiefer, P. Gumbsch, and M. Wegener, "Large Characteristic Lengths in 3D Chiral Elastic Metamaterials", Communications Materials 2, 1–9 (2021) (cited on pages 52, 54–57).

[124] P. Ziemke, T. Frenzel, M. Wegener, and P. Gumbsch, "Tailoring the Characteristic Length Scale of 3D Chiral Mechanical Metamaterials", Extreme Mechanics Letters, 100553 (2019) (cited on page 54).

[125] T. Frenzel, "On 3D Chiral Mechanical Metamaterials" (Karlsruher Institut für Technologie (KIT), Karlsruhe, 2020), 208 pp. (cited on page 55).

[126] L. Kong and M. Cui, "A High Throughput (>90%), Large Compensation Range, Single-Prism Femtosecond Pulse Compressor", June 20, 2013 (cited on page 55).

[127] A. Wickberg, A. Abass, H.-H. Hsiao, C. Rockstuhl, and M. Wegener, "Second-Harmonic Generation by 3D Laminate Metacrystals", Advanced Optical Materials 7, 1801235 (2019) (cited on pages 58, 95).

[128] U. T. Sanli, T. Messer, M. Weigand, L. Lötgering, G. Schütz, M. Wegener, C. Kern, and K. Keskinbora, "High-Resolution Kinoform X-Ray Optics Printed via 405 Nm 3D Laser Lithography", Advanced Materials Technologies n/a, 2101695 (2022) (cited on page 58).

[129] B. E. A. Saleh and M. C. Teich, *Fundamentals of Photonics*, red. by J. W. Goodman, Wiley Series in Pure and Applied Optics (John Wiley & Sons, Inc., New York, USA, Aug. 14, 1991) (cited on pages 58, 131).

[130] T. Aderneuer, O. Fernández, and R. Ferrini, "Two-Photon Grayscale Lithography for Free-Form Micro-Optical Arrays", Optics Express **29**, 39511–39520 (2021) (cited on pages 59, 60, 98).

[131] S. A. Self, "Focusing of Spherical Gaussian Beams", Applied Optics **22**, 658–661 (1983) (cited on page 59).

[132] J. B. Mueller, J. Fischer, Y. J. Mange, T. Nann, and M. Wegener, "In-Situ Local Temperature Measurement during Three-Dimensional Direct Laser Writing", Applied Physics Letters **103**, 123107 (2013) (cited on pages 64, 120).

[133] M. Göppert-Mayer, "Über Elementarakte Mit Zwei Quantensprüngen", Annalen der Physik **401**, 273–294 (1931) (cited on page 65).

[134] C. Decker, "Kinetic Study of Light-Induced Polymerization by Real-Time UV and IR Spectroscopy", Journal of Polymer Science Part A: Polymer Chemistry **30**, 913–928 (1992) (cited on page 67).

[135] P. Klán and J. Wirz, *Photochemistry of Organic Compounds: From Concepts to Practice* (Wiley, Chichester, West Sussex, U.K, 2009), 563 pp. (cited on pages 72, 73, 75).

[136] N. J. Turro, *Molecular Photochemistry* (W. A. Benjamin, New York, 1967) (cited on pages 72, 73, 76, 77, 81, 82, 104, 106).

[137] M. J. Jeudy and J. J. Robillard, "Spectral Photosensitization of a Variable Index Material for Recording Phase Holograms with High Efficiency", Optics Communications **13**, 25–28 (1975) (cited on page 73).

[138] Y. Kobayashi, K. Mutoh, and J. Abe, "Stepwise Two-Photon Absorption Processes Utilizing Photochromic Reactions", Journal of Photochemistry and Photobiology C: Photochemistry Reviews **34**, 2–28 (2018) (cited on page 73).

[139] Y. Kobayashi, K. Mutoh, and J. Abe, "Fast Photochromic Molecules toward Realization of Photosynergetic Effects", The Journal of Physical Chemistry Letters **7**, 3666–3675 (2016) (cited on page 73).

[140] Y. Zhang and H. Gross, "Systematic Design of Microscope Objectives. Part I: System Review and Analysis", Advanced Optical Technologies **0**, 10.1515/aot-2019-0002 (2019) (cited on pages 75, 143).

[141] Y. Zhang and H. Gross, "Systematic Design of Microscope Objectives. Part II: Lens Modules and Design Principles", Advanced Optical Technologies **8**, 349–384 (2019) (cited on page 75).

[142] M. Shimizu, M. Schelper, K. Mochida, T. Hiyama, M. Adachi, Y. Sasaki, S. Akiyama, S. Maeda, H. Kanbara, Y. Mori, and T. Kurihara, "A Novel Strategy for Two-Photon Holographic Recording: Stepwise Two-Photon Absorption of α-Quinquethiophene Followed by Energy Transfer to an Aryl Azide", Advanced Materials **19**, 1826–1829 (2007) (cited on page 76).

[143] K. Hirabayashi, H. Kanbara, Y. Mori, T. Kurihara, M. Shimizu, and T. Hiyama, "Multilayer Holographic Recording Using a Two-Color-Absorption Photopolymer", Applied Optics **46**, 8402–8410 (2007) (cited on page 76).

[144] J. H. Brannon and D. Magde, "Absolute Quantum Yield Determination by Thermal Blooming. Fluorescein", The Journal of Physical Chemistry **82**, 705–709 (1978) (cited on page 76).

[145] Q. Shen and K. Hagen, "Gas-Phase Molecular Structure and Conformation of Benzil as Determined by Electron Diffraction", The Journal of Physical Chemistry **91**, 1357–1360 (1987) (cited on page 80).

[146] C. J. Brown and R. Sadanaga, "The Crystal Structure of Benzil", Acta Crystallographica **18**, 158–164 (1965) (cited on page 80).

[147] L. Flamigni, F. Barigelletti, S. Dellonte, and G. Orlandi, "Photophysical Properties of Benzil in Solution: Triplet State Deactivation Pathways", Journal of Photochemistry **21**, 237–244 (1983) (cited on pages 80, 81).

[148] A. A. Lamola and G. S. Hammond, "Mechanisms of Photochemical Reactions in Solution. XXXIII. Intersystem Crossing Efficiencies", The Journal of Chemical Physics **43**, 2129–2135 (1965) (cited on pages 80, 120).

[149] D. J. Morantz and A. J. C. Wright, "Structures of the Excited States of Benzil and Related Dicarbonyl Molecules", The Journal of Chemical Physics **54**, 692–697 (1971) (cited on pages 80, 81).

[150] W. G. McGimpsey and J. C. Scaiano, "A Two-Photon Study of the "Reluctant" Norrish Type I Reaction of Benzil", Journal of the American Chemical Society **109**, 2179–2181 (1987) (cited on pages 81, 82).

[151] T.-S. Fang, R. E. Brown, C. L. Kwan, and L. A. Singer, "Photophysical Studies on Benzil. Time Resolution of the Prompt and Delayed Emissions and a Photokinetic Study Indicating Deactivation of the Triplet by Reversible Exciplex Formation", The Journal of Physical Chemistry **82**, 2489–2496 (1978) (cited on pages 81, 82).

[152] A. P. Darmanyan, C. S. Foote, and P. Jardon, "Interaction of Singlet Oxygen with Peroxy and Acylperoxy Radicals", The Journal of Physical Chemistry **99**, 11854–11859 (1995) (cited on pages 81, 82, 127).

[153] T. Cáceres, M. V. Encinas, and E. A. Lissi, "Photocleavage of Benzil", Journal of Photochemistry **27**, 109–114 (1984) (cited on pages 81, 82).

[154] M. Mukai, S. Yamauchi, and N. Hirota, "A Time-Resolved EPR Study of One- and Two-Photon Processes in the Photochemical Reactions of Benzil", The Journal of Physical Chemistry 93, 4411–4413 (1989) (cited on page 82).

[155] H. L. J. Bäckström and K. Sandros, "The Quenching of the Long-Lived Fluorescence of Biacetyl in Solutions", Acta Chemica Scandinavica 12, 823–832 (1958) (cited on pages 82, 105, 114, 118, 119).

[156] W. M. Nau and J. C. Scaiano, "Oxygen Quenching of Excited Aliphatic Ketones and Diketones", The Journal of Physical Chemistry 100, 11360–11367 (1996) (cited on pages 82, 127).

[157] P. Gijsman, "A Review on the Mechanism of Action and Applicability of Hindered Amine Stabilizers", Polymer Degradation and Stability, Modification, Degradation and Stabilisation of Polymers: Concepts and Applications (MoDeSt 2016) 145, 2–10 (2017) (cited on pages 82, 128).

[158] R. B. Grubbs, "Nitroxide-Mediated Radical Polymerization: Limitations and Versatility", Polymer Reviews 51, 104–137 (2011) (cited on page 83).

[159] A. S. Tatikolov, P. P. Levin, T. A. Kokrashvili, and V. A. Kuz'min, "Quenching of the Triplet States of Carbonyl Compounds by Nitroxyl Radicals", Bulletin of the Academy of Sciences of the USSR Division of Chemical Science 32, 465–468 (1983) (cited on page 83).

[160] L. J. Johnston, M. Tencer, and J. C. Scaiano, "Evidence for Hydrogen Transfer in the Photochemistry of 2,2,6,6-Tetramethylpiperidine N-oxyl", The Journal of Organic Chemistry 51, 2806–2808 (1986) (cited on page 83).

[161] K. Ikuta, S. Maruo, and S. Kojima, "New Micro Stereo Lithography for Freely Movable 3D Micro Structure-Super IH Process with Submicron Resolution", in Proceedings MEMS 98. IEEE. Eleventh Annual International Workshop on Micro Electro Mechanical Systems. An Investigation of Micro Structures, Sensors, Actuators, Machines and Systems (Cat. No. 98CH36176) (Jan. 1998), pp. 290–295 (cited on pages 90, 98).

[162] M. T. Do, T. T. N. Nguyen, Q. Li, H. Benisty, I. Ledoux-Rak, and N. D. Lai, "Submicrometer 3D Structures Fabrication Enabled by One-Photon Absorption Direct Laser Writing", Optics Express 21, 20964–20973 (2013) (cited on pages 90, 98).

[163] S.-H. Hsu, T. Chi, J. Kim, P. Somers, B. W. Boudouris, X. Xu, and L. Pan, "High-Speed One-Photon 3D Nanolithography Using Controlled Initiator Depletion and Inhibitor Transport", Advanced Optical Materials 10, 2102262 (2022) (cited on pages 90, 98).

[164] P. Mueller, M. Thiel, and M. Wegener, "3D Direct Laser Writing Using a 405 Nm Diode Laser", Optics Letters 39, 6847–6850 (2014) (cited on pages 92, 94, 98).

[165] A. Wickberg, "On Second-Harmonic Generation in Nanolaminates and 3D Nanolaminated Photonic Crystals" (Karlsruher Institut für Technologie (KIT), 2019) (cited on pages 93, 95).

[166] M. Deubel, "Three-Dimensional Photonic Crystals via Direct Laser Writing: Fabrication and Characterization" (2006) (cited on page 93).

[167] M. Deubel, G. von Freymann, M. Wegener, S. Pereira, K. Busch, and C. M. Soukoulis, "Direct Laser Writing of Three-Dimensional Photonic-Crystal Templates for Telecommunications", Nature Materials 3, 444–447 (2004) (cited on pages 93, 94).

[168] N. Otsu, "A Threshold Selection Method from Gray-Level Histograms", IEEE Transactions on Systems, Man, and Cybernetics 9, 62–66 (1979) (cited on page 94).

[169] S. H. Park, T. W. Lim, D.-Y. Yang, R. H. Kim, and K.-S. Lee, "Improvement of Spatial Resolution in Nano-Stereolithography Using Radical Quencher", Macromolecular Research 14, 559–564 (2006) (cited on page 94).

[170] W. Haske, V. W. Chen, J. M. Hales, W. Dong, S. Barlow, S. R. Marder, and J. W. Perry, "65 Nm Feature Sizes Using Visible Wavelength 3-D Multiphoton Lithography", Optics Express 15, 3426–3436 (2007) (cited on page 94).

[171] M. Thiel, J. Fischer, G. von Freymann, and M. Wegener, "Direct Laser Writing of Three-Dimensional Submicron Structures Using a Continuous-Wave Laser at 532 Nm", Applied Physics Letters 97, 221102 (2010) (cited on pages 94, 98).

[172] I. Sakellari, E. Kabouraki, D. Gray, V. Purlys, C. Fotakis, A. Pikulin, N. Bityurin, M. Vamvakaki, and M. Farsari, "Diffusion-Assisted High-Resolution Direct Femtosecond Laser Writing", ACS Nano 6, 2302–2311 (2012) (cited on page 94).

[173] P. Urbancová, D. Pudiš, A. Kuzma, M. Goraus, P. Gašo, and D. Jandura, "IP-Dip-based Woodpile Structures for VIS and NIR Spectral Range: Complex PBG Analysis", Optical Materials Express 9, 4307–4317 (2019) (cited on page 94).

[174] P. Delrot, D. Loterie, D. Psaltis, and C. Moser, "Single-Photon Three-Dimensional Microfabrication through a Multimode Optical Fiber", Optics Express 26, 1766–1778 (2018) (cited on page 98).

[175] M. Kuramoto, S. Kobayashi, T. Akagi, K. Tazawa, K. Tanaka, K. Nakata, and T. Saito, "Watt-Class Blue Vertical-Cavity Surface-Emitting Laser Arrays", Applied Physics Express 12, 091004 (2019) (cited on page 98).

[176] J. Fischer, G. von Freymann, and M. Wegener, "The Materials Challenge in Diffraction-Unlimited Direct-Laser-Writing Optical Lithography", Advanced Materials **22**, 3578–3582 (2010) (cited on page 98).

[177] Y. Lee and M. Song, "Adaptive Color Selection to Limit Power Consumption for Multi-Object GUI Applications in OLED-Based Mobile Devices", Energies **13**, 2425 (2020) (cited on page 99).

[178] G. Lazarev, P.-J. Chen, J. Strauss, N. Fontaine, and A. Forbes, "Beyond the Display: Phase-Only Liquid Crystal on Silicon Devices and Their Applications in Photonics [Invited]", Optics Express **27**, 16206–16249 (2019) (cited on pages 104, 132).

[179] K. Eriks, T. D. Hayden, S. H. Yang, and I. Y. Chan, "Crystal and Molecular Structure of Biacetyl (2,3-Butanedione), (H3CCO)2, at -12 and -100 °C", Journal of the American Chemical Society **105**, 3940–3942 (1983) (cited on page 104).

[180] G. A. Burdock, *Fenaroli's Handbook of Flavor Ingredients* (CRC Press, Dec. 3, 2004), 2041 pp. (cited on page 104).

[181] G. M. Almy, H. Q. Fuller, and G. D. Kinzer, "The Fluorescence of Diacetyl", The Journal of Chemical Physics **8**, 37–45 (1940) (cited on pages 105, 127, 128).

[182] M. B. Rubin, "Photochemistry of o-Quinones and α-Diketones", in Photochemistry, edited by J. L. R. Williams, M. B. Rubin, L. B. Jones, V. K. Jones, C. v. Sonntag, E. Koerner von Gustorf, and F.-W. Grevels, Fortschritte Der Chemischen Forschung (1969), pp. 251–306 (cited on page 105).

[183] B. M. Monroe, "The Photochemistry of α-Dicarbonyl Compounds", in *Advances in Photochemistry*, Vol. 8 (John Wiley & Sons, Ltd, 1971), pp. 77–108 (cited on page 105).

[184] M. B. Rubin, "Recent Photochemistry of α-Diketones", in Photochemistry and Organic Synthesis, Topics in Current Chemistry (1985), pp. 1–56 (cited on page 105).

[185] H. L. J. Bäckström, K. Sandros, J.-E. Lindgren, E. Varde, and G. Westin, "Transfer of Triplet State Energy in Fluid Solutions. I. Sensitized Phosphorescence and Its Application to the Determination of Triplet State Lifetimes.", Acta Chemica Scandinavica **14**, 48–62 (1960) (cited on page 105).

[186] G. N. Lewis and M. Kasha, "Phosphorescence and the Triplet State", Journal of the American Chemical Society **66**, 2100–2116 (1944) (cited on page 105).

[187] J. W. Sidman and D. S. McClure, "Electronic and Vibrational States of Biacetyl and Biacetyl-d6 I. Electronic States", Journal of the American Chemical Society **77**, 6461–6470 (1955) (cited on pages 105, 134).

[188] M. Almgren, "The Natural Phosphorescence Lifetime of Biacetyl and Benzil in Fluid Solution", Photochemistry and Photobiology **6**, 829–840 (1967) (cited on pages 105, 114, 120, 123).

[189] G. M. Almy and P. R. Gillette, "The Quantum Yield of Diacetyl Fluorescence", The Journal of Chemical Physics **11**, 188–195 (1943) (cited on page 105).

[190] A. Singh, A. R. Scott, and F. Sopchyshyn, "Flash Photolysis of Camphorquinone and Biacetyl", The Journal of Physical Chemistry **73**, 2633–2643 (1969) (cited on pages 105, 106, 112, 120).

[191] A. Horowitz and J. G. Calvert, "Emission Studies of the Mechanism of Gaseous Biacetyl Photolysis at 3450, 3650, 3880, and 4358 a and 28°C", International Journal of Chemical Kinetics **4**, 207–227 (1972) (cited on page 105).

[192] C. O. Concheanainn and H. W. Sidebottom, "Temperature Dependence of the Triplet Lifetime of Biacetyl in the Gas Phase", Journal of Photochemistry **13**, 55–66 (1980) (cited on pages 105, 119).

[193] R. Bensasson and E. J. Land, "Triplet-Triplet Extinction Coefficients via Energy Transfer", Transactions of the Faraday Society **67**, 1904 (1971) (cited on pages 106, 112).

[194] T. Hanemann and K. Honnef, "Optical and Thermomechanical Properties of Doped Polyfunctional Acrylate Copolymers", Polymers **10**, 337 (2018) (cited on page 109).

[195] I. M. Irshadeen, S. L. Walden, M. Wegener, V. X. Truong, H. Frisch, J. P. Blinco, and C. Barner-Kowollik, "Action Plots in Action: In-Depth Insights into Photochemical Reactivity", Journal of the American Chemical Society **143**, 21113–21126 (2021) (cited on pages 112, 113, 159).

[196] C. C. Badcock, H. W. Sidebottom, J. G. Calvert, B. R. Rabe, and E. K. Damon, "Triplet-Triplet Annihilation Reaction in Biacetyl Vapor Excited at 4365 Ang and 25.Deg.", Journal of the American Chemical Society **94**, 19–24 (1972) (cited on page 117).

[197] C. Richard, M. Bouchy, J. C. Andre, and M. Niclause, "Radiationless Transitions between Excited Singlet States of Biacetyl", International Journal of Chemical Kinetics **10**, 213–226 (1978) (cited on page 117).

[198] S. M. Wolf, "Applied Photochemistry for Multicolor Photolithography" (2018) (cited on pages 117–119, 128).

[199] J. C. Scaiano, "Intermolecular Photoreductions of Ketones", Journal of Photochemistry **2**, 81–118 (1973) (cited on page 118).

[200] S. A. Greenberg and L. S. Forster, "The Photolysis of Biacetyl Solutions [1]", Journal of the American Chemical Society **83**, 4339–4344 (1961) (cited on page 118).

[201] E. Andrzejewska, L.-Å. Lindén, and J. F. Rabek, "The Role of Oxygen in Camphorquinone-Initiated Photopolymerization", Macromolecular Chemistry and Physics **199**, 441–449 (1998) (cited on page 119).

[202] Y. Sawaki and C. S. Foote, "Mechanism of Photoepoxidation of Olefins with .Alpha.-Diketones and Oxygen", The Journal of Organic Chemistry **48**, 4934–4940 (1983) (cited on page 119).

[203] N. Uppal and P. S. Shiakolas, "Modeling of Temperature-Dependent Diffusion and Polymerization Kinetics and Their Effects on Two-Photon Polymerization Dynamics", Journal of Micro/Nanolithography, MEMS, and MOEMS **7**, 043002 (2008) (cited on page 119).

[204] J. Lemaire, "Photoenolization of Biacetyl", The Journal of Physical Chemistry **71**, 2653–2660 (1967) (cited on page 120).

[205] L. F. Shampine and M. W. Reichelt, "The MATLAB ODE Suite", SIAM Journal on Scientific Computing **18**, 1–22 (1997) (cited on page 124).

[206] R. E. Schwerzel and R. A. Caldwell, "Quenching of Excited States by Stable Free Radicals. II. Mechanism of Triplet Quenching by Di-Tert-Butyl Nitroxide", Journal of the American Chemical Society **95**, 1382–1389 (1973) (cited on page 127).

[207] E. A. Lissi and M. V. Encina, "Polymerization Photosensitized by Carbonyl Compounds", Journal of Polymer Science: Polymer Chemistry Edition **17**, 2791–2803 (1979) (cited on page 127).

[208] P. Debye, "Reaction Rates in Ionic Solutions", Transactions of The Electrochemical Society **82**, 265 (1942) (cited on page 127).

[209] Y. Sawaki, "Mechanistic Study on the Photo-Oxidation of α-Diketones: Interaction of Triplet α-Diketones with Oxygen", Tetrahedron **41**, 2199–2205 (1985) (cited on page 128).

[210] B. Richter, V. Hahn, S. Bertels, T. K. Claus, M. Wegener, G. Delaittre, C. Barner-Kowollik, and M. Bastmeyer, "Guiding Cell Attachment in 3D Microscaffolds Selectively Functionalized with Two Distinct Adhesion Proteins", Advanced Materials **29**, 1604342 (2016) (cited on page 130).

[211] T. Kurihara and Y. Takaki, "Using Electronic Holography to Generate Speckle-Free and Shaded Reconstructed Images", in , edited by H. I. Bjelkhagen and V. M. Bove (Mar. 1, 2013), 86440E (cited on page 132).

[212] Texas Instruments Incorporated, *System Design Considerations Using TI DLP® Technology in UVA*, Application Report DLPA060A (Texas Instruments Incorporated, Jan. 2020), p. 15 (cited on page 132).

[213] R. McCluney, *Introduction to Radiometry and Photometry* (Artech House, Boston, 1994), 402 pp. (cited on page 135).

[214] F. M. Dickey, *Laser Beam Shaping: Theory and Techniques, Second Edition* (CRC Press, June 23, 2014), 592 pp. (cited on page 135).

[215] J. W. Goodman, *Speckle Phenomena in Optics: Theory and Applications* (Roberts and Company Publishers, 2007), 422 pp. (cited on page 135).

[216] O. E. Olarte, J. Andilla, E. J. Gualda, and P. Loza-Alvarez, "Light-Sheet Microscopy: A Tutorial", Advances in Optics and Photonics **10**, 111–179 (2018) (cited on page 136).

[217] I. Powell, "Design of a Laser Beam Line Expander", Applied Optics **26**, 3705–3709 (1987) (cited on page 136).

[218] S. Saghafi, K. Becker, C. Hahn, and H.-U. Dodt, "3D-ultramicroscopy Utilizing Aspheric Optics", Journal of Biophotonics **7**, 117–125 (2014) (cited on page 136).

[219] R. Shi, W. Kleinschmidt, G. Herbst, H. Richter, and C. Hoyer, "Immersion Objective and Light Microscope", German pat. 102012007359B3 (Carl Zeiss Microscopy GmbH, Oct. 2, 2013) (cited on pages 143, 164).

[220] J. H. Campbell, N. Nicole, O. Stein, Y. Liu, Y. Lu, and L. Jiang, "Three-Dimensional Printing and Deformation Behavior of Low-Density Target Structures by Two-Photon Polymerization", in Nanoengineering: Fabrication, Properties, Optics, and Devices XIV, edited by E. M. Campo, E. A. Dobisz, and L. A. Eldada (Aug. 31, 2017), p. 66 (cited on page 148).

[221] Y. Chen, M. Kadic, and M. Wegener, "Roton-like Acoustical Dispersion Relations in 3D Metamaterials", Nature Communications **12**, 3278 (2021) (cited on page 151).

[222] J. F. Arnett, G. Newkome, W. L. Mattice, and S. P. McGlynn, "Excited Electronic States of the .Alpha.-Dicarbonyls", Journal of the American Chemical Society **96**, 4385–4392 (1974) (cited on page 152).

[223] F. Mayer, S. Richter, J. Westhauser, E. Blasco, C. Barner-Kowollik, and M. Wegener, "Multimaterial 3D Laser Microprinting Using an Integrated Microfluidic System", Science Advances **5**, eaau9160 (2019) (cited on pages 153, 159).

[224] M. P. de Beer, H. L. van der Laan, M. A. Cole, R. J. Whelan, M. A. Burns, and T. F. Scott, "Rapid, Continuous Additive Manufacturing by Volumetric Polymerization Inhibition Patterning", Science Advances 5, eaau8723 (2019) (cited on page 153).

[225] K. S. Anseth, S. M. Newman, and C. N. Bowman, "Polymeric Dental Composites: Properties and Reaction Behavior of Multimethacrylate Dental Restorations", in *Biopolymers II*, Vol. 122, edited by N. A. Peppas and R. S. Langer, red. by A. Abe, H. Benoit, H.-J. Cantow, P. Corradini, K. Dušek, S. Edwards, H. Fujita, G. Glöckner, H. Höcker, H.-H. Hörhold, H.-H. Kausch, J. P. Kennedy, J. L. Koenig, A. Ledwith, J. E. McGrath, L. Monnerie, S. Okamura, C. G. Overberger, H. Ringsdorf, T. Saegusa, J. C. Salamone, J. L. Schrag, and G. Wegner, Advances in Polymer Science (Springer Berlin Heidelberg, Berlin, Heidelberg, 1995), pp. 177–217 (cited on page 153).

[226] B. Wang, E. Engay, P. R. Stubbe, S. Z. Moghaddam, E. Thormann, K. Almdal, A. Islam, and Y. Yang, "Stiffness Control in Dual Color Tomographic Volumetric 3D Printing", Nature Communications 13, 367 (2022) (cited on page 153).

[227] A. S. Quick, A. de los Santos Pereira, M. Bruns, T. Bückmann, C. Rodriguez-Emmenegger, M. Wegener, and C. Barner-Kowollik, "Rapid Thiol-Yne-Mediated Fabrication and Dual Postfunctionalization of Micro-Resolved 3D Mesostructures", Advanced Functional Materials 25, 3735–3744 (2015) (cited on page 159).

[228] C. E. Hoyle and C. N. Bowman, "Thiol–Ene Click Chemistry", Angewandte Chemie International Edition 49, 1540–1573 (2010) (cited on page 159).

[229] P. V. Braun and M. L. Brongersma, "Photochemistry Democratizes 3D Nanoprinting", Nature Photonics 15, 871–873 (2021) (cited on page 159).

[230] C. L. Benson, G. Triulzi, and C. L. Magee, "Is There a Moore's Law for 3D Printing?", 3D Printing and Additive Manufacturing, 10.1089/3dp.2017.0041 (2018) (cited on page 160).

Acknowledgments

> ...standing on the shoulders of giants.
>
> *Sir Isaac Newton*

It is my pleasure to thank the many people who have made this thesis possible.

First, I would like to thank Prof. Dr. Martin Wegener for the opportunity of doing research with him on this exciting topic. His support in any regard has been outstanding at all times.

Likewise, I have enjoyed the continuous collaboration with Jun.-Prof. Dr. Eva Blasco, who kindly agreed to co-referee this thesis. I am incredibly grateful for the chemical expertise that she shared with me.

I would further like to thank the many collaborators I had the opportunity to work with at the Institute of Applied Physics. Dr. Joachim Fischer and Dr. Benjamin Richter provided me with valuable scientific and professional advice early on. Dr. Patrick Müller and Dr. Jingyuan Qu lend me a hand while assembling the multi-focus 3D printer. Qinglei Hu from Huazhong University of Science and Technology provided us with optics for the dispersion-compensating telescope. Dr. Tobias Frenzel printed many of the tetragonal metamaterial structures, allowing me to work on other projects.

I thank Tobias Messer for taking his time and rebuilding the setup in Lab 3 with me. I am grateful for the ultrathin cuts and the 3D reconstructions prepared by Ronald Curticean, Dr. Irene Wacker, and Prof. Dr. Rasmus Schröder (Ruprecht Karl University of Heidelberg). Further, I thank Dr. Max Bojanowski for answering my short-witted chemistry questions.

I would like to thank Dr. Tobias Schlöder, Dr. Philipp Jöckle, Prof. Dr. Andreas Neil-Unterreiner, and Prof. Dr. Christopher Barner-Kowollik for stimulating discussions on photochemistry. I am highly indebted to Dr. Rhiannon Batchelor and Dr. Martina Nardi. They kindly synthesized, purified, and analyzed chemicals for me. Throughout my thesis, I also appreciated Alexander Münchinger's visits in the lab and the inspiring discussions I had with him. Dr. Robert Schwerzel kindly shared his memories of Wyn Kelly Swainson and the early days of 3D printing with me, which I highly appreciated.

Research at the Institute of Applied Physics would have been impossible without